2D AND 3D ANALYSIS ON THE DEFORMATION AND FRACTURE OF COMMERCIALLY PURE MAGNESIUM

By MICHAEL J. NEMCKO, B. Eng.

A Thesis Submitted to the School of Graduate Studies in Partial Fulfilment of the Requirements for the Degree Doctor of Philosophy

McMaster University DOCTOR OF PHILOSOPHY (2015) Hamilton, Ontario

(Department of Materials Science and Engineering)

TITLE: 2D and 3D Analysis on the Deformation and Fracture of Commercially Pure Magnesium

AUTHOR: Michael J. Nemcko, B.Eng. (McMaster University)

SUPERVISOR: Professor David S. Wilkinson

NUMBER OF PAGES: xxxi, 264

Abstract

Carbon dioxide emissions from the transportation sector contribute 25% of Canada's total greenhouse gas emissions. As a result, the automotive industry aims to reduce emissions by reducing vehicle weight. Magnesium is an excellent candidate for a lightweight structural material. However, the lack of active deformation modes at room temperature limits its formability. This research uses several approaches to examine the deformation and fracture behavior of commercially pure magnesium to help guide the development of materials with acceptable properties.

The first approach uses in-situ tensile testing coupled with electron microscopy, applied to thin sheet samples with pre-drilled holes in the gage section. The results reveal the heterogeneous nature of deformation leading to fracture dominated by twin and grain boundary related failure. This is qualitatively different from the damage processes observed in FCC materials such as aluminum and copper. As a consequence, classical theories cannot be used to predict ductile fracture in magnesium.

The second approach involves in-situ tensile testing under optical microscopy. Here digital image correlation is used to determine the strain distribution on the surface. Localized deformation is observed at twin and grain boundaries. The results introduce a length scale which is not present in classical continuum theories. Therefore, a crystal plasticity finite element approach is employed to understand the role of the deformation mechanisms during deformation.

The last approach couples in-situ tensile testing with x-ray microtomography to observe the fracture processes in sheet materials without pre-drilled holes. Twin and grain boundaries again dominate damage nucleation. Once nucleated voids show rapid growth and linkage. The final fracture occurs by a macroscopic shearing process related to the crystallographic texture.

In summary, this project demonstrates how fracture in magnesium is fundamentally different from that in non-HCP metals and what approaches can be used to fully understand this.

Acknowledgements

To begin, I would like to express gratitude to my supervisor Dr. David S. Wilkinson for his support and guidance during my graduate studies. His unique supervision philosophy gave me the freedom to explore my own ideas. In addition to his research expertise, he also gave me valuable advice concerning my career. I enjoyed getting to know Dr. Wilkinson during his Honorary Symposium in Jamaica.

I thank my supervisory committee members Dr. Marek Niewczas and Dr. Hatem Zurob for their contributions and interesting discussions during our supervisory committee meetings.

I would also like to express my appreciation to Dr. Peidong Wu and his students Dr. Huamiao Wang and Hua Qiao for allowing me to use their crystal plasticity finite element code.

Funding for this project was contributed by the Magnesium Network. I thank Dr. Warren Poole for providing the sheet material, and his student Hanqing Che as well as Dr. Zohreh Keshavarz for rolling the sheet at the University of British Columbia.

I acknowledge Dr. Arnaud Weck and his student Jean-Michel Guay for use of the laser facilities at the University of Ottawa. In addition, I thank Dr. Harold Haugen and his student Dr. Eugene Hsu for use of the laser facilities at McMaster University.

I thank the following people for technical support: Jim Garrett, Chris Butcher, Doug Culley, Ed McCaffery, Connie Barry and Kjell Lapperre.

Many interesting discussions concerning this work were carried out with the following people: Dr. Jidong Kang, Dr. Guilhem Martin, Dr. Mosei Bruhis, Dr. Akihide Hosokawa, Dr. Fumiaki Hiura, Dr. Arnaud Weck, Dr. Eric Maire, Yaning Hu, Mahdi Habibnejad and Jing Li.

I would like to express gratitude to my summer student Pauline Mas for helping me develop the experimental technique dealing with the digital image correlation method and enlightening me on French culture.

Finally I would like to acknowledge my friends and family for their support.

Table of Contents

List of Figures

List of Tables

Chapter 1

Introduction

Magnesium and magnesium alloys have gained significant interest over the past decade for use in lightweight components. The low density (1.74g/cm^3) and relatively high specific strength of magnesium make it an excellent candidate as a lightweight structural material, particularly in the automotive, aerospace and defense industries. However, magnesium has a hexagonal-close packed (HCP) crystal structure, which leads to limited ductility prior to fracture at room temperature. As a result, high temperatures are required to form magnesium into complex components and energy costs associated with heat generation are incorporated into the processing route. The current motivation of magnesium research is to produce components with acceptable strength and formability while developing an economically feasible processing route. This can be achieved through effective alloy design strategies or modification of the microstructure using deformation processing. However, one must understand the deformation and fracture mechanisms which govern the formability of these materials, to determine how to alter the microstructure and processing routes, in order to produce materials with enhanced properties. As a result, the deformation and fracture mechanisms of magnesium must be understood in fine detail before one can fully exploit its use in industry.

Ductile fracture in metallic materials involves the nucleation, growth and linkage of microvoids. In general, void nucleation occurs at heterogeneities in the microstructure. Therefore, in alloys void nucleation typically occurs at second phase particles by two mechanisms: decohesion of the particle-matrix interface and particle cracking. However, void nucleation has also been observed to occur at other interfaces, such as twin and grain boundaries. In addition, the process of nucleation is stochastic and strongly dependent on the microstructure of the material. Once a void has nucleated, the stress free surface causes local stress and strain concentrations in the adjacent plastic field. As deformation continues the void experiences volumetric growth as well as a shape change. Voids grow in a plastically deforming matrix until they link with other voids, leading to the final failure of the material. Void linkage is the most important process in ductile fracture as it dictates the ductility of the material. However, void linkage in magnesium materials is difficult to predict due to the stochastic nature of the process and the anisotropic mechanical behavior of magnesium.

The objective of this project is to understand the deformation and fracture mechanisms in commercially pure magnesium on the microstructural level. A variety of characterization, experimental and modelling techniques are used to study these mechanisms in fine detail. The data provides detailed information on the microstructural aspects of deformation and fracture which can be used as a guideline for alloy development. Furthermore, the experimental results are used in this work to aid in the development of a crystal plasticity modelling approach.

The thesis has been organized in the following manner. A literature review of deformation and fracture mechanisms as well as characterization and modelling techniques are presented in Chapter 2. The experimental procedures used in the thesis, which consist of three different approaches, are described in Chapter 3. These approaches break down the chapters to follow. In Chapter 4 the heterogeneous nature of deformation is observed through in-situ tensile testing under an Environmental Scanning Electron Microscope (ESEM). The heterogeneous deformation is quantified in Chapter 5 using the digital image correlation method for strain mapping. In-situ tensile testing is carried out under an optical microscope in order to maximize the surface pattern contrast. The experimental results are compared with a crystal plasticity finite element approach. In Chapter 6 x-ray microtomography is used to study the 3D nature of fracture and to compare the fracture characteristics observed within the bulk of the material with the surface observations from the previous chapters. The main conclusions are summarized in Chapter 7 along with some comments on potential future work.

Chapter 2

Literature Review

2.1 Introduction

A variety of materials characterization, experimental testing and modelling techniques have been used in this project to study the deformation and fracture behavior of magnesium. In ductile materials, a significant amount of plastic deformation takes place before the final failure. Deformation is a crystallographic process and thus deformation depends on the kind of crystal structure exhibited by a material. As a result, the first part of the literature review will provide a brief overview of the HCP crystal system and introduce important planes and directions which will be referred to throughout the thesis. The second section will give a detailed review of the deformation mechanisms in magnesium with emphasis on room temperature properties. Once an understanding of deformation mechanisms has been developed the fracture mechanisms of metallic materials will be addressed in the third section. Experimental and modelling approaches are presented along with their limitations. The last section of the literature review will focus on the main characterization techniques employed in this project and present recent studies using these techniques to investigate magnesium alloy systems.

2.2 HCP Crystallography

The Miller-Bravais index system is used throughout the thesis to characterize directions and planes. Figure 2.1 shows some significant planes and directions in the hexagonal system. The close packed directions belong to the $\langle\bar{2}110\rangle$ set of directions. Planes of type $\{hki0\}$ intercept the basal plane at 90°. These are called prism planes which can be classified into two types. Type I prism planes are of the form $\{01\bar{1}0\}$ while Type II prism planes are represented by $\{11\bar{2}0\}$. In addition, planes of the type $\{hkin\}$, where n≠0, are known as pyramidal planes (Partridge, 1967). The magnitude of n determines the order of the plane.

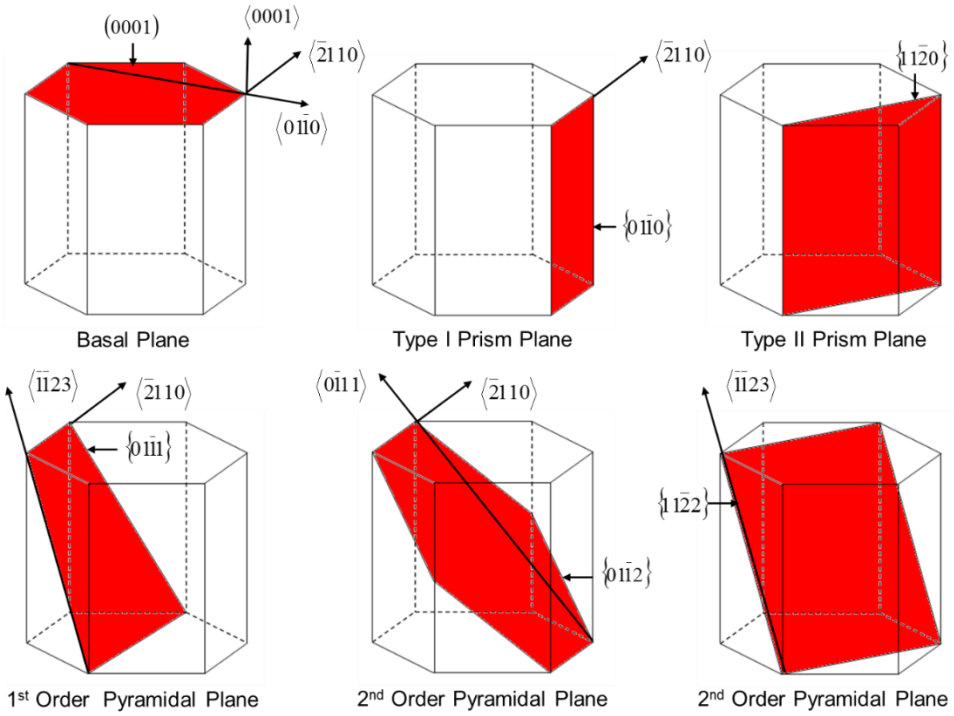

Figure 2.1: Important planes and directions in the HCP system.

2.3 Deformation Mechanisms in Magnesium

A significant amount of plastic deformation is required prior to fracture. This section will review the deformation mechanisms in the magnesium system. The three main deformation mechanisms observed in magnesium at ambient temperature include dislocation slip, twinning and grain boundary sliding. As a result, emphasis will be placed on these mechanisms.

2.3.1 Dislocation Slip

Slip initiates on a specific plane when the shear stress resolved on the plane reaches a critical value. This value is known as the critical resolved shear stress (CRSS) (Dunne and Petrinic, 2005). An extensive amount of research has been carried out on precisely oriented magnesium single crystals in order to obtain CRSS values for the various slip systems. Table 2.1 shows the CRSS values for the main slip systems reported in magnesium along with their respective references.

Basal <a> slip is the dominant deformation mechanism in magnesium at room temperature due to its low CRSS. However, this slip system only provides two independent slip systems out of the necessary five (Mises, 1928; Taylor, 1932). As a result, strain incompatibilities arise at grain boundaries in polycrystalline samples when basal <a> slip is the only active deformation mechanism. When the grain boundaries are strong enough, additional stresses occur to maintain strain compatibility between grains. This compatibility stress results in stress concentrations at the grain boundaries, which are

sufficient to activate other deformation mechanisms such as non-basal slip and twins. Kobayashi et al. (2003) confirmed this phenomenon through the observation of dislocations using transmission electron microscopy (TEM) in an equal-channel angular-extruded AZ31 magnesium alloy with an average grain size of 50 μm. They found that non-basal dislocations were generated in a region within several microns from the grain boundaries at a tensile strain of 2 percent. The results provide insight into the magnitude of the compatibility stresses as they are large enough to activate these slip systems.

Table 2.1: CRSS values for the slip systems reported in magnesium systems.

Burgers Vector	Slip Plane	Slip Direction	CRSS (MPa)	Reference
<a>	{0001} Basal	$\langle 11\bar{2}0 \rangle$	2	Reed-Hill and Robertson, 1957
<a>	$\{1\bar{1}00\}$ Type I Prismatic	$\langle 11\bar{2}0 \rangle$	45	Akhtar and Teghtsoonian, 1969
<c+a>	$\{11\bar{2}2\}$ 2nd Order Pyramidal	$\langle 11\bar{2}3 \rangle$	50	Obara et al., 1973

Type I Prismatic <a> slip has been reported at room temperature by several authors (Agnew and Duygulu, 2003; Ohyama et al., 2004). Koike and Ohyama (2005) provided evidence of prismatic <a> slip through slip trace analysis in a rolled AZ61 magnesium alloy with an average grain size of 20 μm. The results showed that when the basal planes are tilted by more than 16.5˚ towards the tensile axis, basal <a> slip is the dominant deformation mechanism and an elongation of 8 percent is obtained. Otherwise, prismatic <a> slip became a dominant deformation mechanism and elongations greater than 20

percent were obtained. The results indicate that the ductility is enhanced when prismatic <a> slip is activated. However, prismatic <a> slip only provides two independent slip systems and when activated along with basal <a> slip, there are still only a total of four independent slip systems. The results pose the question of whether <a> dislocations are capable of producing good ductility without satisfying the von Mises criterion. Tensile strain is accommodated by the reduction of the cross sectional area of a sample. This reduction is controlled by the thickness and width strain. In rolled magnesium sheet with a strong basal texture, the width strain is produced by prismatic <a> slip while the thickness strain is produced by pyramidal <c+a> slip and twinning. As a result, it may be argued that a positive tensile strain can be accommodated by a negative width strain through the activation of prismatic slip and that no thickness strain is required.

There are few reports which indicate the activation of 2nd Order Pyramidal <c+a> slip at room temperature (Agnew et al., 2001). Obara et al. (1973) utilized slip trace analysis to identify pyramidal slip in magnesium single crystals. The results indicate that the work hardening rate associated with this deformation mechanism was very high. It has been suggested that <c+a> dislocations are split into mobile <a> and immobile <c> components. Therefore, the activation of pyramidal slip appears to cause negative effects on the ductility. Other studies have shown that this slip system is possible but its contribution to the total strain is negligible. Therefore, it has been established that the anisotropic nature of dislocation slip in magnesium requires additional deformation mechanisms to ensure continuity throughout the microstructure at room temperature.

2.3.2 Deformation Twinning

Twinning is an essential deformation mechanism which is required to accommodate strain incompatibilities along the c-axis in magnesium. Several twin systems have been reported extensively in literature including $\{10\bar{1}2\}$, $\{10\bar{1}1\}$ and $\{10\bar{1}1\}$-$\{10\bar{1}2\}$ double twins. The dominant twinning mode in magnesium is the $\{10\bar{1}2\}$ twin system. This twin system is activated when the applied load is either in tension parallel to the c-axis or in compression perpendicular to the c-axis. These twins will be referred to as extension twins since they result in extension of the c-axis. The CRSS for extension twinning in magnesium single crystals has been reported as 2 MPa at room temperature (Reed-Hill and Robertson 1957; Miura et al., 2005). As a result, this twin system is easily activated at room temperature and is a dominant deformation mechanism in magnesium. Extension twins reorient the basal plane 86.3 degrees from the undistorted matrix. Barnett (2007a) studied the tensile behavior of extruded AZ31 with two orientations. One sample was fabricated such that the majority of the grains were oriented for c-axis extension and the other was oriented for c-axis compression. Figure 2.2 shows the stress-strain behavior of single crystals for these orientations. The effects of $\{10\bar{1}2\}$ twinning on the strain hardening behavior are apparent in the sample oriented for c-axis extension. The initial section of the stress-strain curve represents the activation of extension twins. During twinning the stress remains virtually steady, rising rapidly to failure once it was complete. It has been argued that extension twins accommodate strain incompatibilities along the c-axis and thus increase the uniform elongation in magnesium alloys.

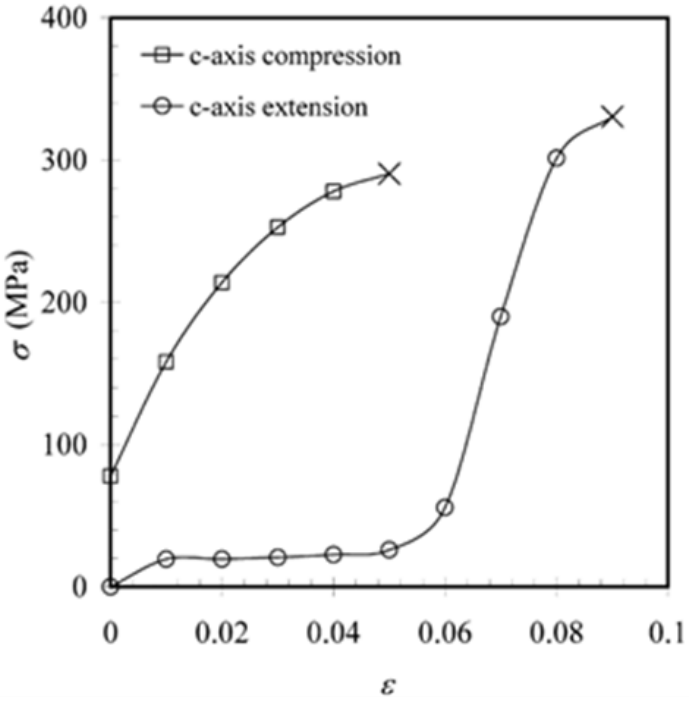

Figure 2.2: Stress strain behavior of single crystals oriented for c-axis extension and compression (Schmid and Boas, 1968).

Other types of twins observed in magnesium that are reported in the literature are $\{10\bar{1}1\}$ twins and $\{10\bar{1}1\}$-$\{10\bar{1}2\}$ double twins. The $\{10\bar{1}1\}$ twin system is activated when the applied load is either tension perpendicular to the c-axis or compression parallel to the c-axis. Therefore, these twins are referred to as contraction twins since they result in contraction of the c-axis. Wonsiewicz and Backofen (1967) attempted to determine the CRSS for the $\{10\bar{1}1\}$ twins and found that the CRSS value varies from 76 – 153 MPa, depending on the direction of the applied stress. The orientation dependence led to the conclusion that there is no clear CRSS law for this twin system. Contraction twins reorient the basal plane 56˚ from the original matrix. In addition, once a contraction twin has

nucleated the resulting microstructure within the twinned volume is oriented such that there is a tensile component along the c-axis. Therefore, $\{10\bar{1}2\}$ twins can occur inside the contraction twins resulting in a $\{10\bar{1}1\}$-$\{10\bar{1}2\}$ double twin. This process is illustrated in Figure 2.3. Double twins reorient the basal plane 37.5˚ from the undistorted matrix. As a result, for materials with a strong rolling texture, the matrix inside the double twin is oriented preferentially for basal slip, a similar case to that of primary contraction twins. This produces a local softening effect which has been reported to contribute significantly to deformation and fracture.

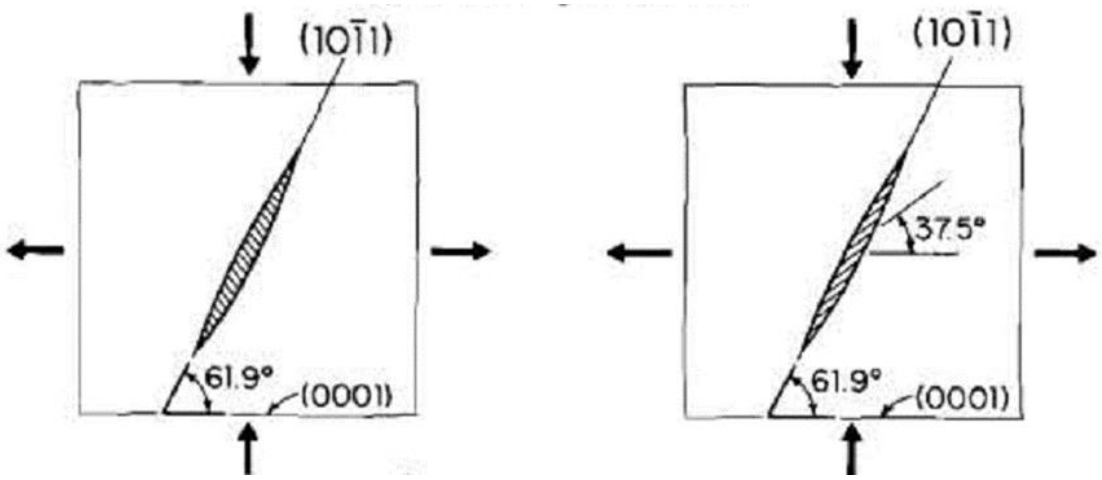

(a) (b)

Figure 2.3: Schematic of the double twinning process (a) twinning on $\{10\bar{1}1\}$ followed by (b) retwinning along $\{10\bar{1}2\}$ (Wonsiewicz and Backofen, 1967).

Kelley and Hosford (1968) carried out channel die compression tests on single crystals in order to assess the anisotropic mechanical behavior of magnesium. In these detailed experiments they applied the load and constrained several orientations, in order to isolate the various deformation mechanisms associated with each orientation. Furthermore,

slip trace analysis was carried out to identify the deformation mechanisms observed in each case. Figure 2.4 shows the stress strain response of each orientation. The results show that the crystallographic orientation has a significant impact on the stress strain response. This is particularly useful to keep in mind during the deformation of polycrystals with a range of textures. The deformation of polycrystalline magnesium is analogous to pulling a composite composed of hard and soft orientations. Therefore, large strain concentrations may be expected at grain boundaries between these relatively hard and soft orientations due to incompatibility. This may lead to grain boundary sliding or the initiation of damage which will be covered in the review to follow.

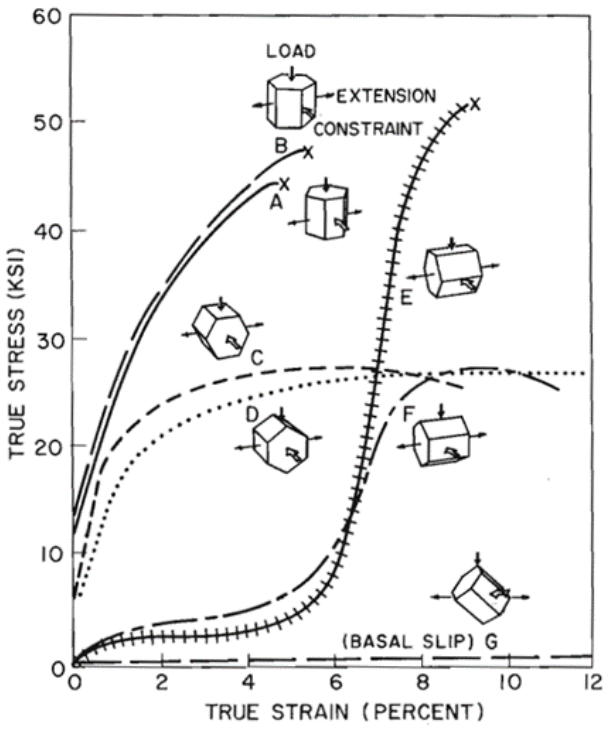

Figure 2.4: Stress strain response for various orientations of magnesium single crystals loaded in channel die compression (Kelley and Hosford, 1968).

2.3.3 Grain Boundary Sliding

Grain boundary sliding (GBS) contributes to plastic deformation at room temperature through the accommodation of concentrated stresses at grain boundaries. Koike et al. (2003) provided experimental evidence of GBS which is shown in Figure 2.5. The figure shows a focused ion-beam (FIB) image of rolled AZ31 sheet deformed at room temperature to 10 percent. Lines were etched by FIB on the polished surface prior to deformation. After a deformation of 10 percent, a discontinuous shift of the lines can be seen at grain boundaries indicating GBS. The contribution of GBS to the total strain was determined by measuring the surface step height at the grain boundary locations, using a laser microscope. The ratio between the GBS strain and total strain was found to be 8 percent. There is limited data on the role of grain boundary sliding at room temperature and as a result, further work is required to comment on the role it plays in deformation.

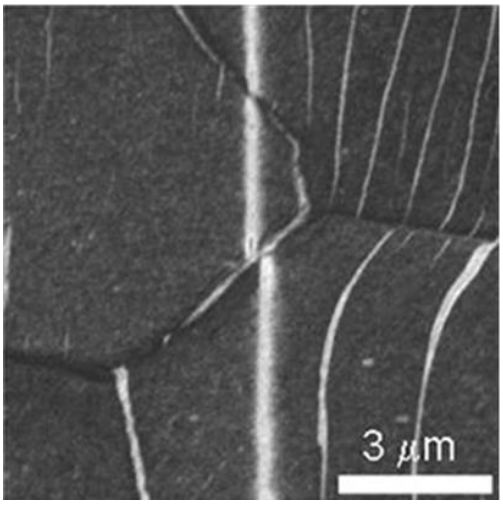

Figure 2.5: FIB image of a sample of AZ31 rolled sheets after a tensile deformation to 10 percent at room temperature (Koike et al., 2003).

2.4 Damage and Fracture in Magnesium

The yielding and deformation behavior of magnesium and its alloys is well documented in the literature. However, research focused on the damage and fracture of magnesium materials is sparse. Ductile fracture in metals typically occurs by the nucleation, growth and linkage of voids. As a result, this section will review the literature devoted to each of these processes in magnesium systems at ambient temperature.

2.4.1 Void Nucleation in Magnesium

Void nucleation in metallic alloys is typically associated with second phase particles and inclusions. However, it has been reported that void nucleation in magnesium alloy systems is not always associated with particles (Calhoun and Stoloff, 1970; Lhuissier et al., 2012). Microstructural heterogeneities such as grain boundaries (Greenwood et al., 1954; Goods and Brown, 1979) and twin boundaries (Hartt and Reed-Hill, 1967; Barnett, 2007b) have been identified as nucleation sites in the absence of particle associated damage nucleation. Barnett (2007b) has characterized contraction and double twins using electron backscatter diffraction (EBSD) patterning in an extruded ZK60 magnesium alloy. A twin-like void parallel to existing contraction twins and double twins is shown in Figure 2.6. The results provide evidence that voids were associated with these twins. Void nucleation can be explained in terms of shear localization within the twinned region which results in intense compatibility stresses and nucleation of damage to accommodate this stress. Studies in the literature have emphasized the role of contraction and double twins on void

nucleation (Hartt and Reed-Hill, 1967; Barnett, 2007b). However, there are relatively few studies devoted to understanding the role of the more common extension twin system on void nucleation. Furthermore, the relationship between grain boundary sliding and void formation at room temperature is not well understood in magnesium systems.

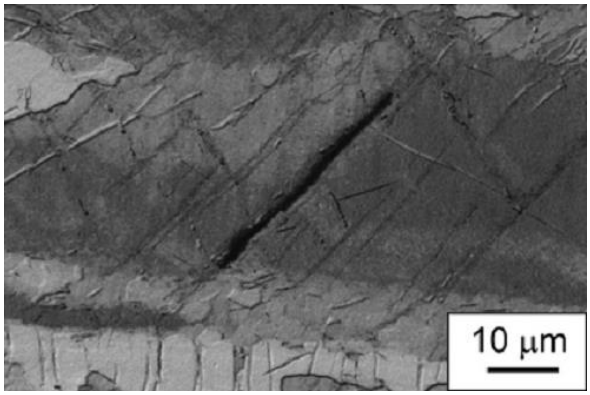

Figure 2.6: Twin-like void parallel to existing twins in ZK60 magnesium alloy (Barnett, 2007).

2.4.2 Void Growth in Magnesium

The mechanism of void growth in magnesium systems is not well established at ambient temperature. However, it has been reported that dislocation creep as well as grain boundary sliding play a role in cavity growth at elevated temperatures (Lhuissier et al., 2012). Based on the temperature dependence of the CRSS values of the various slip systems in magnesium, one may speculate that dislocation creep does not play such a crucial role at room temperature. Kang et al. (2013) provided evidence that the crack path is insensitive to the particle distribution during V-bending of AZ31B sheet material carried out at ambient temperature. The results suggest that twin and grain boundaries also play a role on crack

propagation. Somekawa et al. (2009) showed that twin boundaries create strain localizations and sites for crack propagation in coarse grained alloys during fracture toughness tests. EBSD was used to reveal the microstructure adjacent to the crack tip. It was established that extension twins were primarily responsible for the damage and Figure 2.7 shows several extension twins in the vicinity of the crack tip.

Figure 2.7: EBSD results near crack tip region after the fracture toughness test (Somekawa et al., 2009).

This result is expected due to the relatively low CRSS of the twin system. However, the contribution of extension twins to fracture is not reported as extensively in the literature.

2.4.3 Void Linkage in Magnesium

Void linkage is a difficult process to capture experimentally as it occurs within the bulk of the material. However, several authors reported on this phenomenon in magnesium systems using X-ray tomography (Barnett et al., 2008; Steglich and Morgeneyer, 2013; Kang et al., 2013). Steglich and Morgeneyer (2013) showed that void linkage occurs by void sheeting in Kahn specimens tested at room temperature. In addition, Kang and coworkers (2013) provided evidence of the shear nature of fracture in AZ31 tested in uniaxial tension at ambient temperature. Figure 2.8 shows the macroscopic shear nature of fracture in AZ31 as well as the flat "penny" shaped voids observed in the vicinity of the fractured surface. Voids of this nature were also reported by Barnett and coworkers (2008). However, there is controversy in the literature with respect to the formation of these voids. Therefore, a detailed study is required to understand the origin and linkage of these voids.

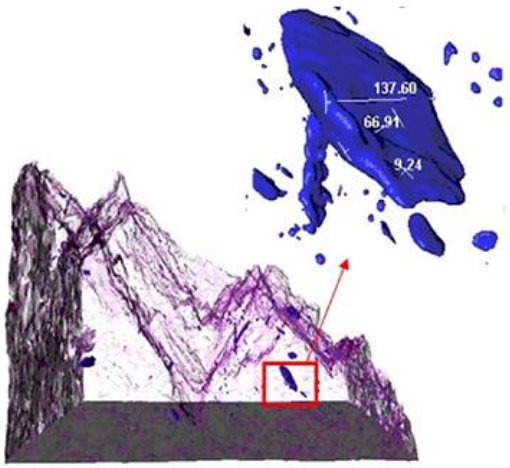

Figure 2.8: 3D model of a fractured AZ31 tensile sample showing the shape and size of a void under the surface (Kang et. al., 2013).

2.5 Ductile Fracture in Metallic Materials

Ductile fracture in metals typically occurs by the nucleation, growth and coalescence of voids within the bulk of the material. However, this phenomenon is difficult to model due to the stochastic nature of fracture. This section introduces previous experimental work as well as modeling attempts for each phase of fracture. The experiments and models will be discussed in terms of their range of applicability.

2.5.1 Void Nucleation in Metallic Materials

Void nucleation can be characterized as homogeneous or heterogeneous (Goods and Brown, 1979). Homogeneous nucleation occurs within grains without any apparent association with second phase particles, boundaries or surface irregularities. Alternatively, heterogeneous nucleation is associated with inhomogeneities in the microstructure such as grain boundaries, second phase particles and twin boundaries. Heterogeneous nucleation is most commonly encountered in industry because most engineering materials contain second phase particles. It has been established that voids generally nucleate at second phase particles through two mechanisms; decohesion of the particle-matrix interface and particle cracking. Figure 2.9 illustrates these two modes of void nucleation in a 6061 aluminum alloy containing a dispersion of Al_2O_3 second phase particles.

For a given particle-matrix interface strength and particle strength, parameters that determine which nucleation mechanism dominates include the matrix flow properties (yield strength and hardening capacity), particle aspect ratio and loading orientation, the particle-

matrix stiffness mismatch and the state of stress (Benzerga and Leblond, 2010). Table 2.2 summarizes the general trends which are currently accepted throughout the field of ductile fracture.

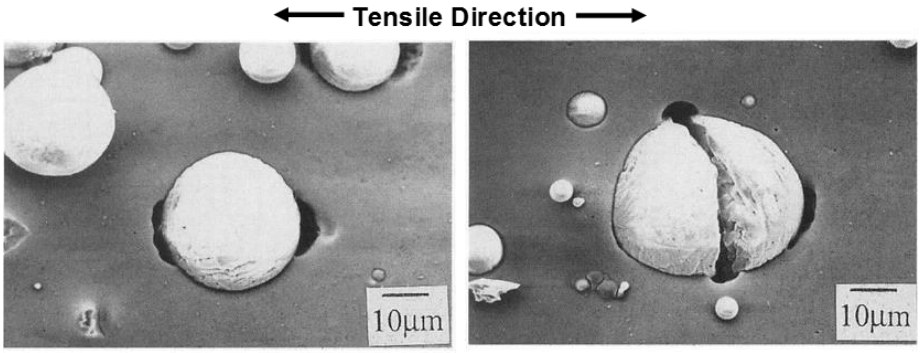

(a) (b)

Figure 2.9: Modes of void nucleation by (a) interface decohesion and (b) particle cracking (Kanetake et al., 1995).

Table 2.2: Relative trends upon increasing the parameter on the nucleation mechanism (Benzerga and Leblond, 2010).

Parameter	Type	Trend	
		Decohesion	Cracking
Matrix yield strength		↘	↗
Matrix hardening exponent		↘	↗
Particle elongation		↘	↗
Particle stiffness		↗	↗
Load orientation	Axial	↘	↗
	Transverse	↗	↘
Load triaxiality		↗	↘

Babout et al. (2004) investigated the effect of the matrix properties on void nucleation in an aluminum matrix reinforced with hard ceramic particles under uniaxial loading. The stress triaxiality, defined as the ratio of the mean stress to the equivalent stress, is 1/3 for such loading conditions. Commercially pure aluminum was used as the soft matrix and a 2124 aluminum alloy was used to simulate a hard matrix. They used in situ X-ray computed microtomography to detect the nucleation process. The tomographs are shown in Figure 2.10. In the soft matrix, particle-matrix decohesion was found to be the dominant mechanism of void nucleation Figure 2.10(a). In contrast, particle cracking occurred more frequently in the hard matrix Figure 2.10(b) (Babout et al., 2004).

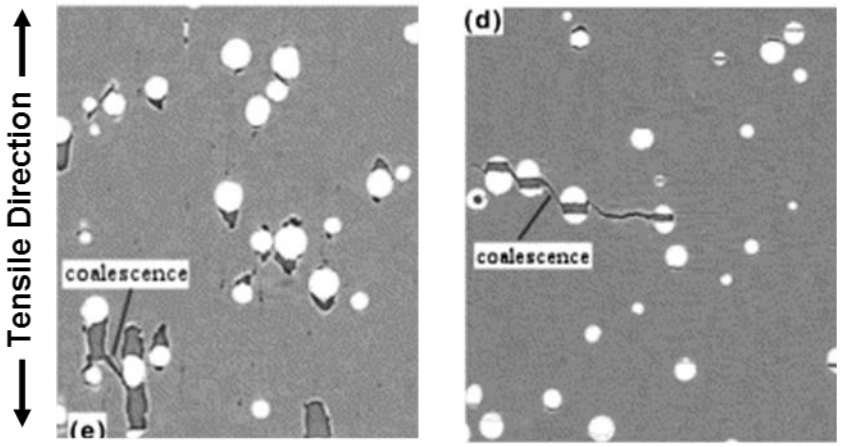

(a) (b)

Figure 2.10: Tomographs of (a) interface decohesion (soft matrix) and (b) particle cracking (hard matrix) (Babout et al., 2004).

Although the nucleation process has been studied extensively in the literature and the mechanisms are well understood, some of the most complex modeling problems in the theory of ductile fracture are associated with the nucleation of voids at second phase

particles. Second phase particles can range from ~0.01 μm to >>1 μm. Dislocation models are required for particles < 1 μm since the interaction of individual dislocations with particles on this scale has a significant impact on the local flow stress (Brown and Stobbs, 1976; Goods and Brown, 1979). On the contrary, continuum models can be adopted for particles > 1 μm since the local work hardening behavior around the particle is on a scale much greater than the average dislocation spacing (Argon et al., 1975; Argon and Im, 1975). In addition, particles vary in shape and these effects must be considered in the models. Most magnesium alloys contain particles which are larger than 1 μm. As a result, the continuum approach will be discussed in more detail.

A necessary condition for void nucleation to occur by particle-matrix decohesion is that the elastic strain energy released by the particle is at least equal to the surface energy created by the new interface. However, it has been found that this condition is likely to be satisfied at the onset of deformation for particles larger than ~0.025 μm (Tanaka et al., 1970). Therefore, there must be an additional condition, such as that a critical normal stress must be attained at the particle-matrix interface. Argon and co-workers (1975) proposed the following criterion:

$$\bar{\sigma} + \Sigma_m = min(\sigma^d, \sigma^c) \tag{2.1}$$

where $\bar{\sigma}$ is the effective stress and $\Sigma_m$is the mean normal remote stress. σ^d and σ^c are the interface strength and brittle strength of the particle, respectively. These values were obtained through experimental measurements (Argon and Im, 1975).

Void nucleation by particle cracking generally occurs in particles with large aspect ratios which are elongated in the direction of maximum principal strain and particles that initially contain flaws (Le Roy et al., 1981). Elongated particles are subjected to fiber loading effects which can lead to the buildup of a large axial tensile stress and premature fracture (Barnby, 1967). For relatively equiaxed particles which are initially damaged, the critical stress required for damage propagation can be approximated by the Griffith equation:

$$\sigma_f = A\sqrt{\frac{2E\gamma}{\pi c}} \tag{2.2}$$

where E is Youngs modulus, γ is the fracture surface energy, c is the length of the initial crack and A is a geometrical constant (Griffith, 1921). For a specified critical stress there exists a critical flaw size for which particle failure occurs. Therefore, an increase in particle size will promote premature cracking, since the probability of a particle containing a crack of critical length will increase with particle size (Thomason, 1990).

2.5.2 Void Growth in Metallic Materials

Once a void has nucleated, the stress-free surface causes local stress and strain concentrations in the adjacent plastic field (Thomason, 1990). As deformation proceeds the void will experience volumetric growth as well as a shape change. Early studies of ductile fracture examined void growth with standard metallographic techniques (Puttick, 1959; Cox and Low, 1974). The experiments allow for a qualitative assessment on the effect of

plastic strain and stress state on void growth. However, this technique does not provide information on the growth history of a given void and does not consider the 3D distribution of voids within the bulk of the material.

The first landmark study on void growth in nonlinear solids was the pioneering work of F.A. McClintock (1968a). McClintock provided an analytical solution for the expansion of a cylindrical void in a strain hardening cylindrical representative volume element as shown in Figure 2.11. The solution utilized the von Mises yield criterion given by:

$$f = \frac{1}{2} s_{ij} s_{ij} - \frac{Y^2}{3} \tag{2.3}$$

where f defines the yield surface, s_{ij} is the deviatoric stress tensor and Y is the uniaxial yield stress.

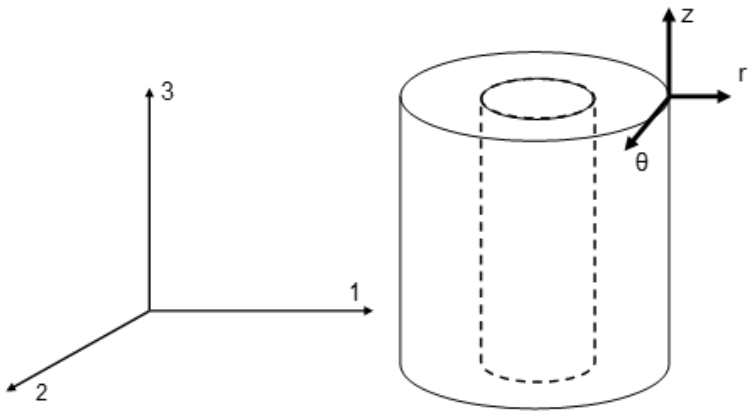

Figure 2.11: Cylindrical hole in a representative volume element.

The continuity condition and normality rule are two fundamental principles required to derive the laws of plastic flow. The continuity condition states that any stress increment whose path is located on the yield surface produces zero plastic strain increment. Furthermore, Drucker's postulate of stability establishes that any additional stress imposed on an element in an initial state of stress, will cause the additional stress to do positive work if a plastic strain increment occurs (Drucker, 1960). It follows from this postulate that the plastic strain increment must be normal to the yield surface.

The continuity condition along with the normality rule allow for the attainment of the following flow rule (Reuss, 1930):

$$\dot{\varepsilon}_{ij}^{p} = \dot{\lambda}\frac{\partial f}{\partial s_{ij}} = \dot{\lambda}s_{ij} \tag{2.4}$$

where $\dot{\varepsilon}_{ij}^{p}$ is the plastic strain rate tensor and $\dot{\lambda}$ is a scalar factor of proportionality related to the rate of plastic work, and therefore depends on the complete deformation history. Equations (2.3) and (2.4) were used to determine the constitutive relation at the micro level (Hill, 1950):

$$\dot{\varepsilon}_{ij}^{p} = \frac{3}{2}\frac{\dot{\bar{\varepsilon}}^{p}}{Y}s_{ij} \tag{2.5}$$

where $\dot{\bar{\varepsilon}}^{p}$ is the effective plastic strain rate. The radial stress for a given increment of hole growth was found by the substitution of Equation (2.5) into the equilibrium equation in cylindrical coordinates. The result is given by Equation (2.6).

$$\frac{\partial \sigma_{rr}}{\partial r} = -\frac{2Y}{3r}\frac{(\dot{\varepsilon}_{rr} - \dot{\varepsilon}_{\theta\theta})}{\dot{\bar{\varepsilon}}^{p}} \tag{2.6}$$

where r is the radius of the representative volume element, and σ and ε are the local stresses and strain rates respectively in cylindrical coordinates. The local strain rate equations were derived from the velocity field that is produced by a cylindrical hole growing inside a cylindrical representative volume element (Li, 2008). The resulting equations are:

$$\dot{\varepsilon}_{rr} = \frac{d\dot{u}_r}{dr} = -\frac{a^2}{r^2}\left(\frac{\dot{a}}{a} + \frac{\dot{\varepsilon}_z}{2}\right) - \frac{\dot{\varepsilon}_z}{2} \tag{2.7a}$$

$$\dot{\varepsilon}_{\theta\theta} = \frac{\dot{u}_r}{r} = \frac{a^2}{r^2}\left(\frac{\dot{a}}{a} + \frac{\dot{\varepsilon}_z}{2}\right) - \frac{\dot{\varepsilon}_z}{2} \tag{2.7b}$$

$$\dot{\varepsilon}_{zz} = \frac{d\dot{u}_z}{dz} = \dot{\varepsilon}_z \tag{2.7c}$$

where a is the radius of the void. Substitution of Equation (2.7a) and (2.7b) into Equation (2.6) and integration over the radial direction from the void surface to infinity yields McClintock's solution. The solution is given by:

$$\frac{da}{a} = \frac{\sqrt{3}}{2}|d\varepsilon_z| \sinh\left(\frac{\sqrt{3}\sigma_\infty}{Y}\right) - \frac{1}{2}d\varepsilon_z \tag{2.8}$$

where σ_∞ is the remote radial stress. Several simplifying assumptions can be made to yield the solution in Cartesian coordinates along with the effects of strain hardening. This is given by Equation (2.9).

$$\ln\left(\frac{R}{R_0}\right) = \frac{\sqrt{3}\bar{\varepsilon}^p}{2(1-n)}\sinh\left(\frac{\sqrt{3}(1-n)}{2}\frac{(\sigma_1+\sigma_2)}{\bar{\sigma}}\right) + \frac{\varepsilon_1+\varepsilon_2}{2} \tag{2.9}$$

where R and R_0 are the average and initial average radius of the void respectively and n is the strain hardening exponent.

Weck and Wilkinson (2008) studied void growth in 2D model materials which consisted of sheet materials containing laser drilled holes. Void growth was quantified through tensile testing coupled with electron microscopy. The history of void growth was captured with measurements obtained in increments during deformation. Figure 2.12 shows the ESEM images that were taken at various far field true strain values. The voids were measured at each increment of deformation and the average local strain was plotted as a function of the far field strain. The results are plotted in Figure 2.13.

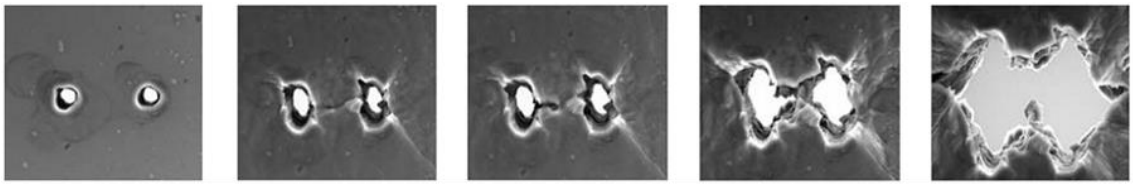

Figure 2.12: ESEM images of deformation history of two voids in an aluminum 5052 alloy at various values of far field true strain. (a) 0.000, (b) 0.204, (c) 0.213, (d) 0.220 and (e) 0.223 (Weck and Wilkinson, 2008).

The McClintock model predicts void growth at low applied far-field strains. However, the model clearly deviates from the results at high strains. This can be attributed to the

interactions between voids. The interaction of voids results in an amplification in void growth while the McClintock model does not consider void interactions.

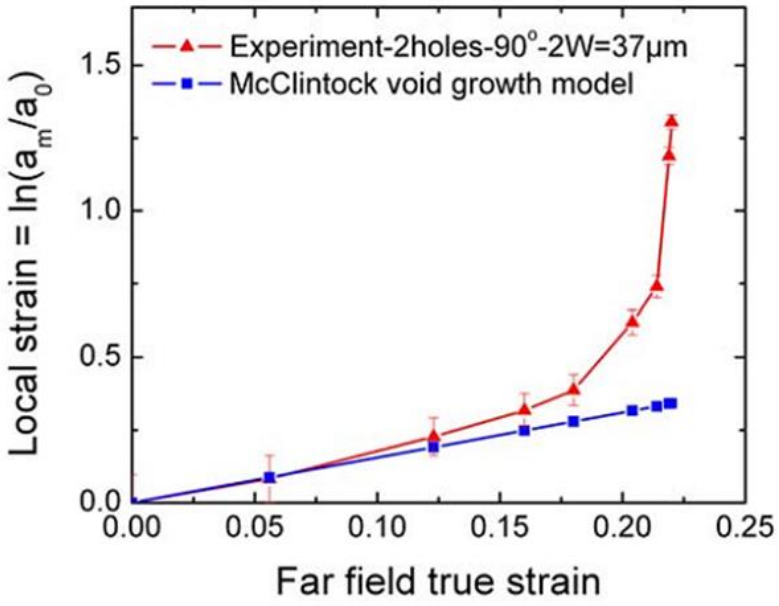

Figure 2.13: Comparison between the McClintock model for void growth and experimental results (Weck and Wilkinson, 2008).

Rice and Tracey (1969) developed a solution for the growth of an initially spherical void in a rigid plastic material. The case of a spherical void is a more realistic approach. A variational principle was established to characterize the flow field in an elastically rigid, incompressible, plastic material containing voids, subjected to a remotely uniform stress and strain rate field. The resulting functional has the form:

$$Q(\dot{u}) = \int_V \left[s_{ij}(\dot{\varepsilon}) - s_{ij}^{\infty}\right]\dot{\varepsilon}_{ij}dV - \sigma_{ij}^{\infty}\int_{S_V} n_i \dot{u}_j dS \tag{2.10}$$

where the first term represents the elastic strain energy and the second term is the input work from surface tractions. Therefore, Q is a measure of the energy release rate and the objective is to seek a velocity function that minimizes the total energy of the system. The Rayleigh Ritz method was employed to approximate a velocity field. The velocity field $\dot{u}_i$ was divided into three parts: (i) a velocity field resulting in a uniform strain rate field which satisfies the remote boundary conditions $\dot{\varepsilon}_{ij}^{\infty} x_j$, (ii) a spherically symmetric velocity field corresponding to volumetric growth of the void without a change in shape $\dot{u}_i^D$, and (iii) a velocity field, which changes the void shape but not its volume $\dot{u}_i^E$. The resulting velocity field is given by:

$$\dot{u}_i = \dot{\varepsilon}_{ij}^{\infty} x_j + D\dot{u}_i^D + E\dot{u}_i^E \tag{2.11}$$

where D and E are the amplification factors associated with volumetric and shape changes respectively. The amplification factors were determined so as to minimize the functional Q. The following are numerical solutions for the values of D and E which have been validated by experiments.

- $1 + E \approx \frac{5}{3}$ for linear hardening materials and low values of mean stress with non-hardening materials.
- $1 + E \approx 2$ for high values of mean stress with non-hardening materials.
- $D = 0.75 \frac{\sigma_m}{\bar{\sigma}}$ for linear hardening materials.
- $D = 0.558 \sinh\left(\frac{3}{2}\frac{\sigma_m}{\bar{\sigma}}\right) + 0.008v \cosh\left(\frac{3}{2}\frac{\sigma_m}{\bar{\sigma}}\right)$ for non-hardening materials.

The strain rate field was characterized in terms of the principal components such that $\dot{\varepsilon}_1 \geq \dot{\varepsilon}_2 \geq \dot{\varepsilon}_3$, by the load variable v given by:

$$v = -\frac{3\dot{\varepsilon}_2}{\dot{\varepsilon}_1 - \dot{\varepsilon}_3} \tag{2.12}$$

v = 1 for uniaxial tension, 0 for pure shear and -1 for biaxial tension. The load variable can be used to rewrite the principal strain rates in terms of the maximum value. The solution for the growth rate of the void in the principal strain rate directions 1, 2 and 3 is of the form:

$$\dot{R}_K = \left\{(1+E)\dot{\varepsilon}_K + \left(\frac{2}{3}\dot{\varepsilon}_L\dot{\varepsilon}_L\right)^{1/2} D\right\} R \tag{2.13}$$

where (K,L) = 1, 2, 3. This strictly applies to the case of a perfectly spherical void and upon integration of the equation under conditions where the void no longer remains spherical it is necessary to replace R by R_{mean}.

$$R = R_{mean} = exp\left(\frac{2\sqrt{3+v}}{(3+v)} D\varepsilon_1\right) R_0 \tag{2.14}$$

Substitution of Equation (2.14) into (2.13) and integration along the respective strain paths yields the expressions for the principal radii of the void given by Equations 2.16(a-c):

$$A = exp\left(\frac{2\sqrt{v^2+3}}{3+v} D\varepsilon_1\right) \tag{2.15a}$$

$$B = \left(\frac{1+E}{D}\right)(A-1) \tag{2.15b}$$

$$R_1 = \left(A + \frac{(3+v)}{2\sqrt{v^2+3}}B\right)R_0 \tag{2.16a}$$

$$R_2 = \left(A - \frac{vB}{\sqrt{v^2+3}}\right)R_0 \tag{2.16b}$$

$$R_3 = \left(A + \frac{(v-3)}{2\sqrt{v^2+3}}B\right)R_0 \tag{2.16c}$$

The Rice and Tracey model emphasizes the effects of stress triaxiality on void growth. Hosokawa et al. (2013) studied the 3D growth of an array of voids using in situ X-ray computed tomography. The model material used in the investigation consisted of several sheets containing holes embedded in hole free sheets, to simulate holes embedded in the bulk of the material. These will be referred to as 3D model materials in the discussion to follow. Figure 2.14 shows the 3D reconstruction of two voids in a copper matrix taken at various far field strain increments. The dimensions of the voids were measured in the three principal directions and compared to the Rice and Tracey void growth model. The results are shown in Figure 2.15. The Rice and Tracey model predicted the void growth in the tensile direction throughout deformation. In addition, the experimental results are in agreement with the lateral behavior of the model until a critical point in deformation at which lateral expansion of the voids initiates. This phenomenon exists for low values of triaxiality (Worswick and Pick, 1990; Hosokawa et al., 2012) and is strongly associated with void interactions. Therefore, this deviation from the model is expected. Hosokawa

(2011) has defined this point in deformation as the coalescence strain. The interaction of voids with the microstructure or other voids is critical in the development of void growth models.

The void growth models presented were significant in advancing the field of solid mechanics. However, these numerical techniques are not used as frequently today due to the development of the finite element method. More recent void growth studies employ the use of the finite element method to predict the growth behavior (McMeeking and Hom, 1990; Keralavarma et al., 2011).

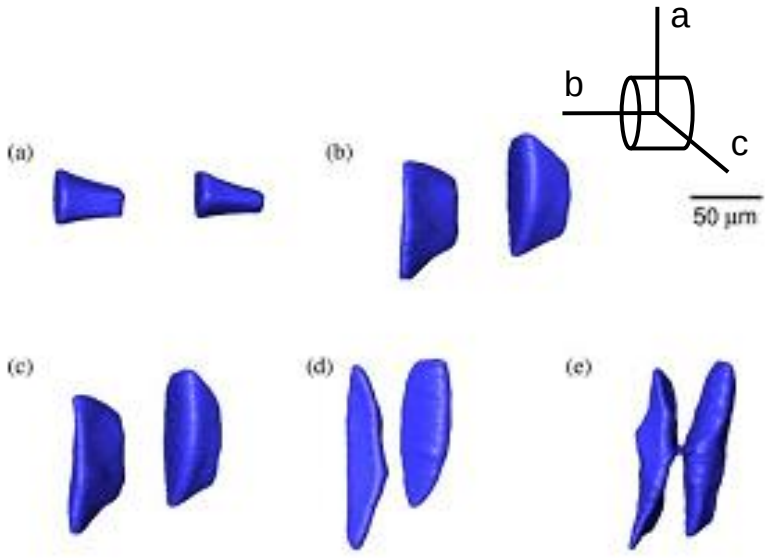

Figure 2.14: 3D reconstruction of two voids at various far field strain values (a) 0 (b) 0.44 (c) 0.51 (d) 0.61 (e) 0.96 (Hosokawa, 2011).

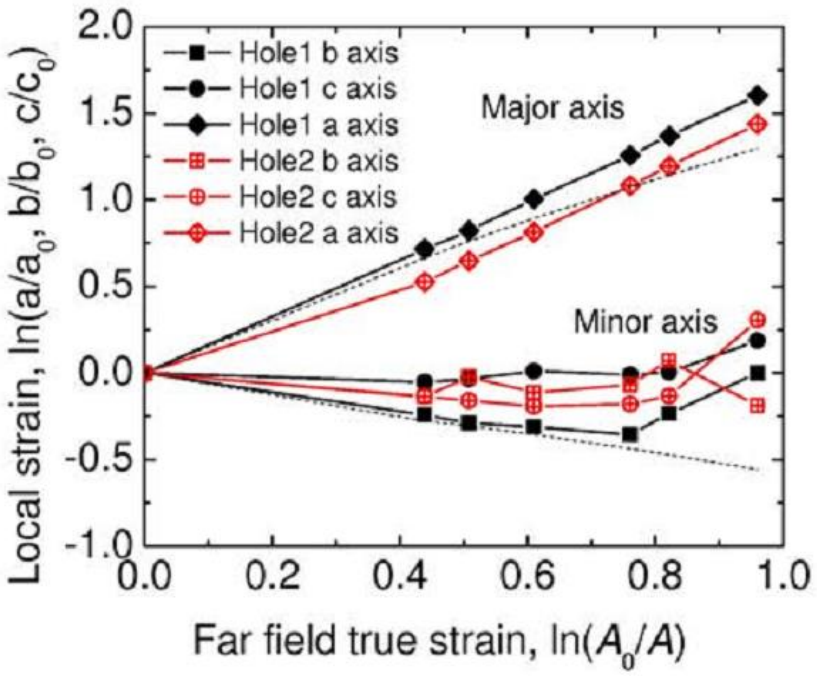

Figure 2.15: Comparison between the Rice and Tracey model predictions for void growth and experimental results (Hosokawa, 2011).

2.5.3 Void Coalescence in Metallic Materials

Voids will grow in a plastically deforming matrix until they coalesce with other voids leading to final fracture. Void coalescence is the most important process in ductile fracture as it determines the ductility of a material. However, it is the least understood due to its stochastic nature. As a result, it is difficult to capture this event experimentally. The early studies of ductile fracture show evidence of two mechanisms of coalescence; internal necking and void sheeting as shown in Figure 2.16 (Puttick, 1959; Cox and Low, 1974).

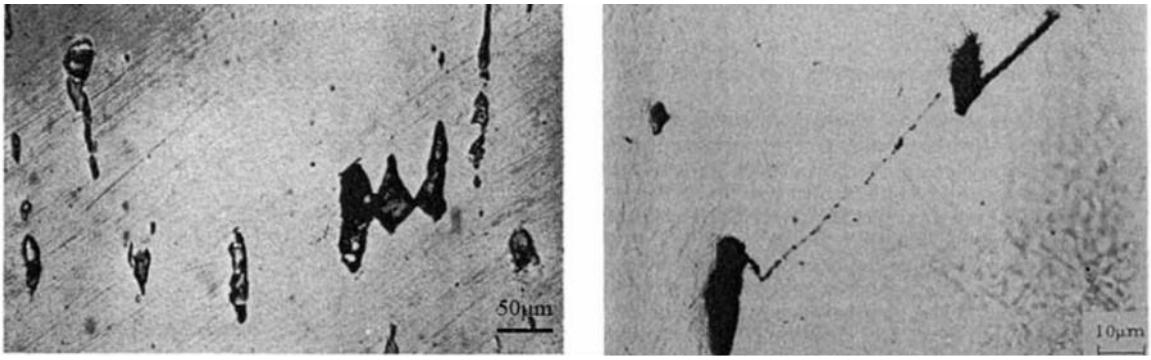

(a) (b)

Figure 2.16: Experimental evidence of void coalescence by (a) internal necking in 99.9% copper (Puttick, 1959) and (b) void sheeting in AISI 4340 steel (Cox and Low, 1974).

Internal necking typically occurs in materials of high purity containing a single population of particles. In this case voids nucleate at second phase particles and begin to grow in the tensile direction. Lateral shrinkage occurs until a critical point in deformation is attained whereby lateral expansion of the voids ensues. The voids will grow in the lateral direction until they coalesce by the internal necking mechanism as depicted in Figure 2.16(a). This has been established to occur at low stress triaxiality by the modeling work of Worswick and Pick (1990) and validated experimentally by Hosokawa and co-workers (2012). In addition, void sheeting has been observed in materials that contain multiple particle populations. Cox and Low (1974) provided evidence of this mechanism in a tempered AISI 4340 steel. In their experiment, the larger voids in Figure 2.16(b) nucleated earlier in deformation at larger MnS particles. The voids grew until a secondary population of voids nucleated at smaller carbide particles which led to coalescence by the void sheeting mechanism.

Although the experimental work on void coalescence is sparse, several models have been proposed to model the event. McClintock proposed a plane strain criterion based on the void growth model represented by Equation (2.9). The model predicts that coalescence occurs by the impingement of two voids growing in a deforming matrix given by (McClintock, 1968b):

$$\bar{\varepsilon}^f = \frac{(1-n)\ln\left(\frac{l_a^0}{2a^0}\right)}{\sinh\left[\frac{\sqrt{3}(1-n)}{2}\frac{(\sigma_1+\sigma_2)}{2}\right]} \tag{2.17}$$

where $\bar{\varepsilon}^f$ is the strain at which void impingement occurs, l_a^0 is the initial spacing between two voids and a^0 is the initial radius of the voids. As stated earlier, this model neglects void interactions and thus, provides a significant overestimate of the failure strain.

Brown and Embury (1973) proposed a geometric model to predict the onset of coalescence. The model predicts that the onset of void coalescence occurs when the void length is equal to the intervoid spacing. Figure 2.17 illustrates the stages of the model.

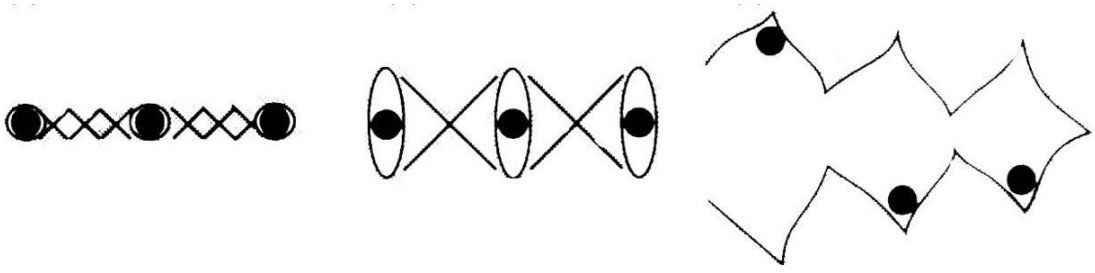

(a) (b) (c)

Figure 2.17: Schematic of the Brown and Embury model (a) nucleation of voids in constrained matrix (b) loss of constraint (c) final failure (Brown and Embury, 1973).

Consider two voids that nucleate at second phase particles on a plane normal to the tensile axis in which the intervoid spacing of the voids is much larger than their length. Once the voids have nucleated it is assumed that they grow by plastic extension. Initially, the ductile matrix between the voids cannot suffer very large local deformations because it is constrained by the surrounding matrix. This stage is represented by planes of maximum shear drawn between neighboring voids in Figure 2.17(a). Once the void length is equivalent to the intervoid spacing the plastic constraint preventing local deformation is lost. Plastic flow is localized on the planes of maximum shear and the onset of coalescence ensues as represented in Figure 2.17(b). This leads to the linkage and final failure of the material as depicted in Figure 2.17(c). The numerical representation of this model can be given by:

$$2r(1 + e_g) = r\left(\sqrt{\frac{2\pi}{3V_f}} - \sqrt{\frac{8}{3}}\right) \tag{2.18}$$

where r is the initial radius of the void or particle, e_g is the elongation at which the void length is equal to the intervoid spacing and V_f is the volume fraction of voids. Therefore, the left hand side of the equation represents the current void length and the right hand side is the mean intervoid spacing. The true fracture strain is the sum of the elongation to nucleate a void, e_n, and the elongation required to grow the void to the critical size given by:

$$\varepsilon_f = \ln(1 + e_g + e_n) = \ln\left(\sqrt{\frac{\pi}{6V_f}} - \sqrt{\frac{2}{3}} + e_n\right) \tag{2.19}$$

Le Roy et al. (1981) modified the Brown and Embury theory to account for stress triaxiality. Weck (2007) carried out experiments to assess the validity of the Brown and Embury model. The average void length and intervoid spacing of two voids in various orientations were plotted as a function of the local stress as shown in Figure 2.18. The point at which the void length and intervoid spacing intersect was taken as the coalescence strain as predicted by the Brown and Embury model. The results are summarized in Table 2.3. It should be noted that the experimental strains in Table 2.3 were taken at the point of ligament failure since the event was reproducible. The onset of coalescence as defined by Hosokawa (2011) was not captured in Weck's results. However, the results show a good agreement with the failure strains for voids that are perpendicular to the tensile direction. The model underestimated the coalescence strain when a shear component of void growth was introduced. Therefore, a more complex criterion is required when voids coalesce in an angled orientation. Hosokawa (2011) carried out similar experiments on 3D model materials. The results were not in agreement with the Brown and Embury model. Therefore, it has been established that the Brown and Embury model is strictly a 2D criterion that predicts normal void coalescence. The model does not consider the stress state of the system or any material parameters.

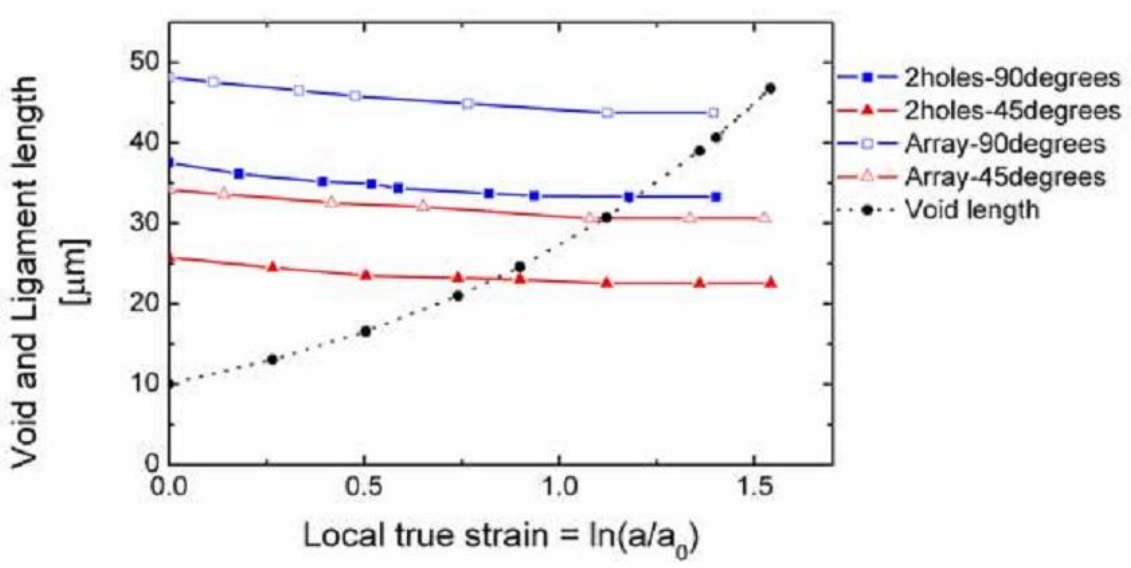

Figure 2.18: Void length and intervoid spacing plotted as a function of local strain (Weck, 2007).

Table 2.3: Experimental coalescence strains and corresponding predictions from the Brown and Embury model (Weck, 2007).

Configuration	Experimental Strain	Model Strain	Percent Difference
2 holes 90˚	1.18	1.2	+2%
2 holes 45˚	1.36	0.83	-39%
Array 90˚	1.39	1.47	+6%
Array 45˚	1.33	1.12	-16%

Thomason (1981) proposed a plane strain model for a state of incipient microvoid coalescence in a work hardening plastic/rigid solid. The condition can be represented in terms of a critical value of mean stress σ_n in the intervoid matrix which is required to initiate localized plastic flow or internal necking in a sheet of voids. The mean stress can be

represented as a plastic constraint factor. Thomason established that the plastic constraint factor could be approximated by a function of the neck geometry parameter $N = {}^{a}/_{d}$ given by:

$$\frac{\sigma_n}{2k} A_n = \frac{0.3}{{}^{a}/_{d}} + 0.6 \tag{2.20}$$

where A_n is the area fraction of the intervoid matrix, a is the void length and d is the length of the ligament between adjacent voids. A finite element analysis carried out by Hosokawa (2011) has confirmed this relation. When the voids are small and widely spaced the mean stress required to initiate localized plastic flow is considerably greater than σ_1 and plastic limit-load failure is prevented. This can be represented by the following equality:

$$\frac{\sigma_n}{2k_n} A_n > \frac{\sigma_1}{2k} = \frac{1}{2} + \frac{\sigma_m}{2k} \tag{2.21}$$

where k_n is the yield shear stress in the intervoid matrix. However, once the voids begin to grow the neck parameter gradually increases which has the effect of reducing the mean stress required for plastic limit load failure of the intervoid matrix. The point where the current applied stress is sufficient to initiate this mode of localized internal necking can be represented by:

$$\frac{\sigma_n}{2k_n} A_n = \frac{\sigma_1}{2k} = \frac{1}{2} + \frac{\sigma_m}{2k} \tag{2.22}$$

The macroscopic and intervoid yield shear strength can be related through a law of mixtures:

$$k = \left(1 - V_f\right)k_n \tag{2.23}$$

Substitution of (2.20) and (2.23) into (2.22) yields the 2D Thomason model given by:

$$\left(\frac{0.3}{a/d} + 0.6\right)\left(1 - V_f\right)^{-1} = \frac{\sigma_1}{2k} = \frac{1}{2} + \frac{\sigma_m}{2k} \tag{2.24}$$

Weck (2007) carried out experiments to verify the Thomason model. The left and right hand side of Equation (2.24) were plotted as a function of local strain for two voids as shown in Figure 2.19. The uniaxial stress triaxiality of 1/3, was used for holes with various configurations. The point of intersection between the left and right hand side of Equation (2.24) was acknowledged as the strain predicted by the Thomason model. The results are summarized in Table 2.4. The model consistently underestimated the coalescence strain. This may be attributed to the fact that the onset of coalescence was not captured and the experimental strains represent the strain at ligament failure.

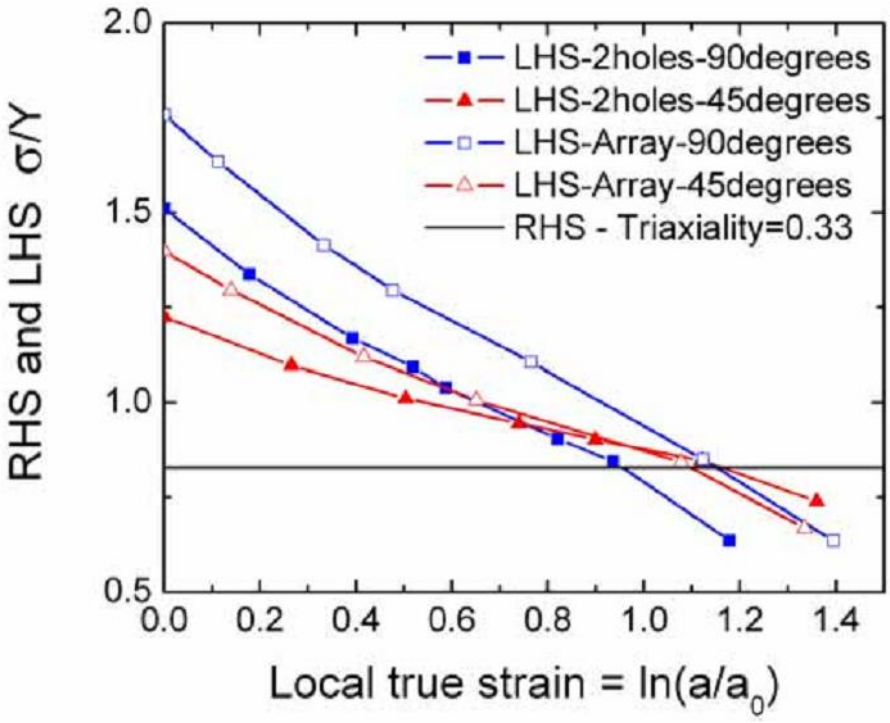

Figure 2.19: LHS and RHS of Equation (2.24) plotted as a function of the local strain (Weck 2007).

Table 2.4: Experimental coalescence strains and corresponding predictions from the Thomason model (Weck, 2007).

Configuration	Experimental Strain	Model Strain	Percent Difference
2 holes 90˚	1.18	0.95	-19%
2 holes 45˚	1.36	1.16	-15%
Array 90˚	1.39	1.15	-17%
Array 45˚	1.33	1.1	-17%

The Thomason model has also been extended to a 3D solution of the form:

$$\left(\frac{0.1}{\left(\frac{a}{d}\right)^2}+\frac{1.2}{\left(\frac{b}{b+d}\right)^{1/2}}\right)\frac{1}{(1-V_f)}\left(1-\left(\frac{3\sqrt{\pi}V_f}{4}\right)^{2/3}\left(\frac{b}{b_0}\right)^2\right)exp(\varepsilon_1) = \frac{\sigma_m}{Y}+\frac{2}{3} \quad (2.25)$$

for uniaxial tension where b is the void width (Thomason, 1985). Experiments by Hosokawa (2011) showed good agreement with the 3D Thomason model when void coalescence occurred normal to the tensile axis. The original Thomason model assumes that the material is a perfectly plastic solid and thus, does not account for the work hardening rate.

Pardoen and Hutchinson (2000) extended the Thomason model to account for the work hardening behavior using a finite element based approach. The Pardoen and Hutchinson model is given by:

$$\frac{\Sigma_z^{loc}}{\bar{\sigma}}=\left[1-\left(\frac{b}{d+b}\right)^2\right]\left[\alpha(n)\left(\frac{a}{d}\right)^{-2}+\beta(n)\left(\frac{b}{d+b}\right)^{-1/2}\right] \quad (2.26)$$

where Σ_z^{loc} is the maximum principal stress when localization occurs, $\bar{\sigma}$ is the effective stress and the parameters α and β were introduced by fitting the results of the finite element simulations to the numerical model. Comparison of Equations (2.25) and (2.26) reveals that the constant values of 0.1 and 1.2 in Equation (2.25) were replaced by the parameters α and β given by:

$$\alpha = 0.1 + 0.217n + 4.83n^2 \qquad (0 \leq n \leq 0.3) \tag{2.27a}$$

$$\beta = 1.24 \tag{2.28b}$$

where n is the work hardening exponent. In addition, Y is replaced by the equivalent stress. As a consequence, the Pardoen and Hutchinson model incorporates the dependency of the work hardening on the onset of plastic localization. Experiments by Hosokawa (2011) showed that the Pardoen and Hutchinson model did not predict localization strains which differed a considerable amount from the original Thomason model. This can be attributed to the fact that low values of the work hardening exponent do not change the parameters significantly from those of the original Thomason model.

A theoretical drawback to the original Thomason model is that the plastic constraint factor becomes unbounded and does not predict coalescence for flat penny shaped cracks. Benzerga (2002) also adjusted the model to account for the coalescence of flat cracks at low values of stress triaxiality. More recent studies have been carried out to incorporate the effects of shear into void coalescence models (Hosokawa, 2011; Tekoglu et al., 2012)

The finite element method has also been used to predict void coalescence. Weck et al. (2007b) used a finite element approach coupled with a non-local damage parameter to predict void coalescence in a 5052 Al alloy. A non-local damage parameter was used to average the strain over a characteristic length. The element deletion technique was then used to evaluate the strain for a given set of elements, defined by the characteristic length,

and delete element regions once they reached a critical strain. Using this methodology Weck was able to predict the crack path within a random array of holes.

2.6 Characterization Techniques for Studies of Deformation and Fracture

In order to study the deformation and fracture of materials with low crystallographic symmetry such as magnesium, a variety of techniques are required to model and understand the material behavior. This section will present the fundamentals associated with the various techniques used throughout this work. In addition, recent studies on magnesium systems will be presented which employ each technique.

2.6.1 EBSD Patterning

EBSD patterning has gained a lot of interest in studies of materials that exhibit mechanical anisotropy. A wide variety of information can be obtained from this technique, however, for the scope of the thesis emphasis will be placed on using EBSD for orientation mapping. This is particularly useful in crystal plasticity simulations where the texture can be used as an input into the model.

The three main components inside an SEM chamber required for EBSD analysis are the electron source, sample and detector. A beam of electrons is aimed at a point of interest on a sample which is tilted 70° from the horizontal. This tilt angle maximizes the yield of backscattered electrons detected. Several types of electrons are produced from the

scattering interactions between the primary electrons and the atoms within the sample. The electrons which take part in elastic scattering and leave the sample are termed backscattered electrons (Goldstein et al., 2012). Some of these backscattered electrons scatter on specific planes satisfying the Bragg condition and produces Kikuchi bands on the detector, characteristic of the plane. Figure 2.20 shows the schematic of the EBSD set up and the Kikuchi bands which are created. The patterns are compared to crystal structures within a database which allows the software to identify the crystallographic plane where the beam is positioned. This process is carried out over a specified region of interest as the beam rasters across the sample surface, obtaining these patterns in each step which allows the crystallographic orientation to be mapped on the sample surface (Day, 2004). The advantage of using EBSD in studies of deformation and fracture is that high resolutions can be obtained allowing for fine microstructural features to be resolved. Hazeli et al. (2015) used EBSD to investigate twinning and detwinning in AZ31 during fatigue tests. Figure 2.21 shows EBSD maps obtained in several regions of the sample during loading and unloading. The detailed analysis clearly captured the twinning and detwinning of the $\{10\bar{1}2\}$ twin system.

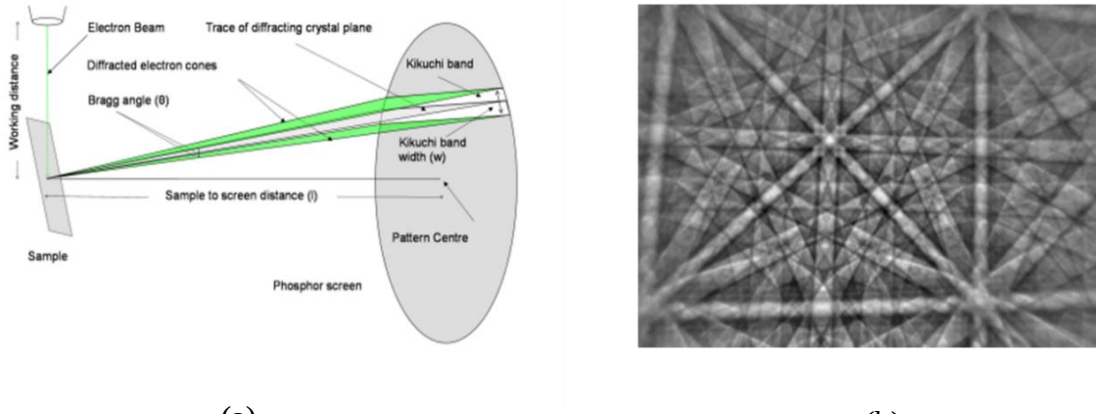

(a) (b)

Figure 2.20: (a) Schematic of EBSD setup and (b) Kikuchi pattern produced by backscattered electrons (Oxford Instruments, 2015).

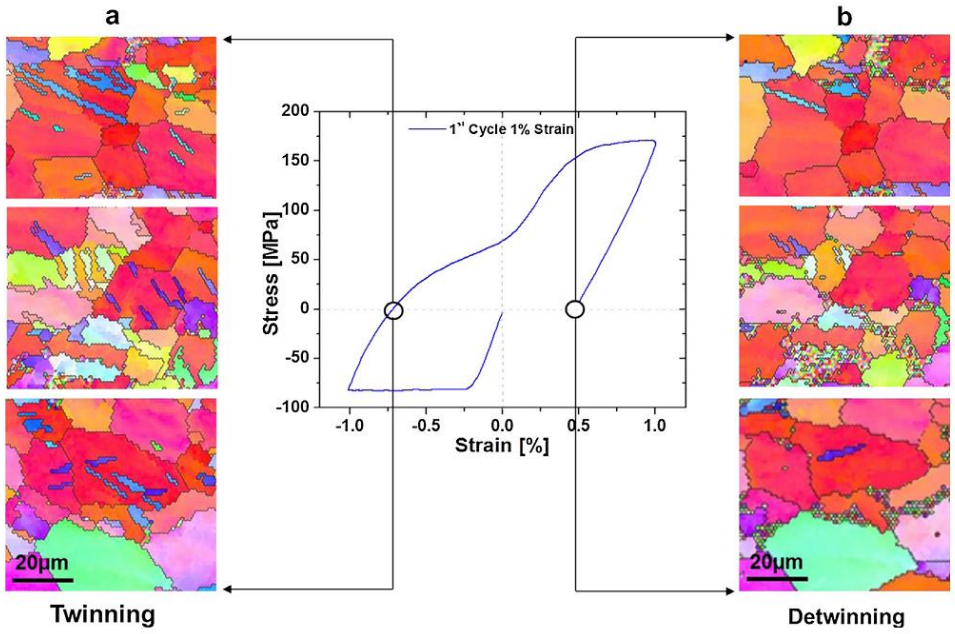

Figure 2.21: First fatigue cycle for 1% imposed fatigue strain amplitude. (a) Twinning and (b) detwinning were identified for three different regions (Hazeli et al., 2015).

2.6.2 Digital Image Correlation (DIC) Method for Strain Mapping

The DIC methodology for strain mapping is an essential tool used in this project. Recent studies have used high resolution strain grids to quantify the heterogeneous deformation of magnesium and other systems (Kang et al., 2007; Hazeli et al., 2013).

Consider two images in the undeformed and deformed states as shown in Figure 2.22. The DIC method involves the use of facets to correlate distributions of grey scale values between the reference and destination states. A facet is an area which can be defined by a length and width of pixels shown as an unfilled quadrilateral in Figure 2.22.

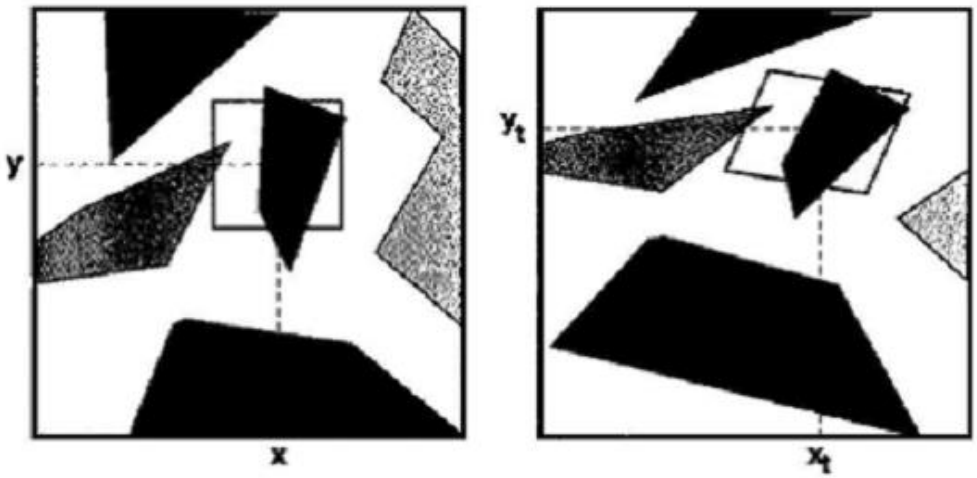

(a) (b)

Figure 2.22: Grayscale image in (a) undeformed and (b) deformed state (GOM, 2005).

In order to correlate the facets, a starting point must be selected in the reference image which can be detected in the destination state. The center pixel of the facet has been used

and is expressed by (x, y) in the undeformed state and (x_t, y_t) in the deformed state. As a result, the following relation exists between the grey scale values at this point:

$$g_1(x, y) = g_2(x_t, y_t) \tag{2.29}$$

The pixels of the facet in the reference image are then related to the destination image by the following transformations:

$$x_t = a_1 + a_2 x + a_3 y + a_4 xy \tag{2.30a}$$

$$y_t = a_5 + a_6 x + a_7 y + a_8 xy \tag{2.29b}$$

where a_1 and a_5 describe the translation of the center pixel, while the others describe the rotation and displacement of the facet. The displacement fields associated with various points are converted into strain values through the deformation tensor (GOM, 2005).

Martin et al. (2014) coupled together EBSD, the DIC methodology of strain mapping and a crystal plasticity simulation to investigate deformation in ZEK100 magnesium alloy. Figure 2.23 shows the results from the model and experimental data. The model predicts that localizations occur at grain boundaries, however, the model does not capture the finer details of the experiments such as the location and intensity of the hotspots.

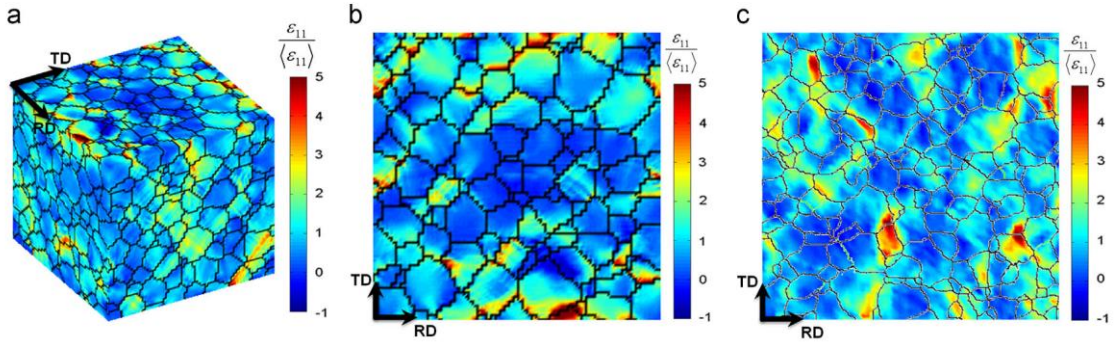

Figure 2.23: Crystal plasticity simulation of ZEK100 at strain of 4% (a) 3D model (b) 2D slice and (c) experimental strain field (Martin et al., 2014).

2.6.3 X-ray Tomography

X-ray tomography is a powerful technique for studying damage as it provides 3D information within the bulk of materials. The schematic of a typical tomography setup is shown in Figure 2.24. The source consists of an x-ray beam which produces x-rays of intensity I_0. As the x-rays interact with the sample they lose some of their intensity. The sample absorbs some of the energy and the x-rays which penetrate through the sample leave with an intensity of I_t. The amount of energy lost depends on the absorption coefficient of the phases within the sample. Contrast is produced and identified by the detector when different phases are present within the material resulting in different absorption along the path of travel. The images produced at a given step are called radiographs. By obtaining radiographs at various steps of rotation and using reconstruction algorithms, the phases of the material can be observed in 3D (Baruchel et al., 2000).

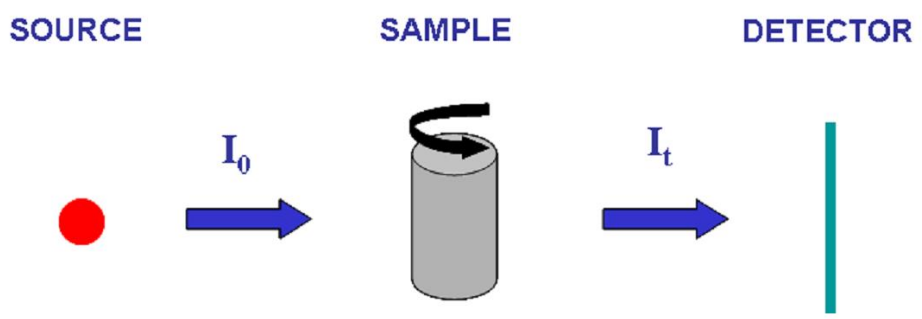

Figure 2.24: Schematic representation of the tomography set-up (Weck, 2007).

Lhuissier et al. (2012) used this technique to study damage in AZ31 magnesium alloy deformed at high temperatures. Figure 2.25 shows the coalescence of cavities as a function of strain. The results showed the complexity of the coalescence event in AZ31 Mg alloy. Some of the cavities observed were associated with particles while others formed with no relation to particles. In addition, the shapes of the cavities observed were rather irregular.

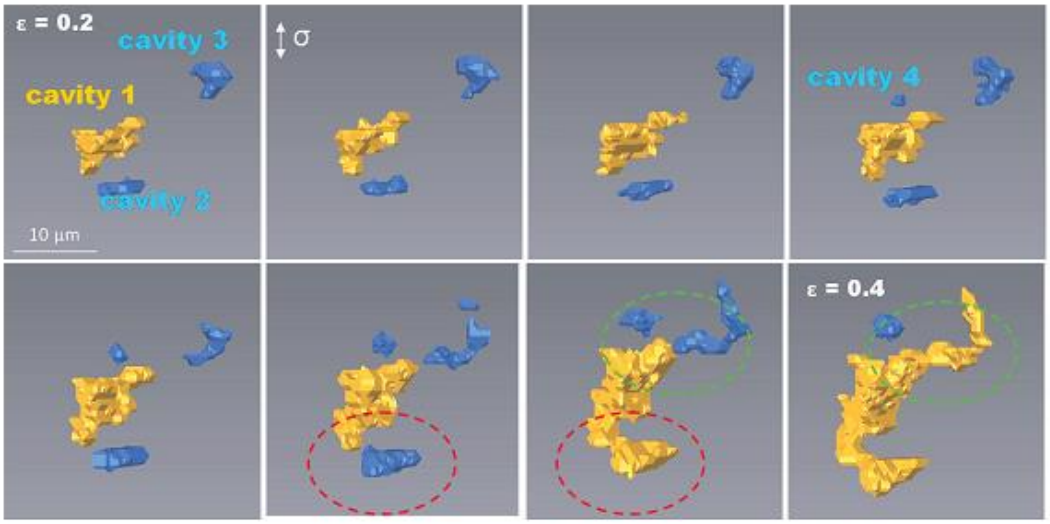

Figure 2.25: 3D model of the coalescence of cavities (Lhuissier et al. 2012).

2.7 Summary

The main conclusions drawn from the literature review, presented in this chapter are summarized below:

- Dislocation slip, twinning and grain boundary sliding are the main deformation mechanisms at ambient temperature in magnesium systems. This is different from the fcc metals discussed in the chapter where dislocation slip dominates the deformation process.
- Void nucleation is a stochastic process in all commercial materials. As a result, model materials are ideal for void growth and linkage studies. The use of model materials allows the experimentalist to know the initial size, configuration and location of the holes which permits a detailed investigation of the growth and linkage processes.
- The McClintock void growth model predicts the average hole size in the aluminum 2D model material presented. The drawback to this model is that the form used does not provide information on growth in specified directions. In addition, it does not account for void interactions.
- The Rice and Tracey void growth model predicts void growth well in the copper 3D model material presented. An advantage of this model is that it can be integrated in a specified direction to give information on the growth behavior for that specific direction. However, the model does not consider void interactions and does not predict the amplified growth of the holes once they begin to interact.

- The Brown and Embury model provides a good prediction for void linkage in the aluminum 2D model materials presented when void linkage occurs normal to the tensile axis. However, it does not provide a good prediction of void linkage in the 3D model materials where the constraint is changed.
- The 3D Thomason and the Pardoen and Hutchinson model predict void linkage in the copper 3D model materials presented when void linkage occurs normal to the tensile axis. However, the model does not predict the shear linkage of holes.
- In order to fully understand the deformation and fracture of commercial materials 2D techniques must be complemented with 3D techniques.

Based on the previous work carried out on fcc materials, approaches have been introduced which have advanced our knowledge of ductile fracture in providing experimental observations for comparison with the modelling work in the field. The purpose of this work is to identify how these approaches can be used and modified in order to understand deformation and fracture in magnesium.

Chapter 3

Experimental Procedures

3.1 Introduction

It has been established in the literature that the fracture of metallic materials occurs by the continuous processes of void nucleation, growth and coalescence. In addition, the stochastic nature of each event has been addressed. In order to investigate the ductile fracture process in detail, Weck et al. (2007a) fabricated model materials by laser drilling holes into the gage section of tensile specimens. This innovative approach permitted a study of some of the key parameters which govern fracture and eliminated effects due to the statistical nature of void nucleation. Laser machining technology allows for the precise positioning of the holes within the gage section. Tensile specimens containing various hole configurations were pulled in-situ under a SEM. Weck and Wilkinson (2008) used this approach to investigate the effects of void fraction and void orientation on fracture. The work enabled a detailed study on these parameters independently, which provided a better understanding of fracture in commercial materials where the voids are distributed randomly.

In the present work, a similar approach has been used to investigate fracture in an emerging structural material with low crystallographic symmetry. Three different experimental approaches have been used to study deformation and fracture in magnesium.

The first experimental technique consists of in-situ tensile testing coupled with electron microscopy. The second consists of in-situ tensile testing under an optical microscope. This approach was adopted because the digital image correlation method is used for strain mapping during these experiments and the optical microscope produces better contrast for strain calculations. The model materials described above were used throughout these two experimental techniques. The third experimental technique involves the use of x-ray tomography to study the fracture processes in bulk magnesium. The objective of this approach is to apply the data obtained from the model materials to describe fracture in a commercial material. This chapter will describe the material studied, material preparation procedures and characterization techniques used for each experimental approach.

3.2 Material

The material used throughout the entire project is hot rolled CP magnesium with a thickness of 1.5 mm. This will be referred to as the as-received material in the sections to follow. Table 3.1 shows the composition of the material which was obtained through inductively coupled plasma (ICP) analysis.

Table 3.1: Composition of the as-received material.

Element	Al	Ca	Cr	Cu	Fe	Mn	Ni	Zn	Mg
Weight %	0.064	0.009	0.005	0.002	0.013	0.012	0.004	0.057	Balance

For each of the experimental techniques used, the as-received material undergoes different processing, annealing and preparation procedures.

3.3 In-situ Tensile Testing with ESEM

The first set of experiments were designed to observe the fracture process in CP magnesium. The model materials discussed above were tailored using pico-second laser machining technology. Tensile tests were carried out in the chamber of an ESEM. The samples investigated contained a single line of holes in the gage section with various configurations. In addition, the samples have been notched to ensure fracture occurs within the region containing the holes. The main parameters which will be investigated are the void fraction and orientation; however, triaxiality effects will also be discussed. Similar studies have been conducted on aluminum (Weck and Wilkinson, 2008) and copper (Li, 2013) materials. This work has been extended to use similar techniques to examine fracture in magnesium. The material processing, fabrication of the model materials, laser system and experimental details for this approach will be addressed in this section.

3.3.1 Material Preparation Procedure for ESEM Experiments

The as-received material was hot rolled, at 300°C to produce sheets with a thickness of 125μm. At this stage the material will be referred to as in the as-rolled state. This procedure was carried out using the rolling mill at the University of British Columbia. A ceramic block was then placed on the sheets, and an annealing process was carried out at

250°C for 1 hour to flatten the sheets for machining. Figure 3.1 shows optical micrographs of the as-rolled and annealed microstructures.

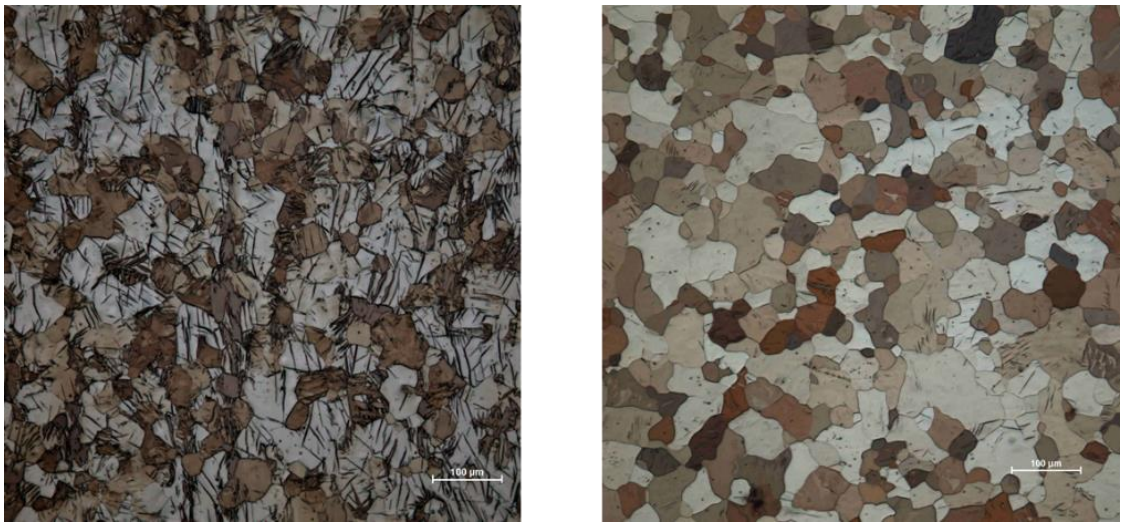

(a) (b)

Figure 3.1: Optical micrographs of the (a) as-rolled and (b) annealed microstructures.

The average grain size, measured using the intercept method (ASTM E112), was approximately 50µm after annealing. Electrical discharge machining (EDM) was used to cut the sheet into tensile samples containing a reduced gage section with a length of 2mm and width of 1mm. The samples were polished with 0.05µm colloidal silica to ensure a smooth surface for characterization and laser machining. Polishing caused a slight variation in the final thickness of the samples tested. On average, the final sample thickness was approximately 100µm. The sample geometry is shown in Figure 3.2.

In order to reduce the statistical uncertainty associated with void nucleation, holes were laser drilled into the gage section of the tensile sample using a Ti:sapphire laser system.

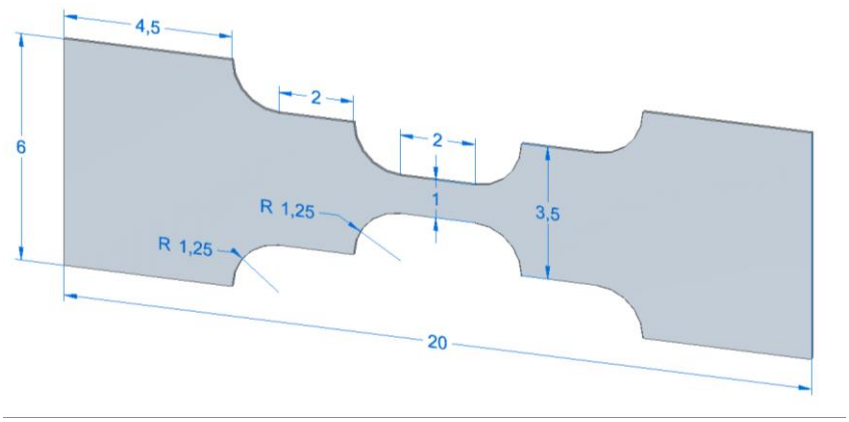

Figure 3.2: Tensile sample geometry for in-situ tensile testing under ESEM. Dimensions are in mm.

A notch was also machined into the sample, adjacent to the holes, to ensure fracture occurred within this region. Figure 3.3(a) shows a sample with a line of holes perpendicular to the tensile axis. Details associated with the laser machining process will be discussed in Section 3.3.2. The samples were annealed at 450°C for 1 hour after laser drilling, to remove the heat affected zone in the vicinity of the holes. Final grain size calculations were obtained using EBSD patterning. The final average grain size was 51±6μm with a standard deviation of 28. Figure 3.3(b) shows an EBSD map used to calculate the final grain size in the gage of the tensile samples.

The grain size and orientation was observed to be different in the vicinity of the holes. Figure 3.4 shows an optical micrograph of an array of holes which have been laser machined into a sheet of magnesium. The image reveals twinning which has occurred in a region adjacent to the holes.

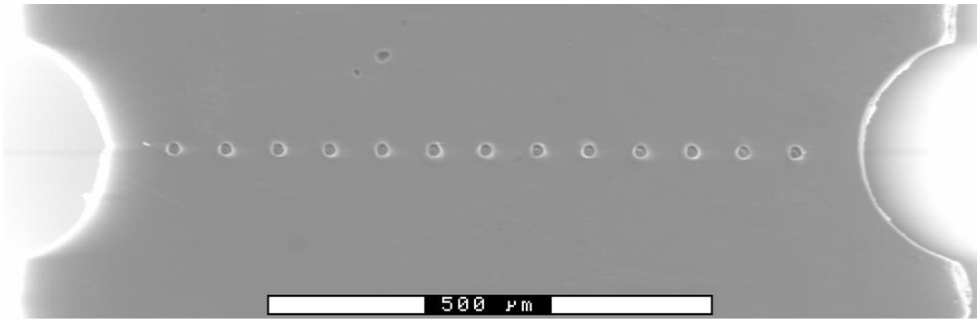

(a)

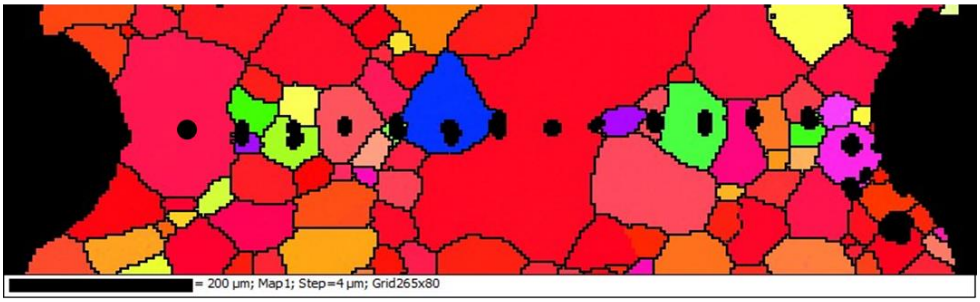

(b)

Figure 3.3: Gage section of the tensile samples (a) ESEM image and (b) EBSD map used for grain size calculation.

This observation suggests that the laser machining process induces some deformation or damage into the laser machined region. Weck (2007) encountered this phenomenon during the laser machining of copper sheets. A refined grain structure was observed within a small region adjacent to the hole edge. Weck used nanoindentation and showed that the material within this localized region is considerably harder. During annealing local recrystallization is driven by this local deformation. This phenomenon introduces difficulties in growing the grains to a scale larger than the void diameter since the voids act as free surfaces which impinge grain growth. As a result, the grain size is smaller and the orientation is altered within this localized region. This explains the large standard deviation in the grain size distribution.

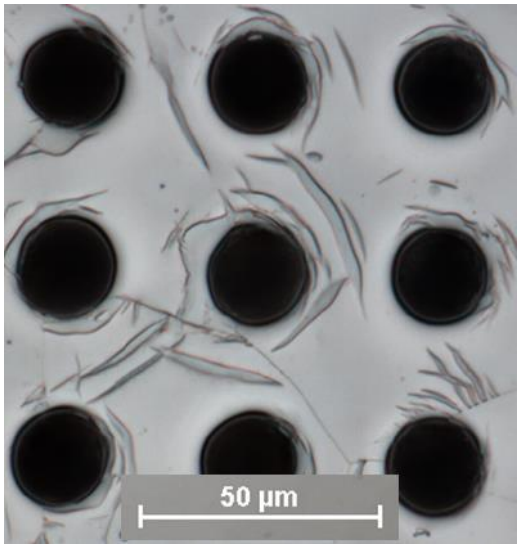

Figure 3.4: Optical micrograph showing laser induced deformation adjacent to the holes.

3.3.2 Laser Machining Systems

The laser machining system used to fabricate the model materials is described here. Laser machining was carried out at McMaster University using a combination of laser systems. Figure 3.5 shows schematically how laser pulses are created. A green laser source ($Nd:YVO_4$) is used to excite electrons of the titanium sapphire crystal in the Tsunami laser system. This process is known as population inversion. After population inversion, the excited electrons relax to various degrees and emit photons with a variety of wavelengths in the infrared range (800nm). When enough photons are present a short pulse is produced by the superposition of the various wavelengths. The Tsunami system produces short pulses of low energy and high frequency. At this point the energy of the pulse is too low for machining. The pulse must be sent to another Ti:sapphire laser system (Merlin) used to amplify the energy of the pulse. However, the pulse produced by the Tsunami system

cannot be sent directly to the Merlin system because the high intensity of the pulse would damage it. One way to decrease the intensity of a pulse is to increase the pulse length. The Milenia V pulse stretching system is used to increase the pulse length to approximately 200 ps. After the pulse stretching process the pulse can enter the Merlin system. This laser is pumped with a green laser source (Nd:YLF) at a frequency of 1kHz. Once the 200ps pulse is amplified, it can leave the system with energies of roughly 500μJ (1kHz at 500mW). The pulse length can then be optimized using pulse compressors. A more detailed description of the laser system can be found in Hsu (2007).

3.3.3 Laser Machining Parameters

The compressed pulse discussed above is sent to the machining system showed in Figure 3.6. A pulse length of 5ps has been used during preparation, to reduce the possibility of generating radiation during machining. However, the optimal pulse energy and number of pulses per hole were determined experimentally for CP magnesium, using an approach developed by Weck et al. (2008).

The pulse energy is controlled by passing the laser beam through neutral density filters which are managed by the filter wheels shown in Figure 3.6. Each filter is characterized by its optical density (OD). Prior to passing through the neutral density filters the beam has an average power of approximately 400mW. A calibration test was completed to determine the output power produced by each OD filter. The output beam power was measured for each filter using a power meter and the results are shown in Figure 3.7.

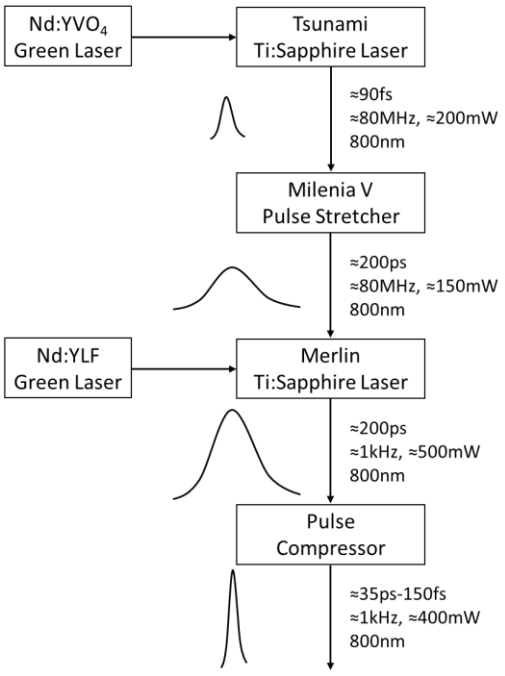

Figure 3.5: Schematic showing the generation of pulses using Ti:Sapphire laser system.

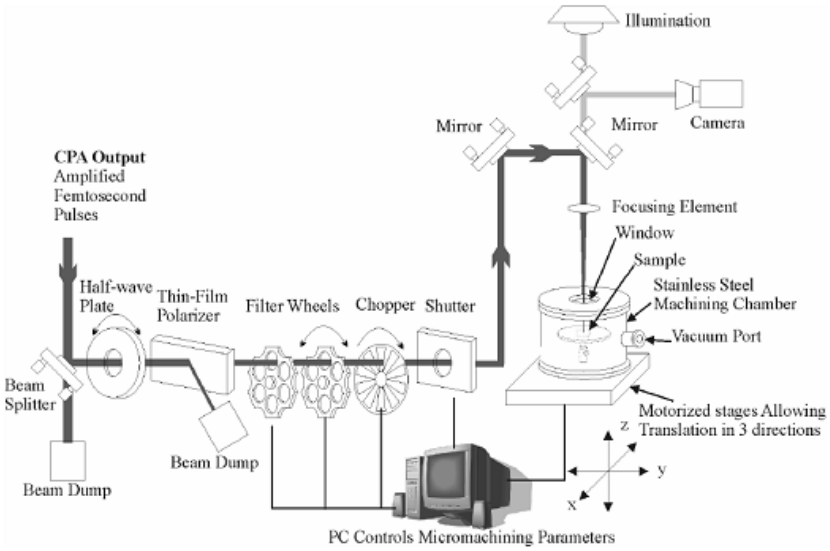

Figure 3.6: Laser machining set-up (Hsu, 2007).

In order to determine the optimal parameters for machining holes into CP magnesium, measurements are required while the beam is penetrating through the material. A photodiode has been used to determine voltage readings after the beam has ablated through the sheet in the machining chamber (refer to Figure 3.6). The photodiode was first calibrated by exposing the diode to 500 pulses from each OD filter. There was no sample between the laser source and diode during this calibration and as a result, the voltage signal approaches a constant value almost instantaneously. The results are shown in Figure 3.8.

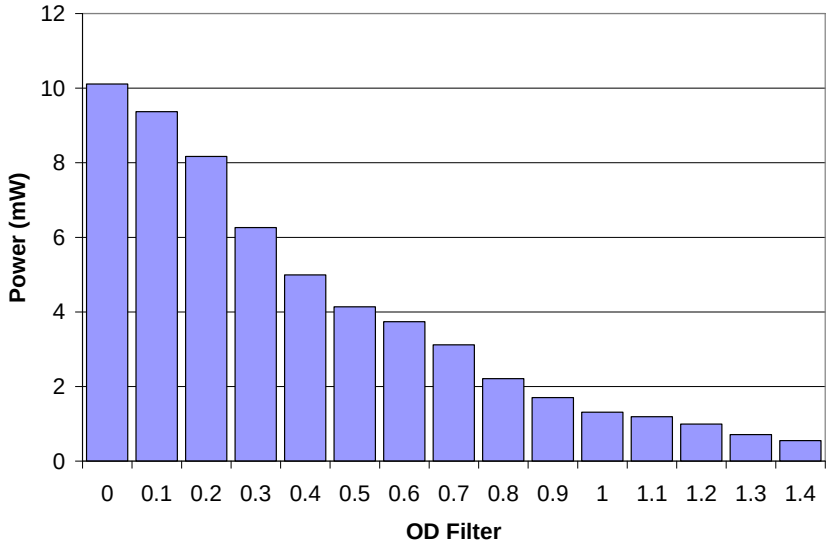

Figure 3.7: Output power of the OD filters.

Figure 3.7 and Figure 3.8 were used to relate the signal voltage to the power of the beam when the beam has fully penetrated through the thickness of the sheet. A sheet of magnesium was then placed between the source and the diode and the output signal was recorded for 10 000 pulses from each OD filter as shown in Figure 3.9.

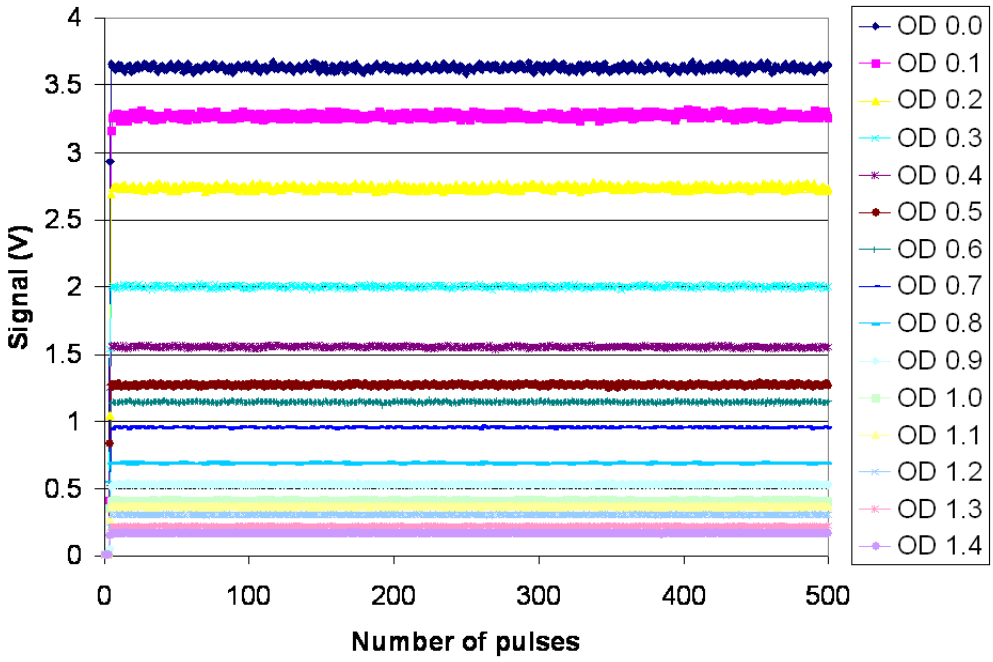

Figure 3.8: Signal vs. number of pulses without sheet between source and diode.

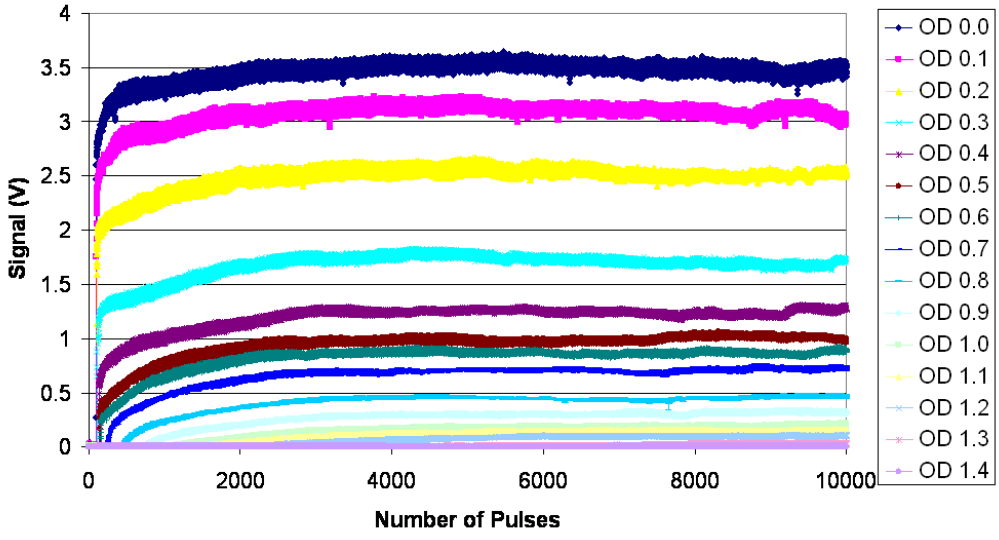

Figure 3.9: Signal vs. number of pulses with sheet between source and diode.

The signal experiences a rapid increase during the initial phase of the test. This is a direct result of the beam ablating through the CP magnesium. Once the beam has propagated through the material, the curve plateaus to a value that approaches the corresponding value obtained during the calibration of the diode. The slight increase in voltage after this point corresponds to further expansion of the hole. Cylindrical holes are the optimal shape desired for the experiments. As a result, the entrance and exit hole diameters were measured after the sample had been exposed to 15 000 pulses and recorded in Figure 3.10.

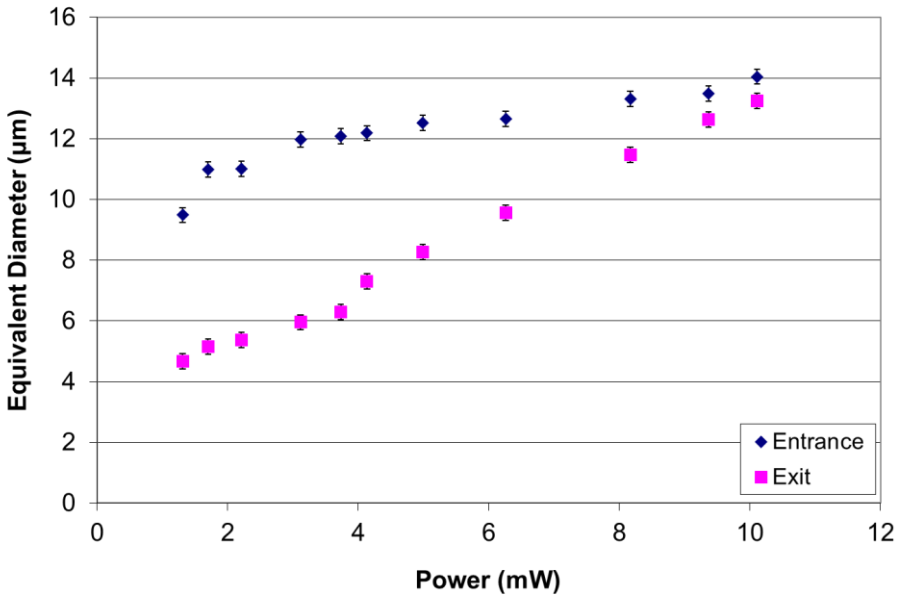

Figure 3.10: Entrance and exit hole diameters vs. power.

The error associated with the measurements was determined by measuring 40 holes using 10mW and 1000 pulses and taking the standard deviation. A standard deviation of 0.25µm was measured. The hole diameters converged as the power was increased. The

experiments were limited to 10mW to reduce the generation of radiation and to eliminate beam distortion at higher energies. 10mW at 1kHz corresponds to a pulse energy of 10μJ. As a result, a pulse energy of 10μJ (OD filter 0.0) has been used for machining to decrease the variability of the hole diameter through the thickness. Figure 3.9 was then examined for OD filter 0.0 to assess the optimal number of pulses per hole. The first plateau became stable at approximately 1 000 pulses per hole. Table 3.2 provides a summary of the parameters used for machining in this study.

Table 3.2: Laser parameters used for machining

Pulse Length	5ps
Pulse Energy	10μJ
Number of Pulses	1 000

A hole drilled with the parameters from Table 3.2 was sectioned using a Focused Ion Beam (FIB) and shown in Figure 3.11. The entrance and exit hole diameters were 14.26μJ and 13.16μJ respectively.

The only difference between the parameters used here and those used by Weck (2007) for the fabrication of the 2D model materials is the pulse length. A pulse length of 5 ps was used here for safety precautions. Both sets of parameters produced cylindrical holes with similar dimensions.

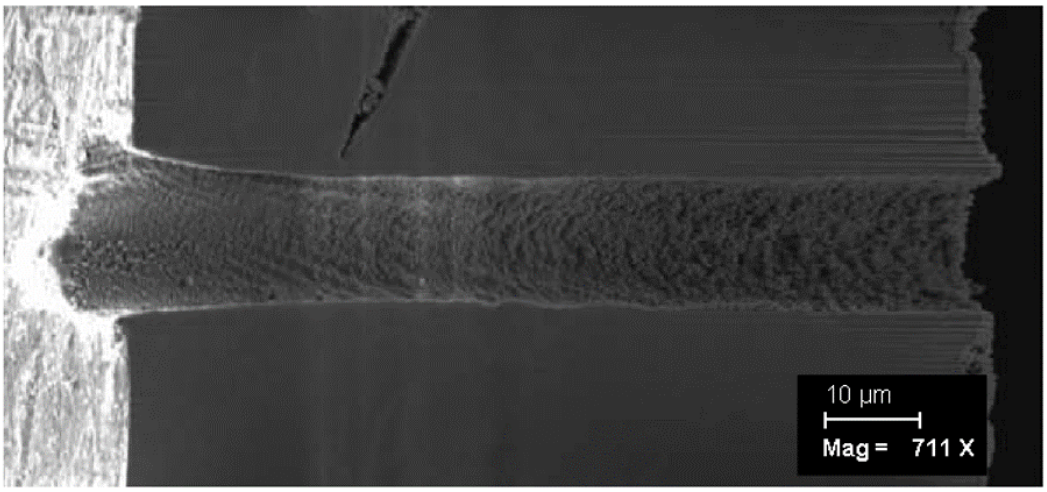

Figure 3.11: Cross section of hole machined with parameters in Table 3.2. The beam entered from the left side of the image.

3.3.4 Tensile Testing in ESEM and Characterization Techniques

EBSD patterns were obtained prior to tensile testing, using a JEOL 7000 scanning electron microscope (SEM) to determine the grain size distribution and initial texture in the gage section of the model materials. HKL Channel 5 post processing software was used for analyzing the EBSD patterns. Samples were pulled in uniaxial tension using a micro-tensile stage, inside the chamber of an Electroscan 2020 ESEM. The tensile stage utilizes a 222 N load cell and experiments were carried out at a constant speed of 10µm/s, which is equivalent to a strain rate of 4×10^{-2} s^{-1}. Displacement is measured using a Linear Variable Differential Transformer (LVDT). This technique permits an experimental investigation of void growth and linkage. The tensile test was stopped and images were obtained in increments during deformation. Geometric parameters associated with the holes, were measured using Image J software to quantify the fracture processes. In some cases, the test

was stopped to obtain EBSD data on the deformed samples, or for a tomography scan to evaluate the internal structure. The fracture surfaces were analyzed using a Phillips 515 SEM.

3.4 In-situ Tensile Testing with Optical Microscopy using DIC for Strain Mapping

The results from the ESEM experiments revealed the heterogeneous nature of deformation and fracture in the CP magnesium tested. It was established that the local microstructure played a significant role in the fracture process. Failure associated with twin and grain boundaries was observed. However, it was difficult to obtain quantitative information related to the microstructure using the experimental approach described in Section 3.3. A new approach has been adopted here in order to quantify the deformation and fracture associated with these microstructural features. A speckle pattern was produced on the surface of the model materials described and tensile tests were performed under an optical microscope. Images were obtained in increments of deformation and inputted into ARAMIS software to obtain strain calculations. The material preparation methods and experimental procedure of this approach will be described in this section.

3.4.1 Material Preparation Procedure for DIC Experiments

The as-received material was hot rolled to a thickness of 125μm using the same procedure discussed in Section 3.3.1. However, the sheets were not flattened prior to

machining. Tensile samples with the geometry shown in Figure 3.2 were cut using EDM. A Marciniak notch was also machined into the gage section to reduce the triaxiality distribution within this region. The sample geometry is shown in Figure 3.12. A schematic of the holes has been included to show their position in the gage section.

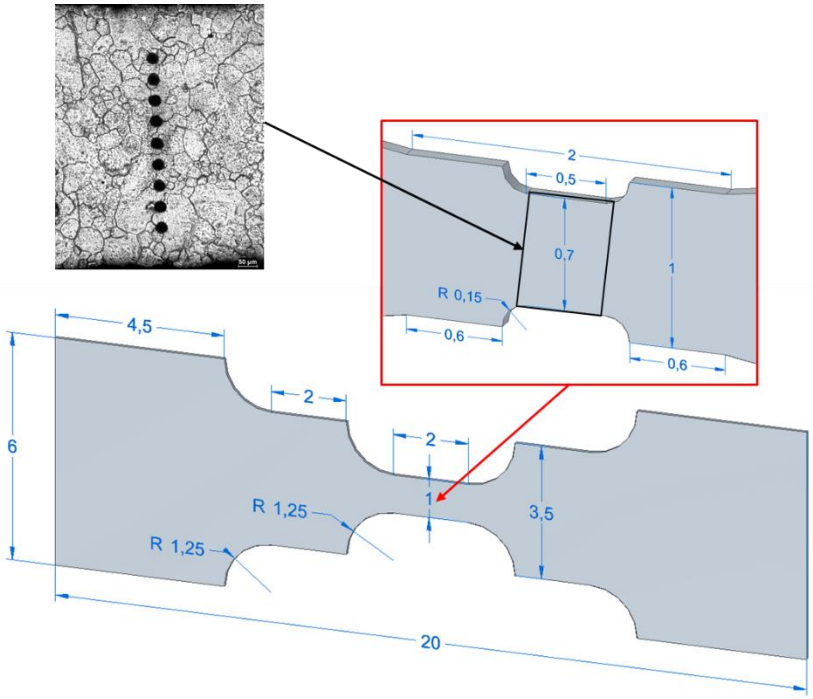

Figure 3.12: Sample geometry for DIC experiments showing schematic of the holes. Dimensions are in mm.

The samples were polished with 0.05µm colloidal silica and laser machining was carried out at the University of Ottawa, using the parameters described in Section 3.3.3. The same model materials examined in Section 3.3 were investigated. Holes with a diameter of approximately 15µm were machined into the gage section. The samples were annealed at 450°C for 1 hour to remove the deformation during rolling and laser machining.

A 5% solution of nitric acid in anhydrous ethanol was used to etch the sample and remove fine scratches. The samples were immersed in the solution for approximately 10 seconds and subsequently rinsed with ethanol.

3.4.2 Surface Patterning Procedure

Grayscale contrast is required on the surface of the samples in order to use the DIC method for strain mapping. Two methods of surface patterning were evaluated in this work. One method used a focused ion beam (FIB) to create a surface pattern and the other method employed chemical methods. The FIB method consisted of exposing the sample to the beam for very short durations. This created small craters, nanometers deep in the sample surface, which produce grayscale contrast when observed under an optical microscope. The second technique used to produce a surface pattern involved chemical methods. Samples were immersed in a solution consisting of 1g $CuSO_4*5H_2O$ per 1L of distilled water for a short period of time. The copper displaced the magnesium atoms on the surface which created the desired contrast. Figure 3.13 shows the surface patterns produced using both methods described. It was established that the chemical method produced a surface pattern with a higher density of grayscale contrast and therefore, finer strain grid during DIC calculations. As a result, the chemical method will be presented more frequently in the results section.

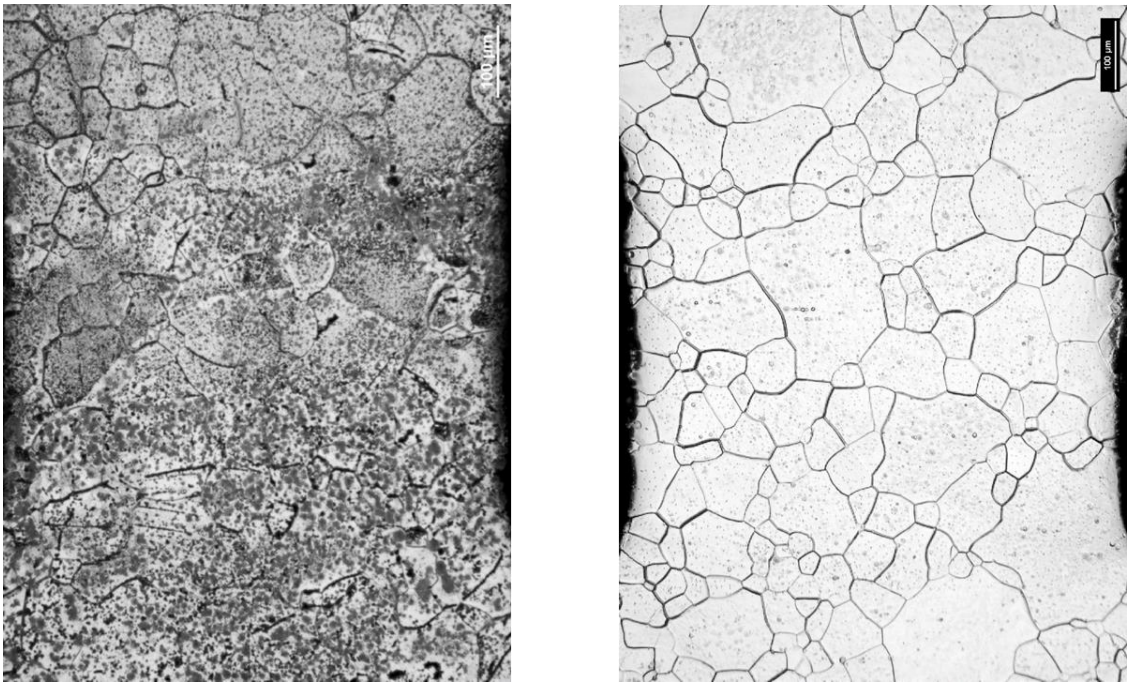

(a) (b)

Figure 3.13: Surface patterns produced by (a) chemical and (b) FIB methods.

One criticism regarding the chemical method is that there is a possibility of degrading the mechanical integrity of the material with long exposure times to the solution. The true stress strain curves were compared for hole free materials with the chemical surface treatment and without the treatment. The results are shown in Figure 3.14. It was established that the true stress strain response of the sample exposed to the $CuSO_4$ solution was indistinguishable, within experimental error, when compared to the sample which was not exposed. Furthermore, the fracture mechanisms observed were similar to the results obtained in the ESEM experiments. This suggests that the conditions used in these experiments do not degrade the mechanical response of the materials tested.

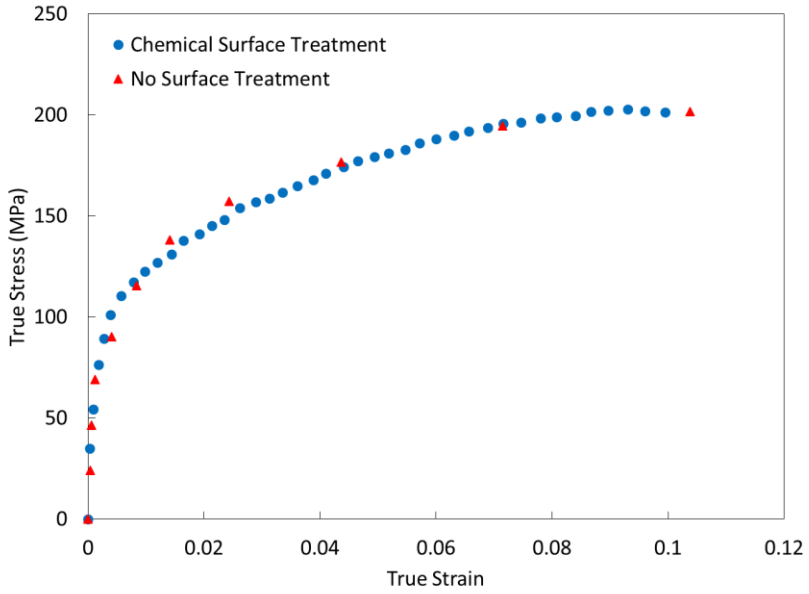

Figure 3.14: True stress strain curves for samples with and without chemical surface treatment.

3.4.3 Tensile Testing and Characterization Techniques

EBSD maps were obtained using the JEOL 7000 SEM prior to surface patterning to increase the percentage of indexing. It is possible to obtain maps after the surface patterns have been created, however, it is recommended to obtain the patterns beforehand. The EBSD data was analyzed to determine the grain size distribution and initial texture. The average grain size was $32 \pm 4\mu m$ with a standard deviation of $19\mu m$. In addition, the samples tested in this section have a stronger basal texture. Samples were pulled in uniaxial tension using a MTII/Fullam SEM micro-tensile stage under a Nikon AZ100M stereoscope. The tensile stage used in these experiments is an upgraded model to the one discussed in Section 3.3.4 and is shown in Figure 3.15.

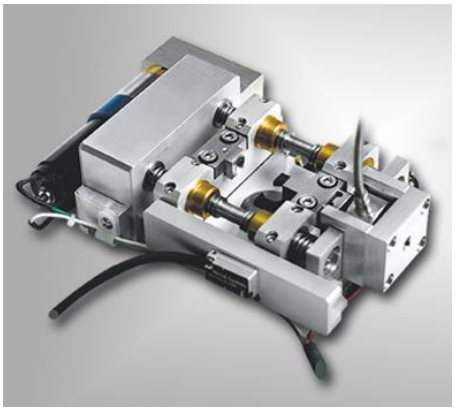

Figure 3.15: MTII/Fullam SEM micro-tensile stage.

Tensile tests were carried out using a 444 N load cell and the samples were pulled at a constant speed of 5μm/s corresponding to a nominal strain rate of 1×10^{-2} s^{-1}. A lower strain rate was used during these set of experiments to capture more information closer to the final failure. The displacement is measured with an LVDT similar to the setup previously discussed. The tests were stopped in increments of deformation to obtain images for analysis. These images were imported into ARAMIS for strain calculations using the DIC method. It should be noted that with the current set up it is not feasible to observe both surfaces without physically taking the sample out of the grips. This would cause relaxation and alter the measurements of the void dimensions. As a consequence, one surface is examined during the experiments which involve the micro-tensile stages.

3.5 In-situ Tensile Testing using Microtomography for 3D Analysis

The experiments described up to this point enable surface observations and measurements to characterize deformation and fracture in the CP magnesium tested. In

practice, damage accumulation typically occurs within the bulk of the sample where constraints are different from those at the surface. The final experimental approach uses x-ray microtomography to observe damage within the bulk of magnesium materials. In-situ tensile tests were performed inside a Skyscan 1172: High Resolution Desktop Microtomography system. Scans were obtained in increments of deformation to observe and quantify the fracture processes in 3D. The objective of this approach is to understand how the results from the surface experiments can be applied to commercial materials. The material used for this study is sheet magnesium free of holes. This section will address the material preparation procedure, experimental method and describe how the data is processed using the SkyScan 1172 system.

3.5.1 Material Preparation Procedure for Microtomography Experiments

Tensile samples were machined from the as-received material using EDM. The sample geometry utilized for the microtomography experiments is shown in Figure 3.16. Table 3.3 shows the polishing procedure used for sample preparation.

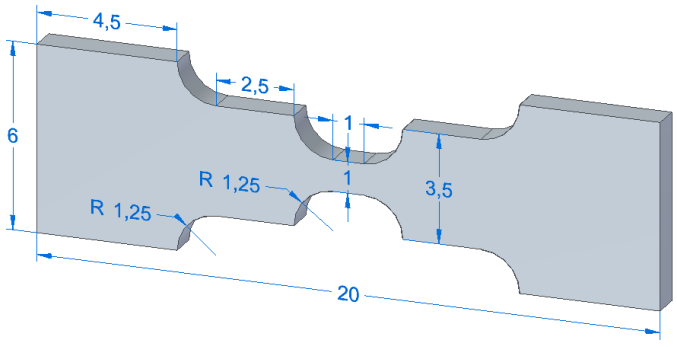

Figure 3.16: Tensile sample geometry for tomography experiments.

Table 3.3: Sample preparation procedure.

Surface	Load (N)	Time (min)
4000 SiC paper	10	1
3μm diamond suspension	10	5
1μm diamond suspension	10	5
0.05μm colloidal silica	10	10

After the mechanical polishing procedure the samples were annealed at 350 °C for 1 hour. A final chemical polishing procedure was then carried out to remove any oxidation and fine scratches produced from the final polishing stage. Samples were immersed in a 10% solution of nitric acid in anhydrous ethanol for approximately 30 seconds and then rinsed with ethanol. The final sample thickness was roughly 1 mm after sample preparation, which led to a square cross section. Axisymmetric cross sections are the most convenient for tomography since the absorption spectrum is similar for each rotation step during the 360 degree rotation. A square cross section has been used here to yield a tolerable difference in the absorption spectrum during rotation. The minimum and maximum thicknesses that the beam travels through are 1 mm and 1.4mm respectively. For cross sections where these values vary significantly, the intensity of the detected beam could be too high or low in regions which could lead to the introduction of artifacts.

3.5.2 Tensile Testing in Microtomography System

Tensile tests were carried out inside the chamber of a Skyscan 1172 microtomography system. A schematic drawing of the tensile stage outlining the main components is shown in Figure 3.17. The electronics which control the stage and communicate with the control software are contained within the body of the stage. A stepper motor with a planetary gearbox configuration is used to move the lower clamp down for tension and up for compression. The displacement is measured by a digital displacement sensor with micron resolution. Tests were carried out using a 444N load cell at a constant speed of 0.002mm/s corresponding to a strain rate of $2x10^{-3}s^{-1}$. The central specimen chamber is composed of a poly methyl methacrylate (PMMA) thin walled tube which is virtually transparent to x-ray radiation. This tensile stage is situated on a rotating plate within the microtomography system. Scans were obtained in increments of deformation in order to observe the fracture process in 3D.

3.5.3 SkyScan 1172 Microtomography System

The fundamentals of x-ray tomography were discussed in Section 2.5.3. As mentioned, the three main components of the system consist of a source, object and detector. A brief description of these components in the Skyscan 1172 system will be presented (Skyscan, 2005).

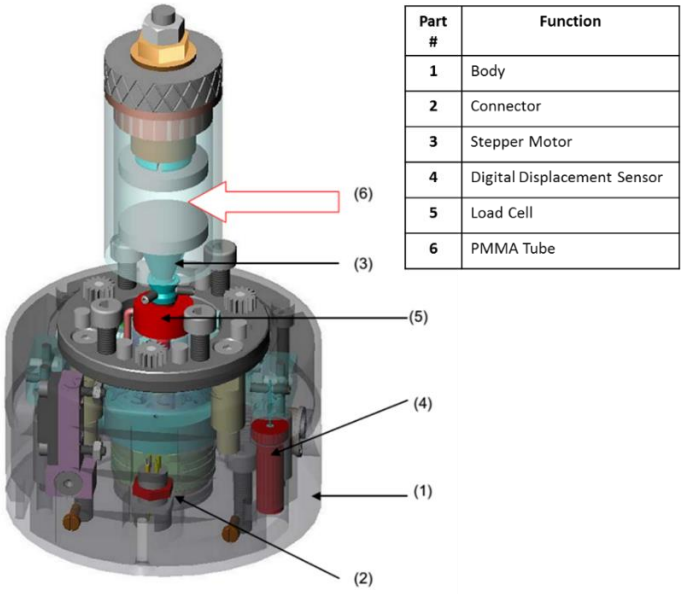

Part #	Function
1	Body
2	Connector
3	Stepper Motor
4	Digital Displacement Sensor
5	Load Cell
6	PMMA Tube

Figure 3.17: Tomography tensile stage schematic (Skyscan, 2010).

The source consists of a sealed microfocused X-ray tube with a lifetime greater than 10 000 hours. An x-ray tube is composed of a vacuum tube which contains two essential components; the cathode emitter and the anode target. A large potential difference is held between the anode and cathode. The cathode emitter is a filament heated by a high voltage power supply. Electrons are generated at the cathode by thermionic emission and are accelerated in the electric field towards the target. When the electrons interact with the target x-rays are produced. The target is angled so that the x-rays are directed through a window in the desired direction. Coils can be used to focus the x-rays to obtain small spot sizes for high resolution imaging. The Skyscan 1172 source produces a cone beam of x-rays with a spot size less than 5μm at 4 W. Table 3.4 summarizes the x-ray source parameters used during the in-situ tensile tests.

Table 3.4: X-ray source parameters.

Energy (kV)	Current (μA)	Power (W)
90	112	10

The object under investigation consists of a tensile specimen loaded on the tensile stage. Adjustments to the resolution of the scan can be made by changing the position of the source and detector, relative to the sample. This relationship is illustrated in Figure 3.18. The tensile stage limits the distance that can be attained between the sample and the source. A voxel edge length of 2.77μm has been used for the experiments.

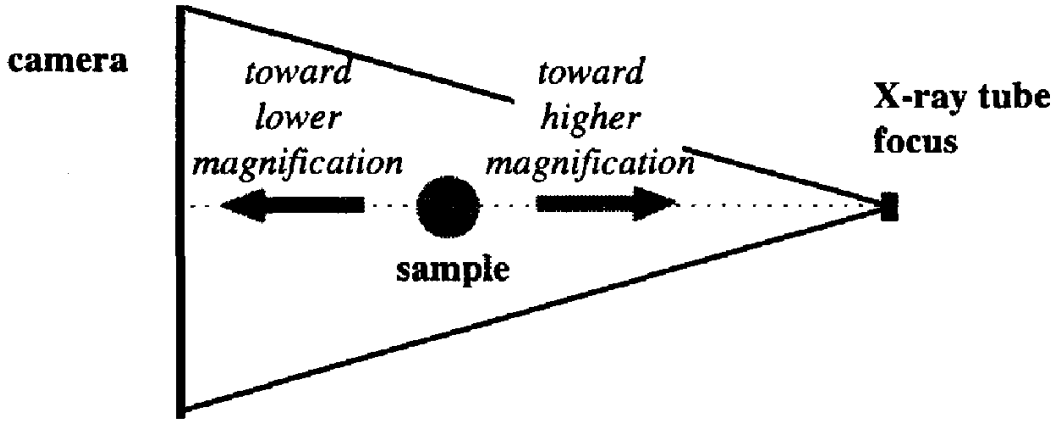

Figure 3.18: Relationship between the position of the object and magnification (Brauchel et al., 2000).

The detector is an essential component of the tomography system as it dictates the resolution of the information obtained. A scintillation detector is used in the Skyscan 1172 system which permits high resolution imaging. The setup consists of a charged-coupled device (CCD) camera based on a 4000 x 2300 (10 Mp) cooled CCD sensor with fibre optic

coupling to a gadox X-ray scintillator. Once the x-rays have penetrated through the sample, they travel through a scintillator screen composed of a phosphorus material that transforms the x-ray radiation into visible light. The light is transferred through optical fibres to the CCD sensor where the x-ray shadow projections are digitized.

3.5.4 Image Processing

The Skyscan 1172 system uses absorption contrast for imaging. Absorption contrast imaging is based on differences in the attenuation coefficient, of the various elements within the object. The attenuation coefficient μ is a quantity that measures how well x-rays can penetrate through a given material and can be expressed as:

$$\mu = K\rho\frac{Z^4}{E} \tag{3.1}$$

where K is a constant, ρ is the density, Z is atomic number and E is the energy of the photons (Brauchel et al., 2000). Therefore, larger attenuation coefficients represent materials which absorb more x-rays. The photons detected by the sensor provide a map of the attenuation coefficient in 2D space (radiograph). For the scans obtained in this thesis, radiographs are obtained in 0.4° increments, during a full 360° rotation of the sample. The radiographs are processed with NRecon software which uses the Feldkamp algorithm for cone beam volumetric reconstructions (Skyscan, 2011). Figure 3.19 shows the cross section of a deformed tensile sample which has been reconstructed and viewed using CTAn software.

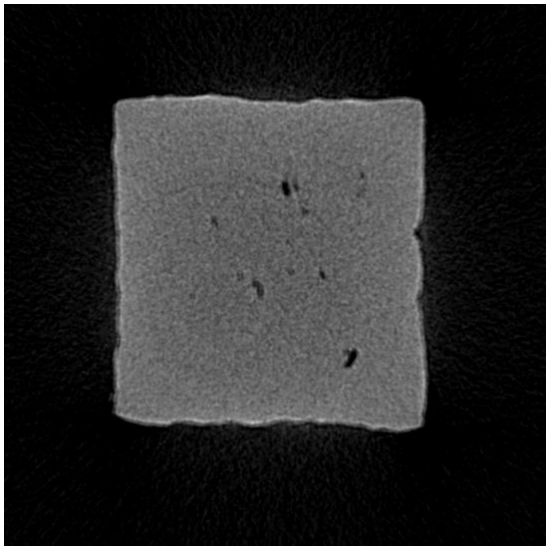

Figure 3.19: Reconstructed cross section of a deformed tensile specimen. Tensile axis is out of the page.

Two types of objects are being examined during the experiments; the magnesium matrix and voids which form as the material is deformed. Since magnesium has a higher density and atomic number than the holes, it absorbs a relatively larger number of photons and can easily be separated from the voids. Grayscale values are assigned according to the number of photons absorbed, therefore, the matrix is represented by large grayscale values. Furthermore, noise is observed surrounding the object in Figure 3.19. In order to eliminate this noise, a region of interest has been applied to the scans, using the shrink wrap function in CTAn. This function uses an algorithm to fit a region of interest to the sample surface based on defined grayscale values. Separation of the matrix and the voids was than achieved in CTAn by creating 3D models from a selected range of grayscale values. Figure 3.20 shows a 3D model viewed in CTVol, consisting of holes with grayscale values of 0 – 39 and a matrix with grayscale values 40 – 255.

Figure 3.20: 3D model of deformed CP magnesium. Matrix shown in transparent grey and holes in red.

Chapter 4

In-situ Tensile Testing under ESEM

4.1 Introduction

The main objective of this chapter is to present observations of void growth and linkage in magnesium, a material showing strong mechanical anisotropy. Tensile testing, coupled with electron microscopy, was used in order to capture these processes experimentally. The growth of the holes was quantified by obtaining measurements associated with the geometry of the holes at various increments of deformation. Similar experiments have been carried out on aluminum (Weck and Wilkinson, 2008) and copper (Li, 2013) materials. The effects of void fraction and void orientation on the growth and linkage of the holes, have been analyzed in these studies by positioning the holes at several void separation distances and at various angles with respect to the tensile axis. A strong correlation between the void configuration and the growth and linkage processes was observed for these materials which exhibit a higher degree of mechanical isotropy. The results were helpful to predict failure more precisely and validate existing models such as those proposed by Brown and Embury (1973) and Thomason (1981). It is of interest to carry out similar experiments on an emerging structural material which has low crystallographic symmetry and strong anisotropic mechanical properties. The effects of void fraction and void orientation on the growth and linkage processes are assessed to aid

in the understanding of deformation and fracture in magnesium. Furthermore, EBSD patterning has been included into the analysis to evaluate the effects of the local microstructure.

The first section of the chapter deals with the measurements that will be used frequently throughout the chapter and discusses the error associated with each quantity. In the second section the effects of void fraction, void orientation and microstructure on void growth will be assessed. Experimental data will be presented and compared with previous results and an isotropic finite element simulation utilizing the material properties obtained from the magnesium used in the study. The results show the significance of anisotropy in the void growth process. The effects of void fraction and void orientation on the linkage process will be evaluated in the third section. Experimental observations and measurements will be presented and compared to previous results. Finally, the effects of the local microstructure and fracture mechanisms will be evaluated in the final section.

4.2 Parameters and Measurements

In order to quantify the growth and linkage processes several parameters and measurements must be defined. This section will define each parameter and measurement used throughout the chapter. Furthermore, the error associated with each measurement is discussed.

4.2.1 Hole Configurations

Two types of hole configurations were examined and shown in Figure 4.1. The parameters d and θ were defined as the centre to centre hole separation distance and the orientation angle, respectively. Holes were machined into a set of samples with the configuration shown in Figure 4.1(a) to assess the effects of void fraction on void growth and linkage. The samples were machined with centre to centre hole separation distances of 40, 55 and 70 μm. Another set of samples were machined with the configuration shown in Figure 4.1(b) to examine the effects of void orientation on the fracture processes. These samples were machined with a constant centre to centre hole separation distance of 40 μm and orientation angles of 15°, 30° and 45°.

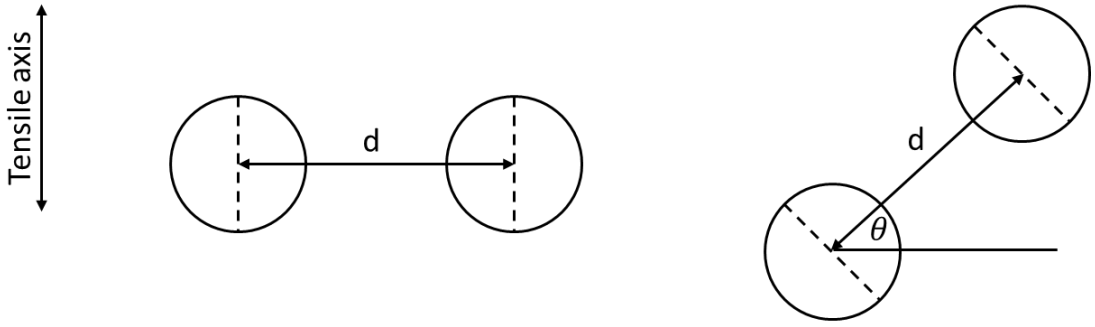

Figure 4.1: Hole configurations examined to observe the effects of (a) void fraction and (b) void orientation angle on deformation and fracture.

4.2.2 Hole Dimensions

The hole dimensions were measured to quantify the local deformation in the vicinity of the holes. Consider the undeformed and deformed schematic of a hole growing in a strain

field as depicted in Figure 4.2. The tensile and lateral dimensions have been defined as a and b, respectively. Undeformed or initial dimensions are represented with a 0 subscript.

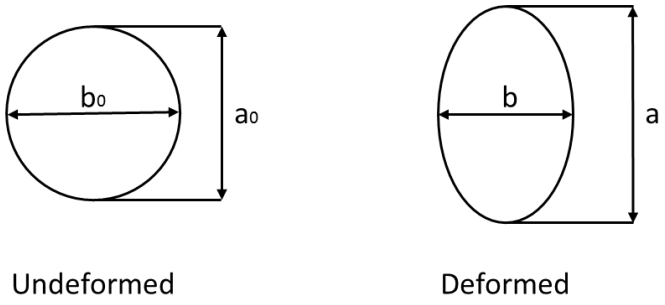

Figure 4.2: Geometric parameters measured to determine local displacements in the vicinity of the holes.

The hole dimensions were measured using ImageJ software. An edge detection algorithm was used to determine the position of the hole edges. Details concerning the algorithm can be found in the ImageJ documentation (Abramoff et al., 2014). A line scan was then used to determine the peak greyscale values corresponding to the hole edges and to measure the dimensions of the holes. Figure 4.3 shows the original ESEM image, the image after the edge detection algorithm has been applied to it and the line scan used to measure the holes.

In order to obtain statistical data based on the error associated with the measurements, the tensile dimensions of 19 holes were measured 10 times at each increment of deformation until linkage occurred. The standard deviation of the measurement defined the precision of the measurement which has been used to represent error. In general, as the deformation of the holes increased, the error related to the

measurement increased as well. This can be attributed to the irregularity of the holes as deformation proceeds. It was more difficult to precisely find the centre of the hole as it became more irregular in shape. Figure 4.4 shows the standard deviation as a function of far field strain for the hole with the maximum standard deviation in the dataset.

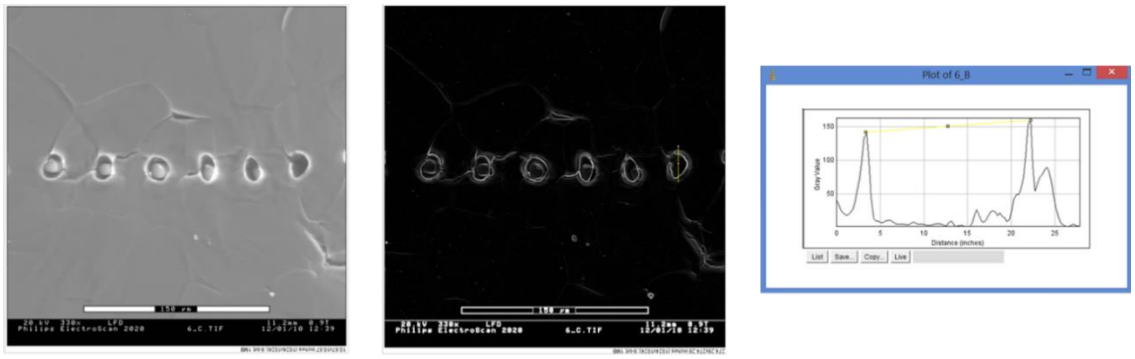

(a) (b) (c)

Figure 4.3: Measurement procedure (a) original ESEM image (b) image with edge detection algorithm applied (c) line scan result for measurement.

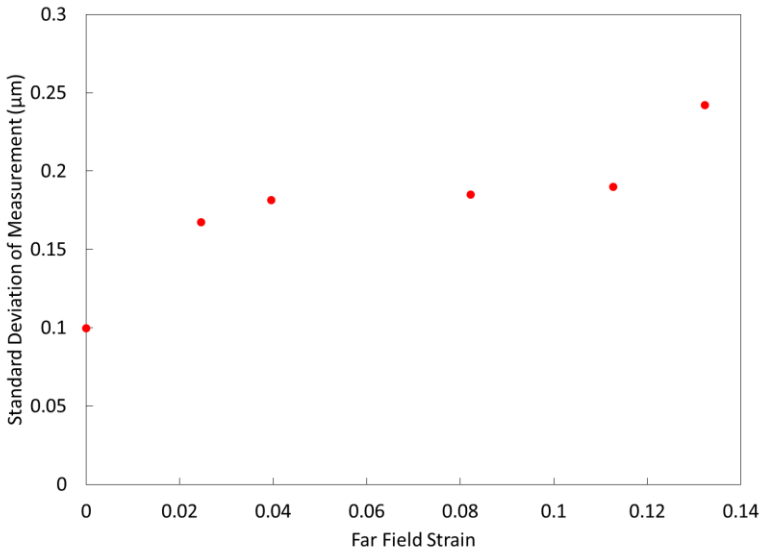

Figure 4.4: Standard Deviation of measurement for the hole with the largest distortion in the dataset vs. far field strain.

The maximum standard deviation was approximately 0.25 μm. This hole was then measured 40 times and the measurements were input into R statistical software for analysis (R Core Team, 2000). The histogram of the measurements is shown in Figure 4.5. The measurements obtained show a normal distribution with a standard deviation of approximately 0.25 μm. As a result, 0.25 μm has been defined as the absolute error δ associated with the measurement of the holes.

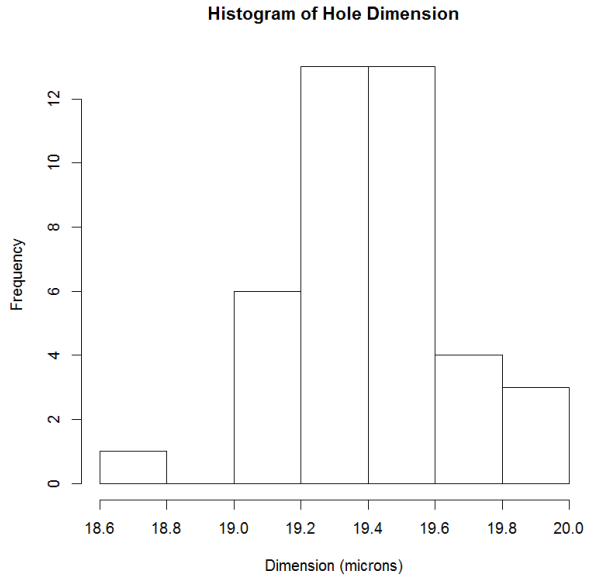

Figure 4.5: Histogram of the measurements obtained for the hole with the greatest distortion at the largest far field strain.

4.2.3 Normalized Void Dimension

The normalized void dimension is a measurement that will be used to describe the growth of the holes. Normalizing the hole dimension by the initial dimension eliminates the slight variation of the initial hole size produced by laser machining.

It was observed that the initial dimension had the smallest standard deviation in the measurements described above. Therefore, the error related to the initial dimension δ_0 is approximately 1% of the hole diameter and has been assumed to be negligible. The normalized void dimension has been defined as

$$\frac{D}{D_0} = \frac{x \pm \delta}{x_0 \pm \delta_0} \tag{4.1}$$

where x is replaced by a and b for the tensile and lateral dimensions respectively.

4.2.4 Far Field Strain

The samples used to examine the effects of void fraction contain a notch as shown in Figure 4.6. It is therefore necessary to define a strain which can be measured accurately and related to the macroscopic behavior of the material. The far field strain has been defined as the average elongation of the notched region and is given by

$$\varepsilon = \ln\left(\frac{l_1 + l_2}{l_{01} + l_{02}}\right) \tag{4.2}$$

where l_1 and l_2 are defined in Figure 4.6. The 0 subscript represents the initial lengths of the notched region.

Furthermore, the samples used to assess the effects of void orientation also contain a notch with a different configuration as shown in Figure 4.7. The far field strain in this case was defined as the maximum elongation of the notched region and is given by

$$\varepsilon = \ln\left(\frac{l_3}{l_{30}}\right) \tag{4.3}$$

where l_3 is defined in Figure 4.7 and the 0 subscript refers to the initial state.

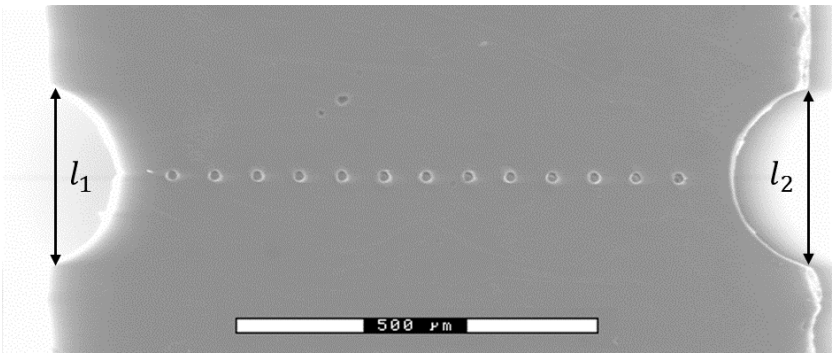

Figure 4.6: Parameters used to measure the far field strain of the notched region for samples examining void fraction.

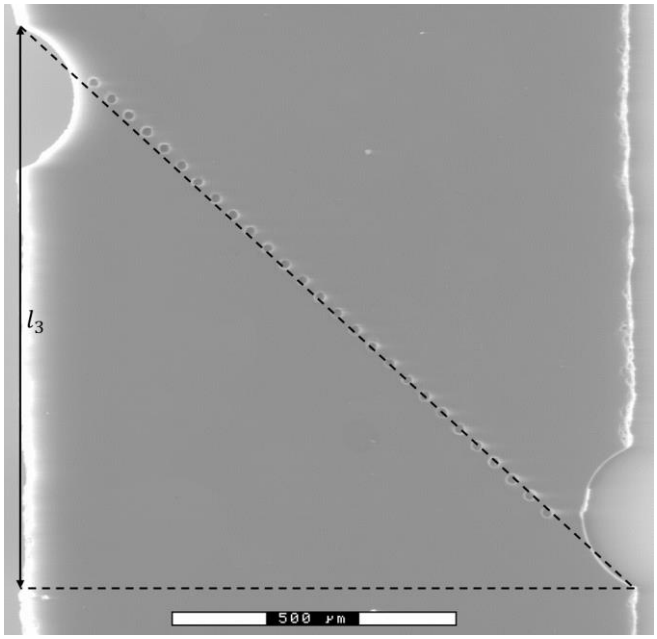

Figure 4.7: Parameters used to measure the far field strain of the notched region for samples examining void orientation.

4.2.5 Void Fraction

One of the objectives of this study is to assess the effects of void fraction on the growth and linkage processes. The void fraction f, can be related to the centre to centre separation distance through the following equation

$$f = \frac{b_0 \pm \delta}{d} \tag{4.4}$$

where b_0 is the average initial lateral dimension of the holes.

4.2.6 Normalized Void Dimension at Failure

There are several models that relate void dimensions to a failure strain. In order to evaluate the effects of void fraction and orientation on the fracture of magnesium, the first two voids that linked have been analysed within each data set. The normalized void dimension at failure has been defined to express the local displacement when these voids link. Figure 4.8 shows the first two holes before and after linkage in one of the samples tested. The tensile dimension is shown in red before and after linkage for the two holes of interest. The normalized void dimension at failure has been defined as

$$\left(\frac{D}{D_0}\right)_{fracture} = \frac{\frac{a_{ibefore} + a_{iafter}}{2}}{a_{i0}} \tag{4.5}$$

where the i subscript can be replaced by 1 and 2 for the voids of interest. The measure represents the average displacement of a given hole when void linkage occurs. The error related to the measurement is given by:

$$\left(\frac{D}{D_0}\right)_{max} = \frac{a_{iafter}}{a_{i0}} \tag{4.6a}$$

$$\left(\frac{D}{D_0}\right)_{min} = \frac{a_{ibefore}}{a_{i0}} \tag{4.6b}$$

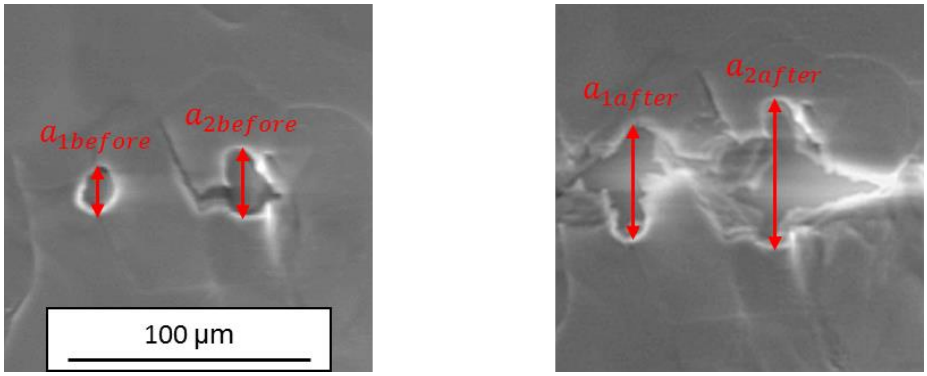

(a) (b)

Figure 4.8: Tensile dimension of two holes (a) before and (b) after linkage.

4.3 Void Growth

Commercial materials contain particles or holes with various separation distances and orientations relative to one another. Therefore, the goal of these experiments is to evaluate the effect of each parameter on void growth in a controllable manner. As a result, samples have been tailored with various centre to centre hole separation distances d and orientations θ. The name and parameters of the samples referred to in this chapter are

summarized in Table 4.1. In order to observe void growth experimentally, the samples were pulled in uniaxial tension under an ESEM. Images where obtained at several increments of deformation and the holes were measured at each increment to quantify the evolution of the holes.

Table 4.1: Void configurations and naming convention for the samples used to evaluate void growth.

Name	d (μm)	θ (°)
40A	40	0
55A	55	0
70A	70	0
15°A	40	15
30°A	40	30
45°A	40	45

4.3.1 Isotropic Finite Element Simulation of Void Fraction Effects on Void Growth

Finite element simulations have been carried out which assume isotropic hardening in order to understand the strain distribution induced by the notch and the role of crystal anisotropy on void growth. Part files were created using measurements from samples 40A and 70A. These two samples were compared to show differences between the highest and lowest void fractions evaluated in this work. Figure 4.9 shows the part files and the boundary conditions imposed for each simulation. The numbers in yellow are void reference numbers for the discussions below. One quarter of the gage section was modelled due to symmetry. As a result, x-symmetry and y-symmetry conditions were assigned to the

corresponding surfaces. A uniaxial stretch was applied to the top surface and the displacement value was measured from the experimental results. The material was modelled as an isotropic hardening material with a Young's Modulus of 42 GPa and Poisson ratio of 0.2875. These values were obtained from Cambridge Engineering Software material data sheets (Granta, 2013). The plastic hardening law was acquired from the experimental stress strain curve (Figure 3.14). 3D linear 8-node brick elements with reduced integration (C3D8R from Abaqus element library) were used for the analysis (Simulia, 2012). The elements on the front surface have an edge length of approximately 4 μm and 10 elements were used through the thickness. Each model consists of approximately 200 000 elements. The normalized void dimensions were extracted from the simulations in the tensile and lateral directions for comparison with the experimental results.

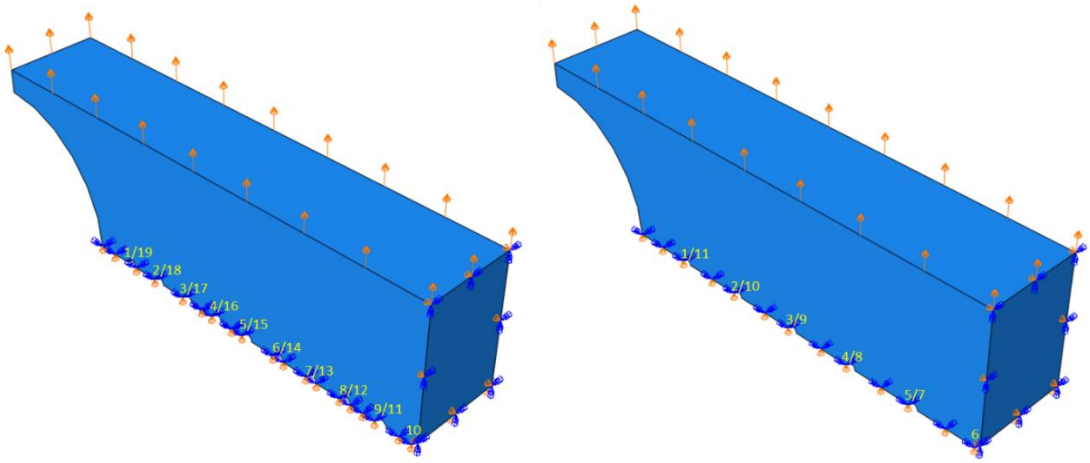

(a) (b)

Figure 4.9: Part files and boundary conditions imposed for samples (a) 40A and (b) 70A.

4.3.2 Void Growth in the Tensile Direction: Void Fraction Effects

Figure 4.10 shows the tensile displacement in the simulated samples 40A and 70A. The average growth of the holes is similar up to a strain of approximately 0.1. At this point the majority of the holes in the simulated sample 40A started interacting with one another and their growth was accelerated in the tensile direction. The distribution of the tensile displacement varied significantly between the samples investigated. In the simulated sample 40A the growth of the hole adjacent to the notch deviated from the average at a relatively low far field strain.

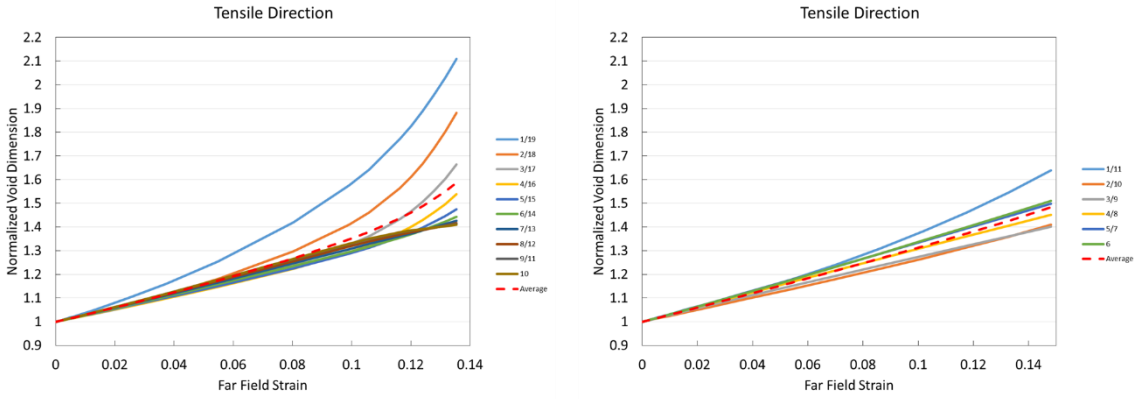

(a) (b)

Figure 4.10: Simulation results of normalized void dimension vs. far field strain for samples (a) 40A and (b) 70A in the tensile direction.

The maximum displacement was observed in the hole closest to the notch and decreased in the holes moving towards the plane of symmetry. For the simulated sample 70A the distribution of tensile strain induced by the notch was quite different from that in simulated sample 40A. The hole adjacent to the notch experienced the maximum displacement. However, holes 2 and 3 exhibited the least amount of displacement and the displacement

of the remaining holes laid between these values. The results show the effects of the notch triaxiality on void fraction for isotropic materials. Furthermore, it was observed that the majority of the holes in the simulated sample 70A did not interact with one another for the range of strains evaluated.

The average normalized dimension values (red dashed lines in Figure 4.10) from the isotropic finite element analysis have been superimposed on the experimental measurements for comparison and the results are shown in Figure 4.11. Interpretation of the simulation leads one to believe that the maximum displacement is always expected in the holes adjacent to the notch. With the exception of hole 11 in sample 70A, this is clearly not the case. It will become apparent later in the chapter that the localization associated with hole 11 in sample 70A was controlled by the microstructure. The majority of the holes in samples 40A and 70A do not show significant growth in the tensile direction. In each case the tensile strain was localized within a region. Holes 7-10 in sample 40A show a good agreement with the average displacement predicted by the model, however, it will become apparent later in the chapter that the growth of these holes are all interrupted by interactions with grain boundaries. Therefore, caution should be taken when interpreting this result. The simulation predicts that the growth is due to homogeneous deformation within the material while the experimental observations suggest that the growth of these holes is due to the localization of strain within adjacent grain boundaries. A similar result was observed in sample 70A. The tensile displacement was localized amongst holes 4, 10 and 11. Two independent localizations were observed in the sample, which are driven by the

microstructure. The results suggest that the notch did not have a significant effect on the growth of the holes in the tensile direction. Alternatively, the local microstructure created a non-uniform deformation field. In addition, the growth of the holes occurs more slowly than the model suggests. This is due to the localized nature of deformation. Microstructural effects create strain concentrations at a length scale similar in magnitude to the grain size. Therefore, the strain localizations induced by the microstructure only effect a small number of holes within the sample.

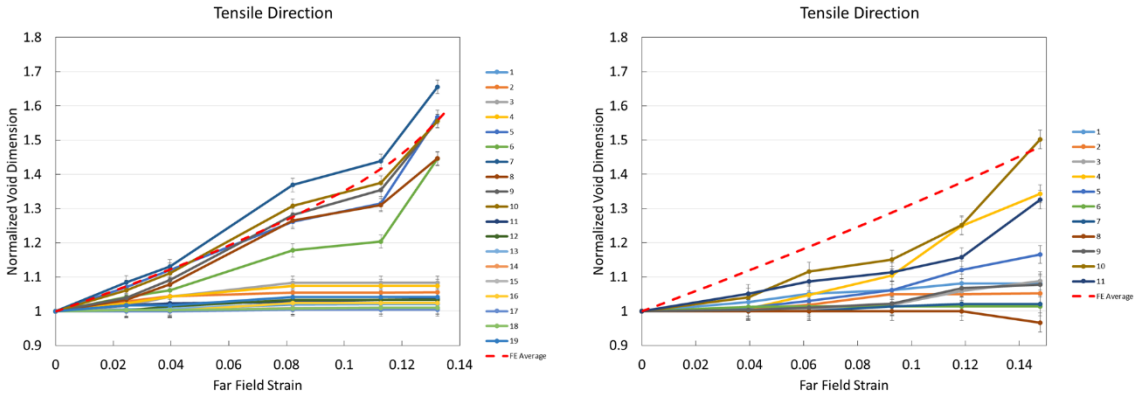

(a) (b)

Figure 4.11: Normalized void dimension vs. far field strain with the average simulation value overlaid on the experimental results for samples (a) 40A and (b) 70A in the tensile direction.

4.3.3 Void Growth in the Lateral Direction: Void Fraction Effects

In the work performed by Hosokawa (2011) on the growth of laser drilled holes in Cu, it was established that the evolution of the lateral dimension revealed important information regarding the interaction of the holes. Consider two holes oriented perpendicular to the tensile axis, deformed in an isotropic homogeneous matrix. At the

onset of plastic deformation it is expected that the holes contract in the lateral direction. With subsequent deformation, there will come a point at which the ligament between the two holes will begin to neck. At this point the holes begin to interact and grow towards one another laterally. The onset of this interaction can be characterized on the normalized void dimension vs. far field strain curve as the minimum value of the curve. This point was defined as the onset of coalescence in the work of Hosokawa, as it represents the point in which a plastic instability is introduced within the ligament between two holes. It is of interest to determine whether this phenomenon can be expected in the notched specimens using the isotropic simulation.

Figure 4.12 displays the lateral evolution of the holes in the simulated samples 40A and 70A. In general, the holes within simulated sample 40A show contraction in the lateral dimension up to a far field strain of roughly 0.05. With subsequent deformation, the ligament between the holes begins to neck and the lateral dimension increases. On average, this minimum value is not achieved until a strain of 0.12 in sample 70A. Furthermore, the distribution of strain induced by the notch in the gage section varies between the samples tested. As expected, the holes adjacent to the notch show unique growth behavior compared to the average value. For the simulated sample 40A, holes 1, 2 and 3 show a deviation from the average growth at relatively low values of strain. Another interesting result from this case relates to the evolution of displacement in the hole adjacent to the notch. This hole does not experience the maximum displacement. The result suggests that the triaxiality induced by the notch reaches a maximum value at a point which is closer in vicinity to hole

2. Holes 1 and 2 in the simulated sample 70A show a significant deviation from the average growth at a strain as low as 0.02. These holes begin interacting with one another at strains of approximately 0.05. In both cases the holes furthest away from the notch show an initial lateral contraction and do not show strong effects from the notch. In fact, in the simulated sample 70A, the holes furthest from the notch are still contracting at strains of approximately 0.14. The holes furthest from the notch in simulated sample 40A show a behavior consistent with the experimental observations of Hosokawa where there is an initial contraction followed by lateral expansion. The results confirm that the holes adjacent to the notch are expected to interact earlier in deformation.

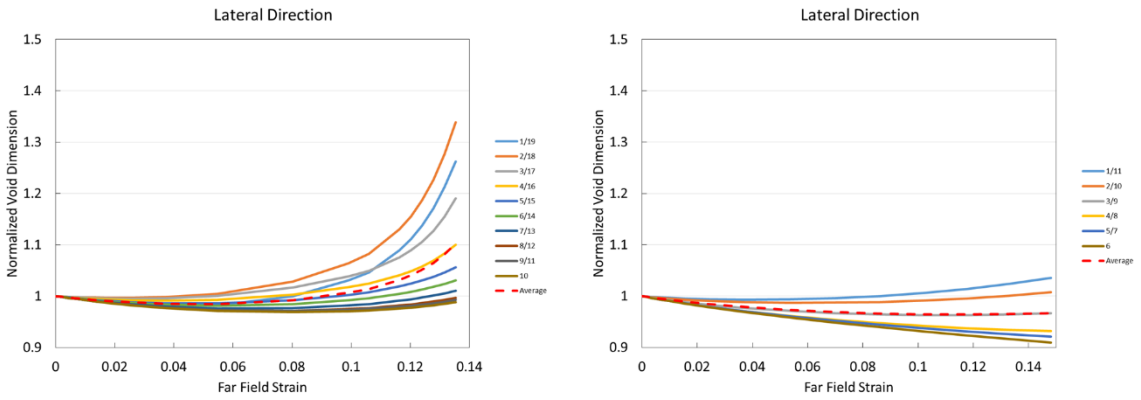

(a) (b)

Figure 4.12: Simulation results of normalized void dimension vs. far field strain for samples (a) 40A and (b) 70A in the lateral direction.

Similar to the treatment of the tensile displacement, the average values from the finite element analysis were overlaid on the experimental results for comparison of the lateral dimensions and the results are shown in Figure 4.13. The evolution of the holes in the lateral direction is very different from what was predicted by the simulation for both

cases. In sample 40A the majority of the holes begin to expand in the lateral direction from the onset of deformation. Holes 4, 8 and 10 show significant lateral expansion while holes 6 and 7 show the greatest lateral contraction. These holes are all within or adjacent to the strain localization in the tensile direction. This result indicates that there is not a strong correlation between the tensile and lateral displacement. For sample 70A the majority of the holes show negligible displacement in the lateral direction until a far field strain of 0.1. The simulation predicts that a significant amount of lateral shrinkage should occur followed by a slight lateral expansion. Holes 1 and 9 show the greatest lateral contraction. However, the simulation predicts that hole 1 should deviate from the average value and expand in the lateral direction at low values of far field strain. The displacement distribution predicted by the simulations is not observed in the experimental observations for both cases. This provides additional evidence that the triaxiality effects induced by the notch are outweighed by the impact of local microstructure. Furthermore, it was established that measurements of the lateral dimensions do not aid in understanding void interactions. The inconsistent behavior associated with the evolution of the lateral dimensions merely reinforces that the deformation is heterogeneous. The experimental behaviour observed is quite different from what is predicted by an isotropic FE simulation. This is not unexpected since Mg exhibits considerable anisotropy and the local microstructure is expected to play a major role. The remainder of this chapter will explore these effects in greater detail.

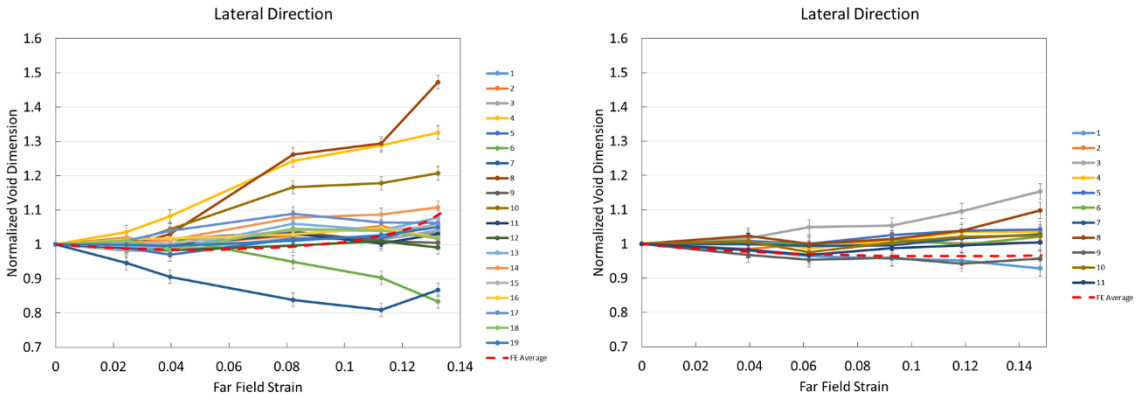

(a) (b)

Figure 4.13: Normalized void dimension vs. far field strain with the average simulation value overlaid on the experimental results for samples (a) 40A and (b) 70A in the lateral direction.

4.3.4 The Effects of Void Fraction on Void Growth

In order to evaluate the effects of void fraction on the growth behavior, void configurations with separation distances d of 40, 55 and 70 μm were investigated experimentally. These separation distances correspond to void fractions of 0.3175, 0.2364 and 0.1429 respectively. Weck (2007) showed that the void fraction has a strong correlation with the growth behavior of holes in a 5052 aluminum alloy. It was established that holes with a smaller separation distance or larger void fraction would begin to interact with one another at smaller far field strains and the holes would display rapid growth in the tensile direction once this interaction occurred. A similar result was obtained for growth in the lateral direction and the results are shown in Figure 4.14. It should be noted that 2W corresponds to d in Figure 4.14 and the minor diameter is the lateral dimension of the hole. Furthermore, it was observed that void growth occurred uniformly in the aluminum

materials tested by Weck. As a result, a single line was used to represent all of the holes in a row of voids.

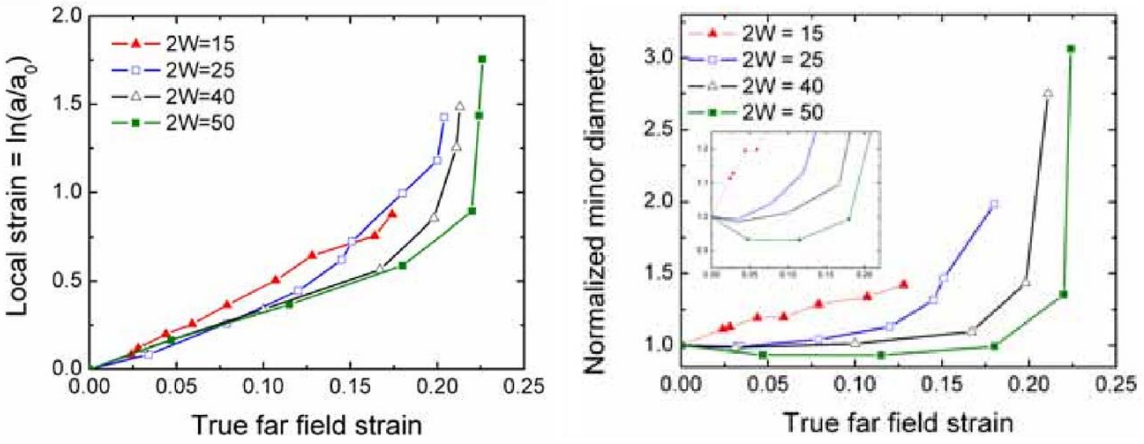

(a) (b)

Figure 4.14: Void evolution in AA5052 (a) local tensile strain vs. far field strain (b) normalized minor diameter vs. far field strain (Weck, 2007).

The ESEM images showing the deformation of a single row of holes in sample 40A are shown in Figure 4.15. This sample corresponds to one of the higher void fractions investigated in this work. The hole numbers are overlaid in yellow on the undeformed image for reference purposes. This convention will be used throughout this section. The normalized void dimensions are plotted as a function of far field strain in Figure 4.18. A localization of strain in the tensile direction is observed in the region containing holes 5-10. The holes in this region show a strong deviation from the average displacement from the onset of deformation. Furthermore, the evolution of these voids in the lateral direction do not show a consistent trend with deformation. Some of the holes in this region experience lateral expansion while others contract. The ESEM images show the roughening

of grain boundaries at a strain of 0.082 in the area of the localization suggesting that the microstructure plays a role in this observation.

Figure 4.16 displays the image series for an intermediate void fraction in sample 55A. The images show significant growth of hole 13, which bursts open at a strain 0.137 due to the failure of a grain boundary. The plot of normalized void dimension vs. far field strain in Figure 4.19 shows rapid displacement of this hole in the tensile direction from a strain as low as 0.04. Furthermore, the lateral dimension experiences significant expansion when this localization occurs in the tensile direction. Features of boundary roughening can be observed in the vicinity of this hole at a strain of 0.056. The majority of the holes do not exhibit significant growth in either direction. Twin boundaries become visible in the vicinity of hole 9 at a strain of 0.137. The shape of the hole becomes rather skewed once the twin has interrupted with the growth process; however, the hole does not experience significant growth.

The ESEM image series associated with one of the smaller void fractions examined in the work is shown in Figure 4.17. Microstructural evolution is observed within the vicinity of hole 11. The normalized void dimension vs. far field strain plot for this sample, 70A, is shown in Figure 4.20. Tensile strain localizations are observed to be associated with holes 4, 10 and 11. Holes 10 and 11 may be associated with the same features; however, the relatively large displacement experienced by hole 4 is independent of this event. This result shows the non-uniform deformation of the holes in this sample. Similar to the other samples tested there are a group of holes which do not experience growth in either direction.

In general, the holes showed an increase in tensile dimension as the far field strain increased for all of the void fractions evaluated. However, the growth of the holes was highly non-uniform. Some holes showed significant growth in the tensile direction while other holes displayed negligible growth. Furthermore, the evolution of the lateral dimension shows diverse behavior. Some of the holes increased while other holes decreased in dimension from the onset of deformation. The result suggests that the deformation is heterogeneous in the magnesium materials tested. When the void fraction is larger (separation distance is smaller) more holes become affected by localizations induced by the microstructure. Furthermore, microstructural features such as twin and grain boundaries have a significant impact on the growth behavior. These results are qualitatively different from what has been observed by Weck in materials with a higher degree of isotropy.

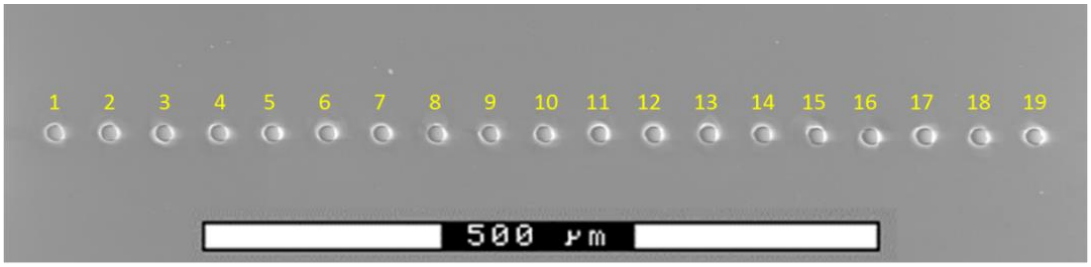

(a)

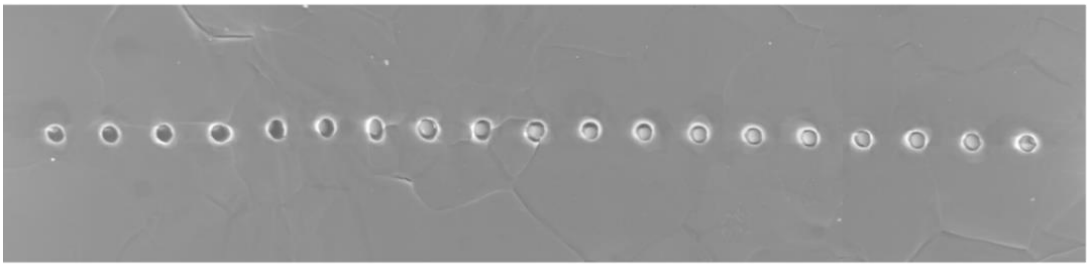

(b)

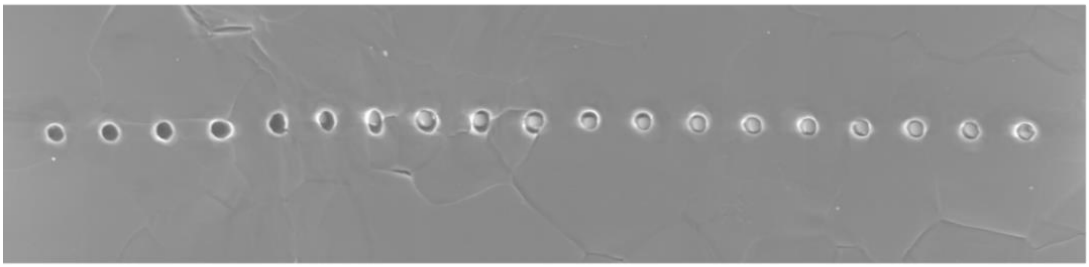

(c)

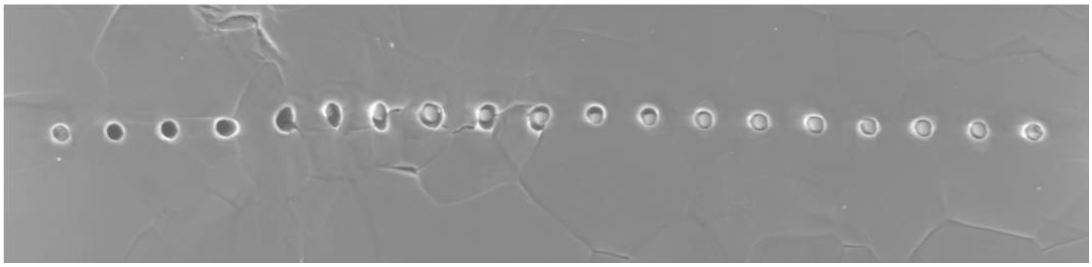

(d)

Figure 4.15: Evolution of holes at far field strains of (a) 0.000, (b) 0.082, (c) 0.113 and (d) 0.132 in sample 40A.

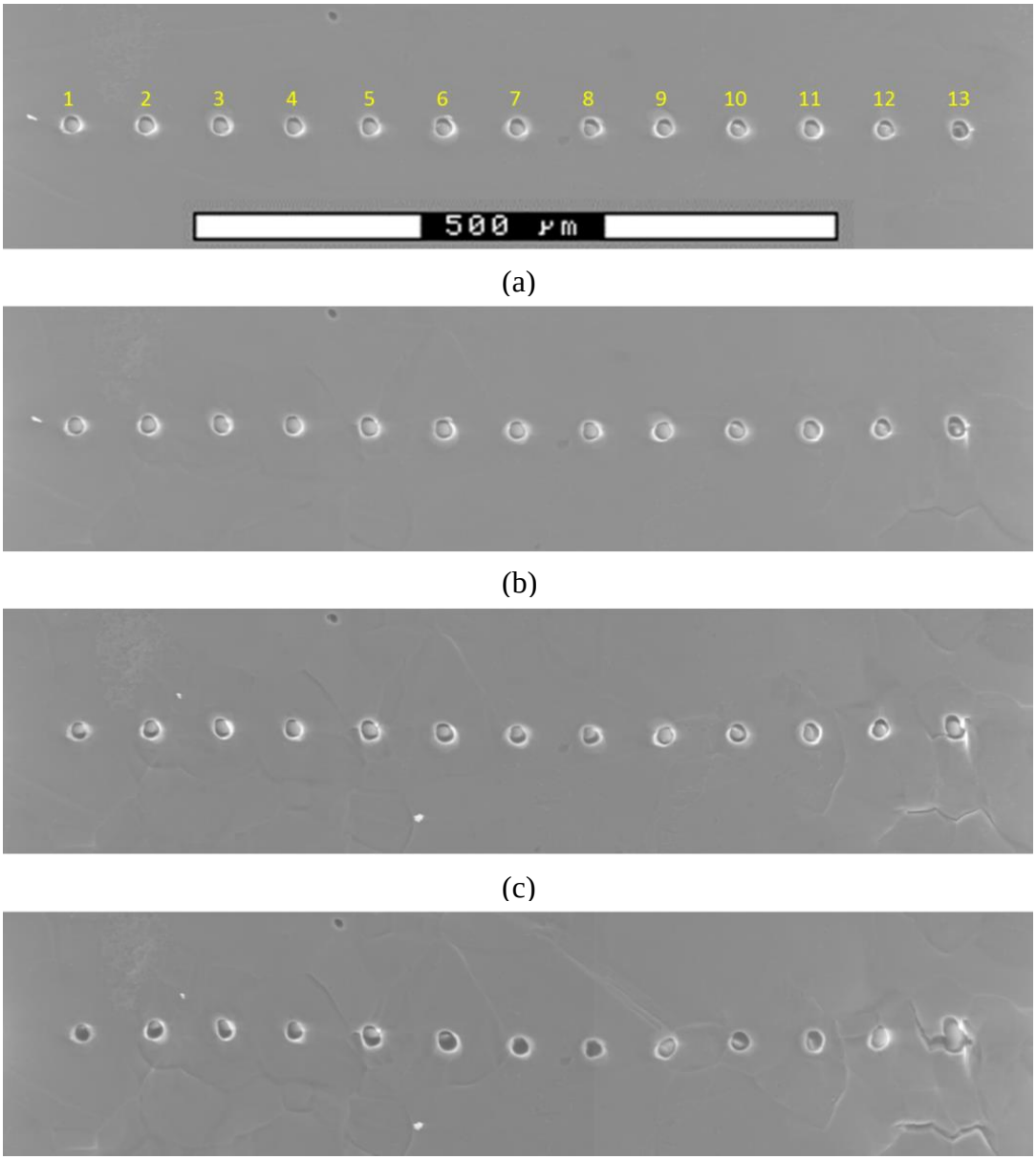

(a)

(b)

(c)

(d)

Figure 4.16: Evolution of holes at far field strains of (a) 0.000, (b) 0.056, (c) 0.098 and (d) 0.137 in sample 55A.

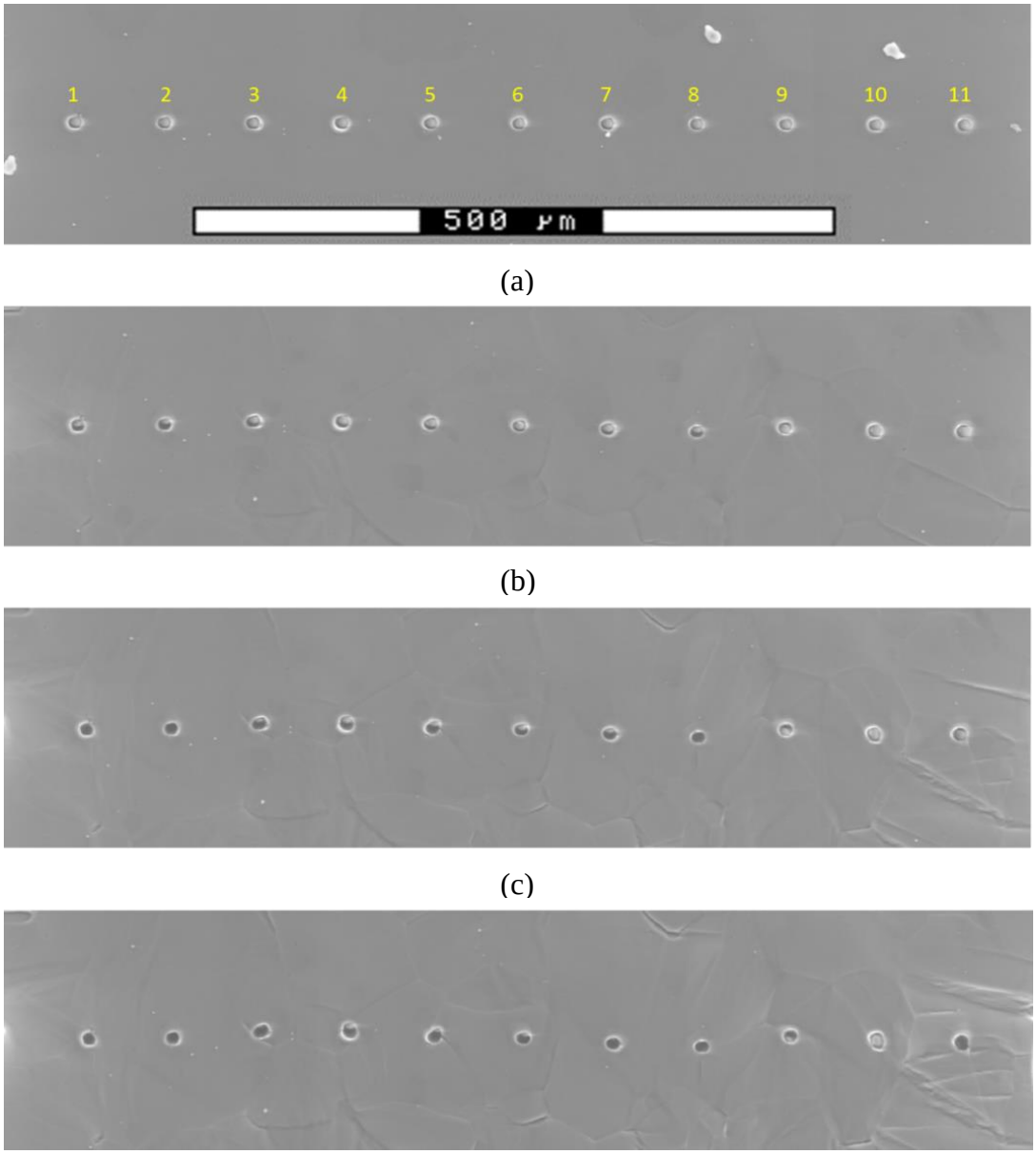

(a)

(b)

(c)

(d)

Figure 4.17: Evolution of holes at far field strains of (a) 0.000, (b) 0.062, (c) 0.119 and (d) 0.148 in sample 70A.

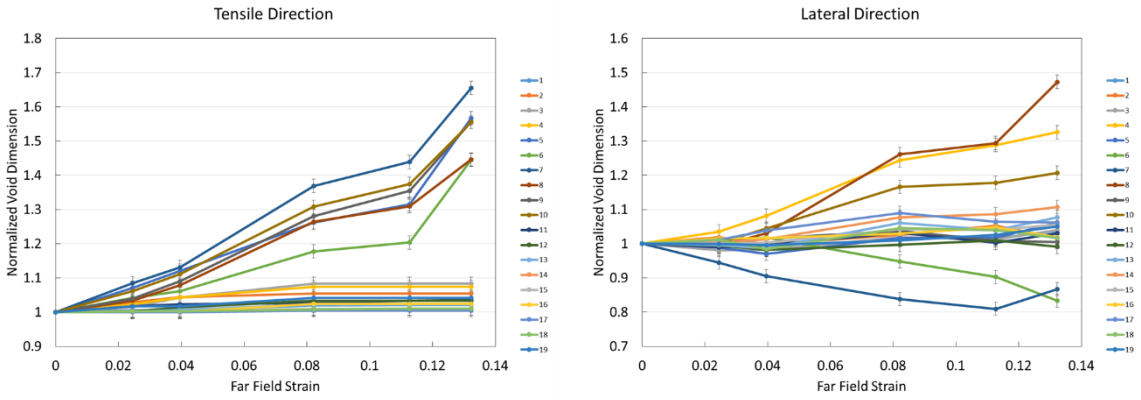

(a) (b)

Figure 4.18: Normalized void dimension vs. far field strain in the (a) tensile and (b) lateral directions for sample 40A.

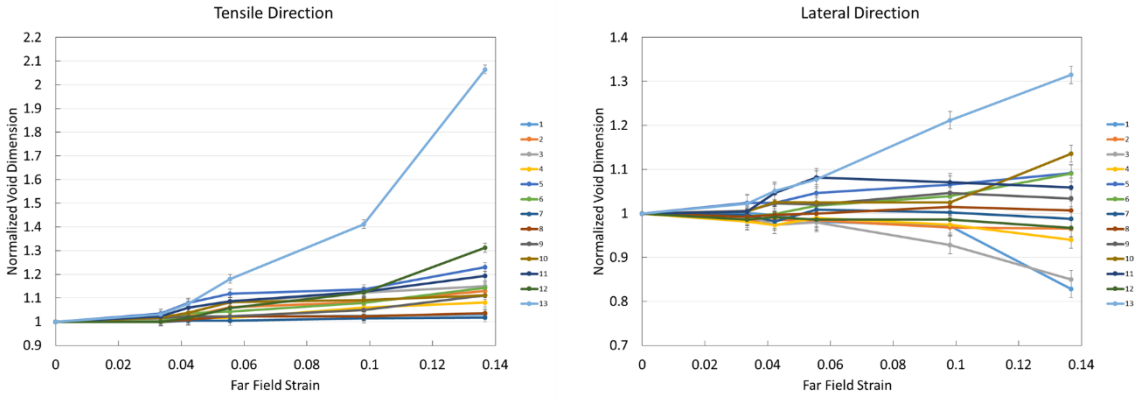

(a) (b)

Figure 4.19: Normalized void dimension vs. far field strain in the (a) tensile and (b) lateral directions for sample 55A.

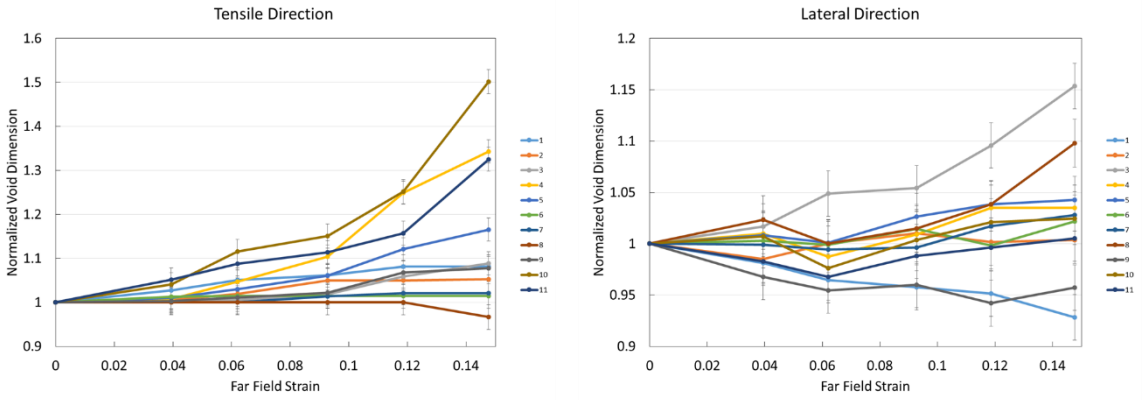

(a) (b)

Figure 4.20: Normalized void dimension vs. far field strain in the (a) tensile and (b) lateral directions for sample 70A.

4.3.5 Impact of Local Microstructure on Void Growth: Void Fraction Effects

The results presented so far suggest that the local microstructure plays a significant role in the deformation of the holes. Deformation was observed to occur non-uniformly for all of the void fractions examined. Kelley and Hosford (1973) showed that the stress-strain response of magnesium single crystals differs significantly when compressed and constrained in various orientations. Therefore, pulling polycrystalline magnesium in uniaxial tension is analogous to pulling a composite composed of regions or grains with soft and hard orientations. EBSD analysis has been carried out on sample 40A and 70A to study the effects of the microstructure on the deformation for relatively small and large void fractions.

Figure 4.21(a) shows the EBSD map of sample 40A in the undeformed state. The yellow numbers define the holes while the black numbers represent grain numbers. This convention will be used throughout this section. Tensile strain was observed to localize

between holes 5-10. The grains adjacent to these holes are grains 8-17. Examination of the inverse pole figure shown in Figure 4.21(b) does not indicate any direct relationship between the orientation and the location of the localization. The points representing the orientations that were involved with the localization of tensile displacement seem to lie randomly on the inverse pole figure. Basal slip is the main deformation mechanism in magnesium with a very low critical resolved shear stress. Consequently, the discussions dealing with deformation will mainly be focused on this deformation mechanism. The EBSD map reveals that grain 9 has a Schmid factor of 0.44 for basal slip. This is a relatively soft orientation for which basal slip will occur during the early stages of deformation. As a result, the growth of the holes adjacent to grain 9 can be attributed to basal slip in the early stages of deformation.

Figure 4.22(a) shows the EBSD map of sample 40A at a strain of 0.082. An appreciable number of extension twins can be found in the region of the localization. Figure 4.22(b) shows the pole figure associated with the map. The grains have rotated due to the activity of deformation mechanisms. The orientation of grain 9 is similar to what was observed in the undeformed state; however, there is a significant portion of this grain with a basal texture. Grain 9 experiences the most extension twinning and is associated with 3 of the holes that contribute to the localization. Furthermore, hole 7 is adjacent to this grain and shows the maximum displacement for all stages of deformation. The data shows that this hole is adjacent to two relatively soft grains. It is therefore probable that strain localization was associated with grain 9 and spread to the neighbouring holes. The tensile

and lateral evolution of the holes associated with grain 9 showed similar trends. Holes 5-7 all show an initial contraction in the lateral direction from the onset of deformation. In contrast, holes 8-10 all expanded laterally. These holes were associated with grain boundaries which contributed to the deformation of the holes. The simulation indicated that the holes closer to the centre of the sample have a greater tendency to contract laterally during the onset of deformation. The influence of the local microstructure in the deformation process did not allow this process to occur.

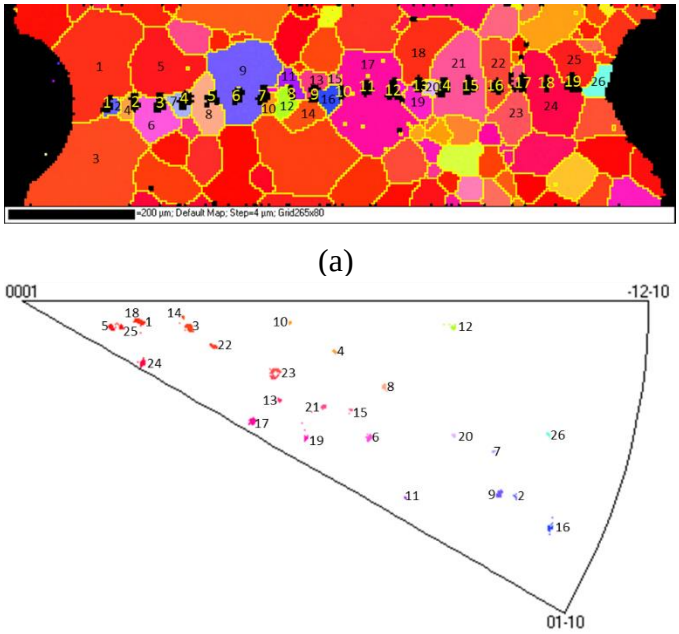

(a)

(b)

Figure 4.21: (a) EBSD map and (b) inverse pole figure for the undeformed state of sample 40A.

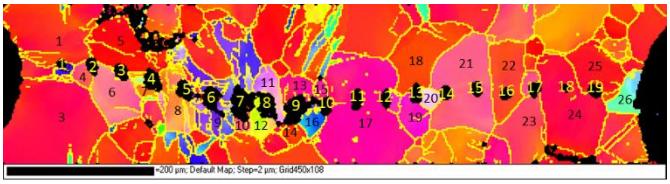

(a)

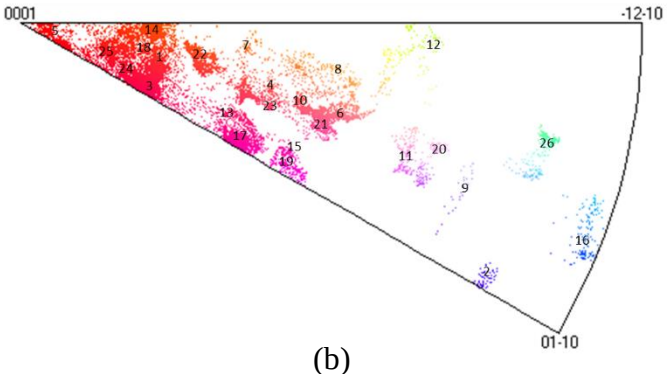

(b)

Figure 4.22: (a) EBSD map and (b) inverse pole figure at a far field strain of 0.082 for sample 40A.

The EBSD map for the undeformed state of sample 70A is shown in Figure 4.23(a). This sample has a stronger basal texture relative to sample 40A as shown in the pole figure (Figure 4.23(b)). The holes which showed the most growth in the tensile direction were holes 4, 10 and 11. The grains associated with hole 4 are grains 4, 6 and 7. Observation of the undeformed pole figure shows that these orientations span a wide range within the orientations of interest. Grain 4 has a relatively low basal Schmid factor of 0.045 while the values associated with grains 6 and 7 are 0.31 and 0.38 respectively. The growth of this hole in the early stages of deformation is likely due to the incompatibility between the hard and soft orientations. Holes 10 and 11 are associated with grain 15 which has a basal Schmid factor of 0.41. However, hole 1 is associated with grains having orientations which are close to that of grain 15. If the growth of the holes was driven solely by the triaxiality

produced by the notch, holes 11 and 1 should exhibit similar growth behavior. The experimental observations reveal that hole 1 displays negligible tensile growth. This result enforces that the effects of the notch triaxiality are not as strong as the local microstructure. It also suggests that there is a complex relationship between the microstructure and the deformation behavior.

Figure 4.24(a) shows the EBSD map of sample 70A at a strain of approximately 0.062. The pole figure is shown in Figure 4.24(b). Extension twins are visible in the vicinity of holes 2 and 3; however, these holes do not show an appreciable amount of deformation. The twins in this case do not lead to local strains in the vicinity of the holes and form in order to accommodate strain incompatibilities within these regions. There are no twins in the immediate vicinity of hole 4 which suggests that the deformation associated with this hole is driven by the adjacent grain boundaries. An interesting observation is the texture evolution associated with grains 4, 6, 7 and 15. The evolution of texture associated with these grains is shown in Table 4.2. The hard orientation associated with grain 4 has rotated into a soft orientation with regard to basal slip and the soft orientations have evolved into harder orientations. In addition, extension twinning is observed to contribute to the growth of hole 11.

The observations suggest that a complex relationship exists between the notch triaxiality, crystallographic texture, and microstructural features such as twin and grain boundaries which must be accounted for to predict the deformation behavior. Furthermore the effects of microstructural evolution have been reported which must also be considered.

The rotations experienced by the grains play a significant role in the local deformation behavior associated with the grains. All of the factors discussed, excluding notch triaxiality, contribute to the deviation from the isotropic analysis presented above.

Table 4.2: Basal Schmid factors in the undeformed and deformed states.

Grain #	Basal Schmid Factor (ε=0.000)	Basal Schmid Factor (ε=0.060)
4	0.045	0.42
6	0.31	0.065
7	0.38	0.018
15	0.41	0.021

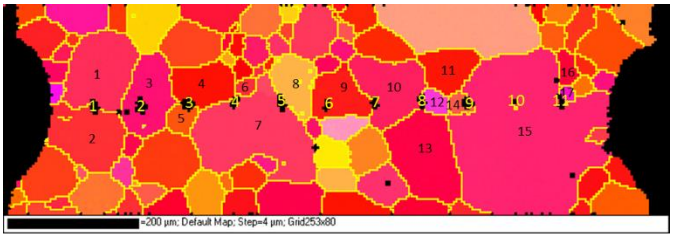

(a)

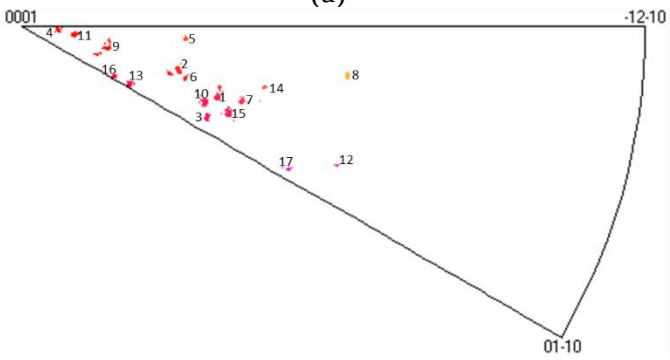

(b)

Figure 4.23: (a) EBSD map and (b) inverse pole figure for the undeformed state of sample 70A.

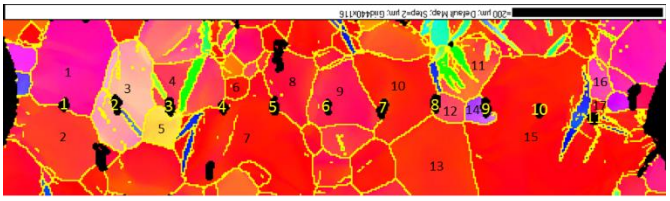

(a)

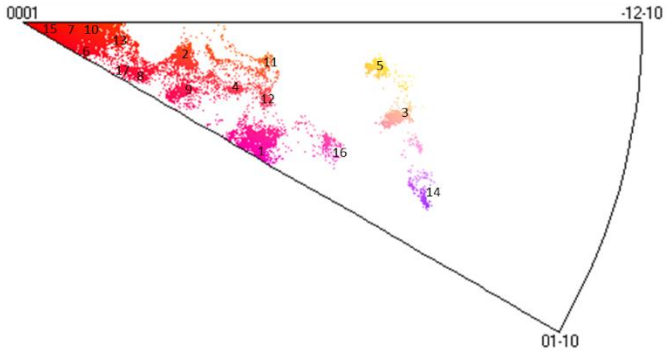

(b)

Figure 4.24: (a) EBSD map and (b) inverse pole figure at a far field strain of 0.062 for sample 70A.

4.3.6 Isotropic Finite Element Simulation of Void Orientation Effects on Void Growth

In order to validate the work carried out by Li (2013) on Cu and understand the notch effects in the arrays tested here on magnesium, an isotropic finite element analysis was performed. Part files were created using measurements from samples 15°A and 45°A. These samples were selected to enable a comparison of results from the lowest and highest orientation angles excluding 0°. Figure 4.25 shows the part files and the boundary conditions used in the simulations. The hole reference numbers are overlaid in yellow for the discussions to follow. Symmetry conditions exist in the z-direction. As a result, half of the thickness was used (approximately 50 microns) and z-symmetry was assigned to the

back surface. The bottom edge was constrained in the y-direction and no rotations were permitted along this edge. A uniaxial stretch was applied to the top surface and displacements were measured from the experimental results. The same material properties and element types discussed in the previous finite element analysis section were used. Similar to the previous finite element analysis, an element edge length of 4 microns was used on the front surface and 5 elements were used through the thickness to simulate a total of 10 elements through the thickness.

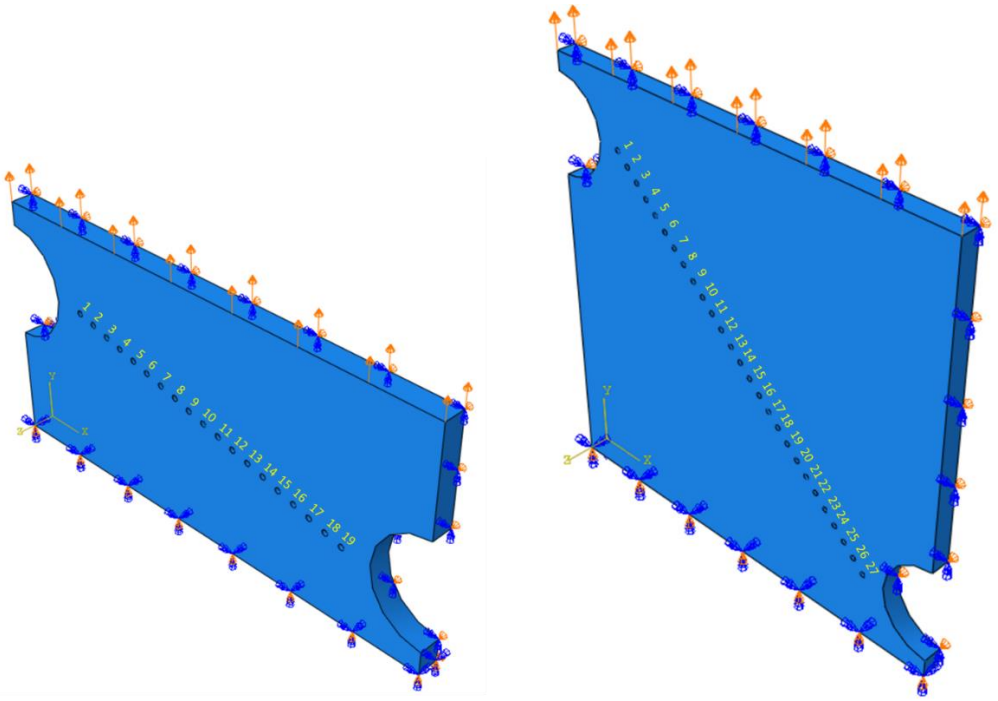

(a) (b)

Figure 4.25: Part files and boundary conditions imposed for samples (a) 15°A and (b) 45°A.

4.3.7 Void Growth in the Tensile Direction: Void Orientation Effects

Figure 4.26 shows the isotropic evolution of the holes in the simulations of samples 15°A and 45°A. On average the holes in the simulated sample 45°A displayed more elongation in the tensile direction compared to the holes in sample 15°A for the far field strains evaluated. The distribution of the strain was similar but varied in magnitude, as the hole closest to the notch experienced the maximum displacement and the hole farthest from the notch experienced the minimum displacement. The results revealed that a larger shear component leads to more rapid void growth in an isotropic material. The result is in contrast to what was observed in the copper materials studied by Li (2013).

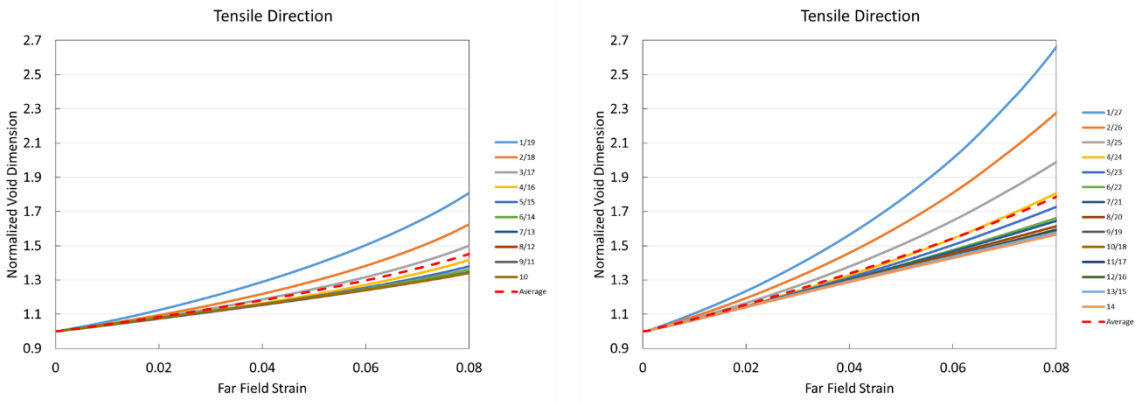

(a) (b)

Figure 4.26: Simulation results of normalized void dimension vs. far field strain for samples (a) 15°A and (b) 45°A in the tensile direction.

The average displacement values from the finite element analysis were superimposed on the experimental results for comparison and the results are shown in Figure 4.27. The majority of the holes in sample 15°A do not show significant growth in the tensile direction. Strain was localized between holes 17-19 in the later stages of

deformation. At first it is difficult to distinguish whether the localization is induced by the notch or the microstructure. Holes 18 and 19 show higher growth than that expected by the finite element analysis suggesting that the localization is associated with the local microstructure. It is most likely a combination of the microstructure and notch that created the localization. The fact that holes 1-3 do not exhibit similar behavior provides evidence that the local microstructure plays a more significant role than the notch in the localization. Growth of the holes in sample 45°A spans a wide range of values. There is still a small group of holes which do not exhibit a significant amount of growth in the tensile dimension; however, a larger number of holes display an appreciable amount of growth. Observation of the ESEM images reveals that these holes are either deforming by a shear process or associated with microstructural features. Holes 7-9 deform by a shear process and show good agreement with the finite element simulation. In addition, holes 27 and 17 are associated with the failure of grain boundaries and show much larger displacements than that predicted by the model. The results show that as the shear angle is increased from 15 to 45° the shear component becomes more prominent in the deformation behavior. However, for all angles tested the local microstructure still played a strong role in the prediction of the deformation.

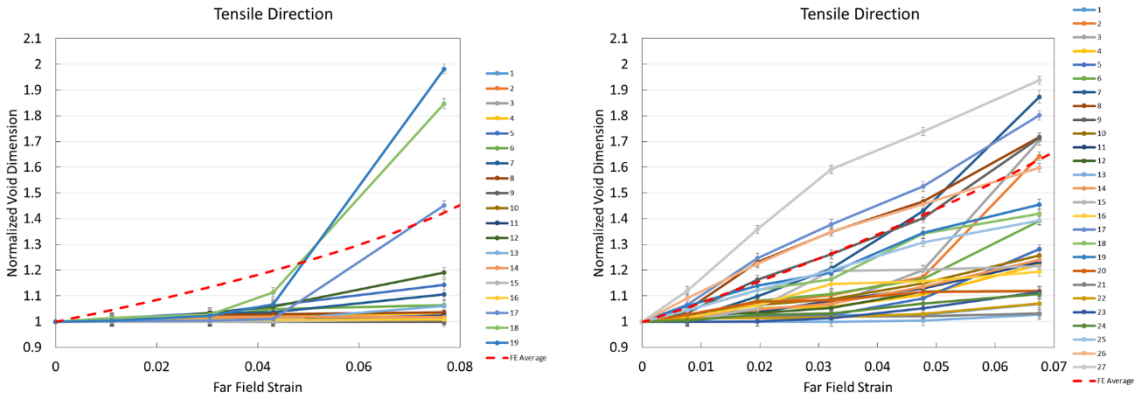

(a) (b)

Figure 4.27: Normalized void dimension vs. far field strain with the average simulation value overlaid on the experimental results for samples (a) 15°A and (b) 45°A in the tensile direction.

4.3.8 Void Growth in the Lateral Direction: Void Orientation Effects

The lateral dimension has been analyzed using a finite simulation to understand the behavior in an isotropic material. Figure 4.28 shows the normalized void dimensions vs. far field strain from the results of the simulation. On average the holes in the simulated sample 15°A show a slight contraction in the lateral direction followed by expansion at a strain of approximately 0.02. The result is similar to what was observed when the holes were perpendicular to the tensile axis. In contrast the majority of the holes in the simulated sample 45°A contract in the lateral direction for all of the far field strains evaluated. The distribution of displacement is consistent in both cases but once again varies in magnitude as the hole closest to the notch experiences the largest evolution while the hole farthest from the notch experiences the most lateral contraction. It should be noted that the lateral displacement results from the finite analysis are consistent with what was observed by Li

(2013); however, the tensile results differ. This result suggests that the introduction of a shear component changes the deformation behavior of the holes. When the holes are oriented perpendicular to the tensile axis the localization occurs by a necking process. In contrast, when the holes are oriented at angles of 30 and 45° the localization occurs by a shearing process.

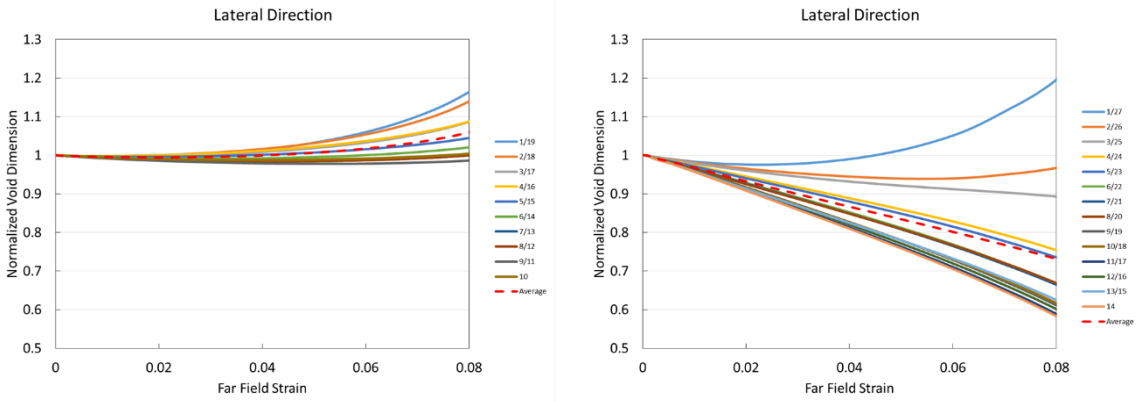

(a) (b)

Figure 4.28: Simulation results of normalized void dimension vs. far field strain for samples (a) 15°A and (b) 45°A in the lateral direction.

The average values from the simulation were compared to the experimental measurements and the results are shown in Figure 4.29. The simulation result agrees well with the results shown for sample 15°A. However, it is more likely a coincidence since the majority of the holes in this region did not show significant tensile growth. Furthermore, the simulation result for sample 45°A captures the trend but not the magnitude of the deformation behavior. It is clear that the majority of the holes are expected to contract in the lateral dimension and this is captured by the simulation result; however, the majority of the holes do not contract as much as the model predicts. The experimental results showed

that holes 7-9 deformed by a shear process. Hole 7 is in good agreement with the simulation; however, holes 8 and 9 contract more than the simulation result. It has been established throughout the chapter that the local microstructure plays an important role in the deformation history of the holes for all of the cases studied. As a result, minor discrepancies from the simulation can be expected and attributed to the effects of the local microstructure.

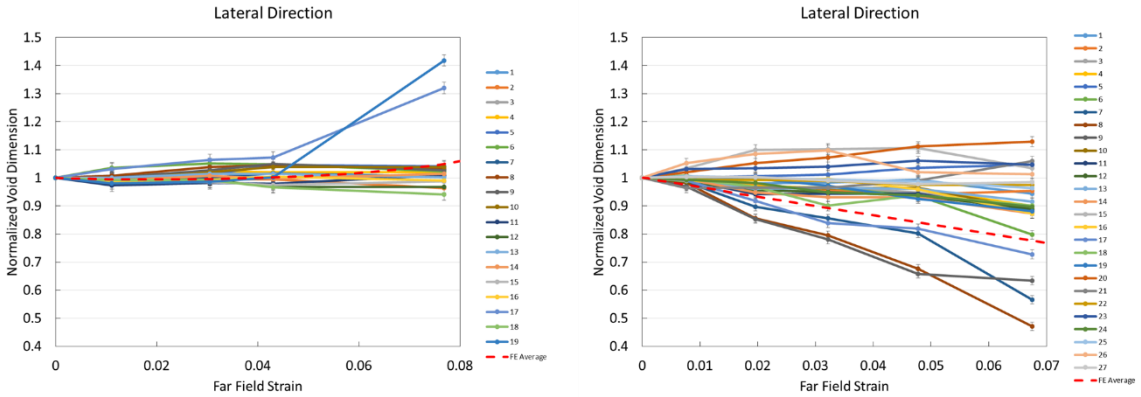

(a) (b)

Figure 4.29: Normalized void dimension vs. far field strain with the average simulation value overlaid on the experimental results for samples (a) 15°A and (b) 45°A in the lateral direction.

4.3.9 The Effects of Void Orientation on Void Growth

Particles or voids in materials are not always aligned perpendicular to the tensile axis and as a result, orientation effects are evaluated in this section experimentally. Li (2013) carried out recent work evaluating the effects of void orientation in copper. The local strain vs. far field strain for various orientations are shown in Figure 4.30 for the

materials tested. It was established that as the orientation angle was increased from 0 to 45°, the holes did not interact until larger far field strain values had been reached.

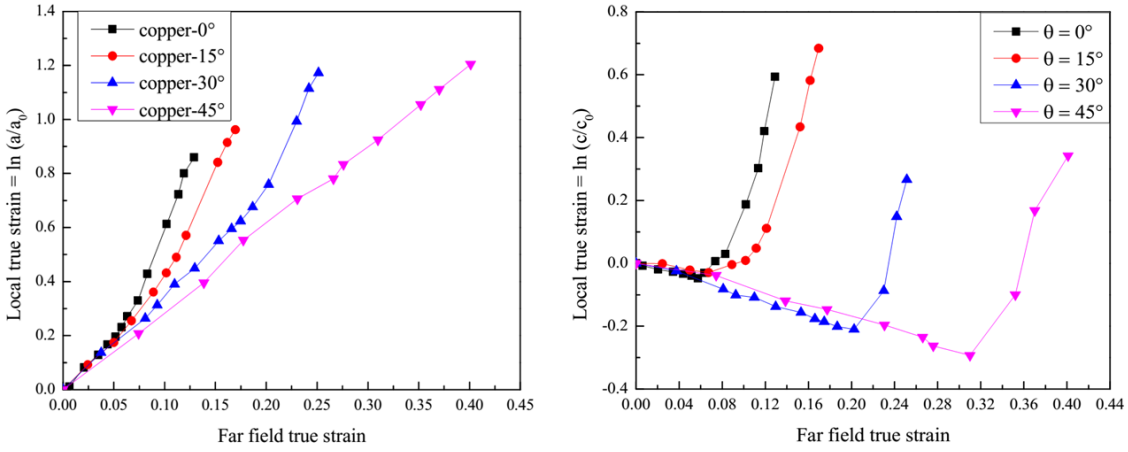

(a) (b)

Figure 4.30: Local strain vs. far field strain in (a) tensile direction and (b) lateral direction (Li, 2013).

In order to assess the orientation parameter in magnesium, the centre to centre separation distance was held constant at 40 μm. Figure 4.31 shows the evolution of a single row of holes in sample 15°A. Deformation in the tensile direction is observed to localize between holes 17-19. The normalized void dimension vs. far field strain plot looks similar to what was observed in the samples with void orientations perpendicular to the tensile axis as shown in Figure 4.34. The tensile deformation is localized in a small region and the majority of the holes exhibit negligible growth. In addition, the growth of the lateral dimensions between these holes is quite different. Hole 17 expands from the onset of deformation while holes 18 and 19 initially contract. At a strain of 0.011 hole 19 begins to expand in the lateral direction while hole 18 continues to contract. There is a possibility

that this deformation was induced by the notch; however, due to the observations presented earlier it is likely due to the microstructure.

The ESEM image series for the holes deforming in sample 30°A are shown in Figure 4.32. Microstructural features are revealed which cause localizations in several different regions. The normalized void dimension vs. far field strain plot for this sample is shown in Figure 4.35. Growth of the holes in the tensile direction can be broken down into 3 groups. Hole 16 exhibits the largest growth in the tensile direction; however, the ESEM images show that the rapid growth of this hole is influenced by the failure of a grain boundary. Another localization occurs between holes 7-14 and observation of the ESEM images show that the holes are influenced by a small shear component. The remaining holes do not show a significant amount of growth in the tensile direction. A similar trend cannot be found for the lateral evolution of these groups of holes. The lateral growth of hole 2 was effected by a grain boundary interaction at the onset of deformation and showed a significant deviation from the majority of the holes. Voids within the grouping of holes 7-14 both show lateral expansion and contraction during deformation. The result suggests that the shear component induced with an orientation angle of 30° is relatively weak since there is not a strong trend in the deformation behavior.

The ESEM image series for holes growing in the largest void orientation angle examined (45°) are shown in Figure 4.33. Once again, microstructural features are visible in the images, however, several holes are observed to deform by a shearing process. The normalized void dimension vs. far field strain for sample 45°A is shown in Figure 4.36. A

relatively larger number of holes show tensile growth as well as lateral contraction in this sample. The variability of growth in these trends is large, nevertheless, the result suggests that the shear component induces more deformation in the holes prior to fracture. The largest tensile strains are found at holes 7-9 as well as in the vicinity of holes 17 and 27. Observation of the ESEM images reveals that holes 17 and 27 are interrupted by grain boundaries during the deformation while holes 7-9 deform by a shear process. These holes show consistent shrinkage in the lateral direction suggesting that the holes are deforming by similar mechanisms in this region. Hole 17 shows significant lateral shrinkage; however, the deformation process becomes interrupted by a grain boundary at a strain of roughly 0.032. The results show that shear localizations are favored in sample configurations with void orientation angles closer to 45°.

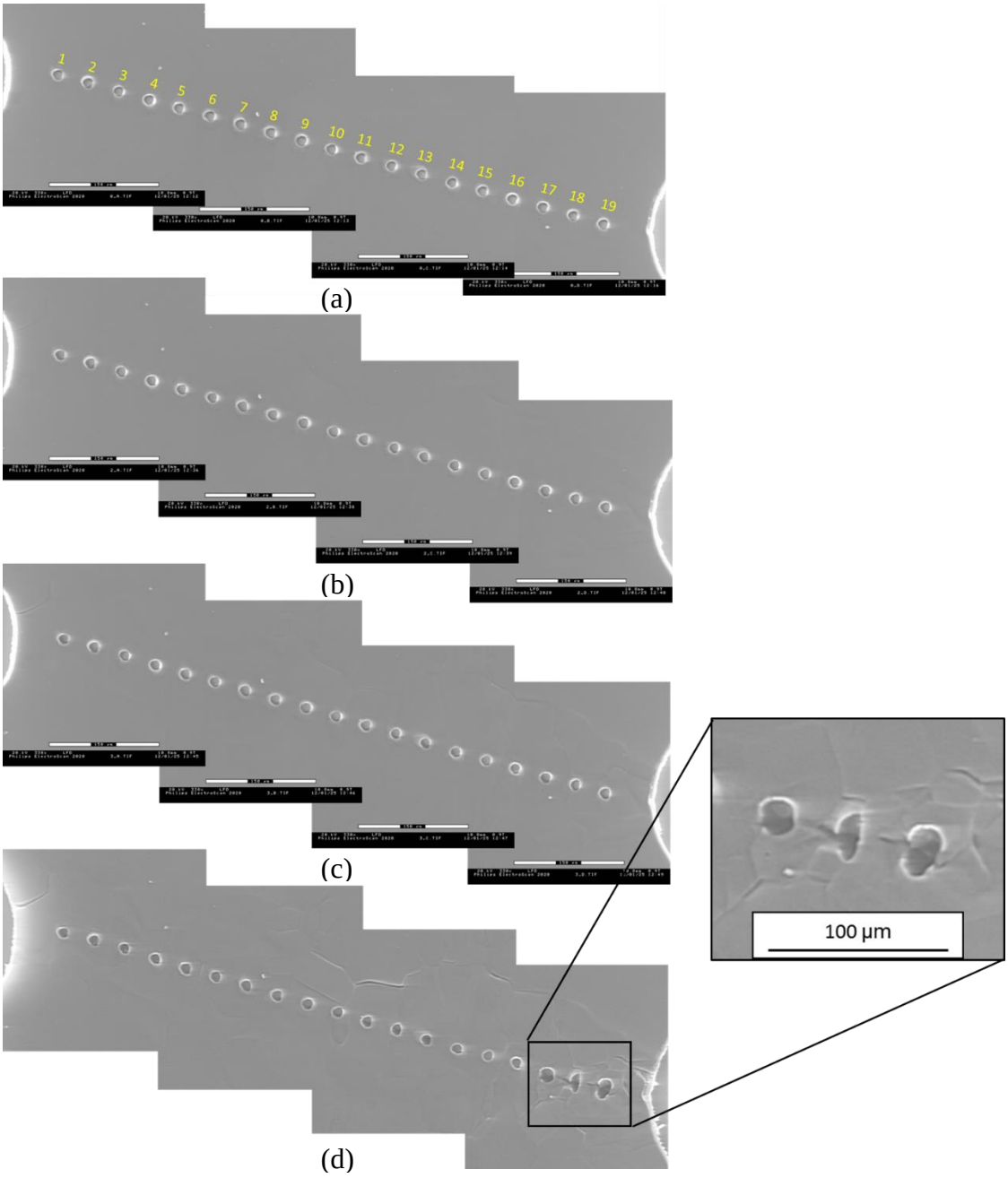

Figure 4.31: Evolution of holes at far field strains of (a) 0.000, (b) 0.031, (c) 0.043 and (d) 0.077 in sample 15°A.

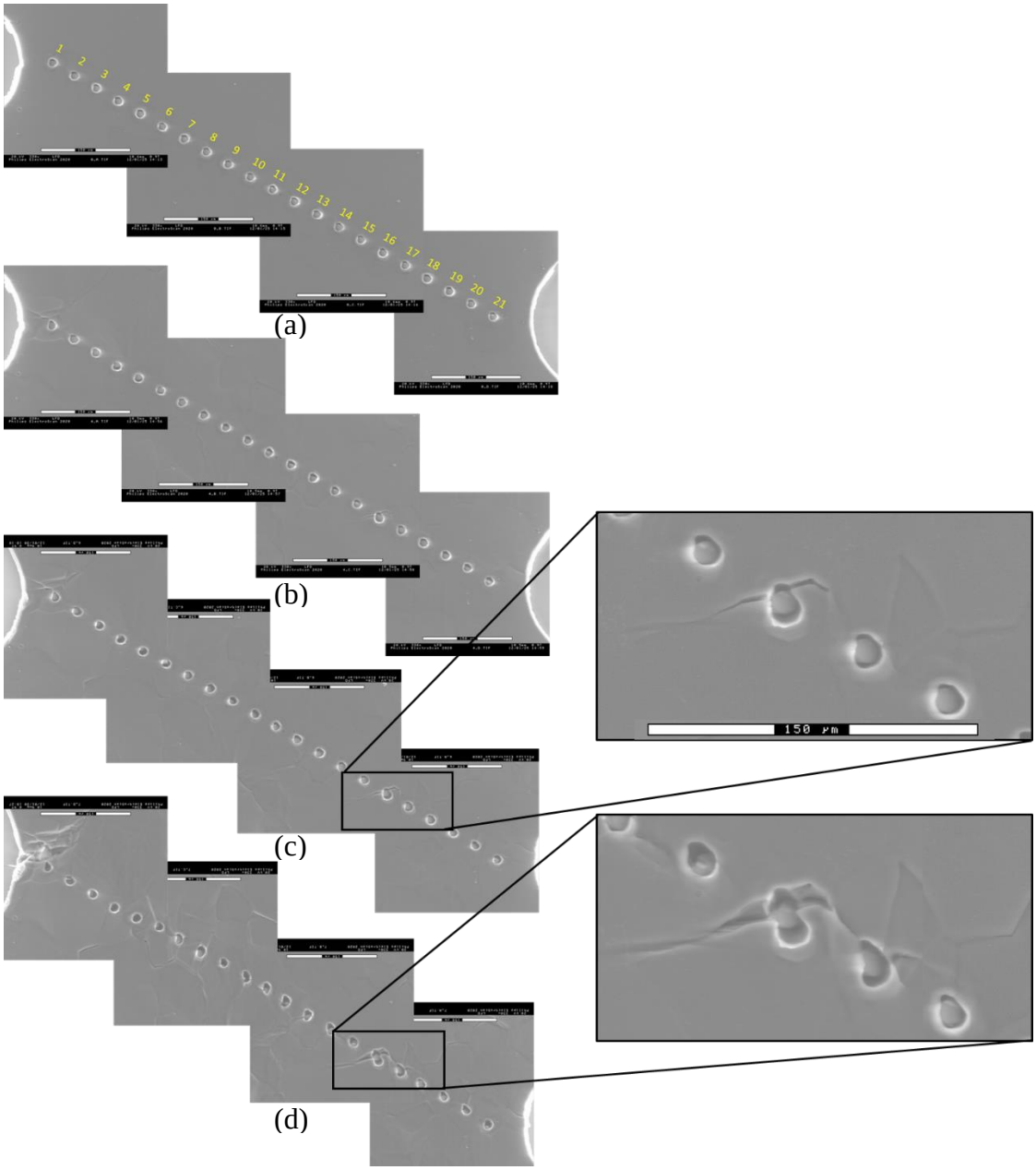

Figure 4.32: Evolution of holes at far field strains of (a) 0.000, (b) 0.025, (c) 0.035 and (d) 0.067 in sample 30°A.

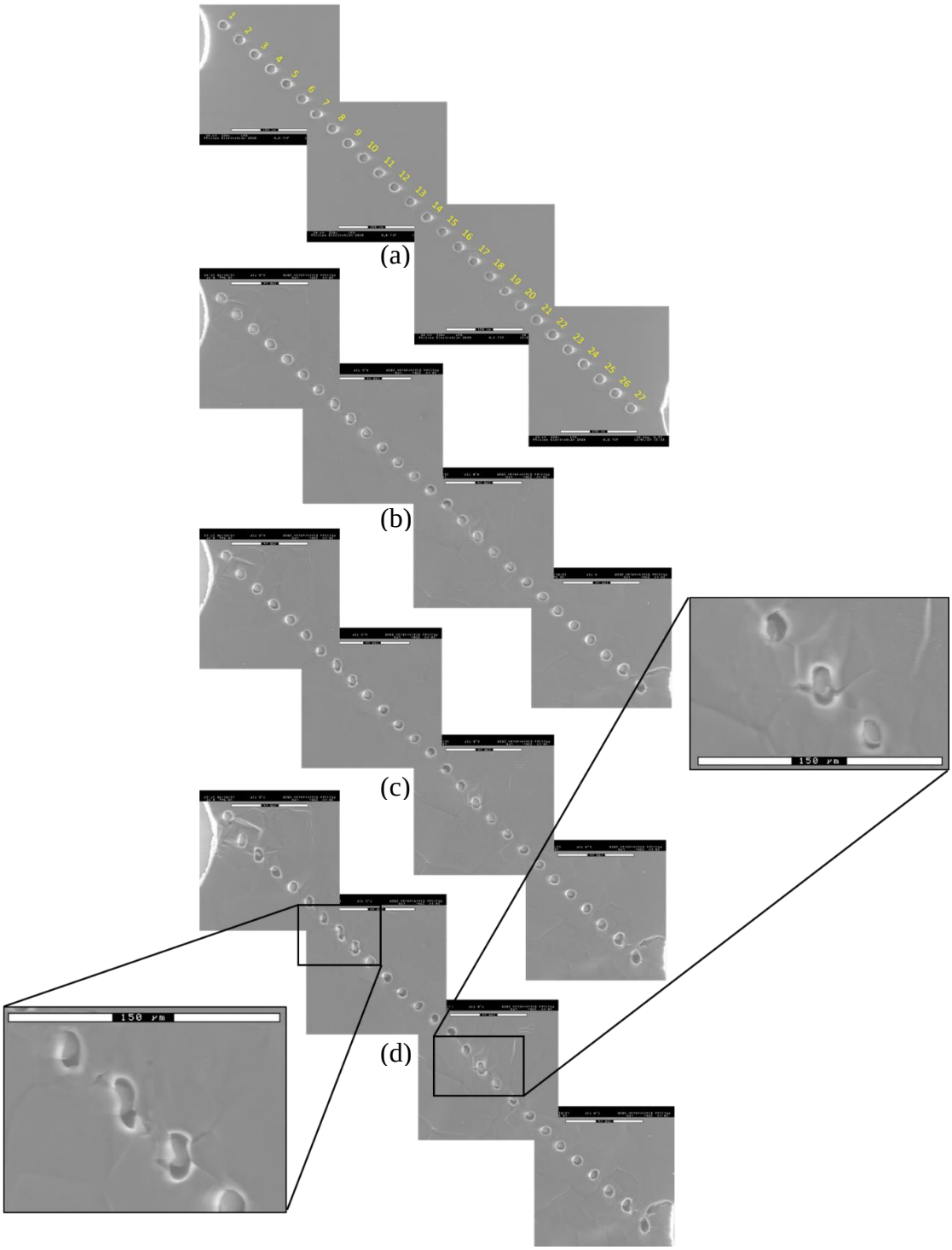

Figure 4.33: Evolution of holes at far field strains of (a) 0.000, (b) 0.032, (c) 0.047 and (d) 0.067 in sample 45°A.

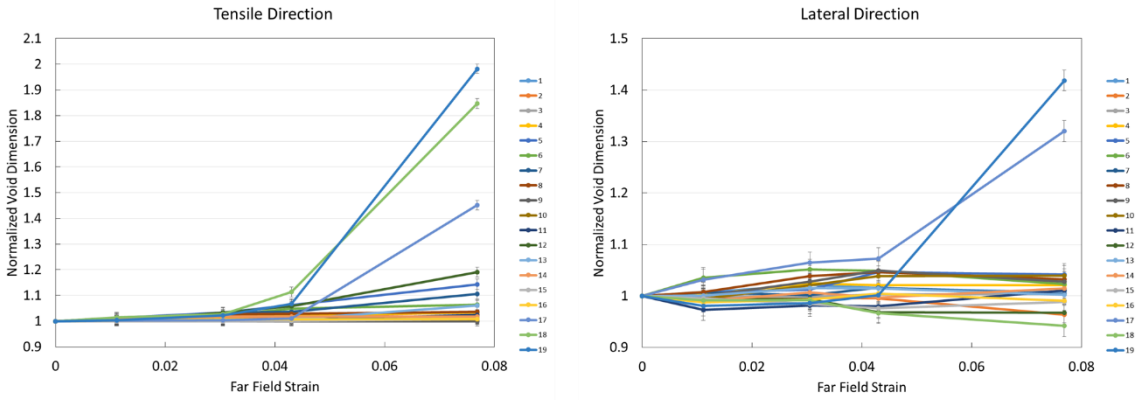

(a) (b)

Figure 4.34: Normalized void dimension vs. far field strain in the (a) tensile and (b) lateral directions for sample 15°A.

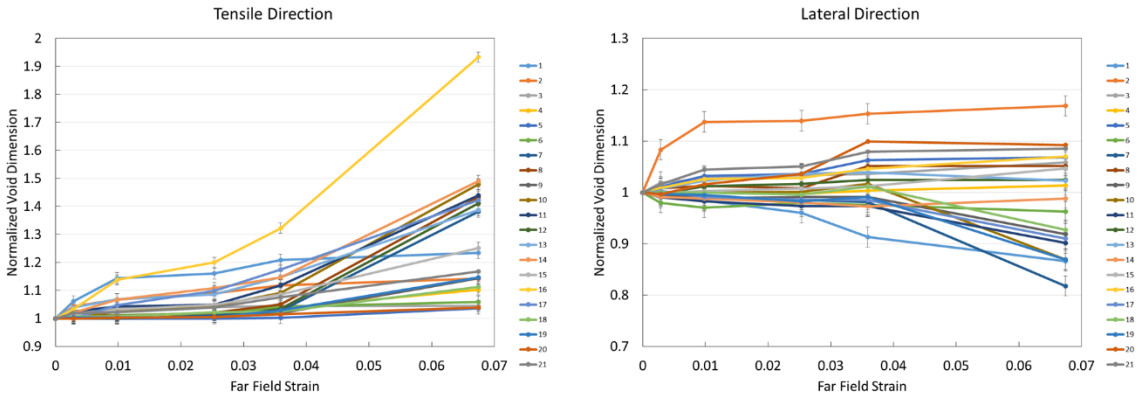

(a) (b)

Figure 4.35: Normalized void dimension vs. far field strain in the (a) tensile and (b) lateral directions for sample 30°A.

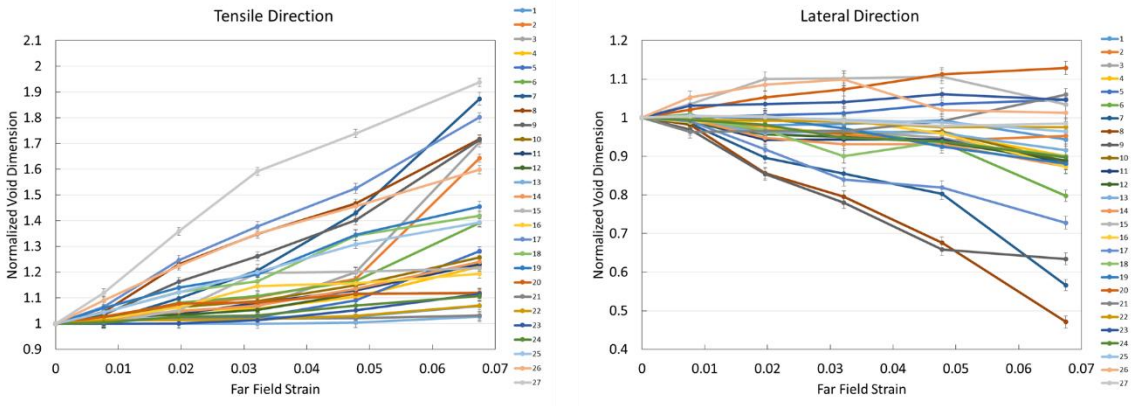

(a) (b)

Figure 4.36: Normalized void dimension vs. far field strain in the (a) tensile and (b) lateral directions for sample 45°A.

Analogous to the configurations normal to the tensile axis heterogeneous tensile void growth was observed. However, as the orientation angle approaches 45° more holes show a significant amount of growth in the tensile direction. A similar observation was found in the lateral direction. As the orientation angle was increased, a greater number of holes showed lateral shrinkage during deformation. The result can be understood in terms of the shear component induced by the orientation angle. The maximum shear stress in a sample tested in uniaxial tension is at 45°. Therefore, as the void orientation angle was increased from 15 to 45°, the holes were forced to shear and their behavior was observed to occur in a more organized manner. However, the microstructure was observed to play a role in deformation in all of the configurations evaluated.

4.3.10 Impact of Local Microstructure on Void Growth: Void Orientation Effects

The deformation observed experimentally was heterogeneous leading to the hypothesis that the microstructure has a strong contribution to the growth of the holes. Similar to the void fraction section, EBSD analysis has been carried on samples 15°A and 45°A to relate the microstructure to the localizations.

Figure 4.37(a) shows the EBSD map of sample 15°A in the undeformed state and the accompanying pole figure is given in Figure 4.37(b). The tensile strain localization occurs in the vicinity of holes 17-19 which are associated with grains 18-24. With the exception of grains 19 and 20 the orientations corresponding to these grains were relatively soft with basal Schmid factors ranging from 0.3-0.44. The deformation of these holes was likely driven by dislocation slip and incompatibilities at grain boundaries in the early stages of deformation.

Figure 4.38(a) displays the EBSD map of sample 15°A at a strain of 0.077. Similar to what was observed in the earlier results there is a spreading of the texture as the deformation proceeds as shown in the accompanying inverse pole figure (Figure 4.38(b)). At this strain the deformation was too large to map the texture in the region between holes 9-19. Extension twins are observed throughout the microstructure suggesting that strain localizations do not always occur when twins form adjacent to a hole.

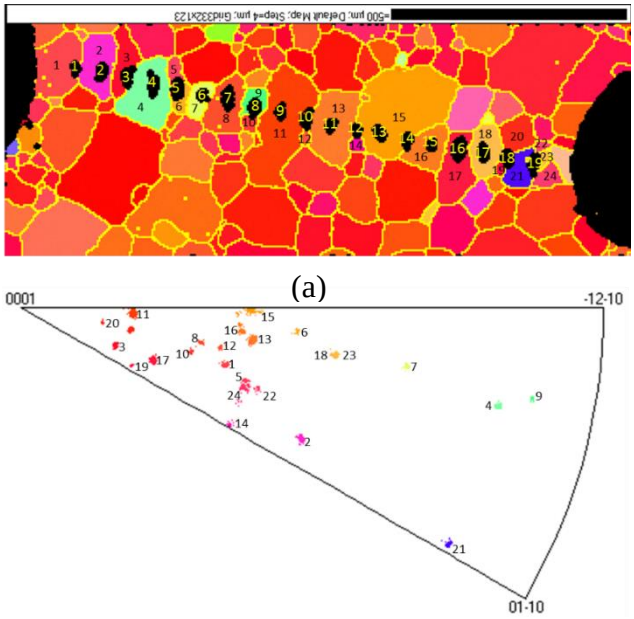

(a)

(b)

Figure 4.37: (a) EBSD map and (b) inverse pole figure for the undeformed state of sample 15°A.

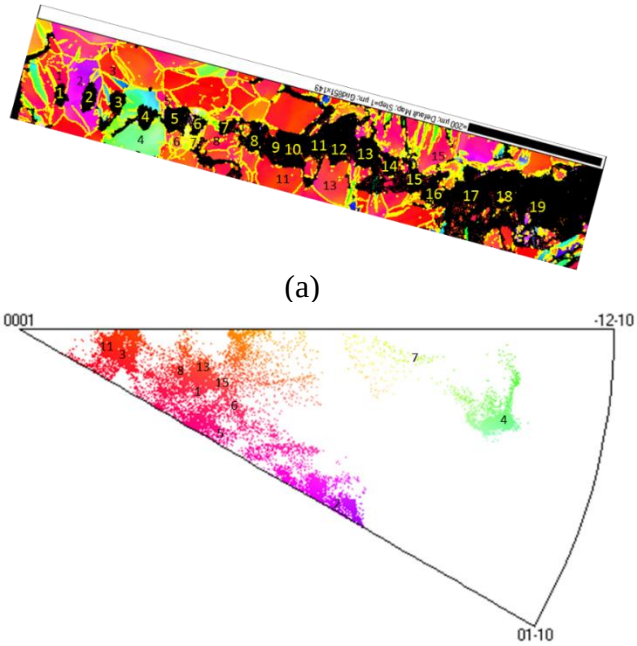

(a)

(b)

Figure 4.38: (a) EBSD map and (b) inverse pole figure at a far field strain of 0.077 for sample 15°A.

Figure 4.39(a) shows the EBSD map of sample 45°A in the undeformed state and the accompanying pole figure is shown in Figure 4.39(b). There were several independent localizations which occurred in this sample. One localization occurred by a shearing process between holes 7-9, and interactions between the holes and the microstructure were observed to be responsible for the localizations associated with holes 17 and 27. Analysis of the EBSD data reveals that the Schmid factor for basal slip associated with grains 8-12 range between 0.3-0.46. This does not come as a surprise since the shearing process that occurs between holes 7-9 requires significant dislocation slip to take place. The boundary which interferes with the growth of hole 17 is between grains 20 and 21. Grain 21 has a relatively low Schmid factor for basal slip compared to that of grain 20. Therefore, incompatibility strains likely occur between these grains, which create strain localizations early in the deformation. The grains will stay intact until the strains are large enough to separate the grains and release the strain energy associated with the incompatibility. The grains associated with hole 27 are 34 and 35 which have basal Schmid factors of 0.33 and 0.49 respectively. These are relatively soft orientations for basal slip; however, the adjacent grains have relatively hard orientations. The ESEM images reveal that the separation of an adjacent boundary interrupts the growth of this hole.

Figure 4.40(a) shows the EBSD map of sample 45°A at a strain of 0.032 along with the associated pole figure in Figure 4.40(b). A lot of extension twins were observed throughout the microstructure. Once again the result reinforces the concept that twins do not always lead to strain localizations. The grains associated with holes 7-9 experience

some rotation and twinning; however, the Schmid factors for basal slip remain similar to the undeformed values. Grains 20 and 21 contain twins at this strain and have rotated to harder orientations relative to the undeformed state. Furthermore, the EBSD mapping reveals separation between grain 34 and the adjacent grain. This separation due to incompatibility strain has a significant effect on the growth of hole 27. The results show the significance of microstructure in all of the configurations examined.

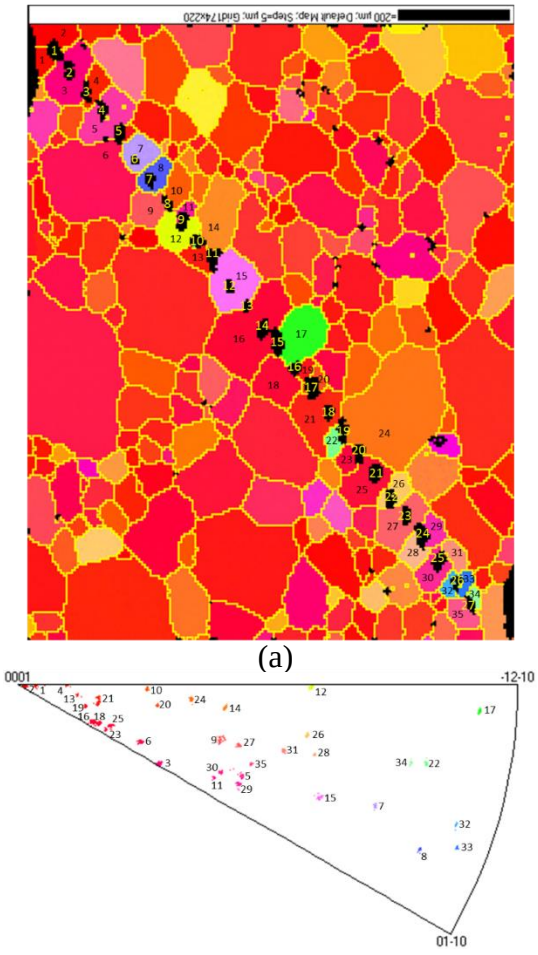

(a)

(b)

Figure 4.39: (a) EBSD map and (b) inverse pole figure for the undeformed state of sample 45°A.

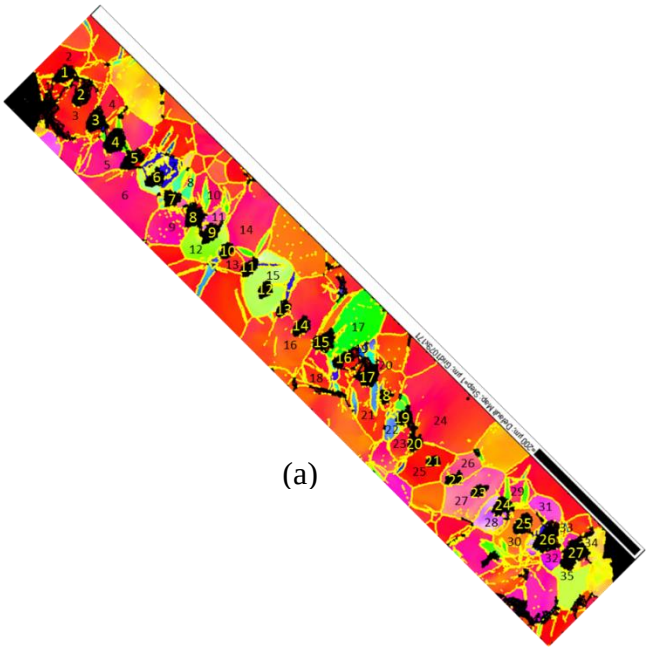

(a)

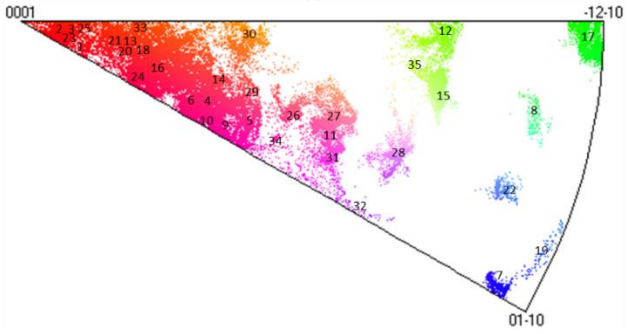

(b)

Figure 4.40: (a) EBSD map and (b) inverse pole figure at a far field strain of 0.032 for sample 45°A.

4.4 Void Linkage

Voids grow in a plastically deforming matrix until void linkage occurs. The final failure of the sample occurs shortly after this process in the magnesium materials examined.

The next section will investigate the linkage of holes with various configurations. ESEM images were obtained before and after fracture initiated within the samples. The first two holes to link were identified and their dimensions were measured to quantify their displacement at fracture. The objective of this section is to establish a relationship between the void fraction and void orientation on the dimensions of the holes at fracture. This way fracture can be predicted in magnesium materials with greater precision.

4.4.1 The Effects of Void Fraction on Void Linkage

It has been well documented that larger particle populations or larger void fractions, for a given material, result in lower failure strains. Brown and Embury (1973) studied the effects of the particle fraction on the strain at failure in spheroidized steel. It was established that as the particle fraction increased, or as holes nucleated closer to one another, the strain at failure decreased. Weck (2007) confirmed the result using aluminum model materials and the result is shown in Figure 4.41. It was established that larger separation distances or smaller void fractions experienced higher local strains at failure. Furthermore, the error associated with the measurements was negligible because the linkage process occurred gradually by the internal necking of the holes. This allowed Weck to determine the point at linkage with great accuracy. It should also be noted that the failure strain for the first two holes to link at a given void fraction could be represented by a single point on the chart because the growth of the holes was uniform. The current work aims at understanding whether this relationship exists in magnesium model materials.

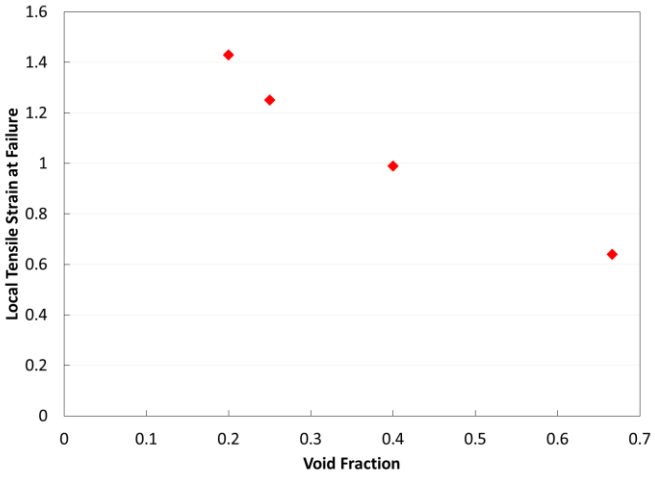

Figure 4.41: Local tensile strain at failure vs. void fraction in AA5052 (Weck and Wilkinson, 2008).

Samples with hole separation distances d of 40, 55 and 70 μm have been investigated in this work to determine the effects of void fraction on the dimension of the holes at failure. Due to the variability of the hole diameter produced by the laser, these dimensions correspond to void fractions which range from 0.159-0.383. Figure 4.42 shows the normalized void dimension at failure as a function of void fraction for the first two holes to link in each of the samples examined. In order to obtain this data measurements were taken before and after fracture. The points on the chart represent the average measurement and the error bars represent the measurements before and after failure. Therefore, large vertical error bars represent a rapid opening of a hole while smaller vertical bars indicate a gradual linkage process. The results obtained for the magnesium model materials tested are very different than the results obtained by Weck with aluminum. Firstly, the void dimension at failure does not show any correlation with the void fraction.

Figures 4.43-4.45 show the history of the first two holes to link for void fractions 0.159, 0.245 and 0.383. These values cover a wide range for the fractions investigated. For each of the fractions presented, the growth of the holes is non uniform. Therefore, the dimension of the holes at linkage cannot meaningfully be represented by a single point. As a consequence, the first two holes to link have been plotted individually for a given void fraction in Figure 4.42. Furthermore, the chart does not show a relationship between the vertical error bar length and the void fraction. It is clear that some holes burst open and some show gradual linkage for all of the void fractions investigated. This suggests that the initial distance between the holes does not influence the type of fracture mechanism that causes linkage. Observation of the ESEM images reveals twin and grain boundaries associated with the final fracture for fractions 0.159 and 0.245. However, internal necking was observed to be the dominant fracture mechanism responsible for the linkage in the sample with a void fraction of 0.383 (Figure 4.45). This was a very rare case and was not observed often in the experiments. Holes in a sample with a larger void fraction are more probable to interact with one another provided that there location with respect to grain and twin boundaries as well as the adjacent crystallographic orientation is favorable. In contrast, the microstructure is more likely to play a role in the linkage process for holes in a sample with a smaller void fraction. The behavior observed in the magnesium materials is qualitatively different from what has been observed in aluminum and copper materials and cannot be analyzed using classical theories. Furthermore, normalized void dimensions have been used in the analysis because some holes experience premature cracking before linking

with a neighboring hole. Cracks relieve local strains and therefore it makes more sense to plot the displacement of the holes rather than the local strain.

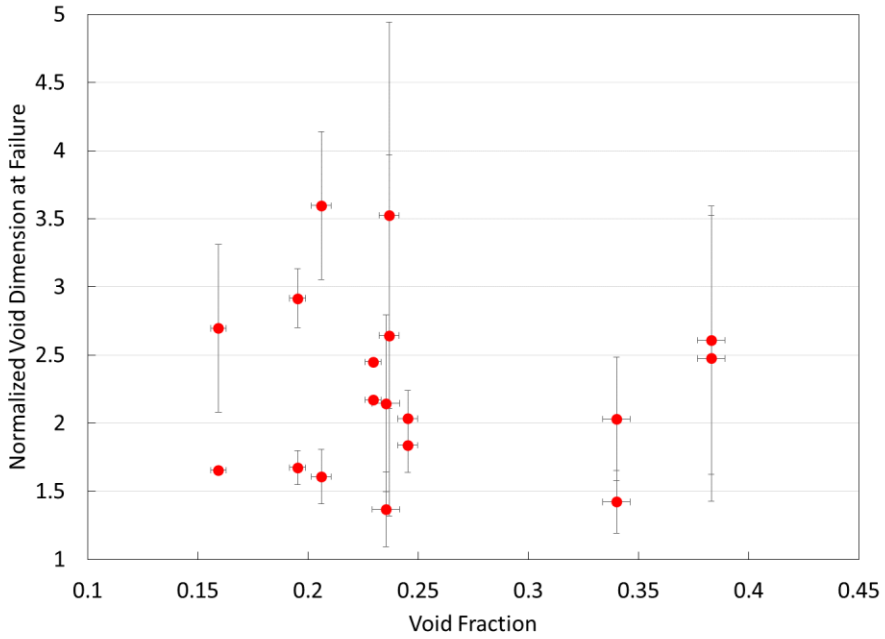

Figure 4.42: Normalized void dimension at failure vs. void fraction.

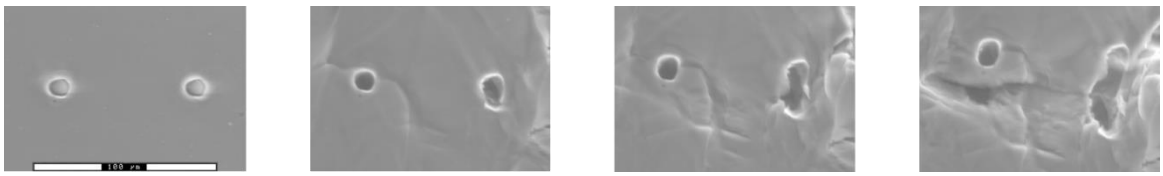

Figure 4.43: First two holes to link in a sample with f=0.159.

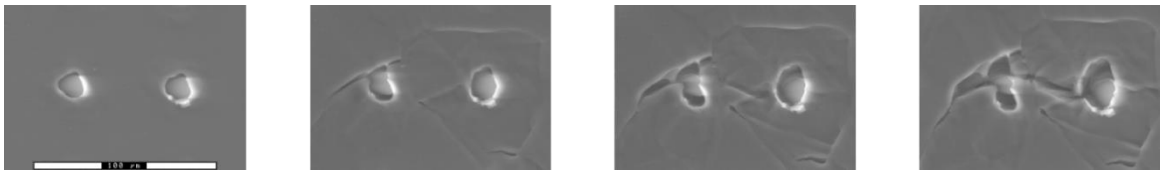

Figure 4.44: First two holes to link in a sample with f=0.245.

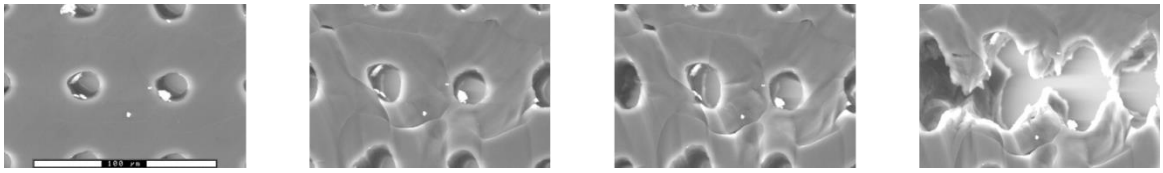

Figure 4.45: First two holes to link in a sample with f=0.383.

4.4.2 The Effects of Void Orientation on Void Linkage

The effects of void orientation on the dimensions of the voids at failure are not as well documented in the literature. Hosokawa (2011) used a finite element approach coupled with a Thomason analysis to examine the plastic constraint factor for voids with various orientation angles. The results showed that as the orientation angle is increased from 0 to 45° the plastic constraint factor decreases and hence less stress is required to initiate shear fracture. However, the experimental results of Li (2013) contradicted this observation and are shown in Figure 4.46. The results showed that larger local strains were required to cause shear fracture when the orientation angle was increased. Once again a single point was sufficient to represent the holes since the growth was uniform. In this section the effects of the orientation angle will be evaluated in the magnesium materials.

Samples containing a row of holes with void orientations of 0°, 15°, 30° and 45° were tested to determine the effects of void orientation on the dimensions of the holes at failure in magnesium materials. Figure 4.47 shows the normalized void dimension at failure as a function of the orientation angle. The normalized void dimension at failure does not show a relationship with the orientation angle of the voids.

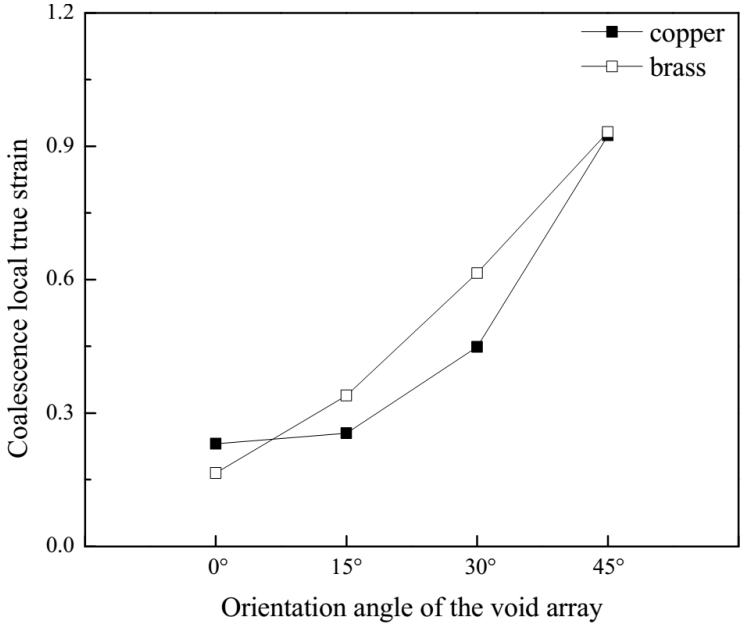

Figure 4.46: Local strain at failure vs. orientation angle in copper and brass materials (Li, 2013).

Figures 4.48-4.50 show the ESEM images of the first two holes to link in the samples with orientation angles 15°, 30° and 45°. The fracture mechanism changes from one that is dominated by the microstructure to a shear fracture as the orientation angle is increased from 15° to 45°. However, in the case of the sample with an orientation angle of 30°, the shear fracture occurs along a grain boundary. The result shows the significance of the microstructure in the linkage of holes in magnesium. There were several fracture mechanisms observed in the materials which all compete with one another. When the local microstructure is favorable any of these mechanisms can contribute to the final fracture.

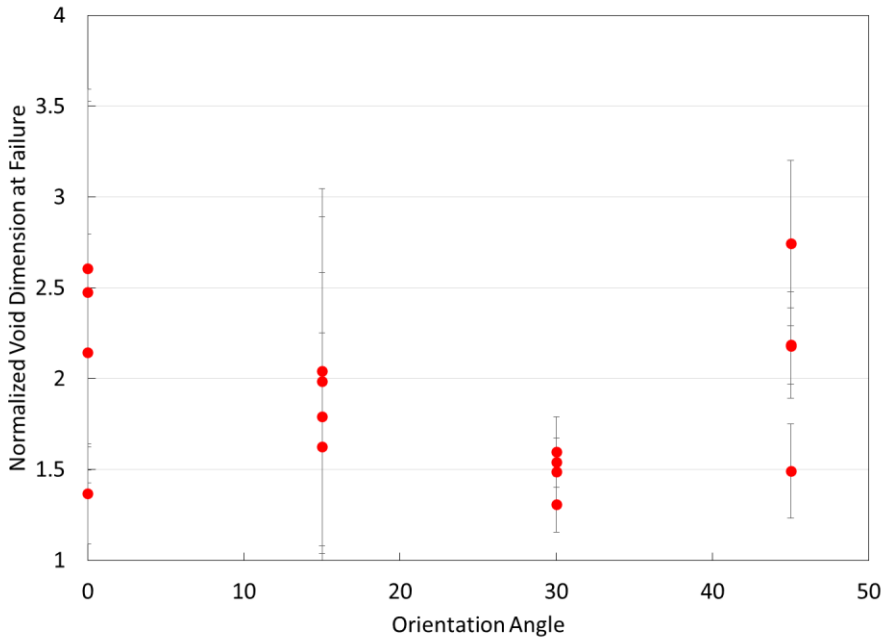

Figure 4.47: Normalized void dimension at failure vs. orientation angle.

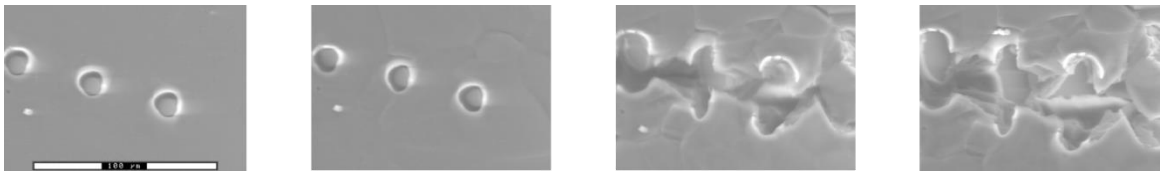

Figure 4.48: First two holes to link in a sample with θ=15°.

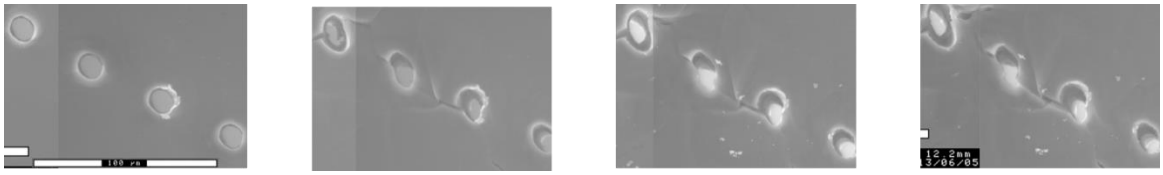

Figure 4.49: First two holes to link in a sample with θ=30°.

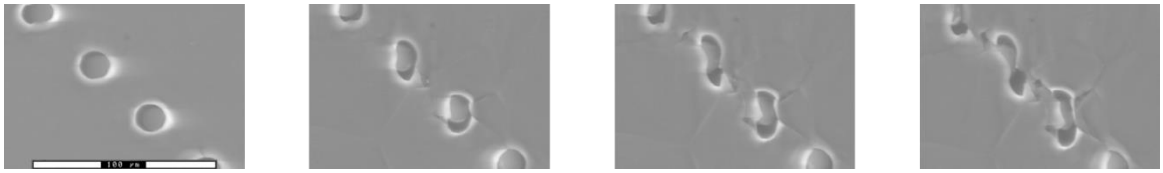

Figure 4.50: First two holes to link in a sample with θ=45°.

4.5 Fracture Mechanisms

It has been established that the normalized void dimension at failure had little if any dependence on the void fraction and orientation angle. The difference between the materials tested in this study and those tested by Li and Weck is the mechanical anisotropy exhibited by the material. Therefore, the local microstructure played a significant role in the fracture and several mechanisms have been observed. These include internal necking, shear fracture, and failure associated with twin and grain boundaries (Nemcko et. al, 2012). The parameters of void fraction and orientation increase the probability of observing these mechanisms; however, failure associated with twin and grain boundaries was common amongst all of the configurations studied. This section will investigate these fracture mechanisms in detail.

4.5.1 Internal Necking

Internal necking is the expected fracture mechanism in orientations were the voids are perpendicular or possibly even at small orientation angles when dealing with isotropic materials that deform homogeneously. This is the fracture mechanism observed by Weck in the aluminum materials he studied. However, this fracture mechanism was a rare

occurrence in the magnesium materials tested. Figure 4.51 shows internal necking between two holes in an array with an initial separation distance of 40 μm corresponding to a void fraction of 0.383. The EBSD pattern is overlaid on the image in the undeformed state. Analysis of the EBSD data shows that the Schmid factor for basal slip in the grain where the neck occurs is approximately 0.4 which is a relatively soft orientation. This suggests that internal necking can occur in these samples when the local microstructure is favorable. The knife edge characteristics on the fracture surface confirm the fracture mechanism was internal necking.

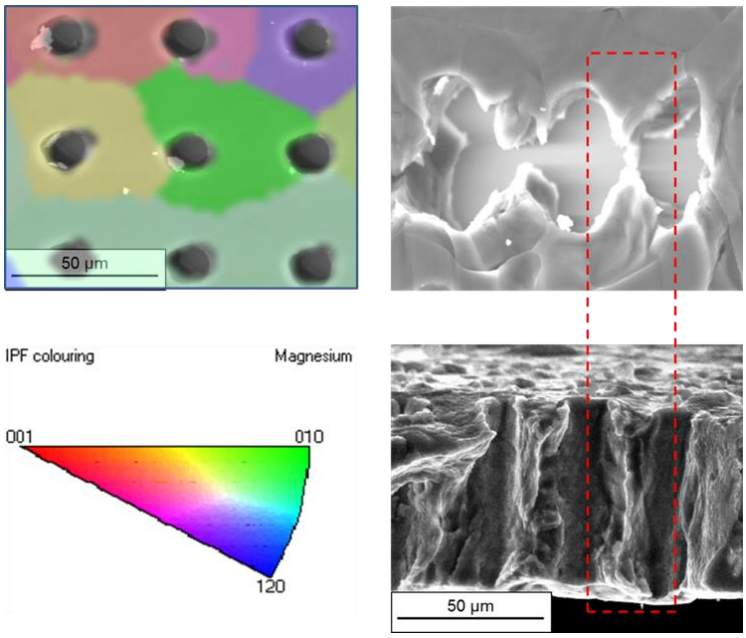

(a) (b)

Figure 4.51: Internal necking mechanism (a) EBSD overlaid on undeformed ESEM image and (b) hole linkage and the corresponding fracture surface.

4.5.2 Shear Fracture

Shear fracture is the expected fracture mechanism for large void orientation angles in materials which deform homogeneously. This fracture mechanism occurred more frequently in the samples with orientation angles of 30° and 45°. Figure 4.52 shows shear fracture in a sample with an orientation angle of 45°. In Section 4.3.10 it was established that this type of deformation can occur in favorably oriented grains. The fracture surface reveals shear lip characteristics between the ligaments of the holes of interest.

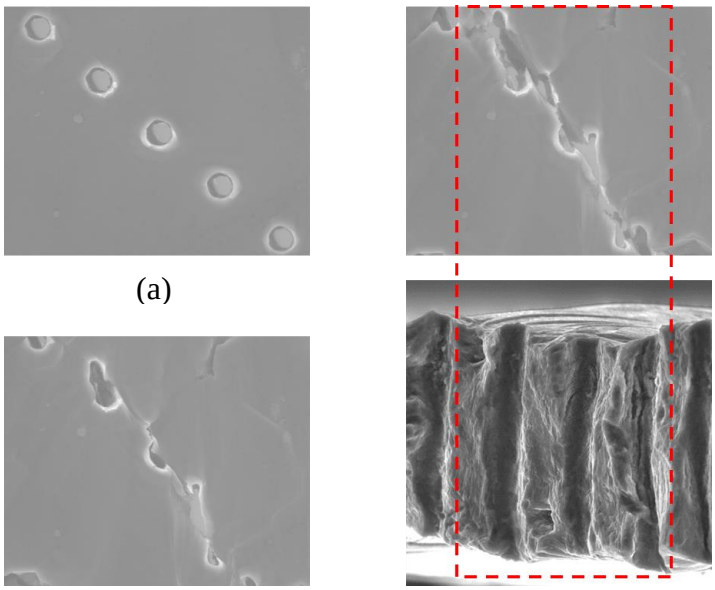

Figure 4.52: Shear fracture mechanism showing a series of holes at far field strains of (a) 0.000, (b) 0.063 and (c) linkage and the corresponding fracture surface.

4.5.3 Grain Boundary Fracture

Failure associated with grain boundaries was observed in all of the configurations tested. This is one of the dominant fracture mechanisms observed in magnesium materials.

This fracture mechanism was observed to lead to premature linkage and interrupted with the plastic growth of the holes. Figure 4.53 shows the fracture of a grain boundary in a sample with a void fraction of approximately 0.2. The EBSD has been overlaid on the undeformed ESEM image and reveals that there are significant differences in the basal Schmid factors between the boundaries of separation. The image below shows the fracture surface of the bottom half of the sample. The grain remains intact on the surface, however, linkage of the holes occurs within the bulk of the material. This observation illustrates the complexity of the fracture in the magnesium materials studied.

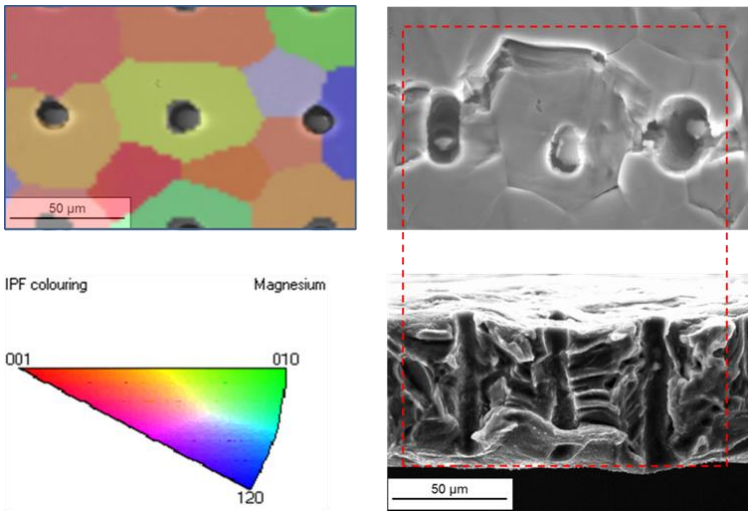

(a) (b)

Figure 4.53: Grain boundary fracture mechanism (a) EBSD overlaid on undeformed ESEM image and (b) hole linkage and the corresponding fracture surface.

This fracture mechanism was also dominant in the materials that were used to observe the effects of void orientation. Figure 4.54 shows the fracture of a grain boundary which leads to premature linkage of holes in a sample with a void orientation of 30°. These are the first two holes to link in the sample and as a result the normalized void dimension

at linkage is much smaller than would be expected during shear fracture. A clear understanding of the relationship between void fraction and void orientation on failure could not be made in these experiments due to this fracture mechanism.

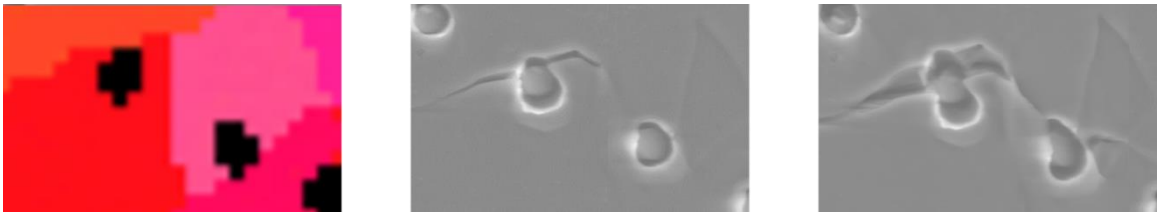

(a) (b) (c)

Figure 4.54: ESEM images of the first two holes to link at far field strain values of (a) 0.000 with EBSD overlay, (b) 0.035, and (c) linkage in a sample with a void orientation of 30°.

Strain localizations associated with grain boundaries also caused the crack path to deviate away from the holes as shown in Figure 4.55. The purpose of the holes was to simulate pre nucleated damage and therefore local strain concentrations in the ligaments between the holes. It was observed that the incompatibility between the grain boundaries caused local strain concentrations which were stronger than those produced by the holes. The grain boundaries were not visible in the undeformed state which made it difficult to obtain quantitative data associated with the localizations.

4.5.4 Twin Boundary Failure

The final fracture mechanism observed was twin boundary failure. This is another dominant fracture mechanisms observed in all of the configurations. The two main twinning types in magnesium are the $\{10\bar{1}2\}$ type twin which enables extension along the

c-axis and the less common $\{10\bar{1}1\}$ type twin that permits c-axis contraction. Both twin types were observed in the experiments; however, the extension twins were encountered more frequently (Nemcko and Wilkinson, 2013b).

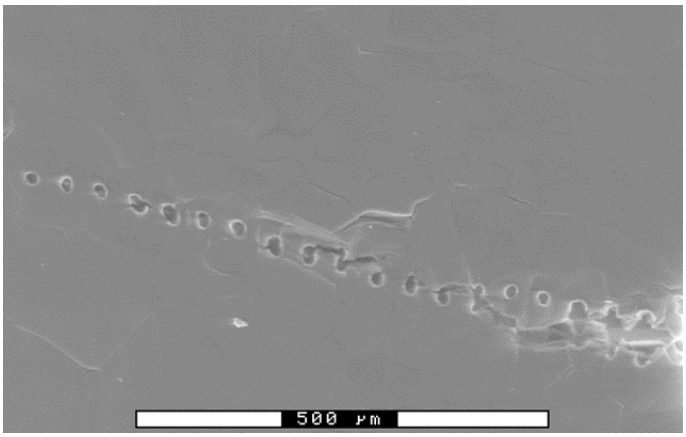

Figure 4.55: Fracture of grain boundaries causing the crack path to deviate from the holes.

Extension Twins

Figure 4.56 shows a series of holes in a sample with a separation distance of 40 µm. At a strain of 0.14 the test was stopped for EBSD analysis. The analysis revealed a twin between the two holes and a magnified view of the twin is shown. An orientation profile was mapped across the boundary showed a misorientation of 86° about the a-axis, characteristic of extension twins. As deformation proceeded the crack developed in the same trajectory as the twin. Grain boundary separation was also observed but did not contribute to the final fracture.

Analogous to the case of grain boundary failure, fracture associated with twin boundaries also caused local strain concentrations in the magnesium materials examined.

Figure 4.57 shows the linkage of holes in a sample with an initial separation distance of 55 μm. In this sample the holes adjacent to the notch linked, however, the crack path deviated from the rest of the holes along a twin boundary. This suggests that the local microstructure has a significant impact in predicting the crack path.

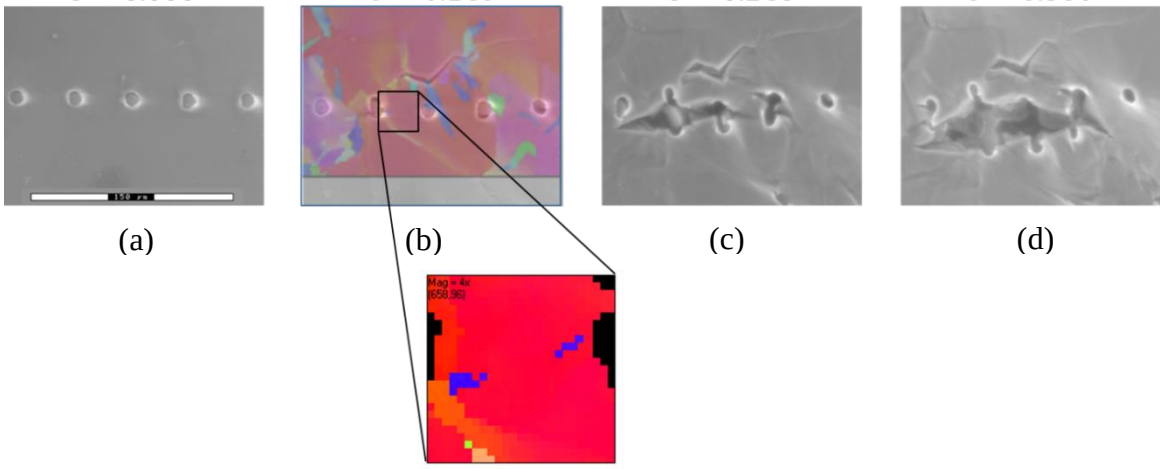

Figure 4.56: Series of holes at far field strains of (a) 0.000, (b) 0.140 with EBSD overlay, (c) 0.246 and (d) linkage showing failure along an extension twin boundary.

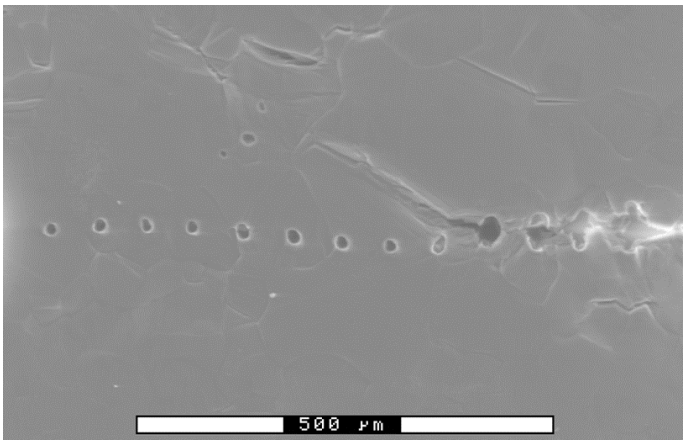

Figure 4.57: Fracture along an extension twin boundary causing the crack path to deviate from the holes.

Contraction Twins

The ESEM images of two holes to link in a sample with a separation distance of 70 μm is shown in Figure 4.58. The test was stopped at a strain of 0.088 for EBSD analysis. The analysis revealed a twin spanning the ligament of the two holes and a magnified view is shown below. An orientation profile was mapped across the boundary of the pink region and showed a misorientation of 56° about the a-axis, characteristic of contraction twins. Furthermore, the misorientation between the pink and green region was 86° about the a-axis suggesting a double twinning mechanism was active. It is probable that the contraction twin was activated first since it was more pronounced in the scan. As deformation proceeded the crack developed in the same trajectory as the twin. This twin type was only observed in this sample.

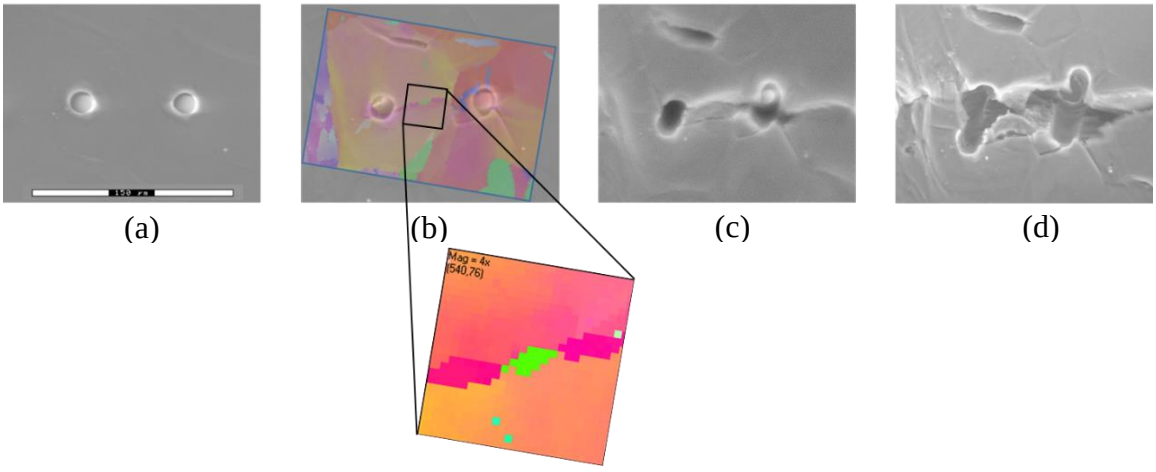

Figure 4.58: Series of holes at far field strains of (a) 0.000, (b) 0.088 with EBSD overlay, (c) 0.143 and (d) linkage showing failure along a contraction twin boundary.

The effects of twinning on deformation and fracture have been described in this chapter. It was established in the void growth section that localizations do not always occur in twinned regions. This suggests that twins serve to accommodate strain along the c-axis due to the lack of deformation mechanism. However, once nucleated they produce a boundary which causes strain incompatibility. When the local microstructure is favorable the twins can lead to strong strain localizations and fracture.

4.6 Summary

The main conclusions drawn from the work presented in this chapter are summarized below:

- Void growth and linkage have been observed experimentally in magnesium model materials using in situ tensile testing coupled with electron microscopy.
- The void fraction has a weak influence on the growth of the holes. In all of the void fractions investigated the deformation was localized in a small region which was observed to be governed by the local microstructure. However, when the void fraction is larger the holes are closer together and more holes become involved in the localization.
- The void orientation angle displays a weak correlation with the evolution of the holes. For all of the orientations investigated deformation was dominated by the local microstructure. The fracture mechanisms observed changed as the void orientation angle was increased from 0° to 45°. Nevertheless, the interruption of the

hole growth with twin and grain boundaries produced a wide variation in the data in all of the orientation angles examined.

- Void growth was observed to occur non-uniformly in all of the configurations tested. The result suggests that the mechanical anisotropy associated with the crystallographic structure of magnesium plays a significant role in the deformation behavior of the polycrystalline materials tested.

- The isotropic finite element analysis does not predict the magnitude of the hole growth or the distribution of the strain induced by the notch. For all of the configurations tested, the model overpredicts the dimensions for the majority of the holes in the sample. Interactions between the holes and microstructural features such as twin and grain boundaries were observed experimentally which interrupt the plastic growth of the holes. This suggests that the deformation of the holes has a strong dependence on the local microstructure.

- The evolution of the texture occurred during deformation due to the rotations caused by active deformation mechanisms. The change in texture was observed to be quite significant in some cases turning soft orientations into hard ones and vice versa. This phenomenon must be accounted for to accurately model the deformation and fracture processes in these materials.

- The displacement of the holes at fracture do not depend strongly on void fraction. The void fraction merely increases the probability of observing different fracture

mechanisms. As the void fraction is increased, it is more probable to see the fracture mechanism move from microstructure dominated fracture to internal necking. However, microstructure dominated fracture was observed in all of the configurations.

- The void orientation angle does not have a strong relationship with the dimensions of the holes at failure. Similar to void fraction the orientation angle simply increases the likelihood of observing a given fracture mechanism. As the void orientation is increased from 0° or 15° to 45° the fracture mechanism changes from a microstructure dominated fracture to shear fracture.

- The dominant fracture mechanisms observed were failure associated with twin and grain boundaries. This type of fracture led to the premature linkage of the holes which made it difficult to establish a relationship with the void fraction or orientation.

- The results show that there are several fracture mechanisms competing with one another which include internal necking, shear fracture, and failure associated with twin and grain boundaries. Depending on factors such as hole position with respect to grain boundaries, local texture and void configuration, each may be favorably activated.

- The holes were introduced into the material to simulate pre-nucleated damage in a magnesium matrix. They also provide sites for strain concentration. In some cases,

the fracture path deviated from the holes and localized at other microstructural features. This suggests that the microstructure creates its own strain concentrations which are stronger than the strain fields induced by the holes. The result emphasizes the role of the microstructure on the fracture process.

Chapter 5

In-situ Tensile Testing with Optical Microscopy

5.1 Introduction

It has been established that the magnesium materials discussed in the previous chapter exhibited heterogeneous deformation. This type of deformation has been observed in other HCP metals with low crystallographic symmetry such as titanium (Yang et al., 2011). Another interesting observation from the previous chapter was the deviation of the crack path from the region containing the holes. The local microstructure was found to develop strain concentrations of its own. In this chapter a new approach is described to obtain quantitative information on the heterogeneity of deformation in the vicinity of the holes as well as from the surrounding microstructure. A speckle pattern is deposited on the sample surfaces using a dilute copper sulphate solution. Images were obtained using an optical microscope after each increment of deformation and the DIC method has been used to map the strain on the sample surfaces. The main objective of this set of experiments is to obtain quantitative information related to strain heterogeneities associated with the microstructure such that the deformation and fracture behavior of magnesium can be understood in greater detail. An advantage of this technique is that the results can be directly compared with a crystal plasticity finite element approach. Furthermore, the samples examined in Chapter 4 contained notches which were expected to create a non-uniform

strain distribution along the gage width. It was observed that the notch did not have a strong effect on the deformation; however, there were a few samples in which fracture occurred within the vicinity of the notch. The samples tested in this section contain a Marciniak type notch which completely eliminates any notch effects (refer to Figure 3.12).

To begin, a brief discussion concerning the differences in material preparation between the samples tested in Chapter 4 and those examined in this chapter will be presented. The texture and grain size distribution varies between the samples which has a significant impact on the results. Secondly, the measurements used throughout the chapter will be defined. The third section deals with a quantitative analysis of the void growth and heterogeneous deformation observed in the void configurations under investigation. The evolution of strain at grain and twin boundaries will be examined in detail. Next the fracture of the void configurations will be assessed using a slightly different approach compared to the previous chapter. It has been established that the void fraction and void orientation do not have a strong relationship with void growth or fracture; therefore, a statistical approach will be used to understand the fracture mechanisms responsible for this observation. Finally, a crystal plasticity based finite element approach will be used to understand the role and hardening of the various deformation mechanisms which lead to the heterogeneous deformation of the magnesium materials studied.

5.2 Material Preparation

The EBSD maps of the samples described in Chapter 4 showed several grains with a texture which deviated significantly from the basal texture, in the undeformed state. These grains were found adjacent to the laser drilled holes which suggests that local recrystallization occurred during the annealing cycle after the laser machining. Figure 5.1 shows a comparison of the inverse pole figures obtained in the undeformed state representing the initial texture of the samples examined in Chapter 4 and the samples tested in this chapter.

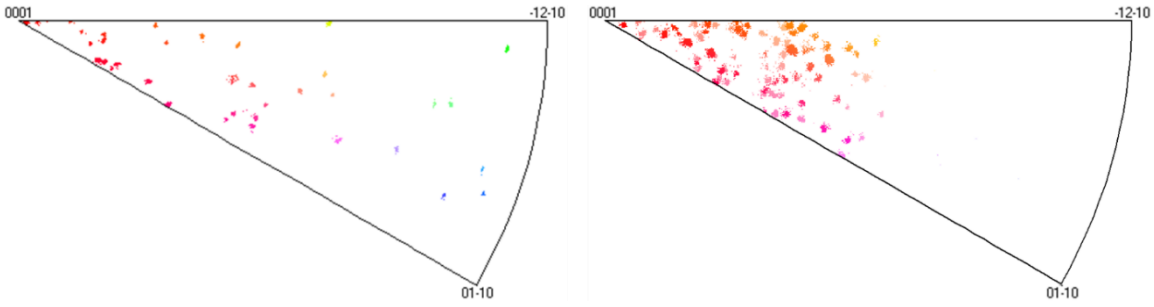

(a) (b)

Figure 5.1: Inverse pole figures in undeformed state of (a) samples tested in Chapter 4 and (b) samples investigated in this chapter.

The texture of the samples investigated in this chapter show a stronger distribution around the basal texture. It is therefore necessary to discuss the differences in the material preparation procedures. The samples examined in this chapter were laser machined in the as-rolled state (refer to Section 3.4.1). This is different from the samples examined in Chapter 4 which were machined in the annealed state (refer to Section 3.3.1). As a result, a significant amount of deformation was already present in the materials tested in this

chapter prior to laser machining. A similar annealing procedure was used for both sets of samples after the laser drilling; however, the texture and grain size distribution differs between the samples. The average grain size of the samples analyzed in this chapter is $32\pm4\mu m$ with a standard deviation of $19\mu m$ vs. the samples tested in Chapter 4, which have an average grain size of $51\pm6\mu m$ and a standard deviation of $28\mu m$. The finer grain size of the samples examined in this chapter increases the probability of observing a grain boundary in the ligament between two neighboring holes. In fact, the majority of the ligaments in this chapter contain a grain boundary.

5.3 Measurements

Several different measurements are used throughout the chapter in order to quantify deformation and fracture. A detailed description of these measurements are given below. The strain was calculated using ARAMIS software which uses the DIC method for the strain calculation. Error associated with the measurements is described in detail in the ARAMIS documentation (GOM, 2005) and Nemcko et al. (2014). For a facet size of 15 pixels the maximum error is 0.67% of the calculated value and has been assumed to be negligible.

5.3.1 Local Strain

The local strain in the vicinity of the holes is used to study the growth behavior of the holes. This measurement is used again later in the chapter to correlate void fraction and orientation to the void dimension prior to failure. It is a similar measurement to the void

dimension; however, the calculation points must lie on the strain grid. Therefore, a more complete definition of the measurement is the strain calculated in a gage section comparable in length to the hole. Figure 5.2 shows the evolution of 3 holes at various increments of deformation. The gage sections used for local strain calculations are shown in red on the undeformed image. The local strain reported is based on the change in dimension of this section of the grid.

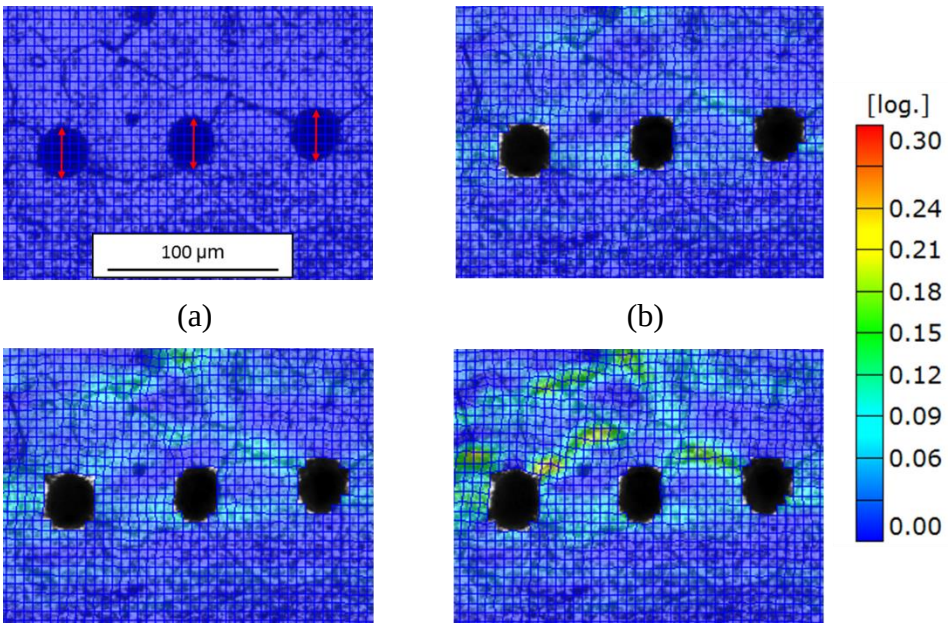

Figure 5.2: Tensile strain distribution of 3 holes deforming perpendicular to the tensile axis at far field strain values of (a) 0.000, (b) 0.011, (c) 0.016 and (d) 0.024.

5.3.2 Far Field Strain

As mentioned above the samples contain a Marciniak type notch to eliminate any probability of having a non-uniform strain distribution induced by notch effects in the gage section. It has already been established that microstructural inhomogeneity leads to non-

uniform deformation. Another advantage of the Marciniak notch is that all of the configurations tested have the same gage lengths. The far field strain is used to determine how the local strains develop with deformation. In addition, the far field strain prior to fracture is compared amongst the configurations to determine if the holes affect the macroscopic properties of the materials. Figure 5.3 shows the gage section of a sample with a void orientation of 45° at various values of far field strain calculated from the gage section shown in red on the undeformed image. The measurement is similar to the local strain as the gage section must be composed of the grid points; however, the calculation is done over a larger section. The center of the grid has been located and a gage section of roughly 0.5 mm is used for the calculation.

5.3.3 Section Strain

The DIC method calculates the strain at each grid point and an interpolation method is used to determine the strain between adjacent points. This experimental technique allows strain to be calculated along a defined section which is particularly useful for quantifying the heterogeneous deformation observed. Figure 5.4 shows the localization of tensile strain at a grain boundary with a defined section and the corresponding strain along the section. The plot shows the relatively large strain associated with the boundary and the negligible amount of strain within the grains adjacent to the boundary. This observation is very common in the magnesium materials tested and this type of measurement will be used to quantify the strain distributions associated with grain boundaries and twins.

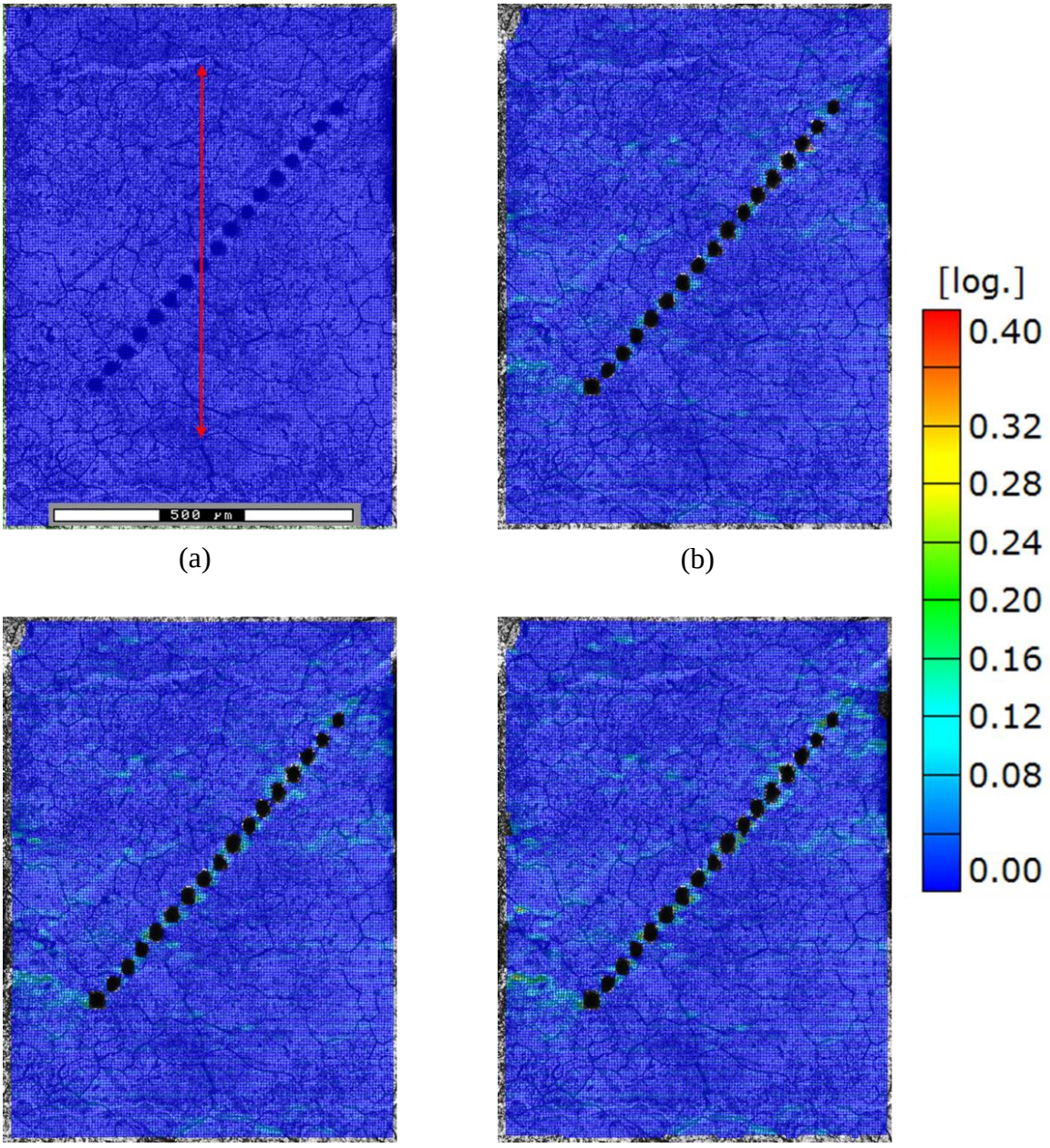

(a) (b)

(c) (d)

Figure 5.3: Tensile strain distribution in the gage of a sample with a void configuration of 45° at far field strains of (a) 0.000, (b) 0.011, (c) 0.016 and (d) 0.018.

5.3.4 Point Strain

Point strains have been used to determine the maximum strain in the samples prior to fracture. The idea is the same as the section strain; however, the strain is calculated at a single point rather than a section of points.

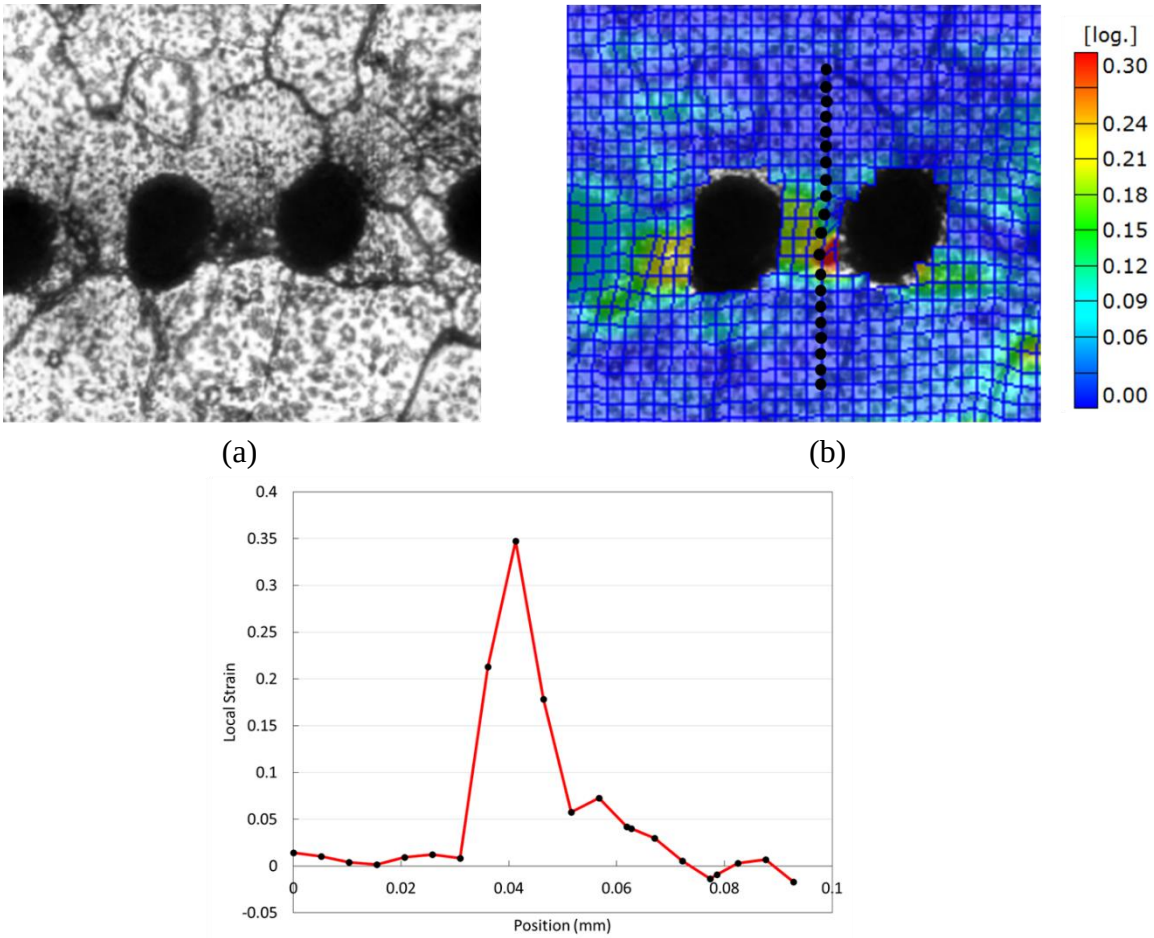

Figure 5.4: Heterogeneous strain distribution associated with a grain boundary (a) optical micrograph (b) tensile strain distribution overlaid on micrograph showing a defined section and (c) local strain vs. position along the section.

5.4 Void Fraction Effects on Heterogeneous Deformation

The results presented in Chapter 4 show that the deformation behavior of the holes displays a weak dependence on the void fraction. As mentioned above, the texture of the materials investigated in this chapter have a more uniform texture and theoretically should deform with more homogeneous characteristics. Therefore, the deformation of the holes will be analyzed to observe void growth in magnesium materials with a stronger texture. Samples with void separation distances of 40, 55 and 70 μm, similar to the configurations examined in Chapter 4, were tested to determine the effects of void fraction on the deformation characteristics. The hole diameters vary somewhat due to the variability of laser machining and the chemical polishing procedure, corresponding to void fractions between 0.286 - 0.5. It should be noted that the analysis of lateral strains have not been included in this chapter. The deformation in the lateral direction merely ensured that the deformation was heterogeneous.

Figure 5.5 shows the deformation of a row of holes and tensile strain distribution in a sample with f = 0.5. The yellow numbers are overlaid on the undeformed image for reference purposes. This convention will be used throughout the chapter. The results show a hotspot which forms between holes 8 and 9 at a strain of 0.003. At this strain there are a few grain boundaries outside of the region of the holes that are developing strain concentrations. With subsequent deformation several other hotspots form in the region of the holes. The grain boundaries outside of this region continue to form strain concentrations; however, the strain concentrations associated with the holes are much

stronger than those produced at the boundaries outside of this region. In Chapter 4, it was established that higher void fractions increase the probability of interactions between holes. Figure 5.5 supports this result, as it shows the magnitude of strain is larger in the ligaments between the holes compared to the surrounding microstructure for this sample with a relatively high void fraction. Figure 5.8 shows the local true strain as a function of far field strain for each of the holes in this sample. On average the holes do not show significant growth in the tensile direction. The average local strain at the largest far field strain is approximately 0.14 corresponding to a tensile stretch of 1 μm. This result does not come as a surprise since the texture is close to the basal orientation which is a relatively hard orientation for basal slip. Figure 5.8 shows that holes 10 – 13 experience negligible deformation while the majority of the deformation localizes within the first 9 holes. The two holes which exhibit the most growth are holes 1 and 5. These holes are not adjacent to one another which suggests that although the texture is more uniform, the deformation is still heterogeneous. This observation will be investigated in samples with smaller void fractions where the microstructure is more likely to play a role in the deformation of the holes.

The tensile strain distribution and optical microscope image series for a sample with f = 0.364 is shown in Figure 5.6. At a strain of 0.009 a hotspot forms along a grain boundary in the ligament between holes 6 and 7. Several other localizations are observed which are independent of the strain concentrations produced by the holes. These strain concentrations are associated with grain boundaries. In addition, there are a few grains which seem to have

a non-uniform strain distribution associated with them such as the grain below holes 1 and 2. As the deformation proceeds, strain becomes localized between holes 6 - 8. At a strain of 0.021, the strain concentrations observed away from the holes remain present and have grown in magnitude. Several of these localizations are stronger than what is observed in the ligaments between the holes. Figure 5.9 shows the local true strain vs. far field strain for this sample. The average growth of the holes for the far field strains investigated is relatively small. At a strain of 0.021 the local strains range from a value of 0.127 to 0.001 corresponding to tensile stretches of 2.6 to 0.2 μm. The result suggests that when the microstructure adjacent to a hole is not favorably oriented for slip, grain boundary sliding plays an important role in accommodating strain. It is observed that holes 6 – 8 deviate from the average void growth value from the onset of deformation. These holes are adjacent to boundaries which contain strain concentrations. Similar to what was observed in Chapter 4, the sliding of grain boundaries is responsible for the heterogeneous growth of the holes in this sample. Furthermore, hole 4 displays rather unusual behavior as it exhibits a small compressive strain prior to stretching in the tensile direction. This observation was also noted in Chapter 4. One explanation for this phenomenon is that there is an evolution of topography on the surface during the deformation. Soft grains tend to show more contraction through the thickness than the harder orientations; this non uniform deformation produces surface topography which may explain this observation. The contraction required in order to produce the compressive strain shown is less than 1 μm which is very probably the result of the evolution of topography on the surface.

Figure 5.7 shows the evolution of a row of holes and the tensile strain distribution on the surface of a sample with f = 0.286. At a strain of 0.011, the strain is localized in the ligaments between several holes; however, the largest strain is observed along a grain boundary near the edge of the sample. As the deformation continues, a hot spot forms in the ligament of holes 4 and 5 with a strain magnitude similar to that of the boundary near the sample edge. Another interesting localization occurs between holes 5 and 6. At a strain of 0.024 there are two paths of strain between these holes. One path is perpendicular to the tensile axis and is transgranular while the other path briefly deviates from the region of the holes along an intergranular path. The magnitude of the strain concentration is higher for the path which follows the grain boundary. The local true strain vs. far field strain for this sample is shown in Figure 5.10. Similar to the cases presented above the average growth of the holes is relatively small for the far field strain values investigated and the growth of the holes is non uniform. Holes 2, 4 and 5 show the most significant growth in the tensile direction. The growth of holes 4 and 5 are driven by the localization of strain associated with a grain boundary in the ligament between them; however, the growth of hole 2 is independent of this and is driven by a separate boundary. This result is similar to what was observed in Chapter 4 where several independent strain concentrations were present.

The results show that the void fraction does not have a strong influence on the deformation of the holes. In each of the void fractions examined the holes exhibited negligible growth prior to fracture. Tensile strains were observed to localize along grain boundaries. The holes positioned adjacent to boundaries which developed strain

concentrations showed significant growth in the tensile direction. This result suggests that grain boundary sliding has a significant contribution to the macroscopic strain. Furthermore, it was observed that the strain concentrations away from the hole region were stronger in the samples with lower void fractions. The holes in the sample with f = 0.5 interacted with one another and the local microstructure at low values of far field strain and did not allow localizations to occur outside of this region. It is difficult to comment quantitatively on the strain concentrations away from the hole region in the samples containing f = 0.364 and f = 0.286. The result confirms that it is more probable for the microstructure to play a role in the fracture process when the void fraction in smaller; however, the extent of this is difficult to quantify.

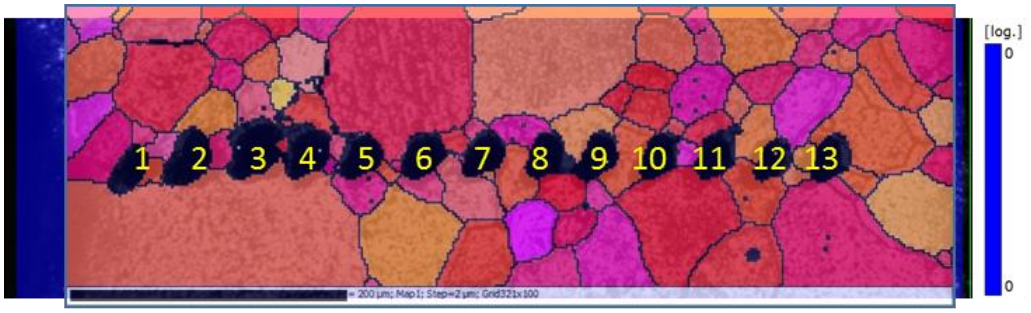

(a)

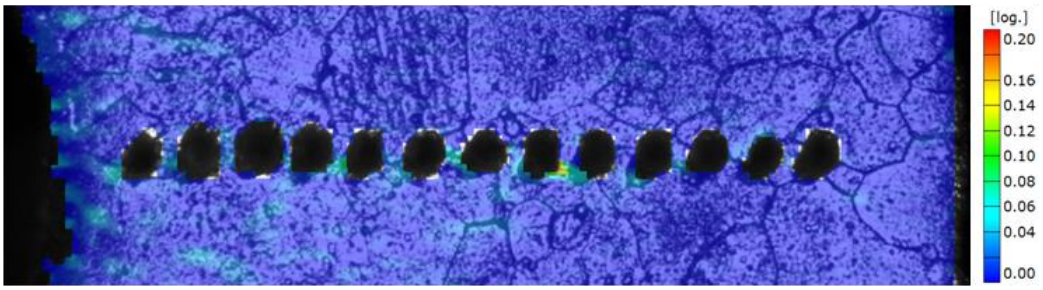

(b)

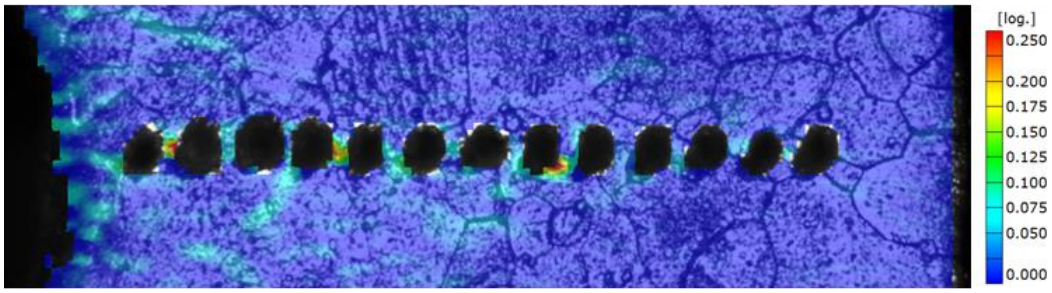

(c)

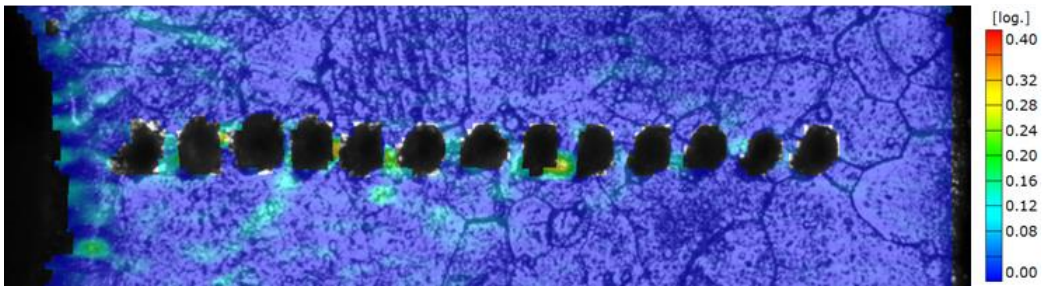

(d)

Figure 5.5: Deformation of holes and tensile strain distribution in a sample with f = 0.5 at far field strains of (a) 0.000 with EBSD overlay, (b) 0.003, (c) 0.008 and (d) 0.011.

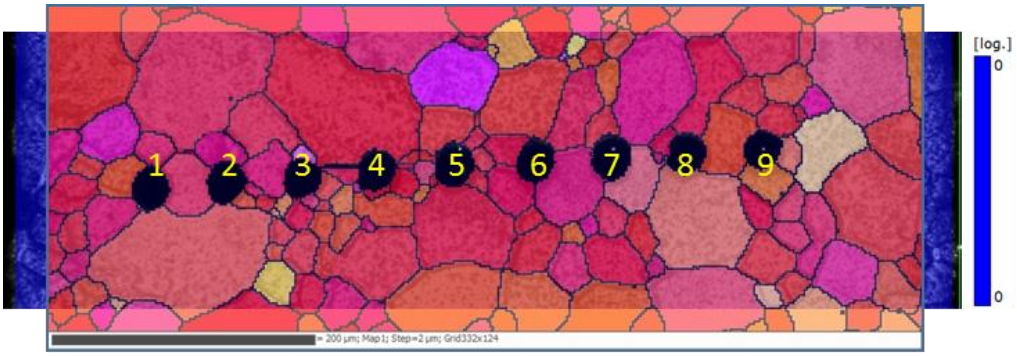

(a)

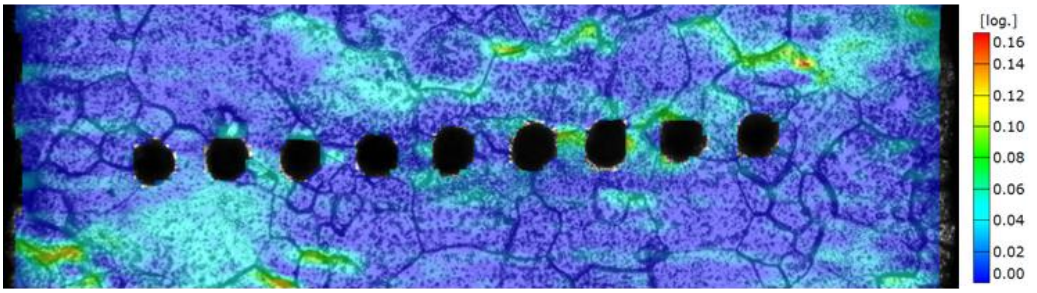

(b)

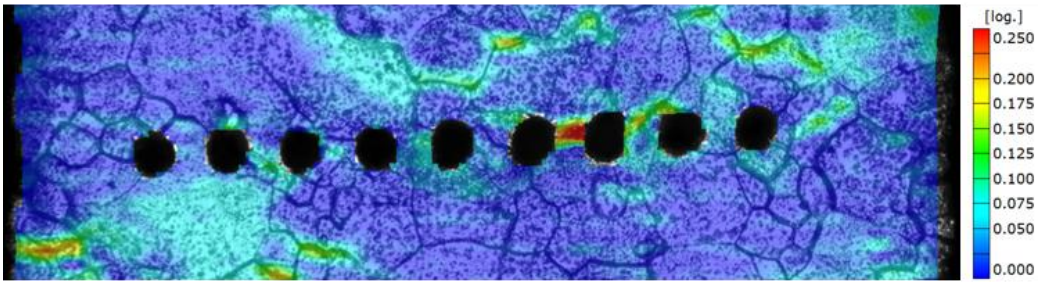

(c)

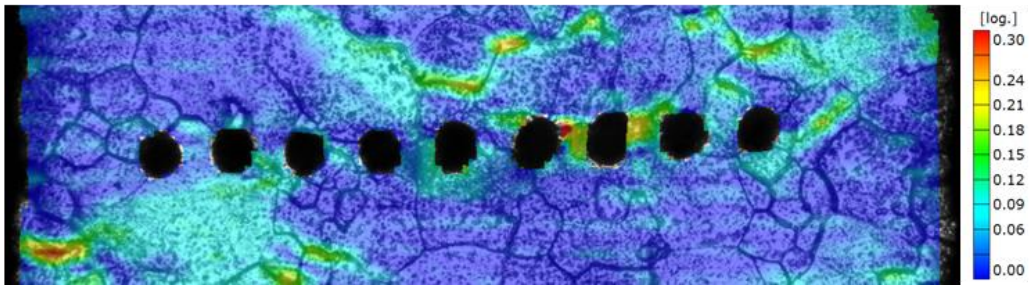

(d)

Figure 5.6: Deformation of holes and tensile strain distribution in a sample with f = 0.364 at far field strains of (a) 0.000 with EBSD overlay, (b) 0.009, (c) 0.016 and (d) 0.024.

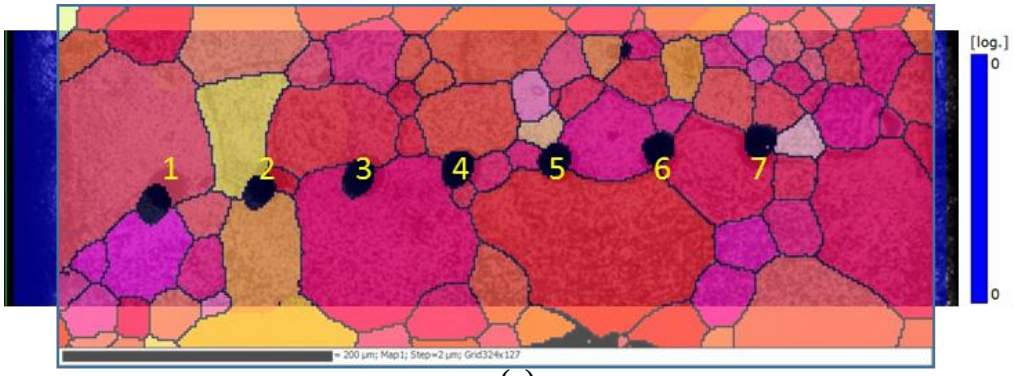

(a)

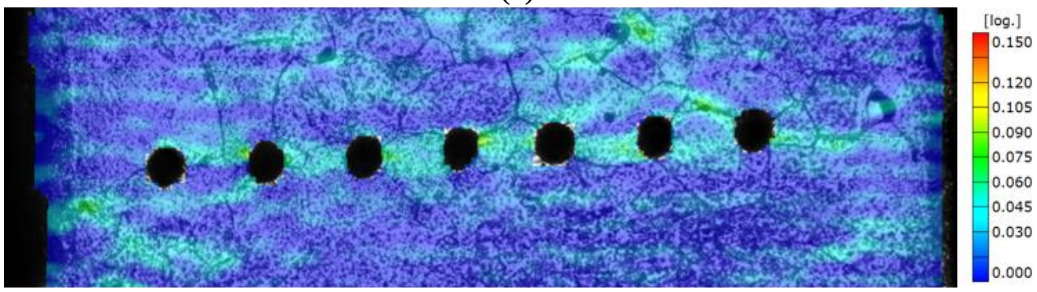

(b)

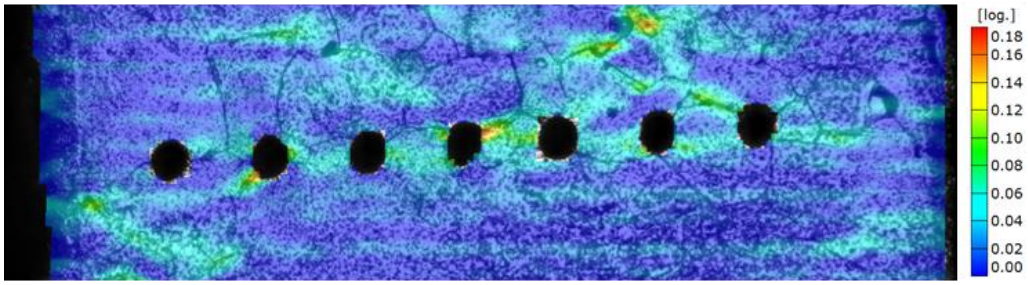

(c)

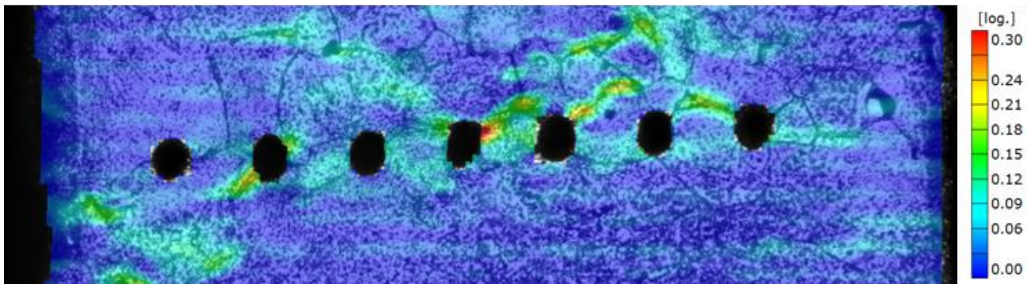

(d)

Figure 5.7: Deformation of holes and tensile strain distribution in a sample with f = 0.286 at far field strains of (a) 0.000 with EBSD overlay, (b) 0.011, (c) 0.016 and (d) 0.024.

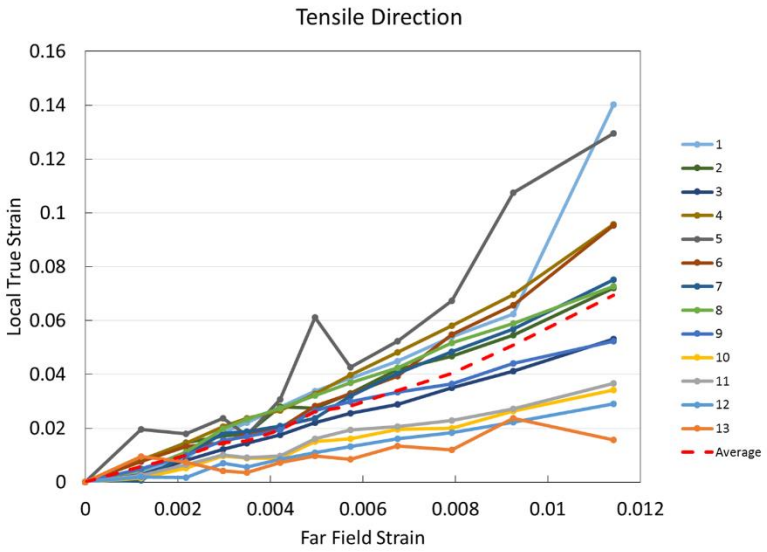

Figure 5.8: Local true strain vs. far field strain for sample with f = 0.5.

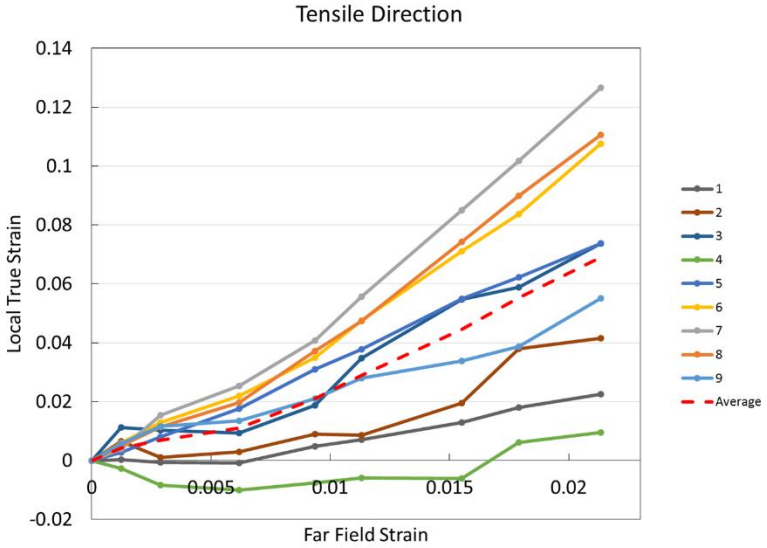

Figure 5.9: Local true strain vs. far field strain for sample with f = 0.364.

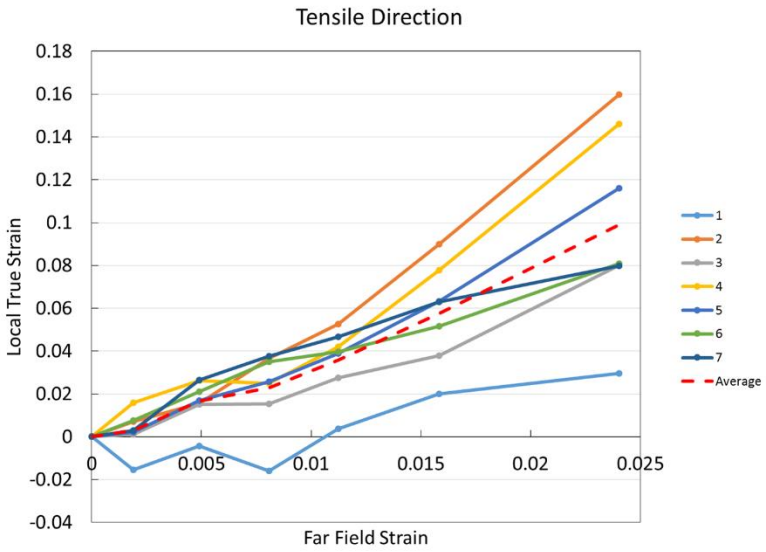

Figure 5.10: Local true strain vs. far field strain for sample with f = 0.286.

5.5 Void Orientation Effects on Heterogeneous Deformation

It was shown in Chapter 4 that the orientation angle of the holes had a weak impact on the growth of the holes. As the orientation angle was increased from 15° to 45° a greater number of holes were observed to deform by a shearing process and showed more significant growth in the tensile direction; however, the effects of the local microstructure were observed in all of the orientation angles examined. The same void orientation angles have been tested here to determine if a stronger trend occurs in the materials with a more uniform texture. Similar to the experiments presented in Chapter 4, the center to center hole separation distance has been held constant at 40 μm and orientation angles of 15°, 30° and 45° have been tested.

The deformation sequence of a row of holes and the tensile strain distribution is shown in Figure 5.11 for a sample with a void orientation angle of 15°. At a strain of 0.009, there are several hotspots which are distributed heterogeneously throughout the material. The strongest strain concentrations are observed within the hole region; however, there are several grain boundaries outside of this region which show significant localizations. It becomes apparent at a strain of 0.012 that the holes associated with the strongest strain concentrations are holes 4 and 5 as well as holes 12 and 13. The magnitude of the strain adjacent to these holes is larger than the concentrations away from the hole region for all of the far field strains examined. Figure 5.14 shows the local true strain as a function of far field strain for the sample. Similar to the configurations tested in Section 5.4, there is a small amount of deformation in the tensile direction and the displacement of the holes is non uniform. At a strain of 0.019, the magnitude of the local true strain ranges from 0.063 to 0.237 corresponding to displacements of 1.2 to 5.4 μm. Holes 4, 5 and 13 show the most significant growth in the far field strain region investigated.

Figure 5.12 shows the deformation of a row of holes and tensile strain distribution for a sample with a void orientation angle of 30°. For all of the far field strain values investigated, the strain localizes in the region of the holes. There are no significant strain concentrations outside of this region. At a strain of 0.004, it becomes apparent that the majority of the strain is distributed amongst holes 6 - 15. With subsequent deformation a hotspot becomes visible adjacent to hole 13. The local true strain vs. far field strain plot for this sample is shown in Figure 5.15. The plot reveals that very little growth is exhibited by

the holes in this sample prior to fracture. In fact holes 1, 2, 3 and 5 all experience displacements less than 1 μm. In addition, the localization adjacent to hole 13 is observed in the plot as this hole experiences the most growth in the tensile direction. At a strain of 0.0055 the local true strain of hole 13 is 0.082 corresponding to a displacement of 1.8 μm. With the exception of these holes discussed, the majority of the holes deformed with behavior similar to that of the average value reported. Therefore, the sample contains holes with negligible growth, a relatively small amount of growth and one localization illustrating the heterogeneous distribution of strain within the region of the holes.

The deformation history of holes and tensile strain distribution for a sample with a void orientation angle of 45° is shown in Figure 5.13. At a strain of 0.011, a hotspot is observed adjacent to hole 8. There is a great deal of strain localized in the vicinity of the holes; however, there are other localizations observed which are associated with grain boundaries. As the deformation continues the strain concentrations adjacent to the holes become stronger and the localizations associated with the microstructure become weaker. At a strain of 0.018, a significant hotspot is observed in the ligament of holes 7 and 8. At this strain the only localization associated with the microstructure observed, is that between hole 17 and the sample surface. The local true strain vs. far field strain for this specimen is shown in Figure 5.16. On average the growth of the holes is relatively larger than what was observed in Section 5.4; however, the deformation is heterogeneous with local true strains ranging from 0.034 to 0.305 at a far field strain of 0.018. Furthermore, the localization in

the ligament between holes 7 and 8 is captured in the chart as these holes exhibit the maximum displacement in the tensile direction.

The void growth behavior shows a weak relationship with the void orientation angle. Heterogeneous deformation has been observed in all of the configurations examined. Strain concentrations were observed to be associated with grain boundaries which has been a consistent result throughout the document. It was established in Section 5.4 that significant differences in the void dimensions can be attributed to the sliding of boundaries and even premature separation. The same observations have been detected here and therefore, it is difficult to determine quantitatively how the void orientation angle effects the growth process.

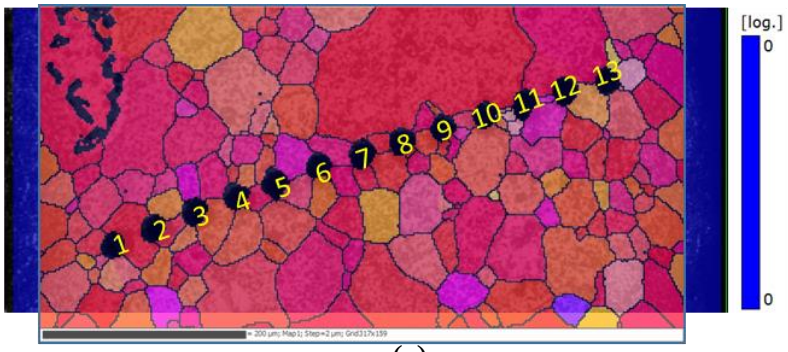

(a)

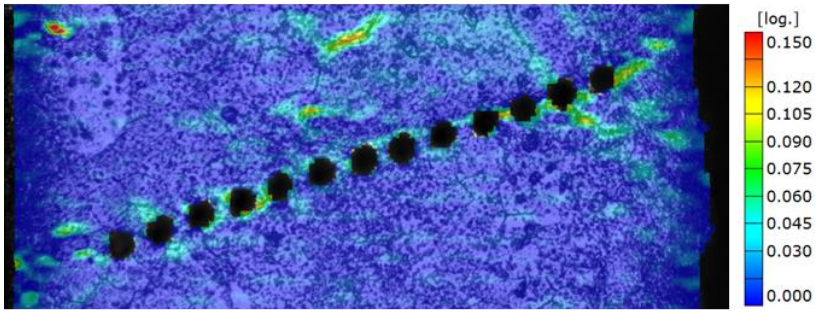

(b)

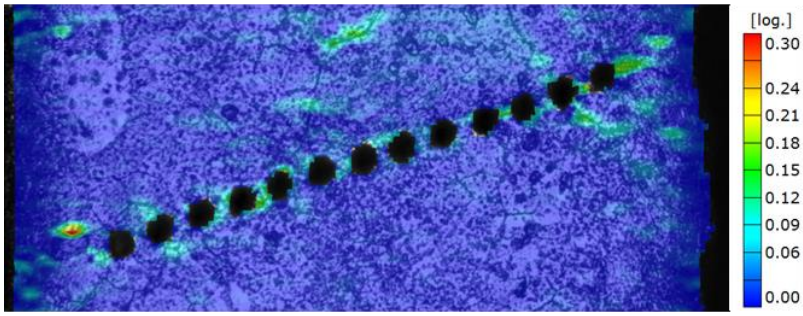

(c)

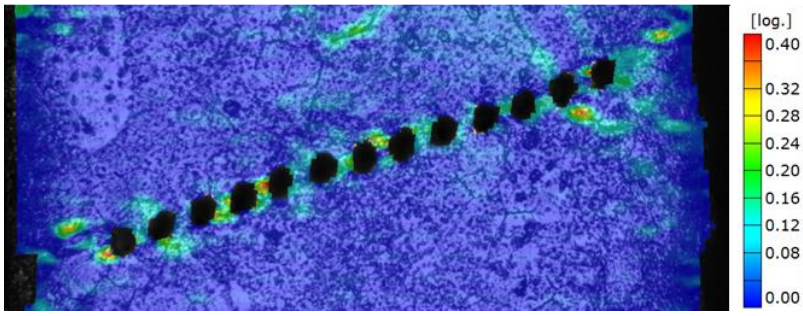

(d)

Figure 5.11: Deformation of holes and tensile strain distribution in a sample with θ = 15° at far field strains of (a) 0.000, (b) 0.009, (c) 0.012 and (d) 0.019.

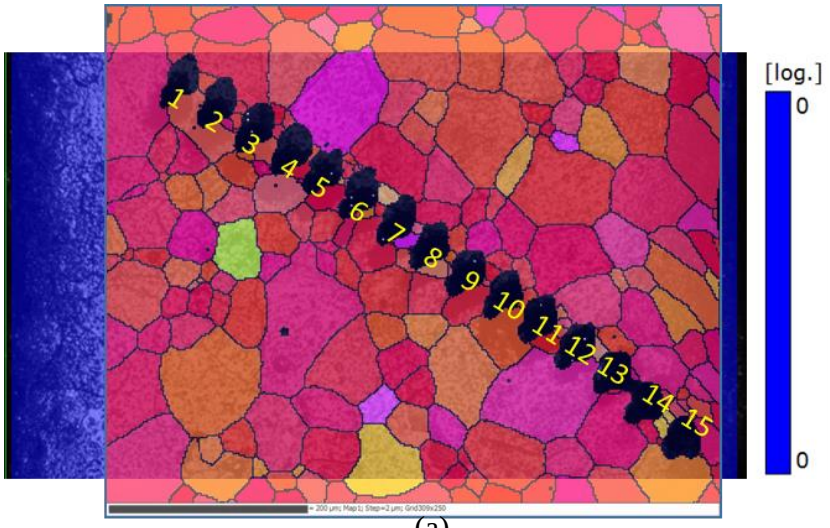
[log.]
0
0
1
2
3
4
5
6
7
8
9
10
11
12
13
14
15

(a)

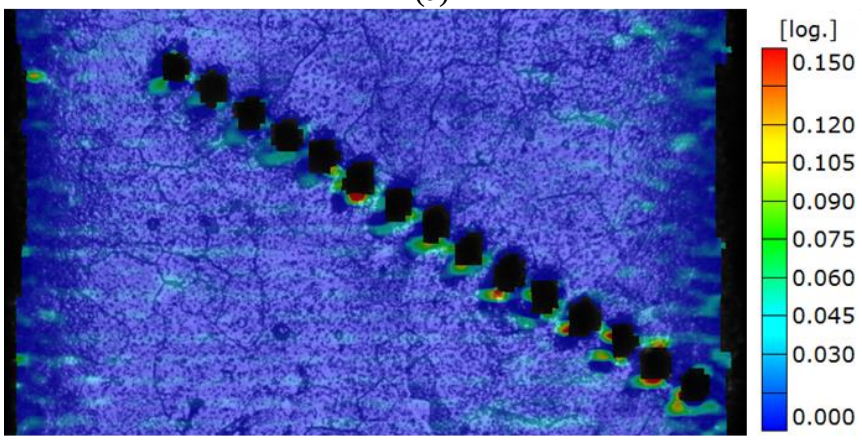
[log.]
0.150
0.120
0.105
0.090
0.075
0.060
0.045
0.030
0.000

(b)

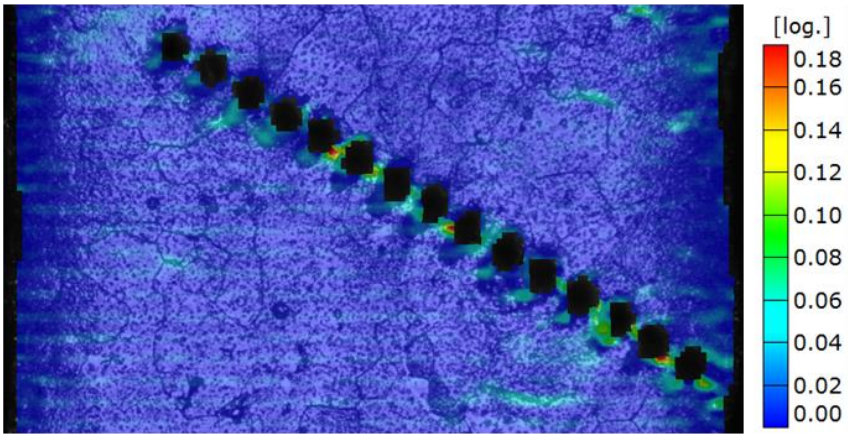
[log.]
0.18
0.16
0.14
0.12
0.10
0.08
0.06
0.04
0.02
0.00

(c)

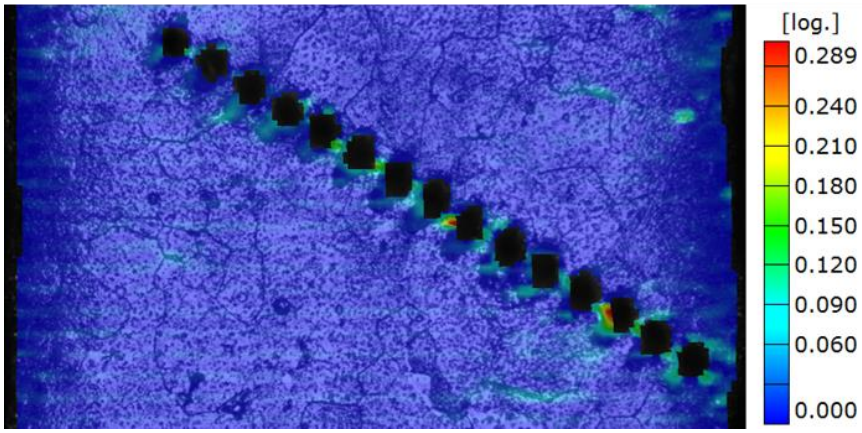

(d)

Figure 5.12: Deformation of holes and tensile strain distribution in a sample with θ = 30° at far field strains of (a) 0.000 with EBSD overlay, (b) 0.003, (c) 0.004 and (d) 0.006.

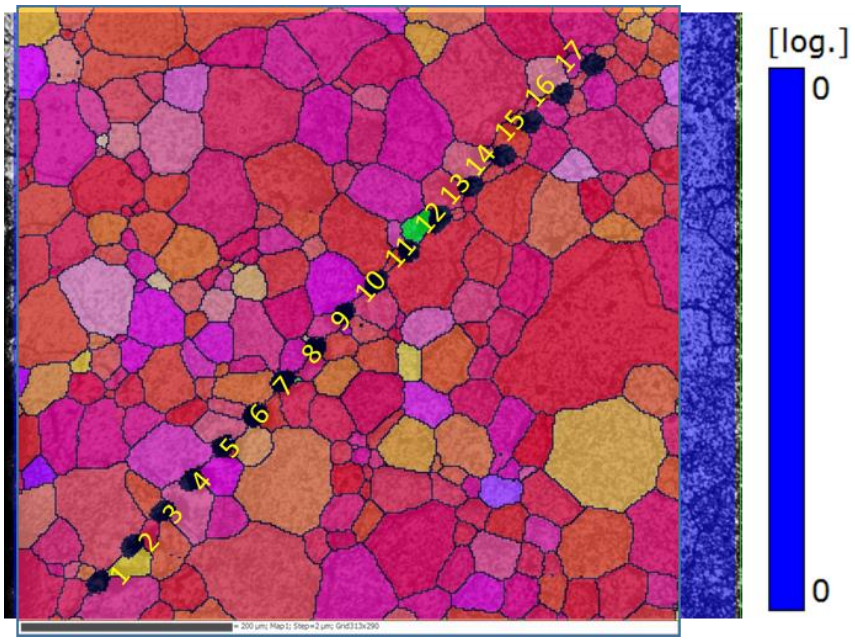

(a)

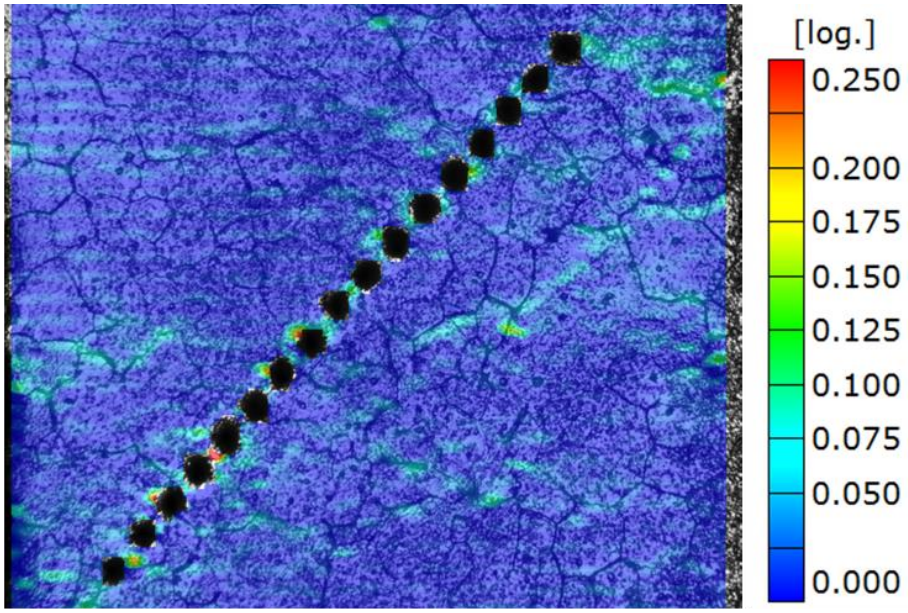
[log.]
0.250
0.200
0.175
0.150
0.125
0.100
0.075
0.050
0.000

(b)

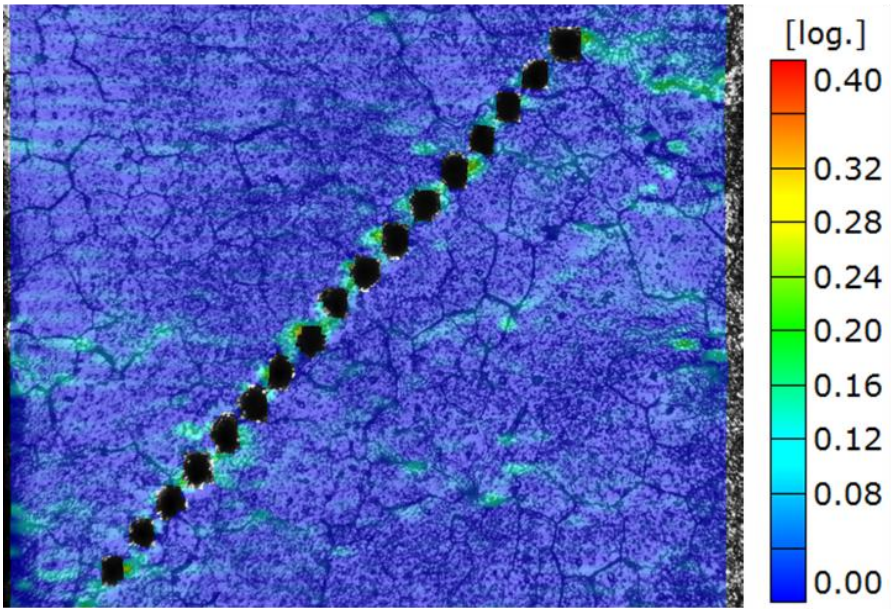
[log.]
0.40
0.32
0.28
0.24
0.20
0.16
0.12
0.08
0.00

(c)

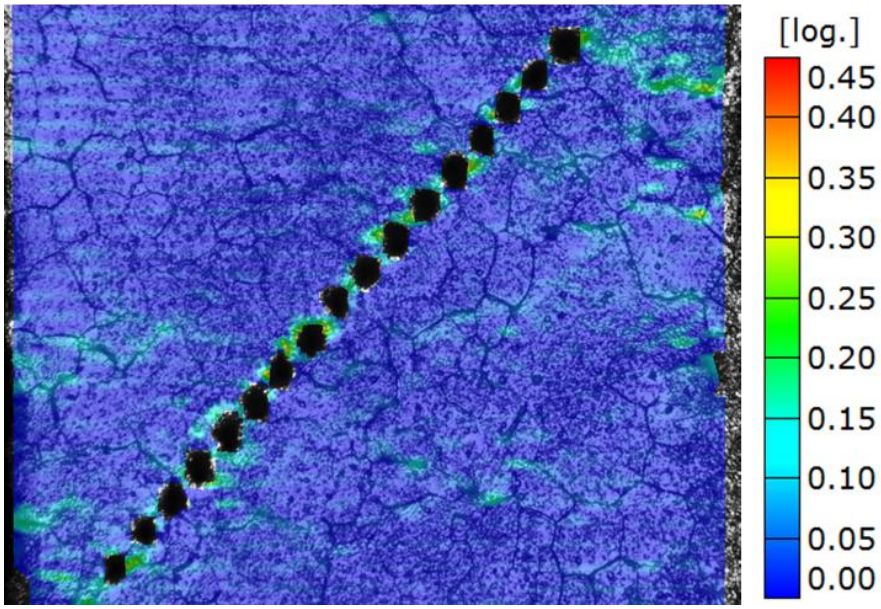

(d)

Figure 5.13: Deformation of holes and tensile strain distribution in a sample with θ = 45° at far field strains of (a) 0.000, (b) 0.011, (c) 0.016 and (d) 0.018.

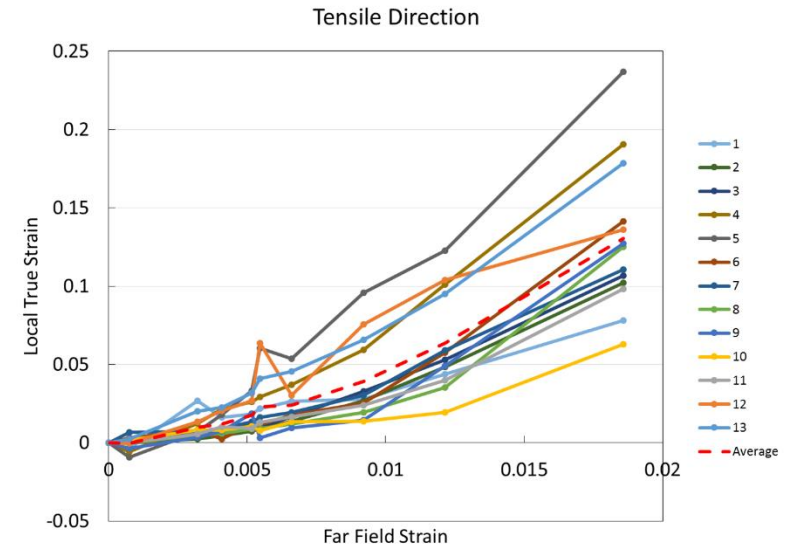

Figure 5.14: Local true strain vs. far field strain for sample with θ = 15°.

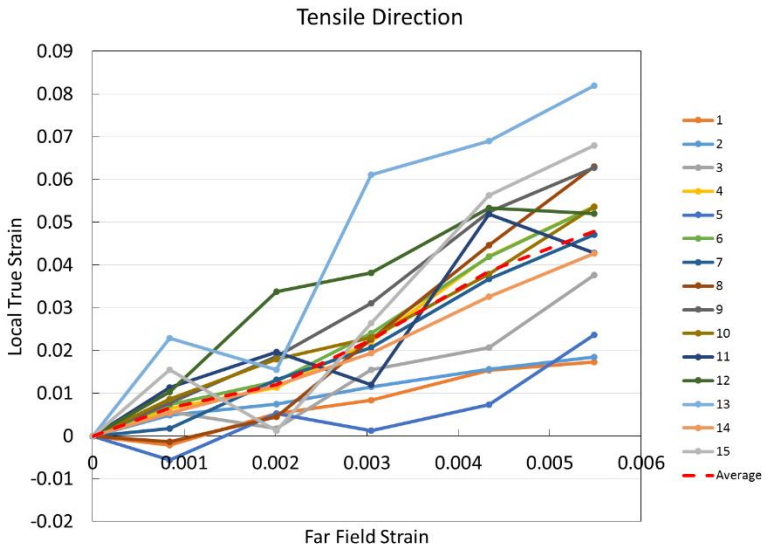

Figure 5.15: Local true strain vs. far field strain for sample with θ = 30°.

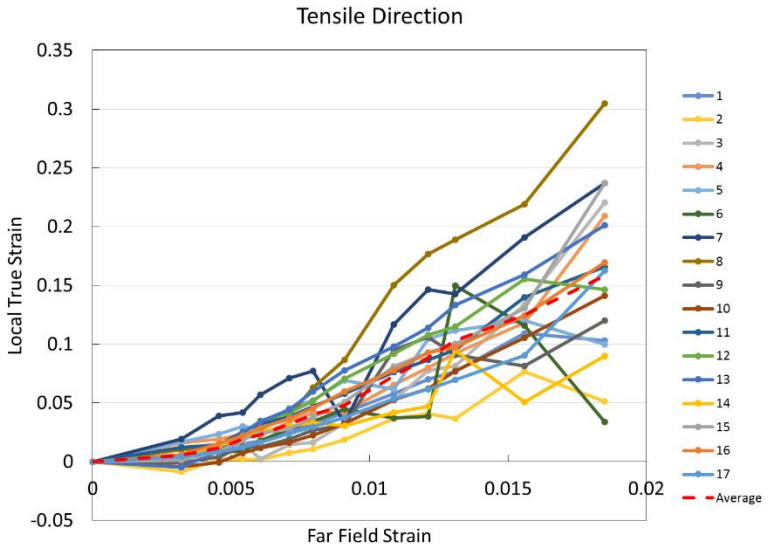

Figure 5.16: Local true strain vs. far field strain for sample with θ = 45°.

5.6 Heterogeneous Deformation

As stated above the deformation observed in all of the configurations was heterogeneous. Strain concentrations were observed in localized regions and the largest strains were associated with grain boundaries. In Chapter 4, the main fracture mechanisms observed were failure associated with grain and twin boundaries. Localizations associated with twins were not observed as frequently in the materials tested in this chapter. This may be due to the texture in which the c-axis is roughly aligned in the through thickness direction or possibly due to the high density of the speckle pattern. Nevertheless, grain boundary localizations dominated. In this section the localizations associated with these boundaries will be analyzed to determine how they evolve with the far field strain. In order to eliminate any additional strain concentrations produced by the holes, the results presented below are carried out on materials free of holes.

5.6.1 Heterogeneous Deformation Associated with Grain Boundaries

Figure 5.17 shows the tensile strain distribution near a grain boundary, one which contributes to the final fracture of the material, at various stages of deformation. In order to quantify the heterogeneous deformation associated with the grain boundary a section has been created as shown by the yellow arrow. The local strain is plotted as a function of position along this section at various values of far field strain. The results are shown in Figure 5.18 and the zero position of the x-axis is defined in Figure 5.17. The strain concentration along the boundary becomes defined from the onset of deformation. During

the early stages of deformation basal slip is the dominant deformation mechanism. This result suggests that slight incompatibilities of basal slip between adjacent grains can cause these strong localizations early in the deformation. With subsequent deformation the strain at the boundary gradually increases. The strains within the grains that form the boundary are relatively small compared to the strains at the boundaries. This result is consistent with what was observed in the Sections 5.4 and 5.5. Even at strains close to fracture there were grains adjacent to strong localizations which displayed negligible strains. At a far field strain of 0.027 the strain at the boundary is 0.281. The separation of the boundary initiates over a small increment of deformation after this point. This value is significant during the discussion of fracture in the section to follow.

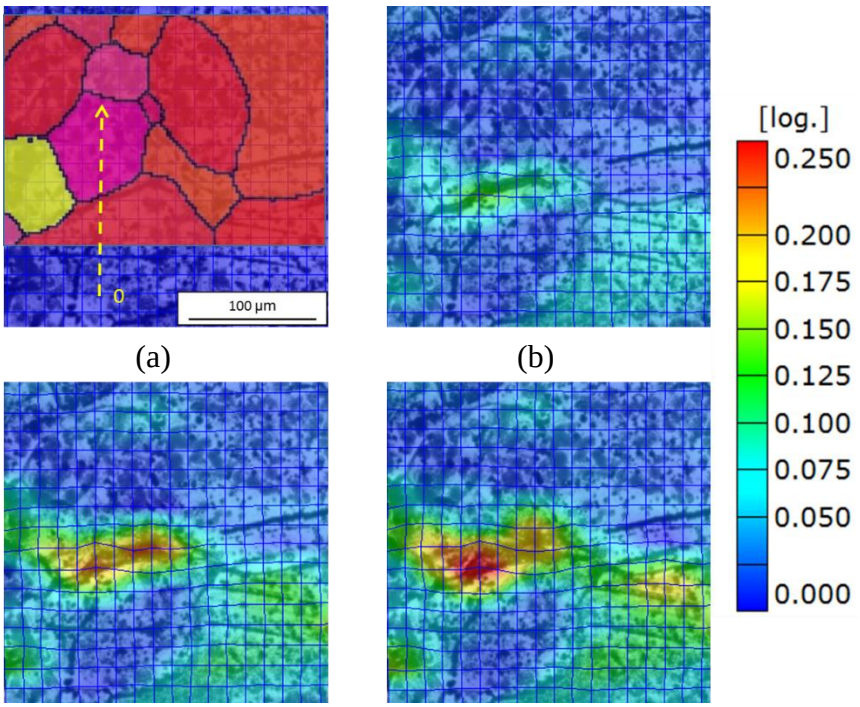

Figure 5.17: Evolution of tensile strain along a grain boundary at far field strain values of (a) 0.000 with EBSD overlay, (b) 0.018, (c) 0.023 and (d) 0.027.

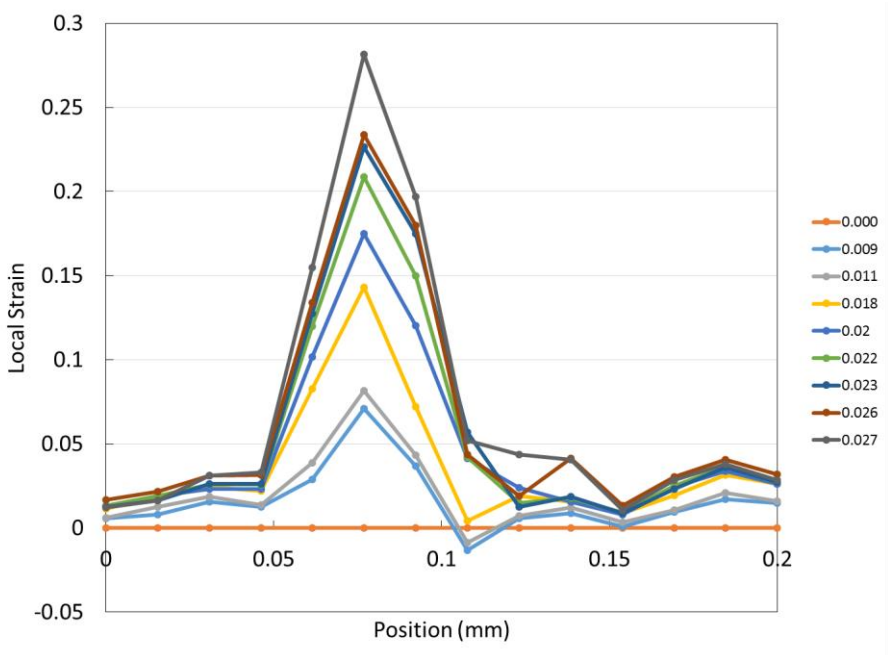

Figure 5.18: Local strain vs. position along section intersecting grain boundary at various values of far field strain.

5.6.2 Heterogeneous Deformation Associated with Twin Boundaries

The tensile strain distribution along a twin boundary which contributes to the final fracture is shown in Figure 5.19. Similar to the grain boundary case a section has been defined with the zero position defined in the figure. The strain is plotted as a function of position for various far field strain values in Figure 5.20. In contrast to the grain boundary, the twin boundary is not present in the microstructure from the onset of deformation. Therefore, the strain concentration is not pronounced early in the deformation. The twin nucleates at a strain of approximately 0.012. At this point there is a relatively small strain concentration associated with the twin. It was established that the effects of twinning could be summarized in two stages. In the first stage the twin forms to accommodate strain

incompatibilities. However, once nucleated the twin acts similarly to the grain boundary where incompatibilities could develop along the boundary as it acts as an obstacle to dislocation movement. This particular twin experiences a rapid accumulation of strain and fails shortly after reaching a strain of 0.283.

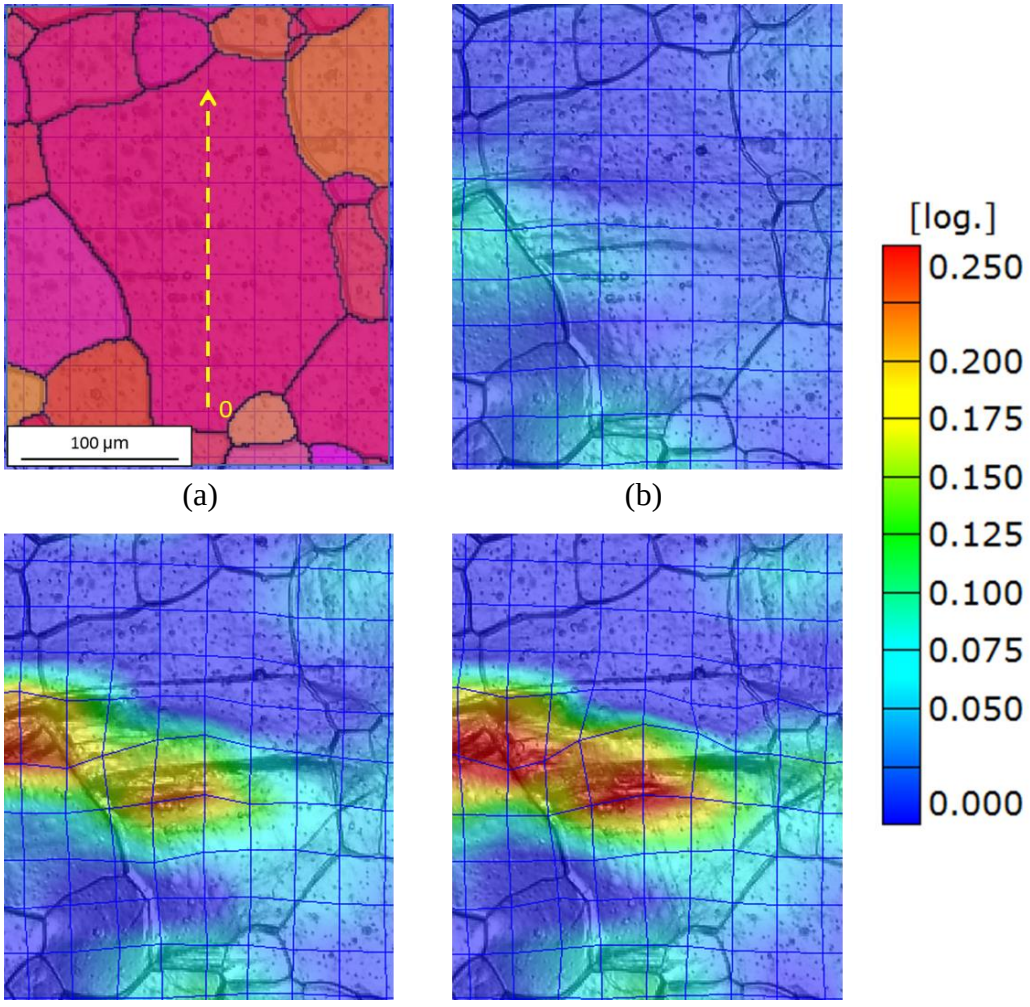

(a) (b)

(c) (d)

Figure 5.19: Evolution of tensile strain along a twin boundary at far field strain values of (a) 0.000 with EBSD overlay, (b) 0.012, (c) 0.020 and (d) 0.022.

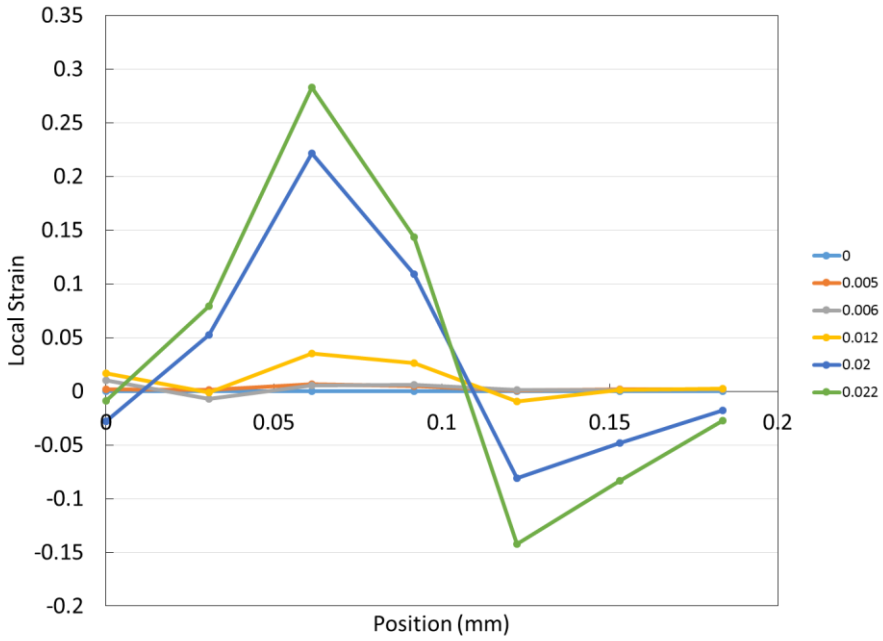

Figure 5.20: Local strain vs. position along section intersecting twin boundary at various values of far field strain.

5.7 Void Fraction Effects on Fracture

It was shown in Chapter 4 that the void fraction had a weak relationship with the void dimension at failure. This was due to the premature linkage of the holes along boundaries and may have also been influenced by the local recrystallization adjacent to the holes, which produced significant orientation differences. The materials investigated in this chapter exhibit a stronger texture compared with the materials tested in the previous chapter, and therefore, this relationship will be assessed once again. Heterogeneous deformation has been observed in the samples examined here; however, the magnitude associated with the differences in displacement at failure are relatively small compared to

what has been observed in Chapter 4. Samples with center to center void separation distances of 40, 55 and 70 μm were tested corresponding to void fractions that ranged from 0.677 - 0.291.

The first measurement that was investigated was the local true strain of the two holes which are associated with the largest strain concentration in their ligament prior to fracture. During these experiments it was difficult to determine the first two holes to link because the fracture occurred very rapidly over a small increment of deformation. Therefore, the two holes plotted are associated with the largest strain concentration just before fracture. This measurement is similar to the minimum error bar values in Figures 4.42 and 4.47; however, it will be presented as local true strain in this section. Figure 5.21 shows the local true strain prior to fracture as a function of the void fraction. With the limited amount of data presented, there is not a clear trend in the data. A straight line at a local true strain of 0.12 can give a good representation of the data if the points at f = 0.291 were excluded. As a result, it is more probable that a critical local strain is reached in the sample prior to the final fracture. Figure 5.22 and Figure 5.23 show the optical microscope images and tensile strain distribution for the largest and smallest void fractions examined. In both cases the strain localizes along a boundary in the ligament between the two holes and the failure of the boundary causes the final fracture. This is a common case for the materials tested in this section and may be a result of the stronger basal texture. The holes in the sample with the lower void fraction exhibited larger deformations prior to fracture; however, the fracture mechanism was similar.

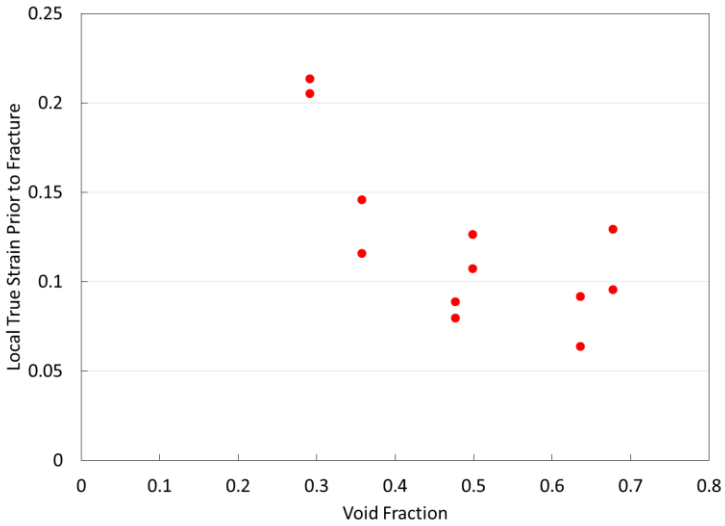

Figure 5.21: Local true strain prior to fracture vs. void fraction associated with the holes adjacent to the largest strain concentration.

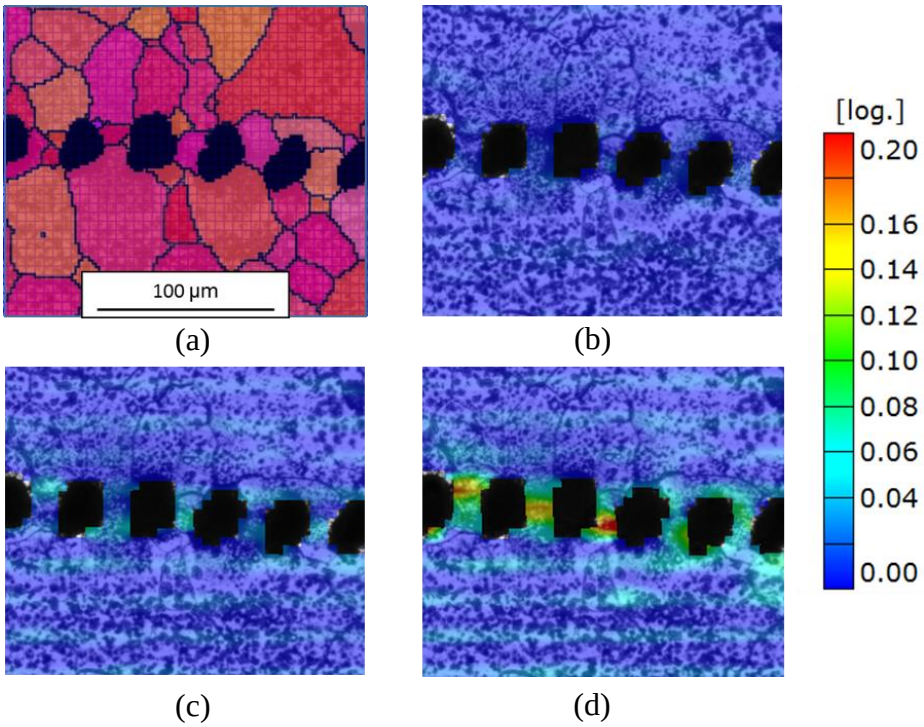

Figure 5.22: Optical image series and tensile strain distribution of the two holes associated with the largest strain concentration prior to fracture at far field strains of (a) 0.000 with EBSD overlay, (b) 0.002, (c) 0.004 and (d) 0.010 in sample with f = 0.677.

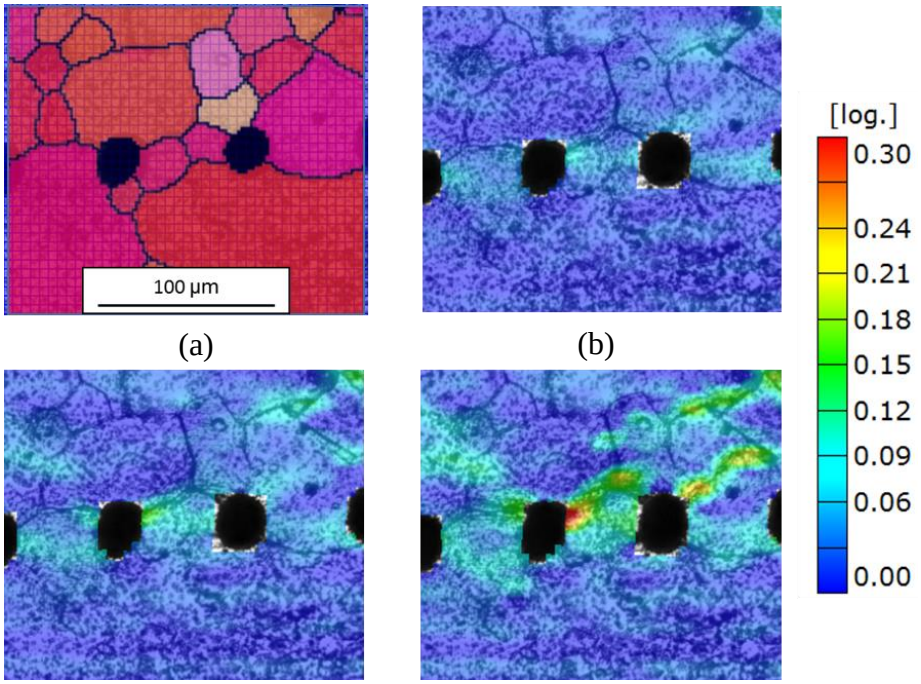

Figure 5.23: Optical image series and tensile strain distribution of the two holes associated with the largest strain concentration prior to fracture at far field strains of (a) 0.000 with EBSD overlay, (b) 0.011 (c) 0.016 and (d) 0.024 in sample with f = 0.291.

During alloy development it is of interest to understand how particles will influence the macroscopic properties of the material. One advantage of the experimental technique used in this chapter, is that it allows for quantitative information to be obtained away from the region of the holes. As a consequence, the effects of the void fraction on the far field strain prior to fracture have been assessed. Isotropic materials all contain heterogeneities such as grain boundaries and particles throughout their microstructure; however, macroscopically they may be modelled by a homogeneous medium. Figure 5.24 shows the far field strain prior to fracture as a function of void fraction. The trend is questionable between the far field strain prior to fracture and the void fraction. In addition, a large range

of far field strain values are observed for comparable values of void fraction. It was established earlier that strain localizations associated with grain boundaries had a significant contribution to the macroscopic strain. As a consequence, the variability of the strains observed for similar void fractions can be explained by the extent of the grain boundary localizations in the samples. Figure 5.25 shows the tensile strain distribution in the gage section for two samples with comparable void fractions just before final fracture. Figure 5.25(a) and Figure 5.25(b) correspond to samples with void fractions of 0.476 and 0.498, which reach far field strains of 0.01 and 0.021, respectively. For a gage section with a length of 0.5 mm these strains correspond to displacements between 5 and 11 μm. It is clear that the strain is distributed over a larger number of boundaries in the sample with f = 0.498. Several smaller hotspots are observed in the sample with f = 0.476; however, the strain has a dense distribution around the region of holes in this sample.

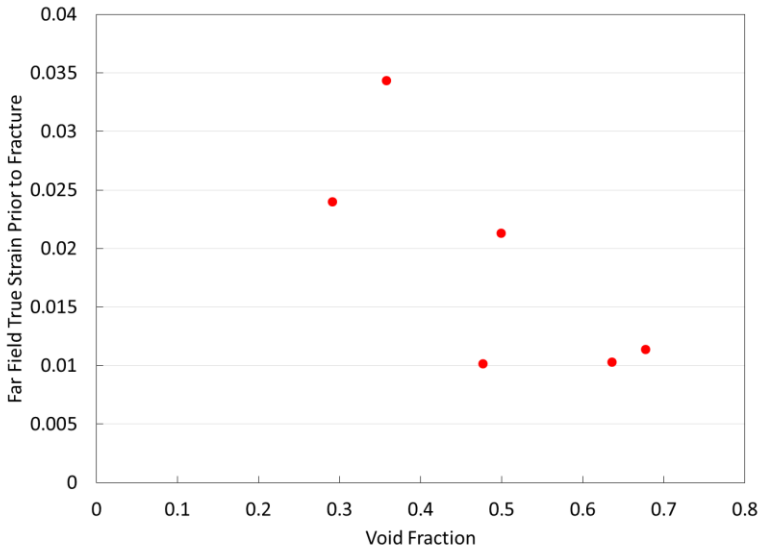

Figure 5.24: Far field strain prior to fracture vs. void fraction.

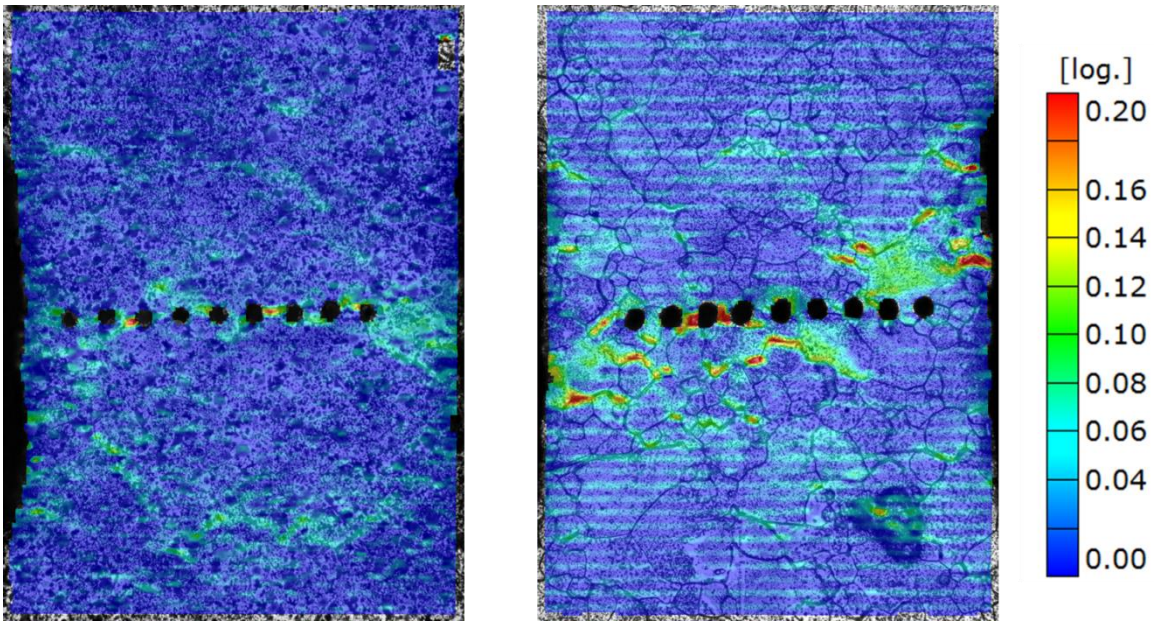

(a) (b)

Figure 5.25: Gage section of two samples prior to fracture with void fractions of (a) 0.476 and (b) 0.498.

There does not seem to be a clear trend between the void fraction and local or far field strain prior to fracture. However, one observation that has been consistent throughout the results presented thus far is the fracture mechanism. Grain boundary failure has been observed in almost every case examined. Therefore, this analysis is devoted to the hypothesis that a critical strain must be obtained to initiate fracture of the boundary. Points were used to determine the location of the maximum strain in the ligament with the largest strain localization. Figure 5.26 shows the maximum point strain prior to fracture as a function of the void fraction. All of the data points lie between point strains of 0.23 and 0.43. At the length scale in which the measurement is taken, these strains correspond to

tensile stretches of 1 to 2 μm. Figure 5.27 shows the ligament associated with the largest strain concentration for the samples with the smallest and largest void fractions investigated. The white points indicate the point where the strain value was obtained. The maximum strain prior to failure obtained at these points is 0.342 and 0.315 and the fracture mechanism observed in both cases was boundary associated failure. As a consequence, it is probable that a critical strain is obtained in the ligament prior to fracture. This idea will be returned to later in the chapter after additional data has been presented.

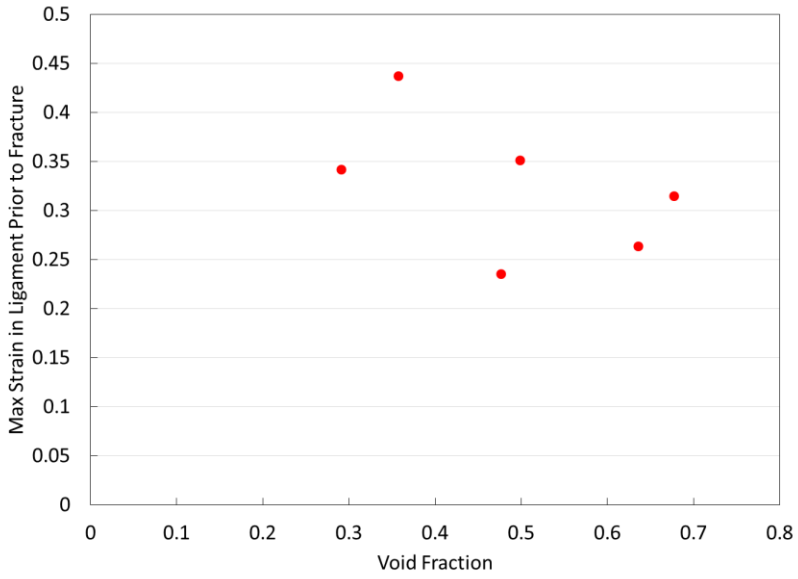

Figure 5.26: Maximum strain in ligament prior to fracture vs. void fraction.

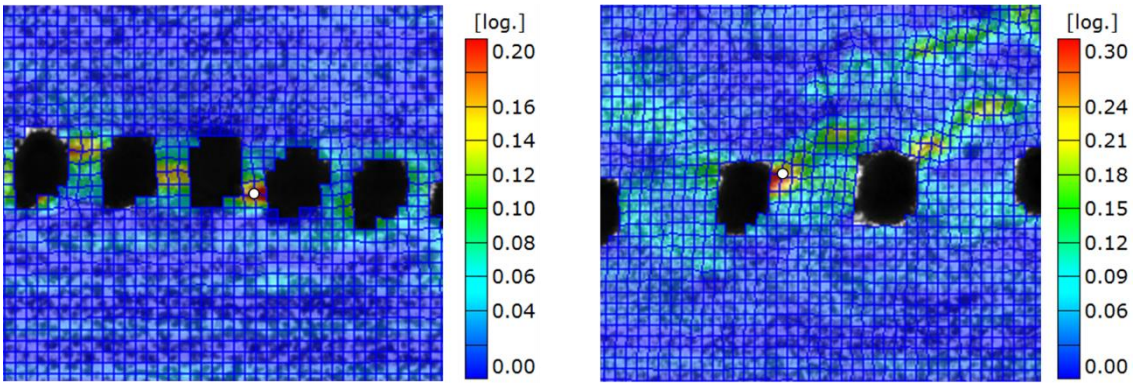

(a) (b)

Figure 5.27: Ligament associated with the maximum strain concentration prior to fracture for samples with void fractions of (a) 0.677 and (b) 0.291.

5.8 Void Orientation Effects on Fracture

In this section the effects of void orientation on the measures of fracture presented above will be assessed. It was established in Chapter 4 that as the void orientation angle was increased from 0° to 45°, the linkage of the holes changed from a microstructure dominated fracture or internal necking type processes to a shear process. However, the effects of the microstructure were observed in all of the orientations tested. The void growth section revealed heterogeneous deformation of the holes and also showed the influence of the microstructure. Void orientation angles of 0°, 15°, 30° and 45° have been investigated here. The void fraction did not have a strong impact on the local strain or far field strain in the samples examined. Fracture was controlled by the separation of boundaries. If this observation is consistent in the samples tested in this section, similar results will be expected to what was obtained in Section 5.7. This hypothesis is likely to be correct since the majority of the ligaments between the holes contain grain boundaries.

Figure 5.28 shows the local true strain of the two holes associated with the largest strain concentration as a function of void orientation. Two samples have been presented for each orientation which represent the samples which were stopped as close as possible to fracture.

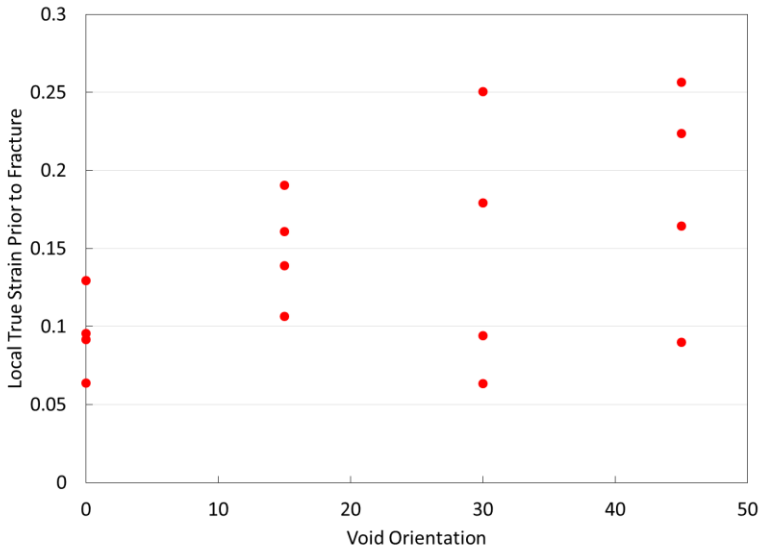

Figure 5.28: Local true strain prior to fracture vs. void orientation associated with the holes adjacent to the largest strain concentration.

A clear trend does not exist between the local strain at failure and the void orientation. There is a relatively large amount of variability in the data for a given orientation. Based on the previous results it can be expected that fracture of the 0° orientation was controlled by a grain boundary. Figure 5.29 and Figure 5.30 show the optical microscope images and tensile strain distribution for the 15° and 45° orientations examined. The images show that in both cases the holes are sheared along a grain boundary. There is not a significant difference in the local strain prior to failure; however, the heterogeneous nature of the

deformation associated with these samples suggests that this may not be a reliable measurement to predict fracture.

Similar to the case of void fraction the effect of the void orientation on the far field strain has been investigated. Figure 5.31 shows the far field strain prior to fracture as a function of void orientation. It is clear that a trend does not exist between these parameters. It should be noted that the center to center spacing between the holes in these samples is relatively small. When the hole spacing is smaller it is more probable for the strain concentrations to develop in the region of the holes prior to fracture.

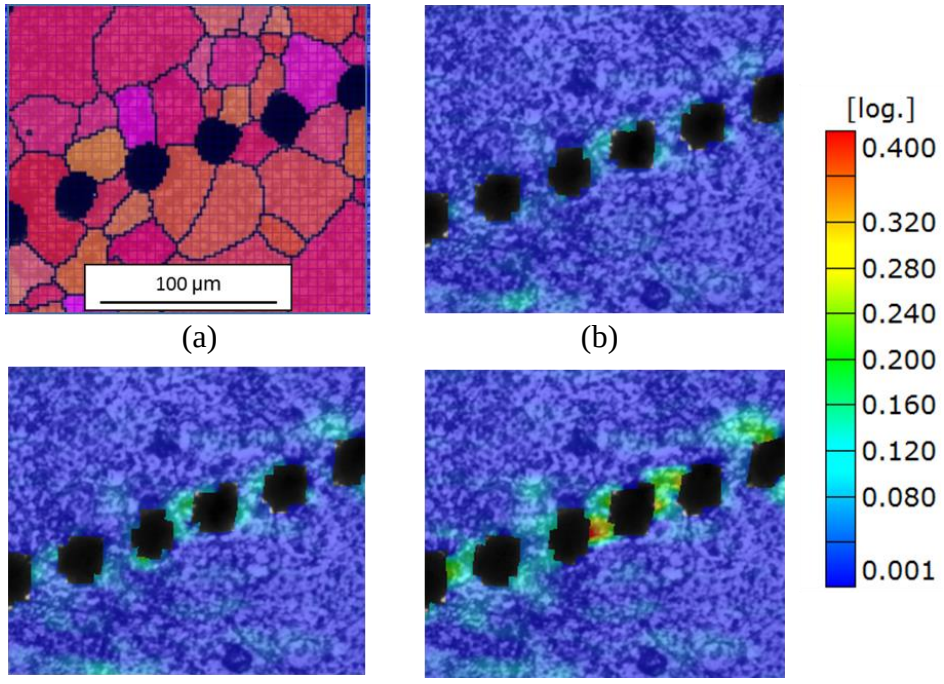

Figure 5.29: Optical image series and tensile strain distribution of the two holes associated with the largest strain concentration prior to fracture at far field strains of (a) 0.000 with EBSD overlay, (b) 0.009, (c) 0.012 and (d) 0.019 in sample with θ = 15°.

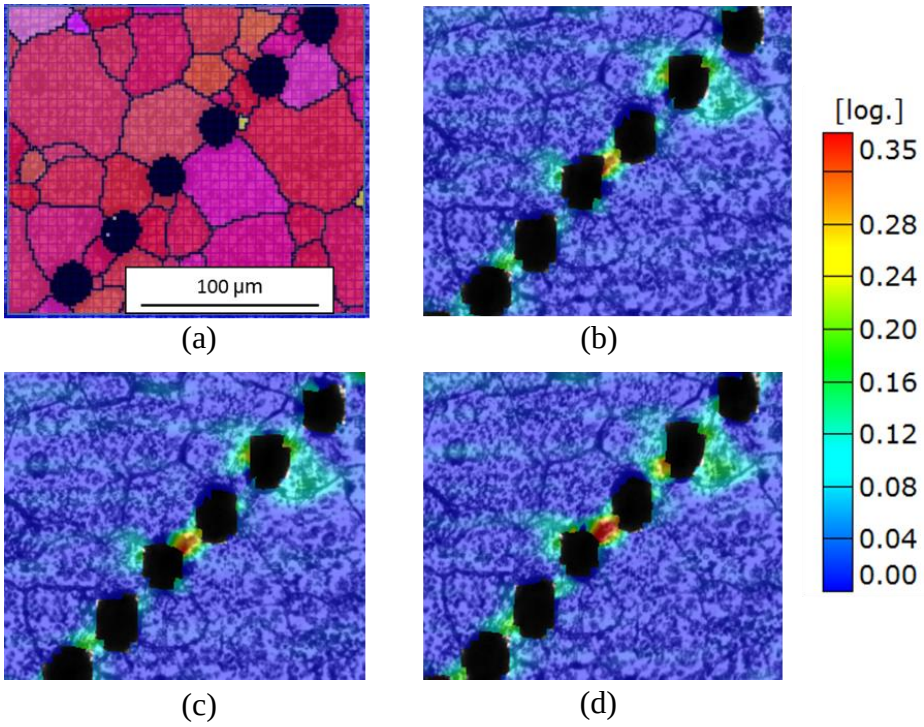

Figure 5.30: Optical image series and tensile strain distribution of the two holes associated with the largest strain concentration prior to fracture at far field strains of (a) 0.000 with EBSD overlay, (b) 0.013, (c) 0.016 and (d) 0.020 in sample with θ = 45°.

Figure 5.32 shows the gage section with the tensile strain distribution overlay just before fracture in samples with void orientations of 15° and 45°. In both cases the strongest strain concentrations are located in the region of the holes and there are a few localizations outside of this region. The sample with a void orientation of 45° shows a slightly larger far field strain prior to failure than the sample with an orientation angle of 15°. Assuming the concentrations adjacent to the holes were similar and that the strain localizations outside of the hole region were negligible this result would be expected. However, the samples with an orientation angle of 30° do not support this trend. Considering the heterogeneous

deformation associated with the samples, the far field strain prior to fracture is not a helpful parameter in predicting fracture in the materials investigated.

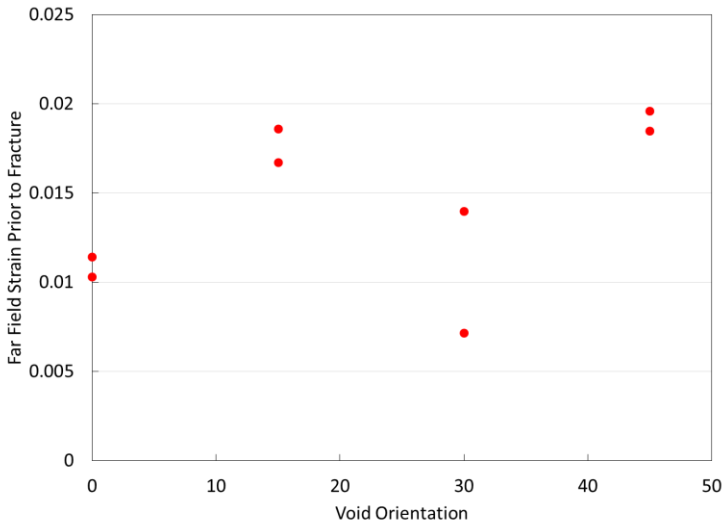

Figure 5.31: Far field strain prior to fracture vs. void orientation.

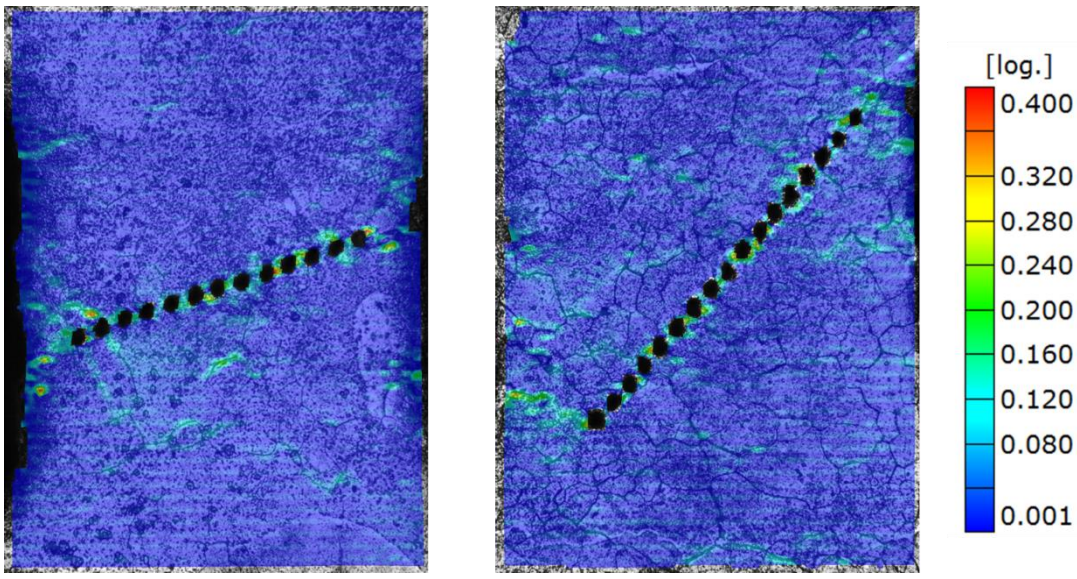

(a) (b)

Figure 5.32: Gage section of two samples prior to fracture with void orientations of (a) 15° and (b) 30°.

The fracture of the majority of the samples tested in this chapter were associated with failure of grain boundaries within the ligaments between the holes. Therefore, the maximum strain in the ligament associated with the largest strain concentration prior to fracture has been obtained for the void orientations investigated and the results are shown in Figure 5.33. The results are similar to what was obtained in Section 5.7. There seems to be a critical strain which triggers the failure of the boundaries. Figure 5.34 shows the tensile strain distribution and grid for samples with void orientations of 15° and 45° prior to fracture. The white dot indicates where the strain was obtained. The hotspots are of similar magnitude. It should be noted that the majority of the samples showed relatively small deformations in the hole regions prior to fracture and most of the significant displacements occurred over a very small increment of deformation. Therefore, it is very difficult to stop these tests when the boundaries begin to separate. This explains the variability of the data. However, since the strains dealt with here are obtained over such small gage lengths, this variability is negligible. The results suggest that there is a critical strain which initiates the fracture of the grain boundaries.

Comparison of Figure 5.33 and Figure 5.26 show that the maximum local strains reached in the ligaments for all of the configurations tested are comparable. In order to test the hypothesis that a critical strain initiates fracture, a more meaningful way to represent the data would be in a histogram or boxplot. The maximum strain prior to fracture was obtained for 15 samples with at least 2 samples from each void configuration and the results are shown in Figure 5.35 and Figure 5.36.

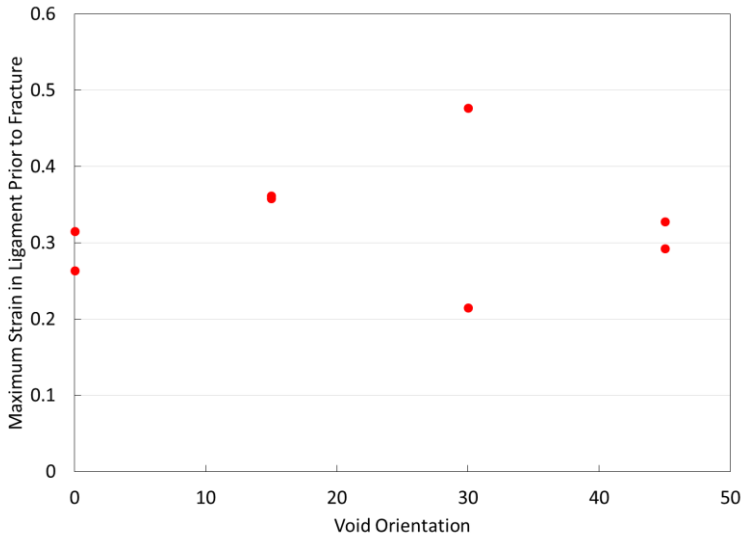

Figure 5.33: Maximum strain in ligament prior to fracture vs. void orientation.

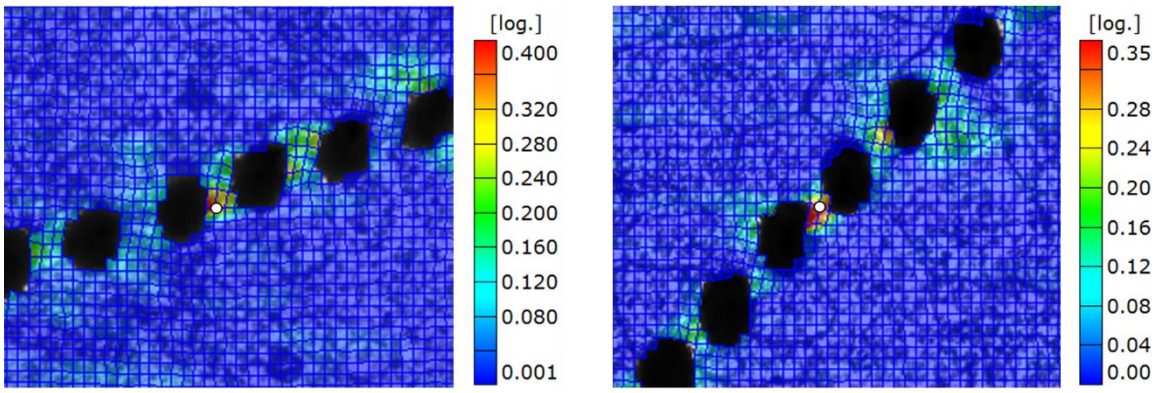

(a) (b)

Figure 5.34: Ligament associated with the maximum strain concentration prior to fracture for samples with void orientations of (a) 15° and (b) 30°.

The histogram reveals that the data follows a normal distribution with a skew to the lower values of strain. It is very probable that this skew comes from the fact that the boundaries exhibit rapid failure. There are two reasons that this rapid failure occurs:

(1) One surface is being investigated during the experiments. As a result, it is just as likely that these features occur on the surface which is not in view. Failure may have already initiated on the other surface leading to the rapid failure on the surface in view.

(2) The compatibility strain accumulated at the boundary is relatively large. Therefore, a large amount of energy is being stored within the boundary. Once fracture initiates a large amount of energy is released which is comparable to the amount of surface area created. As a consequence, it is more likely to stop the test and report a strain localization which is slightly lower than the expected value to initiate fracture.

The red curve overlaid on the histogram in Figure 5.35 represents a normal distribution with a mean and standard deviation calculated from the data used. The mean and standard deviation for the data set are 0.333 and 0.076, respectively. Boxplots are a convenient way of observing the distribution associated with the data. Figure 5.36 shows a boxplot of the data presented above and the quantiles associated with the boxplot are shown in Table 5.1. The median of the data is slightly lower than the mean confirming that there is a slight skew to the left in the data. A standard range of 1.5 times the interquartile range was used for the whiskers of the boxplot. The whisker values correspond to 0.2151 and 0.4447. One data point lies outside of this range on the larger strain value portion of the distribution. It is very probable that this boundary has already separated at this point of deformation. The data suggests that there is a critical strain to initiate fracture in the boundaries investigated. This is particularly useful for finite element simulations where damage is considered. It is reasonable to consider the mean value of 0.333 as the critical

strain in which failure of boundaries initiate at. Once the boundaries reach this strain a small increment of deformation will cause rapid failure of the boundary.

Table 5.1: Quantiles of the maximum strain prior to fracture for all configurations.

Quantile (%)	0	25	50	75	100
Strain Value	0.2151	0.2861	0.3281	0.3599	0.477

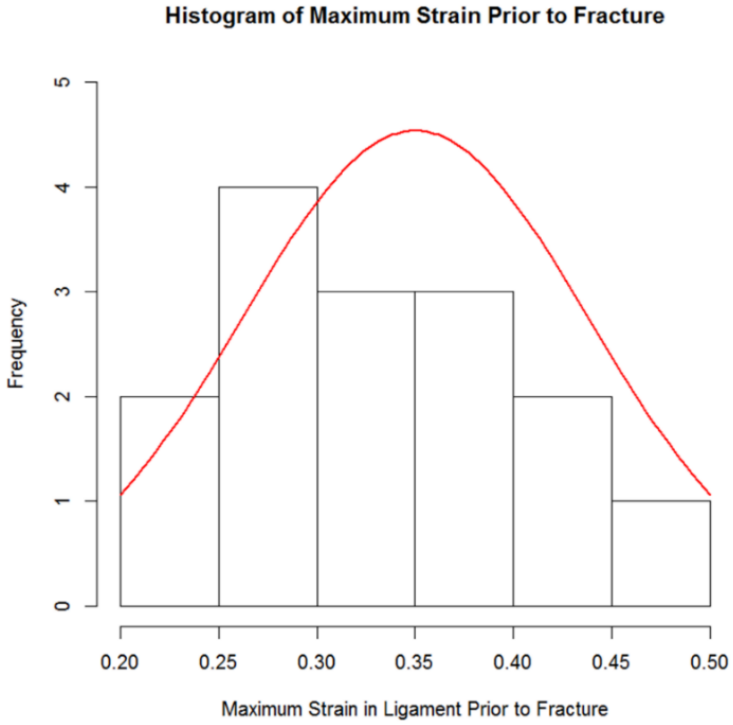

Figure 5.35: Histogram of maximum strain prior to fracture for all configurations.

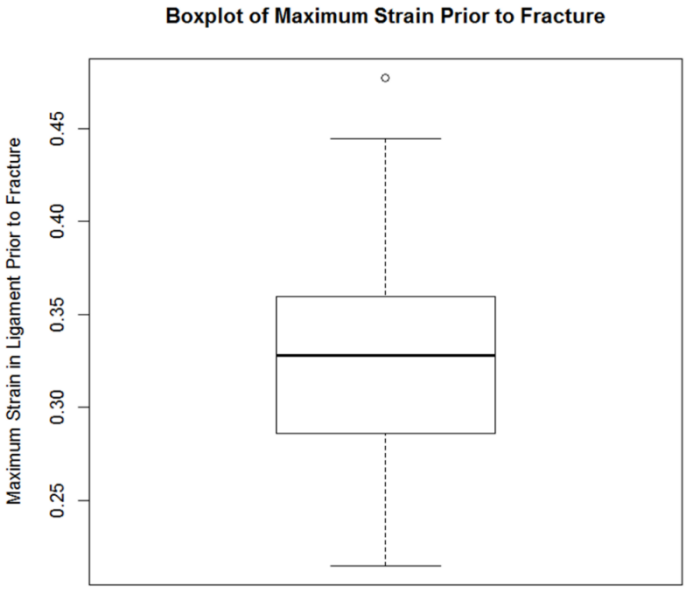

Figure 5.36: Boxplot of the maximum strain prior to fracture for all configurations.

5.9 Crystal Plasticity Finite Element Method

It has been well established that microstructure has a significant impact on the deformation and fracture characteristics of the materials examined. In order to model the material behavior accurately the initial texture and texture evolution must be accounted for. In this section a crystal plasticity finite element approach has been used to understand the deformation mechanisms responsible for the large localizations observed.

The sample examined was free of holes and a part file was created using partitions to represent grain boundaries. It was assumed that the grains were columnar. As a result, the grain geometries shown on the surface propagate through the thickness of the model. The EBSD data was obtained and the corresponding Euler angles were assigned to each

grain. Figure 5.37 shows the part file and boundary conditions imposed as well as the EBSD data used in the analysis. The bottom surface was constrained in the tensile direction and all rotations were inhibited in the plane. A uniaxial stretch was applied to the top surface at a strain rate of $5x10^{-5}s^{-1}$. The magnitude of the stretch was determined experimentally. 3D linear 8-node brick elements with reduced integration were used and the through thickness consisted of 10 elements. The material property is based on a user defined material UMAT which has been developed by Wu et al. (2015). Meshing and the application of the UMAT was done by Qiao (2015). Extension twinning has been included in the model; however, the model is currently under development. As a result, the details associated with twinning cannot be reported here. The slip systems obey a modified Voce type hardening law and the shear stress is given by

$$\tau(\Gamma) = \tau_0 + (\tau_1 + \theta_1\Gamma)\left\{1 - exp\left(-\frac{\theta_0\Gamma}{\theta_1}\right)\right\} \tag{5.1}$$

where τ_0 is the initial critical resolved shear stress, τ_1 is the shear stress extrapolated from the asymptotic hardening value, θ_0 is the initial hardening rate, θ_1 is the asymptotic hardening rate and Γ is the total accumulated shear strain. The hardening parameters used for the simulation are presented in Table 5.2. These values were used to fit the experimental macroscopic stress strain response and the results are shown in Figure 5.38. The simulation displays a good fit to the experimental data using the values shown in Table 5.2.

Table 5.2: Hardening parameters used in simulation.

Deformation mode	τ_0 (MPa)	τ_1 (MPa)	θ_0 (MPa)	θ_1 (MPa)
Basal <a>	15	20	250	0
Prism <a>	80	15	750	0
Pyramidal <c+a>	105	25	900	0
Extension Twinning	25	0	0	0

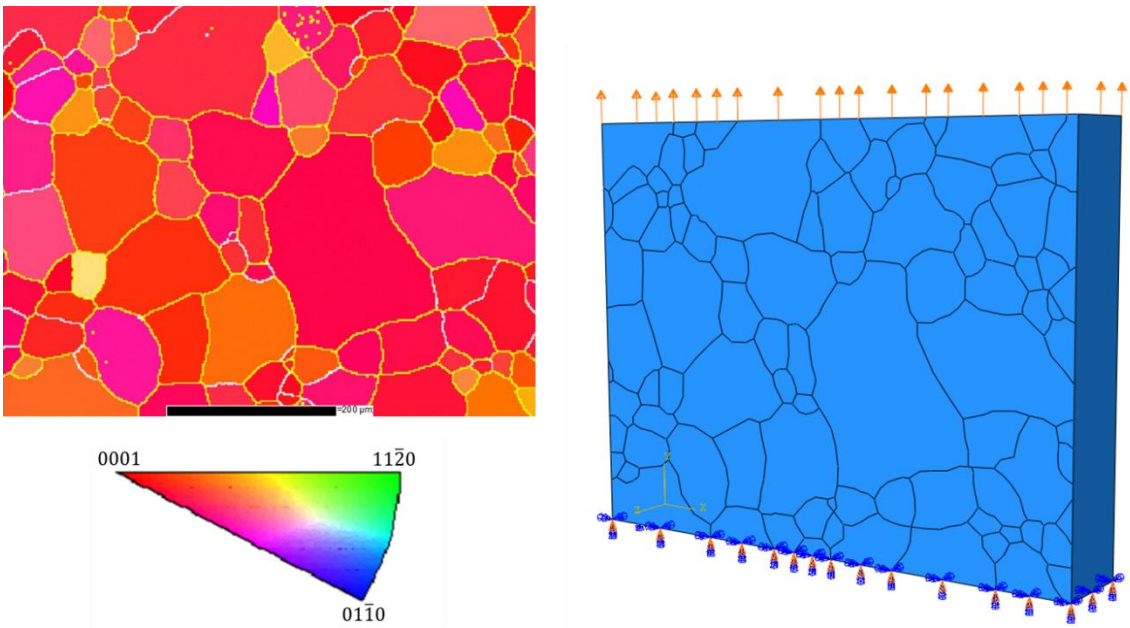

(a) (b)

Figure 5.37: (a) EBSD map and (b) part file with the boundary conditions imposed for the simulation.

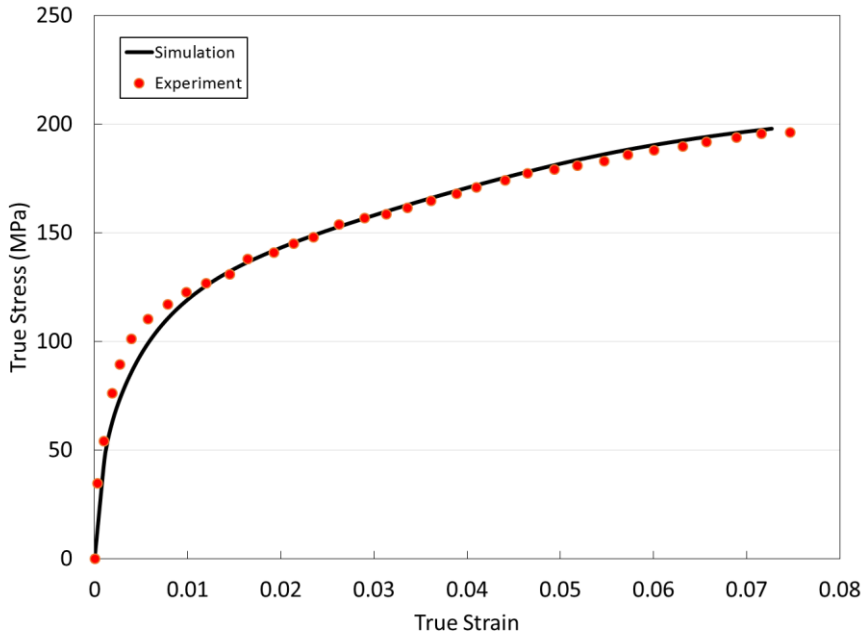

Figure 5.38: Macroscopic true stress strain response of the simulation compared to the experimental data.

The purpose of the investigation is to determine the roles of the various deformation mechanisms on the localizations and understand their hardening behavior. Relative activity is a parameter that has been defined as an output to quantify the contribution of each deformation mechanism to the total shear strain. It is defined as the shear strain produced by a given mechanism divided by the total shear strain of a given grain and has been summed up for all of the grains in the analysis. Figure 5.39 shows the relative activity of the deformation mechanisms as a function of the far field strain. This plot will be referred to frequently in the discussion to follow.

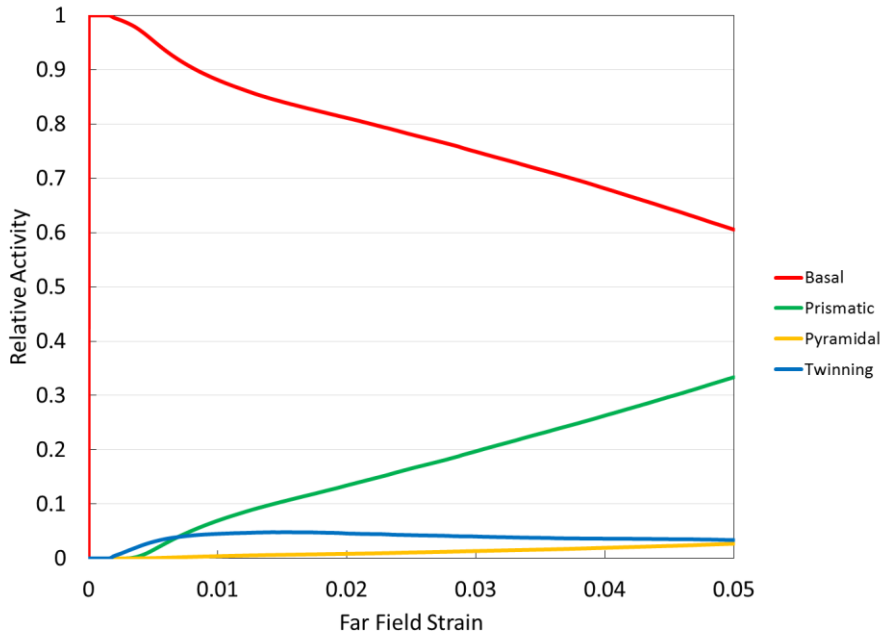

Figure 5.39: Relative activity of the deformation mechanisms vs. far field strain.

The tensile strain distribution predicted by the model and the experimental strain map are shown in Figure 5.40 at several values of far field strain. At a strain of 0.004 several localizations develop and are associated with grain boundaries. With reference to the relative activity plot, it is observed that at this point of the deformation the shear strain is entirely accommodated by basal slip. The strain concentrations observed experimentally are stronger than those predicted by the model; however, the location of the hotspots are accurately modelled. It should be noted that modelling the grain boundaries by the partition method assumes perfect coherency between the boundaries which is an ambitious assumption. At a strain of 0.012 some roughening is observed in the vicinity of the boundaries. This suggests that grain boundary sliding has occurred to accommodate strain concentrations or twins have nucleated adjacent to these boundaries. Several twins have

been detected at this strain which were not predicted by the model. The twins that were predicted by the simulation occur in the regions where the localizations occur. Furthermore, the activity of prismatic slip begins to make a significant contribution to the total strain. The results suggest that basal slip is the dominant deformation mechanism at the early stages of deformation. With subsequent deformation, incompatibility between grains occurs due to slight variations in basal activities between grains. At this point strain localizations occur and twins begin to develop in the vicinity of these strain concentrations. When the strain concentrations are large enough, prismatic slip contributes to accommodate strain incompatibilities. At a strain of 0.02 the model does not predict the behavior. Failure has initiated in the boundary associated with the largest strain concentration. The partitioning method used for the grain boundaries will not predict this behavior. In addition, a twin has formed in the grain adjacent to this localization which was not predicted by the simulation. The model shows good agreement with the experiment with respect to the slip mechanisms; however, does not predict twinning with any accuracy. At this point it should be recognized that the complete 3D microstructure was not accounted for and there is a possibility that the grains through the thickness have contributed to the twins observed on the surface. Nevertheless the simulation gives a good benchmark for understanding the deformation in the materials tested.

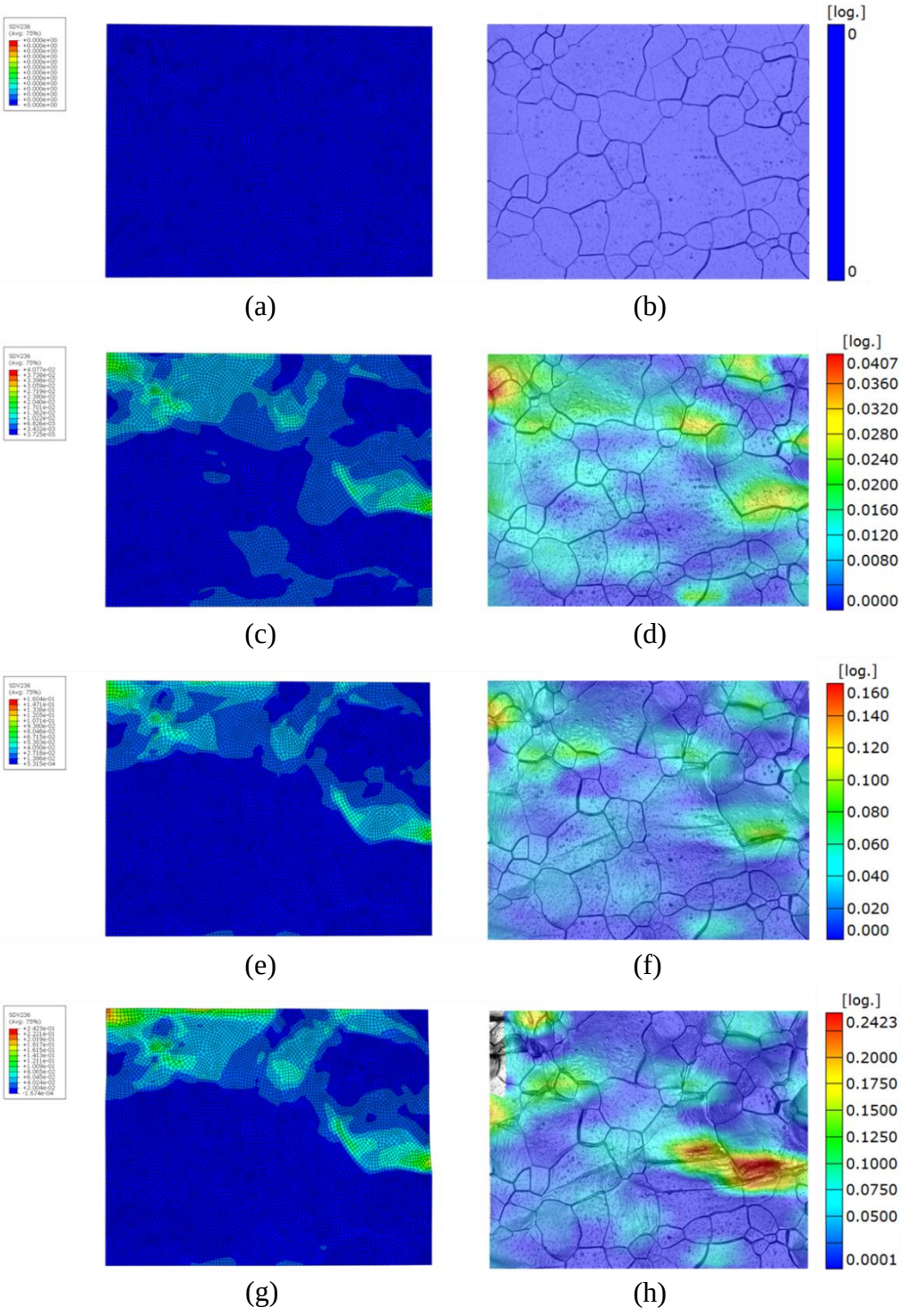

Figure 5.40: Tensile strain distribution (a) simulation ε=0.000, (b) experiment ε=0.000, (c) simulation ε=0.004, (d) experiment ε=0.004, (e) simulation ε=0.012, (f) experiment ε=0.012, (g) simulation ε=0.020 and (h) experiment ε=0.020.

5.10 Simple Model for Deformation-induced Void Linkage

The results presented in this chapter can be coupled together to gain a fuller understanding of the deformation and fracture mechanisms exhibited by the materials tested. Strain localizations were mainly associated with grain boundaries in this chapter; however, there were a few cases where localizations occurred around twin boundaries and several cases presented in the previous chapter. Based on the results of the CPFEM simulation, the role of the various dislocation systems on these strain localizations are discussed. Figure 5.41 shows a schematic of the proposed mechanism for grain boundary failure. From the onset of deformation basal dislocations cause incompatibility strains along the grain boundaries. This increases the strain in the vicinity of the grain boundaries which allows for other deformation mechanisms such as twinning and prismatic slip to occur in these regions. When compatibility can no longer be accommodated by deformation mechanisms grain boundary failure is initiated. This was found to occur at a local strain of roughly 0.33. Furthermore, it was found that this maximum strain was observed to favour one of the holes. As a result, one hole was associated with a relatively larger local strain at failure. This made it difficult to obtain meaningful information from the local strain at failure data. Subsequent deformation resulted in rapid crack propagation and the final fracture of the material.

Although twin boundary failure was not observed frequently in this chapter, it was observed quite often in Chapter 4 and the results presented here allow for a further understanding of the deformation and fracture associated with this boundary. Figure 5.42

shows a schematic of the proposed mechanism for twin boundary related failure. Extension and contraction twins were both observed to contribute to fracture in Chapter 4. These twins first nucleate to either accommodate c-axis tension or c-axis compression respectively. Therefore, the early stages of twin nucleation are beneficial for magnesium materials as they are deformation mechanisms which accommodate strain incompatibilities. However, once nucleated they act similarly to grain boundaries. It should be noted here that not all grain and twin boundaries cause strain localizations. However, when the orientation relationship is unfavorable, twins can cause strain concentrations. Dislocations pile up along the boundaries which increase the local strain in the vicinity of the boundary. When the boundaries are no longer strong enough to maintain compatibility fracture occurs.

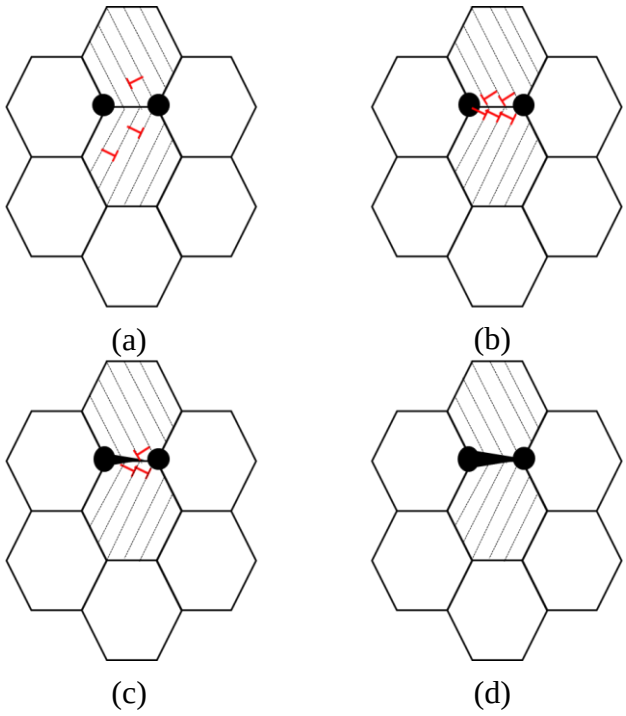

Figure 5.41: Schematic of grain boundary failure between two holes. (a) deformed state, (b) dislocation pile up at grain boundary, (c) initiation of grain boundary separation and (d) linkage of holes.

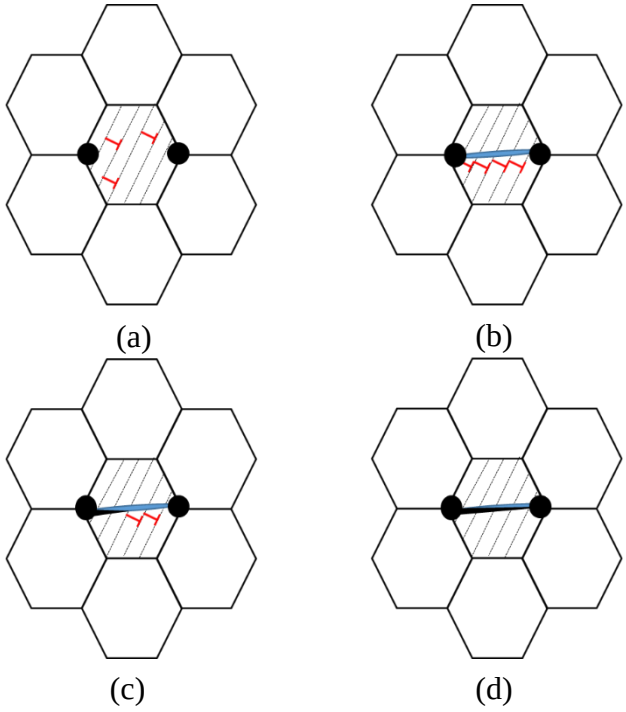

Figure 5.42: Schematic of twin boundary failure between two holes. (a) deformed state, (b) twin nucleation and dislocation pile up at boundary, (c) initiation of twin boundary separation and (d) linkage of holes.

5.11 Summary

The main conclusions drawn from the work presented in this chapter are summarized below:

- Although the samples investigated in this chapter had a stronger basal texture, the void fraction and void orientation did not show a significant impact on the void growth behavior. In addition, the amount of hole growth prior to fracture was relatively low compared to the samples tested in Chapter 4. The result suggests that the randomized texture adjacent to the holes in the samples presented in Chapter 4 lead to improved ductility.

- Strain localizations occurred along grain boundaries for all of the configurations tested. The strain concentrations associated with grain boundaries were observed to have a significant impact on the void growth behavior. Furthermore, grain boundary sliding was observed to make a significant contribution to the macroscopic strain.
- Section strains revealed the heterogeneous nature of deformation associated with twin and grain boundaries. In most cases the strain build up is contained within a small region adjacent to the boundary and the grain interiors experience very little deformation.
- The void fraction and void orientation did not show a correlation with the far field strain or local strain prior to fracture. Grain boundary fracture was the dominant fracture mechanism observed in the samples presented in this chapter. The grain size distribution was favorable to find a grain boundary in the ligament between the holes in all of the configurations tested.
- The maximum point strain prior to failure displayed a normal distribution with a slight skew when compared amongst all of the samples tested in this chapter, including samples free of holes. The average value of the distribution was 0.33. This result suggests that grain boundary associated failure occurs at a critical strain. The skew can be attributed to the rapid failure of the boundaries.
- A crystal plasticity based finite element approach has been used to understand the role of the various hardening parameters during the deformation of CP magnesium. The model was able to predict the location of the hot spots dominated by dislocation slip.

- A simple model for deformation-induced void linkage has been proposed based on the results from the crystal plasticity finite element simulation.

Chapter 6

Tomography Experiments: Linkage of the Results

6.1 Introduction

The results presented so far have indicated a thorough understanding of the mechanisms responsible for deformation and fracture of thin sheet magnesium. However, sheet materials used for industrial applications typically have a thicknesses on the mm scale and thus a larger number of grains through the thickness. The constraint due to the grains within the bulk of the material is quite different from that on the surface. In addition, fracture generally occurs within the bulk of materials. Therefore, two dimensional techniques must be complimented with three dimensional techniques in order to completely understand the fracture process (Nemcko and Wilkinson, 2013b). X-ray tomography has gained a lot of interest in materials science in the past several years as it allows for 3D information to be obtained within the bulk of a material. Tensile testing coupled with x-ray microtomography will be presented in this chapter. The intent is to study damage in magnesium, free of holes, in samples with a thickness of roughly 1 mm. The main objective of this work was to visualize the fracture process in 3D and apply the knowledge presented in the previous chapters to understand these processes. It is expected that grain and twin boundary failure will dominate in the materials tested here and therefore, it is of interest to observe the damage produced by these features in 3D. The majority of the fractography

will be presented in this chapter in order to link the results together and gain a further understanding of the fracture of magnesium.

6.2 Parameters and Measurements

The parameters and measurements used in this chapter are defined in this section. Several results from the previous chapters will be presented and the parameters reported in these cases remain the same from their respective chapters.

6.2.1 True Strain

The true strain has been obtained by analysis of the cross sectional data from the tomograms. A 2D analysis was carried out using CTAn analysis software to determine the minimum cross sectional area in the gage section at each deformation increment. From the assumption of constant volume the true strain is defined by:

$$\varepsilon = ln\left(\frac{A_0}{A}\right) \tag{6.1}$$

where A is the minimum cross section at a given stage of deformation and the 0 subscript refers to the undeformed state. The minimum section can be found with excellent precision in every deformation step and therefore, there is a negligible amount of error associated with the measurement used to calculate this parameter.

6.2.2 True Stress

The true stress-strain response has been reported to compare the various stages of fracture to the constitutive behavior of the material. The load data can been obtained from software that controls the material testing stage and the true stress is given by:

$$\sigma = \frac{F}{A} \tag{6.2}$$

where F is the load at which the test was stopped for the tomography scan.

6.2.3 Engineering Stress and Strain

The engineering stress strain response is used to determine the relationship between the fracture processes and the UTS of the material. As a result the following relationships may be used to relate the engineering and true values.

$$e = exp(\varepsilon) - 1 \tag{6.3a}$$

$$S = \frac{F}{A_0} \tag{6.3b}$$

where e is engineering strain and S is engineering stress.

6.2.4 Sphericity

Sphericity ψ, is a parameter that was defined by Wadell (1933), to describe the shape of rocks. This parameter will be used to evaluate the shape of voids in the work

presented. The sphericity of an object is defined as the ratio of the surface area of a sphere (with the same volume as the given object) to the surface area of the object:

$$\psi = \frac{\sqrt[3]{\pi}(6V)^{\frac{2}{3}}}{A_S} \tag{6.4}$$

where V and A_S are the object volume and surface area respectively.

6.3 Void Nucleation

Ductile fracture occurs by the nucleation, growth and linkage of microvoids. Void nucleation in alloys typically occurs by decohesion of the particle matrix interface or by particle cracking. However, this study was carried out on a pure metal. Up to this point the study has had a large focus on artificial holes to eliminate the stochastic nature of void nucleation. In this analysis void nucleation is examined in a material free of holes. The previous results suggest that the failure of interfaces associated with twins and grains are responsible for damage in the hole-free materials. The characteristics associated with these fracture mechanisms will be presented in 3D here. Therefore, several tests were carried out to determine the strain at which a significant amount of detectable voids were present in the gage section. The largest pixel size used during the analysis was 2.77 μm. In order to detect a void with reasonable certainty 3 adjacent pixels should be used to identify an object. Therefore, voids are considered detectable if they contain at least 3 pixels in each dimension. This corresponds to a void dimension of approximately 575 μm^3. Figure 6.1 shows the number of detectable voids as a function of true strain for several tests. The

results show that a significant number of detectable voids nucleate at strains between 0.05 and 0.15. In addition, the slope of the data sets are comparable suggesting that the rate of nucleation is similar in the tests examined.

Figure 6.2 shows the same data set with a fitting line to determine the nucleation strain and the rate at which these detectable voids nucleate. The zero values have been eliminated here to give a better representation of the nucleation process. The fitting line can be represented as:

$$N = A(\varepsilon - \varepsilon_{nucleation}) \tag{6.5}$$

where N is the number of detectable voids, A is a constant, ε is the true strain and $\varepsilon_{nucleation}$ is the nucleation strain of the detectable voids. The least squares fitting parameters from Figure 6.2 can be used to represent Equation 6.5 in the following form:

$$N = 742.79(\varepsilon - 0.105) \tag{6.6}$$

The nucleation strain is 0.105. During metal forming operations, materials are deformed at stresses between the yield stress and ultimate tensile stress (UTS). Significant void nucleation is typically detected in materials at strains greater than the strain at which the UTS occurs. Observation of the stress strain data in Figure 6.3 shows that the voids are detectable at strains lower than the strain at which the UTS occurs. In fact, voids of significant size have been detected at strains as low as 0.042. It should be noted that the analysis has been limited to detectable voids. Void nucleation is likely to occur at much

lower strains. The results suggest that voids are present within the material from the early stages of plastic deformation. A reasonable hypothesis is that the holes are associated with the failure of twin and grain boundaries. In the analysis to follow the tests will be focused on strain values larger than 0.105 to observe the evolution of the holes. The slope of the fitting line gives the nucleation rate which is 742.79 voids/unit of strain. The r squared value associated with the fitting curve is 0.811 suggesting that Equation 6.6 accounts for 81.1% of the variability in the data.

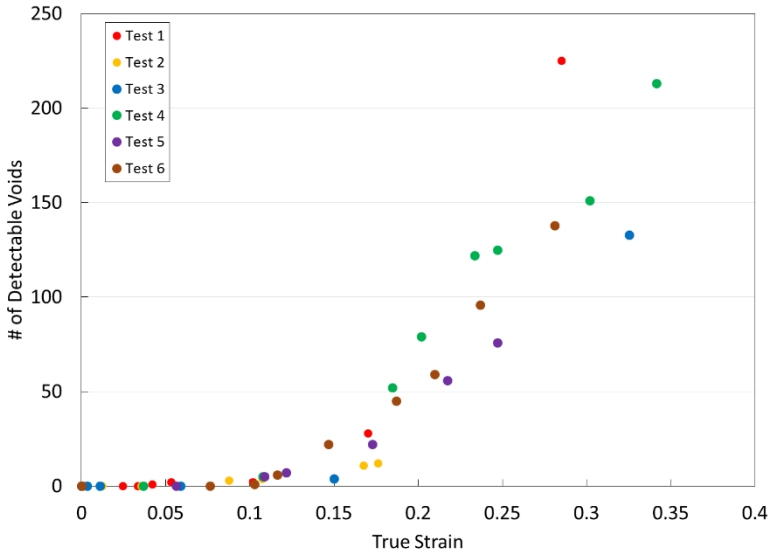

Figure 6.1: Number of detectable voids vs. true strain for several tomography tensile tests.

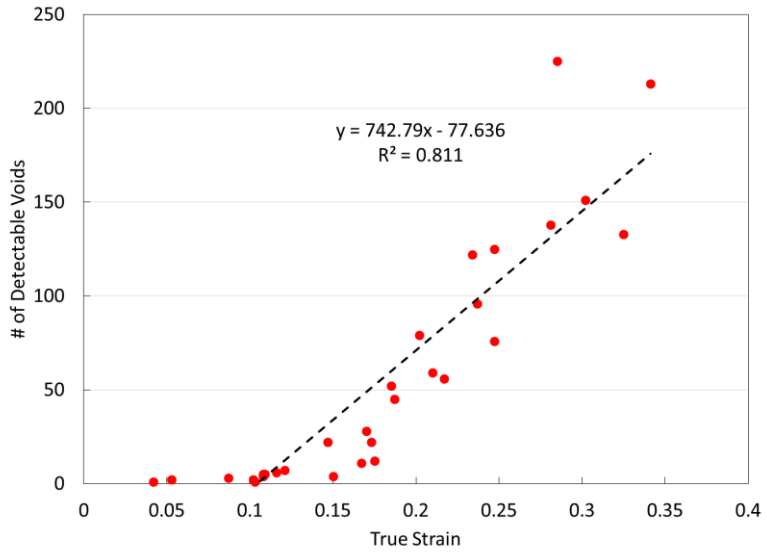

Figure 6.2: Number of detectable voids vs. true strain with least squares fitting parameters.

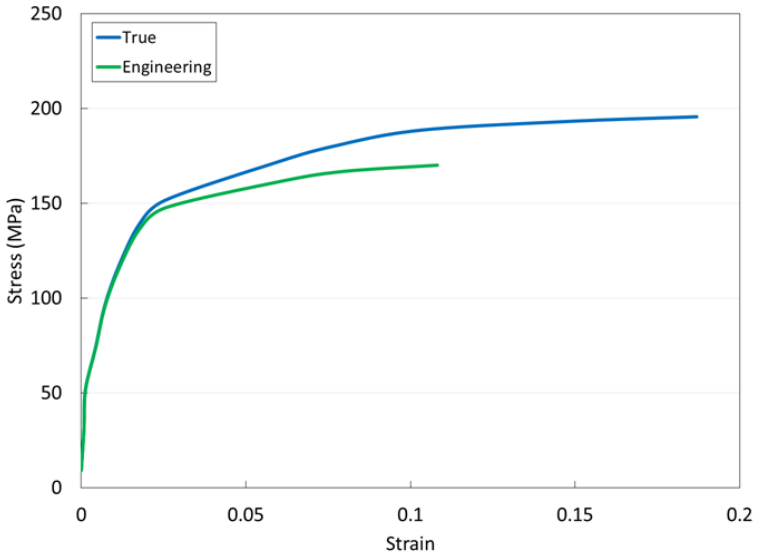

Figure 6.3: Engineering and True stress strain response representative of the materials tested in this chapter.

Figure 6.4 shows the 3D model of the gage section of a specimen at a true strain of 0.15. At this strain there is a significant amount of surface topography which can be

observed by the different shades of grey on the sample surface. The topography is due to the heterogeneous deformation of adjacent grains. As mentioned earlier, softer grains have the tendency to contract in the through thickness direction more than the harder orientations. The figure shows a magnified view of the largest void within the bulk of the material. This void gives a good representation of the shape and orientation of the voids within the gage section. Flat irregular shaped voids are present which tend to form on angles through the thickness. It should be noted that there are several smaller voids with these characteristics in the figure. These holes are likely associated with the failure of twin and grain boundaries; however, this idea will be examined in greater detail in the sections to follow.

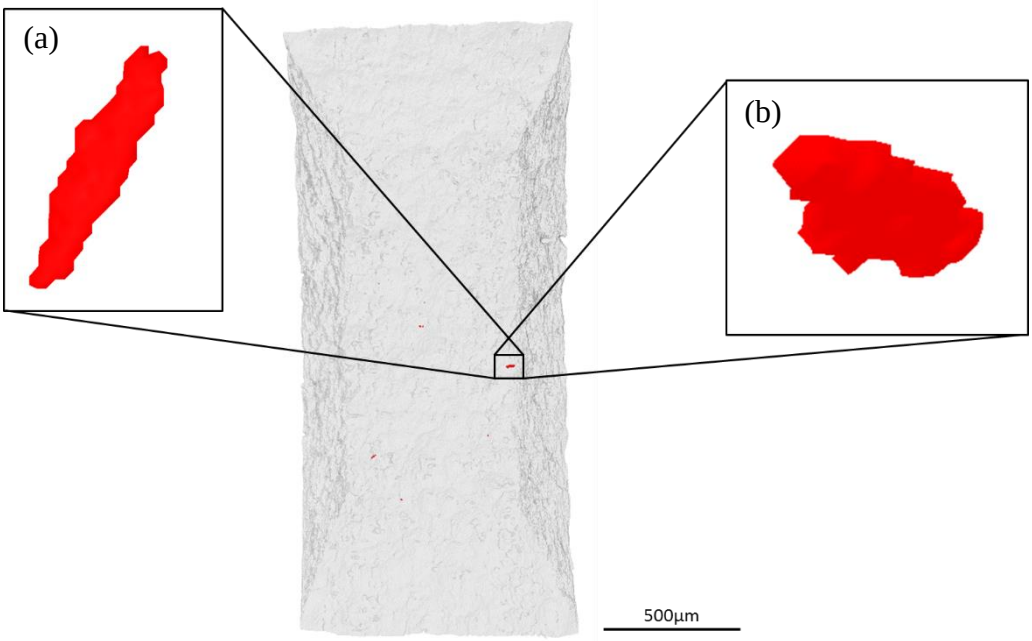

Figure 6.4: 3D model of the gage section of a tomography tensile sample at a true strain of 0.15 and magnified view of the largest void in the material (a) tensile axis out of page and (b) tensile axis vertical. The matrix is transparent grey, voids are red and the tensile axis is vertical.

6.4 Void Growth

Several recent studies have been carried out using x-ray tomography to track the growth of specific voids. Lecarme et al. (2014) studied the heterogeneous growth of voids in a titanium alloy. In this work the group developed an algorithm to identify and track individual holes at each strain increment. Figure 6.5 shows the normalized equivalent diameter as a function of true strain for the voids in the gage section. A modified Rice and Tracey model proposed by Huang (1991) was used to fit the results and is represented by the red solid line.

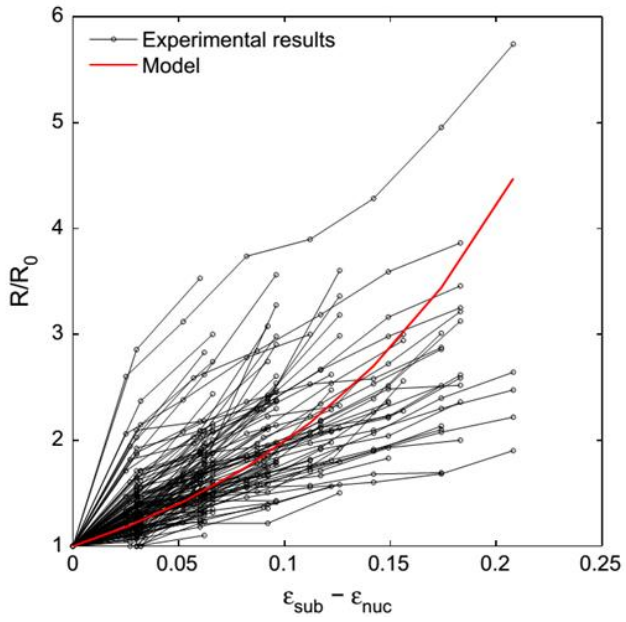

Figure 6.5: Normalized equivalent diameter vs. strain for holes in the gage section of a titanium alloy (Lecarme et al. 2014).

The fitting line gives a good approximation of the average growth value; however, there is still a significant variation in the data. In addition, the Rice and Tracey approach assumes

spherical holes. The volume of each cavity in this case is assumed to be a sphere and an equivalent radius is used to represent the void dimension. It was established that the holes observed in the magnesium materials tested had flat irregular characteristics. Figure 6.6 shows the 3D model of a group of holes growing in the gage section at several values of true strain. All of the holes in this region have these flat irregular characteristics. As a result, the distribution of the sphericity of the 20 largest holes has been investigated to determine whether the modified Rice and Tracey approach is valid for the magnesium materials studied. The 20 largest holes have been selected for the population of interest as larger holes have a higher probability of contributing to the final fracture.

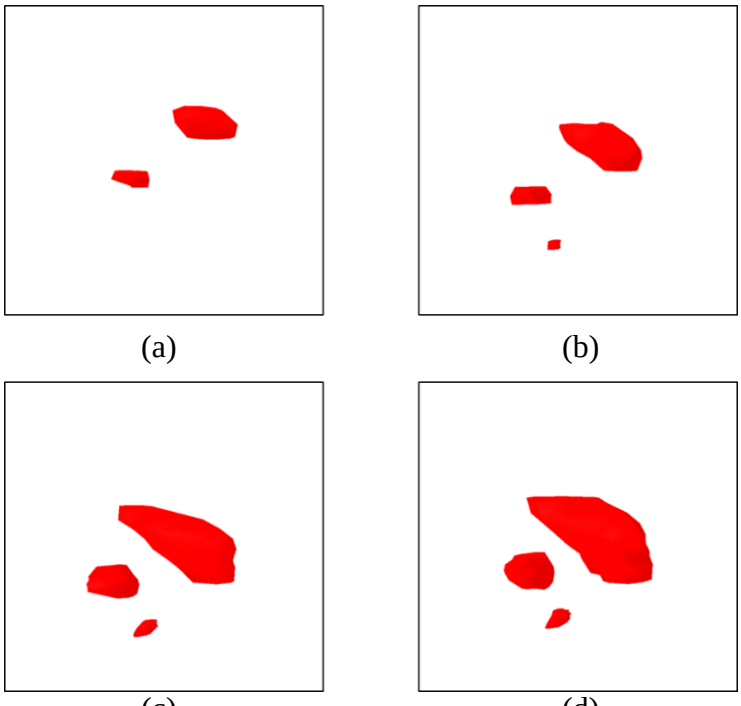

Figure 6.6: 3D model of several holes at true strain values of (a) 0.185, (b) 0.202, (c) 0.234 and (d) 0.247. The voids are red and the tensile axis is vertical.

Figure 6.7 and Figure 6.8 show the distribution of the sphericity for the 20 largest holes at various increments of deformation for two samples. These samples will be referred to as sample 1 and sample 2 respectively, for the discussion to follow. In sample 1 the mean sphericity decreases from 0.55 to 0.38 as the true strain is increased from 0.107 to 0.303. The result suggests that as the strain is increased the holes become less spherical in shape. In addition, the distribution of the sphericity is randomly distributed for all values of strain. A similar result is observed in sample 2. The mean sphericity decreases from 0.61 to 0.49 as the true strain is increased from 0.185 to 0.302. In order to visualize what shapes these values of sphericity correspond to, the voids have been approximated by an ellipsoid with diameters a, b and c, with the condition $a = b \neq c$. The sphericity is plotted as a function of the c/a aspect ratio and shown in Figure 6.9. The sphericity values obtained from the samples investigated range from 0.61 to 0.38, corresponding to flat "pizza shaped" voids with aspect ratios between 1/5 and 1/10, or long "cigar shaped" voids with aspect ratios between 9 and 37. The shapes which best represent the voids observed in the samples are rather irregular. Therefore, representation of the void dimension by an equivalent radius is not sufficient for the magnesium materials investigated here.

Lhuissier et al. (2012) studied damage in an AZ31 magnesium alloy deformed at high temperatures using X-ray tomography. They observed the growth of 60 selected voids and plotted the volume of each cavity as a function of strain as shown in Figure 6.10. The volume displayed an exponential relationship with the strain and a relatively simple model was adopted to describe the observation.

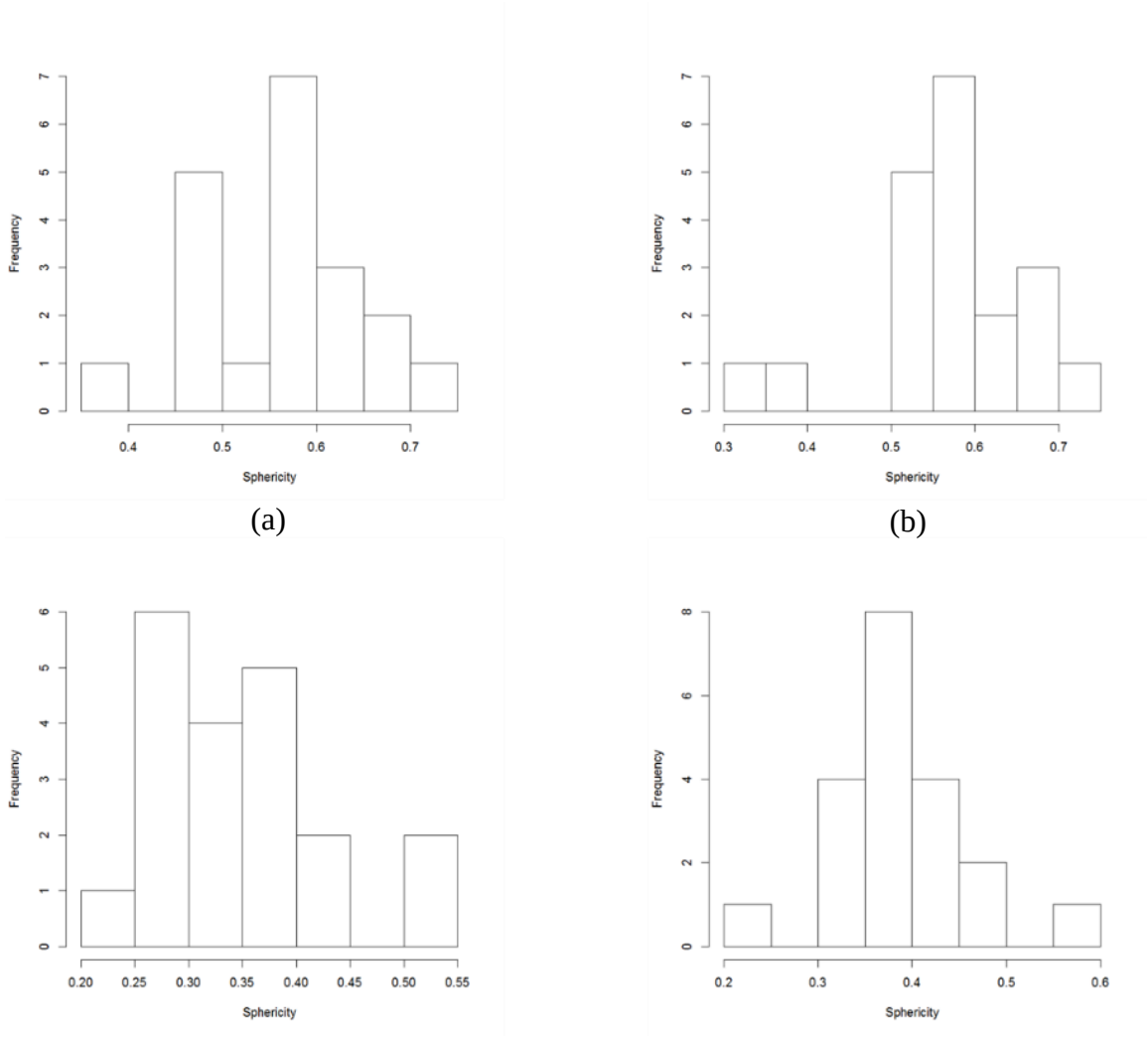

Figure 6.7: Histogram of the sphericity of the 20 largest holes in sample 1 at true strain values of (a) 0.107, (b) 0.133, (c) 0.271 and (d) 0.303.

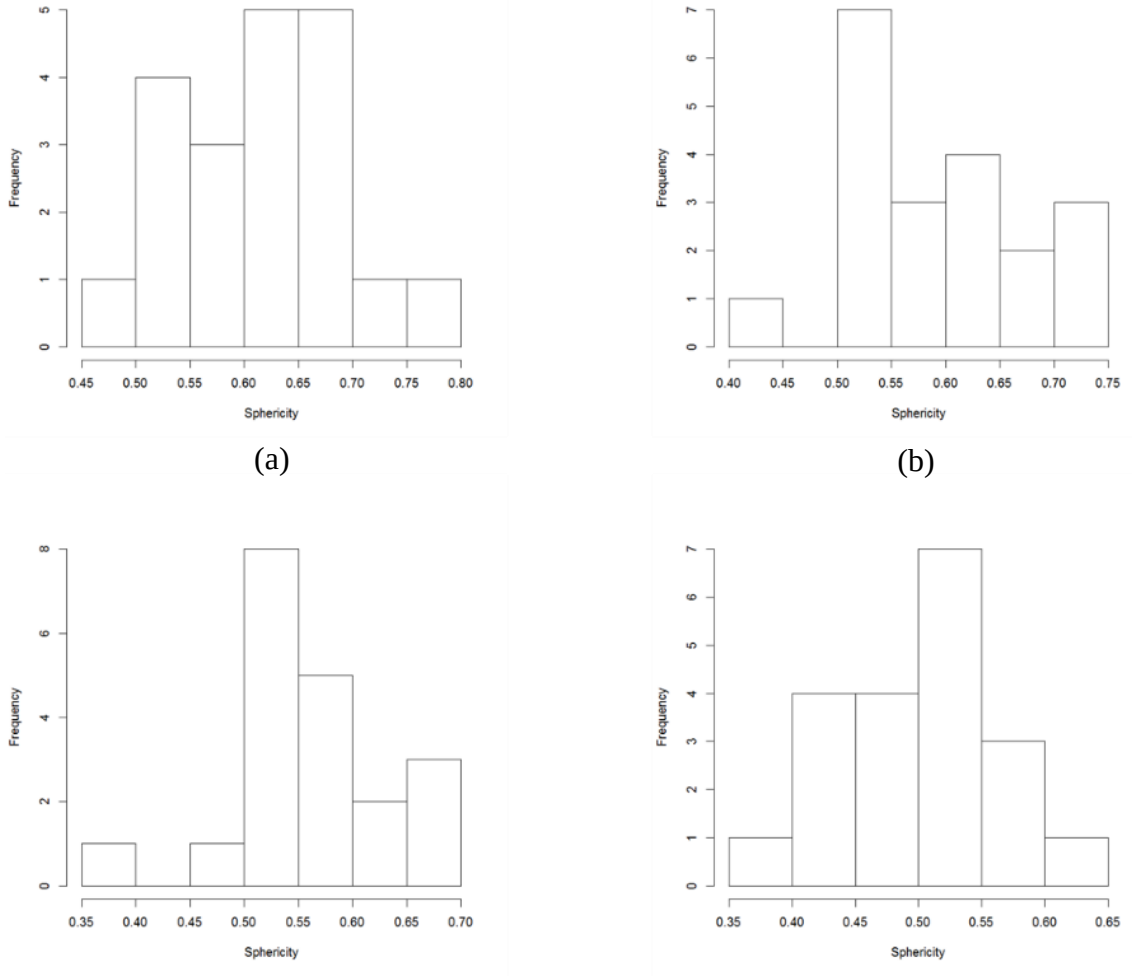

(a) (b)

(c) (d)

Figure 6.8: Histogram of the sphericity of the 20 largest holes in sample 2 at true strain values of (a) 0.185, (b) 0.202, (c) 0.247 and (d) 0.302.

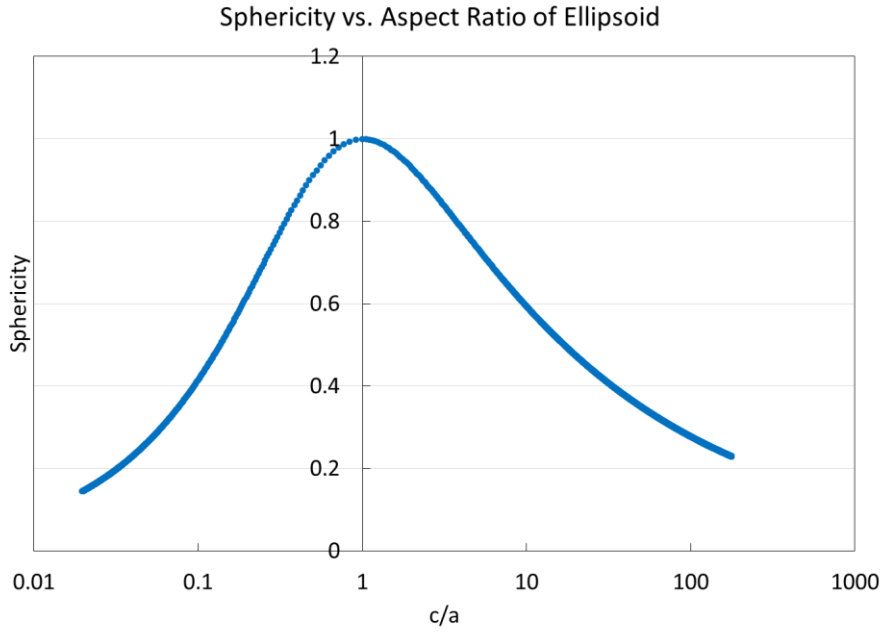

Figure 6.9: Sphericity vs. aspect ratio of an ellipsoid.

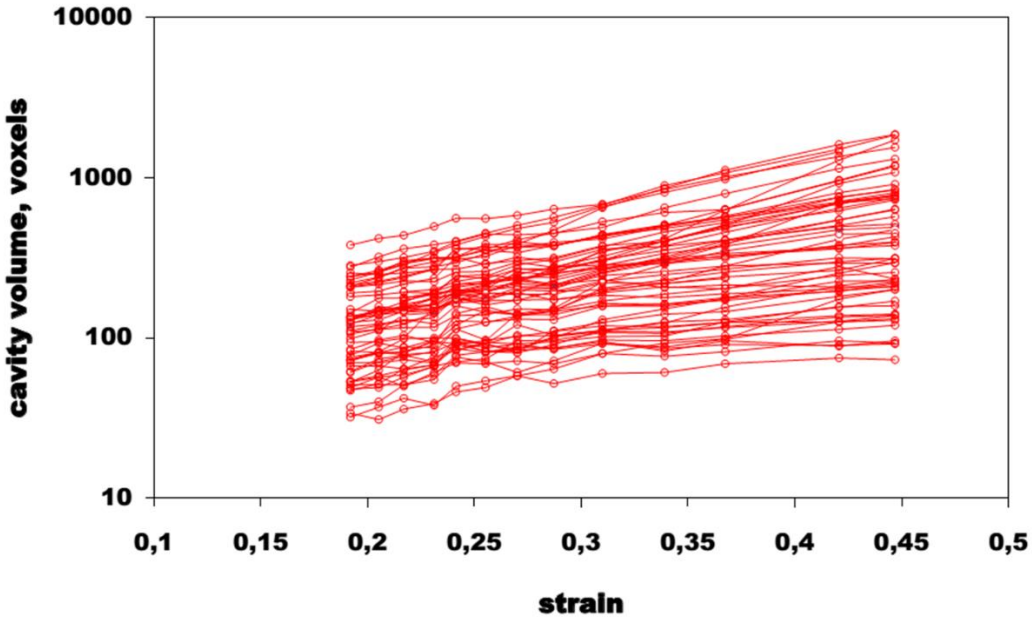

Figure 6.10: Cavity volume vs. strain for 60 selected voids in AZ31 magnesium alloy (Lhuissier et al., 2012).

Pilling and Ridley (1986) approximated the volumetric growth of a cavity by:

$$\frac{dV}{d\varepsilon} = \eta V \tag{6.7}$$

where V is the void volume and η is a void growth parameter. Rearrangement and integration of the equation leads to the following:

$$V = V_0 exp(\eta\varepsilon) \tag{6.8}$$

The relationship fit the average value well; however, there is still a reasonable amount of variation in the data. Both of the models used in the work by Lecarme et al. (2014) and Lhuissier et al. (2012) predicted the average void growth behavior well. Based on the examination of sphericity presented above it clearly makes more sense to describe the growth as a volume rather than an equivalent radius. For this reason the simple model proposed by Pilling and Ridley (1986) (Equation 6.8) will be used to understand void growth in the magnesium materials investigated in this work. A slight modification has been made to the way strain is represented and is given by:

$$V = V_0 exp[\eta(\varepsilon - \varepsilon_{nucleation})] \qquad \varepsilon \geq \varepsilon_{nucleation} \tag{6.9}$$

where $\varepsilon_{nucleation}$ is 0.105 from Section 6.3.

The original model (Equation 6.8) assumes that voids pre-exist in the material in the undeformed state with volume V_0. This may be useful for cast materials; however, the modified representation given by Equation 6.9 states that voids of volume V_0 are present

at the nucleation strain. Figure 6.11 shows the volume vs. true strain for the 20 largest holes in one of the magnesium materials tested in this study. The data has been fit to the model using the least squares method and is shown by the black dashed line in the figure. The fitting parameters are given in Table 6.1.

Table 6.1: Fitting parameters according to model.

Parameter	η	V_0 (μm^3)	$\varepsilon_{nucleation}$
Value	12.69	5000.1	0.105

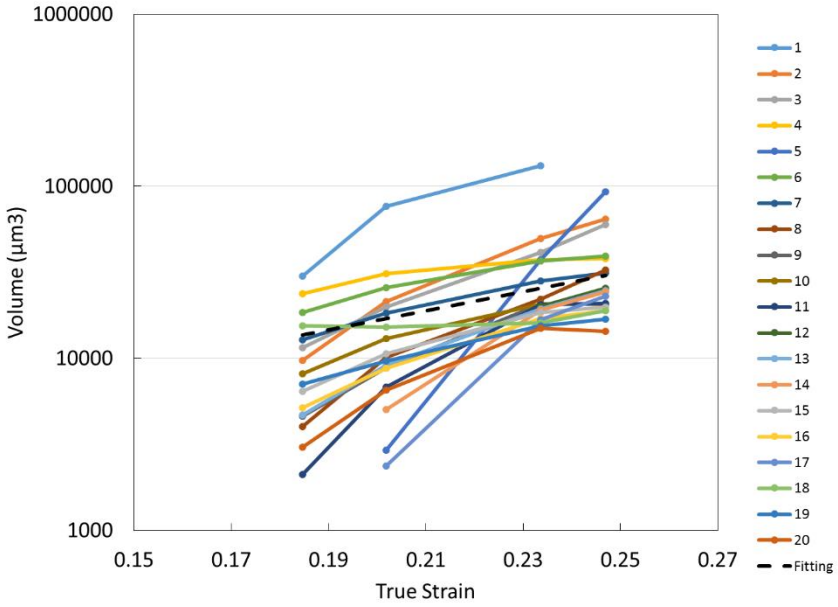

Figure 6.11: Volume vs. true strain for the 20 largest voids in a magnesium tensile sample.

The model suggests that holes are present in the material at the nucleation strain with a volume of 5000.1 μm^3 and the void growth parameter is 12.69. On average the majority of the holes follow the slope of the fitting curve; however, there are several holes which grow

much more rapidly. This is a relatively large void growth parameter compared to values documented in the literature (Pilling and Ridley, 1986). The growth parameter reported by Lhuissier et al. (2012) for AZ31 magnesium alloy was roughly 4.5. However, the tests were carried out at high temperatures where dislocation slip plays a much more active role in the deformation. The result suggests that once nucleated the holes in the magnesium samples examined in this work grow rapidly. This gives a good explanation as to why the tests were difficult to stop at increments close to failure.

The average growth value from the data in Figure 6.11 was compared to the fitting curve to determine how well the model predicts the average growth value and the results are shown in Figure 6.12.

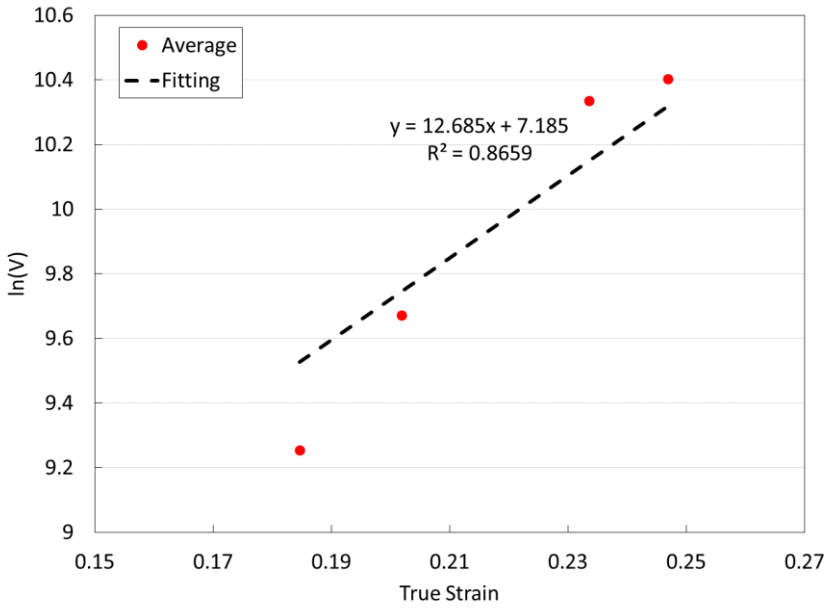

Figure 6.12: lnV vs. true strain and linear regression to determine the coefficient of determination with respect to the average void growth value of the 20 largest holes.

Equation 8 has been rearranged in the form

$$ln\, V = ln\, V_0 + \eta\varepsilon - \eta\varepsilon_{nucleation} \tag{6.10}$$

in order to determine the coefficient of determination. The r squared value is 0.8659, therefore, the fitting parameters determined in Table 6.1 account for 86.6% of the variability in the data.

Figure 6.13 shows the growth of the largest cavity in one of the samples tested. This void was first observed at a strain of 0.185 and the shape of the void was rather flat and irregular. As the deformation proceeded the hole showed rapid growth in a preferential direction. It has been assumed that the failure of grain and twin boundaries is responsible for void nucleation and crack propagation. The result suggests that once nucleated, the crack path is determined by the orientation of the adjacent boundaries. Not only does the crystallographic orientation play a role but also the orientation of the boundary with respect to the tensile axis. The propagation of cracks along preferentially oriented boundaries occurs very rapidly.

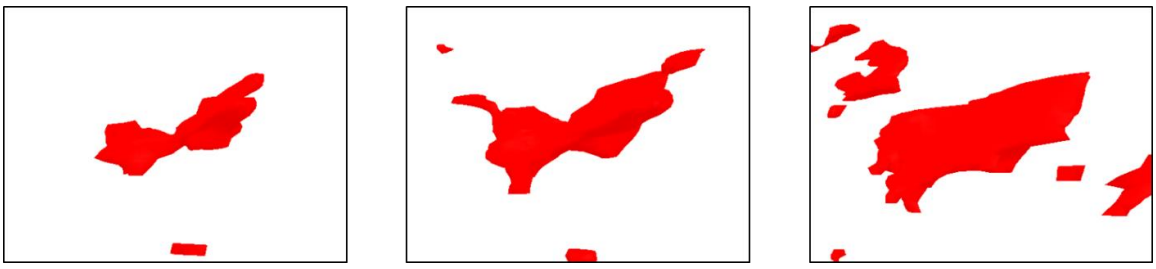

(a) (b) (c)

Figure 6.13: Evolution of the largest void at true strain values of (a) 0.185, (b) 0.202 and (c) 0.234. The void is red and the tensile axis is vertical.

Figure 6.14 shows the distribution and orientation of the holes at a strain increment prior to fracture with respect to the tensile sample. This distribution was observed in all of the cases studied. At strains close to the failure strain the voids have flat irregular characteristics with the major axis oriented at an angle with respect to the through thickness direction. Therefore, preferential growth of the holes is favored through the thickness. The sheet has a rolled texture. As a consequence, the direction of preferential growth is likely related to the c-axis. This axis requires the activation of twinning or <c+a> slip for strain accommodation. The results confirm that there is a strong relationship between the crystallographic orientation and the preferential direction of void growth. This conclusion will be assessed again in the Section 6.5.

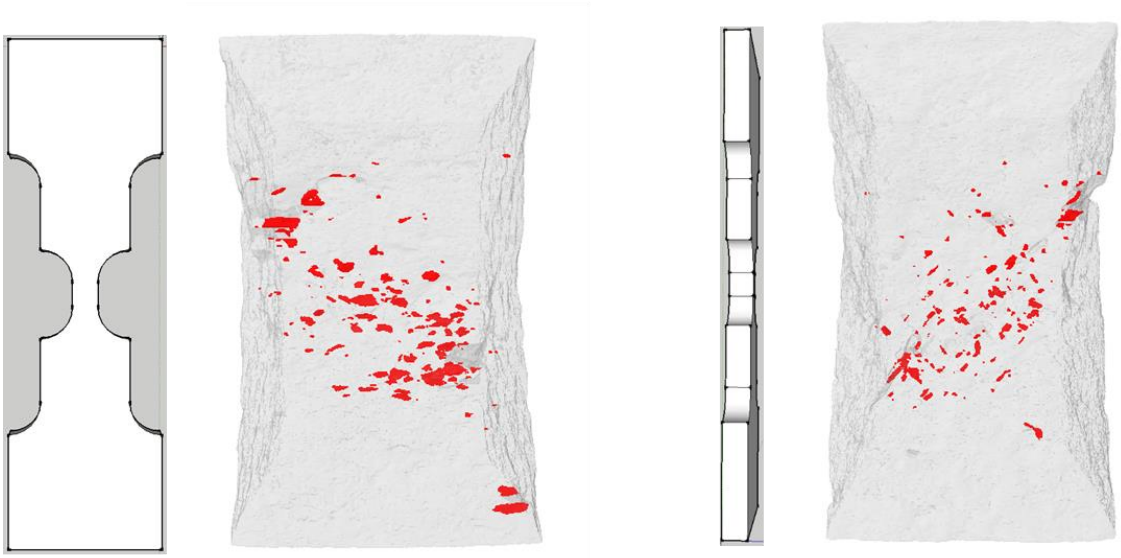

Figure 6.14: Distribution and orientation of the holes at a true strain of 0.247 at different angles of view (a) front view of the sample and (b) side view of the sample. The matrix is transparent grey, voids are red and tensile axis is vertical.

6.5 Void Linkage and Fracture

The final process during fracture involves the linkage of voids. There is an extensive amount of work that has been done to study this phenomenon in FCC structural materials; however, there are very few studies on void linkage in HCP materials. It has been established that once nucleated the voids show rapid growth along preferentially oriented boundaries. Figure 6.15 shows the linkage of two irregularly shaped holes. Reference numbers were assigned to the two holes that link in Figure 6.15(a). The linkage process does not appear to occur by a shear or internal necking type process. In Chapter 4 it was reported that the linkage mechanisms observed consisted of internal necking, shear fracture and failure associated with boundaries. The irregular characteristics of the linkage suggest that it is triggered by the failure of boundaries. In addition, the preferential growth of the void is illustrated. The linkage mechanism is qualitatively different from what has been observed in FCC materials.

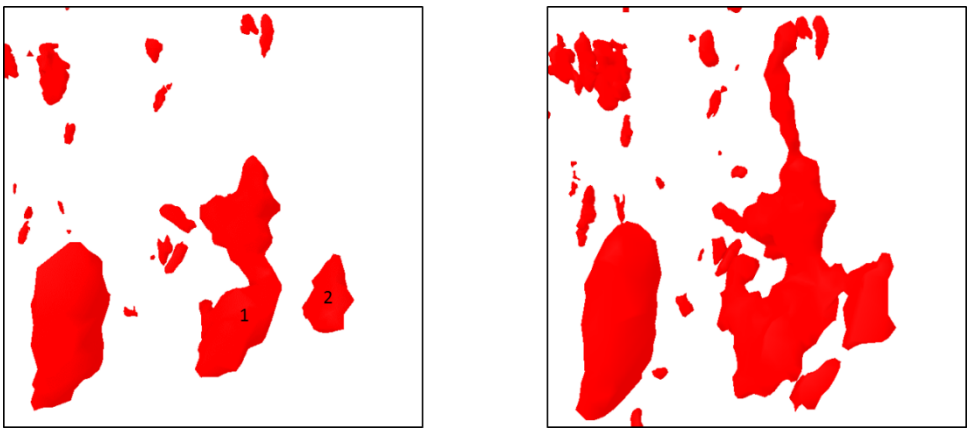

(a) (b)

Figure 6.15: 3D model (a) before and (b) after the linkage of holes 1 and 2. The voids are red and the tensile axis is vertical.

The final fracture of the magnesium samples examined occurs by a macroscopic shearing process (Nemcko and Wilkinson, 2013a). Figure 6.16 shows the damage accumulation and final fracture of the gage section in a magnesium tensile sample. The voids are shown in red and the matrix is represented in transparent grey. Intermediate shades of grey represent surface topography. At a strain of 0.185, the development of a shear crack has initiated on the surface. This region has been identified with a green circle in the figure. Voids are observed in the region adjacent to the boundary which have not yet connected to the surface. At a strain of 0.234 the void links to the sample surface. This is the largest void within the sample and the final fracture occurs over a small increment of deformation as the strain is increased above 0.234. The final fracture occurs at an angle of roughly 45° which corresponds to the angle of maximum shear in a tensile test. This type of fracture is consistent amongst all of the samples tested. As mentioned earlier there is a relationship between the preferential growth and the crystallographic orientation. Therefore, it is not surprising that all of the samples fractured at an angle with respect to the through thickness direction. Figure 6.17 shows the orientation of the fracture surface with respect to the tensile sample geometry (sample reference system). The angle of the fracture is roughly 50° to the normal of the tensile axis.

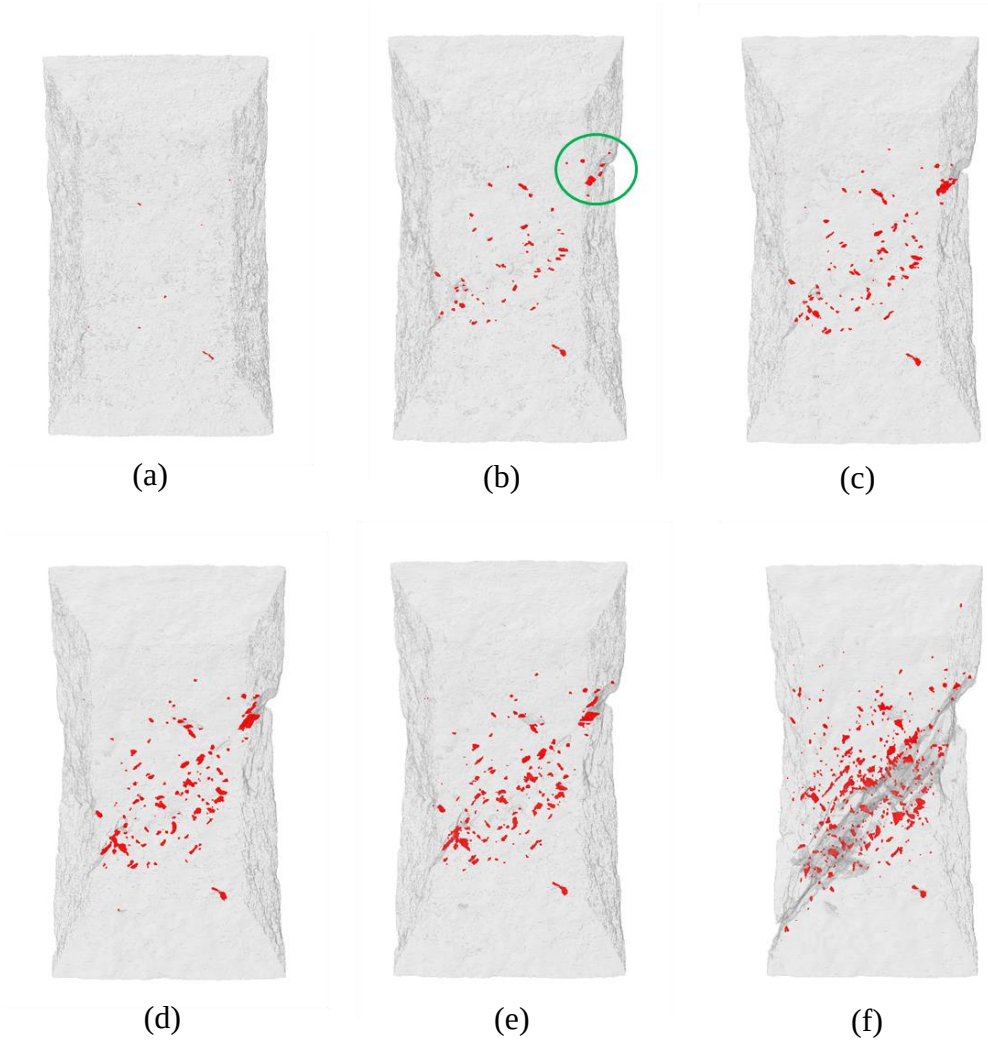

Figure 6.16: 3D model of the gage section at true strain values of (a) 0.107, (b) 0.185, (c) 0.202, (d) 0.234, (e) 0.247 and (f) fracture. The tensile axis is vertical.

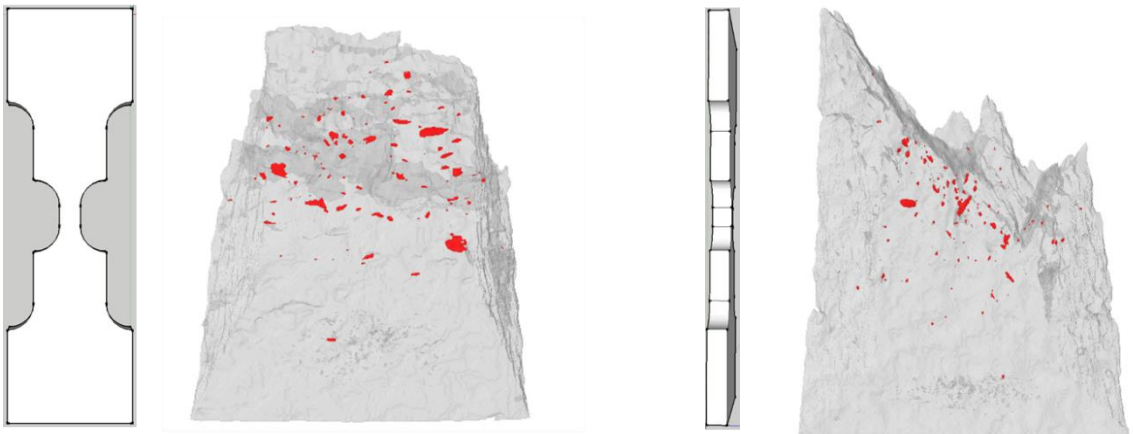

(a) (b)

Figure 6.17: 3D model of fracture surface at (a) front view and (b) side view with respect to the tensile sample. The matrix is transparent grey, voids embedded in the matrix are red and the tensile axis is vertical.

6.6 Fracture Characteristics and Comparison to 2D Experiments

The nucleation, growth and linkage of voids in magnesium has been studied using x-ray microtomography. This section will focus on the fracture characteristics and the results will be compared with the surface observations presented in the earlier chapters to gain a more complete understanding of the fracture of magnesium. Up to this point it has been assumed that twin and grain boundary failure are the dominant fracture mechanisms in the samples tested in this chapter. In order to confirm this hypothesis, the tomography samples were studied under an optical microscope to observe the microstructural features contributing to damage on the surface. Figure 6.18 shows an image of the gage section of a sample prior to fracture. Twins are observed throughout the microstructure and there is a great deal of surface roughening caused by the sliding of grain boundaries. Several cracks have developed in the regions that are consequently out of focus. The green and red arrows

show damage on the surface which are associated with twin and grain boundary failure respectively. Twin and grain boundary failure were the dominant fracture mechanisms observed on the sample surface. Although these are surface observations the result confirms the hypothesis made earlier that twin and grain boundary failure are responsible for the damage. The material under investigation is a commercial purity metal and void nucleation typically occurs at microstructural inhomogenieties. Twin and grain boundaries serve as these sites.

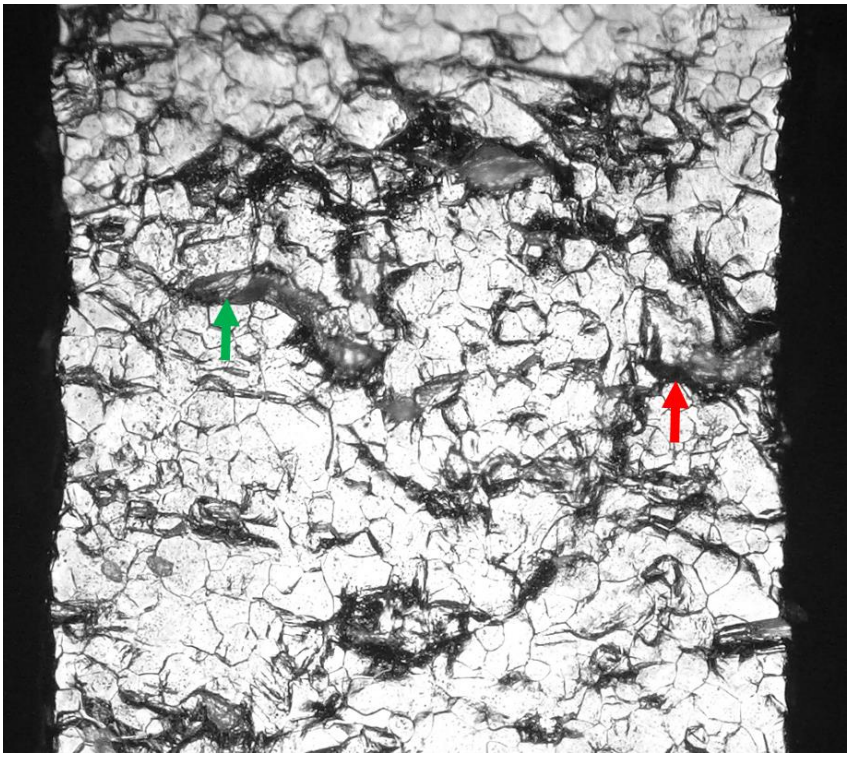

Figure 6.18: Optical microscope image of the gage section of a tomography sample prior to fracture.

Figure 6.19 shows a fracture surface that has been stitched together from a series of images in order to view the whole surface and resolve most of the details of interest. Two main features are observed on the fracture surface. One consists of a faceted surface which tends to align preferentially with the sample geometry, the other is a rather irregular feature. The magnified view shows the structure of the surface inside one of the larger voids observed. Similar to the macroscopic observations, striations are observed on a smaller scale inside of the depression.

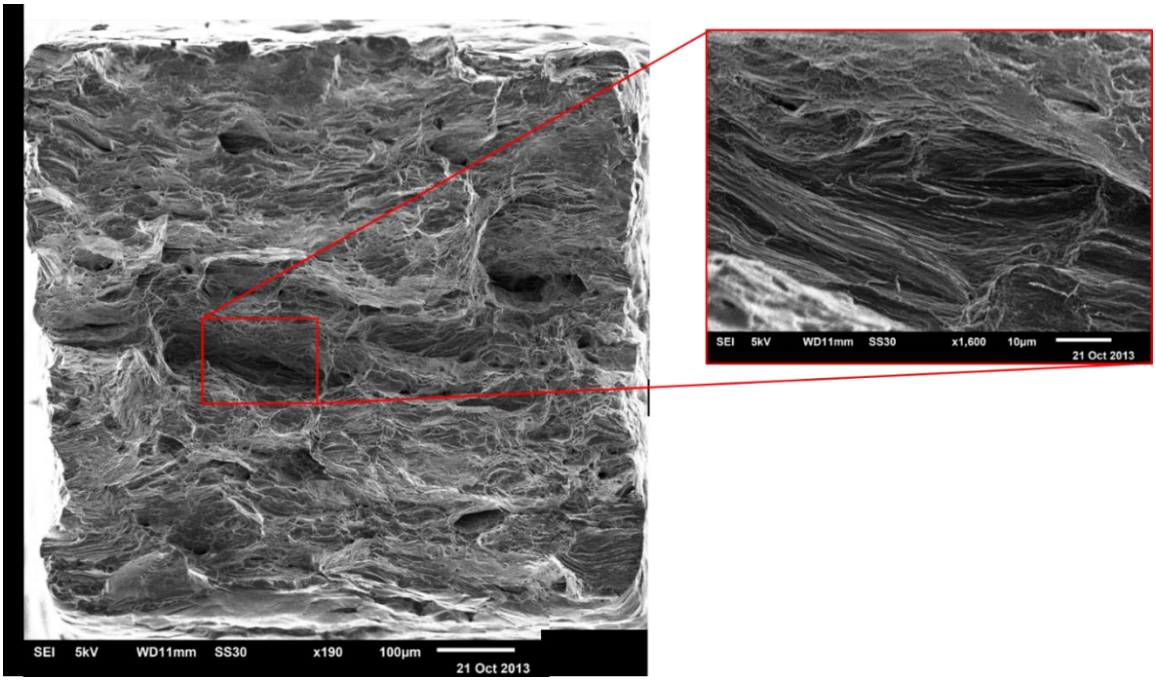

Figure 6.19: Fracture surface of tomography sample and magnified view showing the faceted characteristics.

Figure 6.20 shows the fracture surface which has been stitched together with a magnified view illustrating the second irregular feature observed. The feature does not seem to have any relationship with the sample geometry or crystallographic orientation and

occurs along what is observed to be a defined boundary. The surface inside of this feature is relatively smooth and several facets are observed. There are two contributions to the failure of boundaries; strain localizations associated with the geometrical orientation and strain localizations associated with the local crystallographic orientation. The faceted boundaries which tend to show an orientation dependence are likely a combination of both; however, the irregular boundaries are dominated by the local crystallographic orientation. Nevertheless, the two features described have been observed on all of the samples tested, including the samples examined in the previous chapters. Furthermore, the features described above are consistent throughout the entire sample suggesting that the fracture mechanisms observed on the sample surface are also responsible for damage within the bulk of the material.

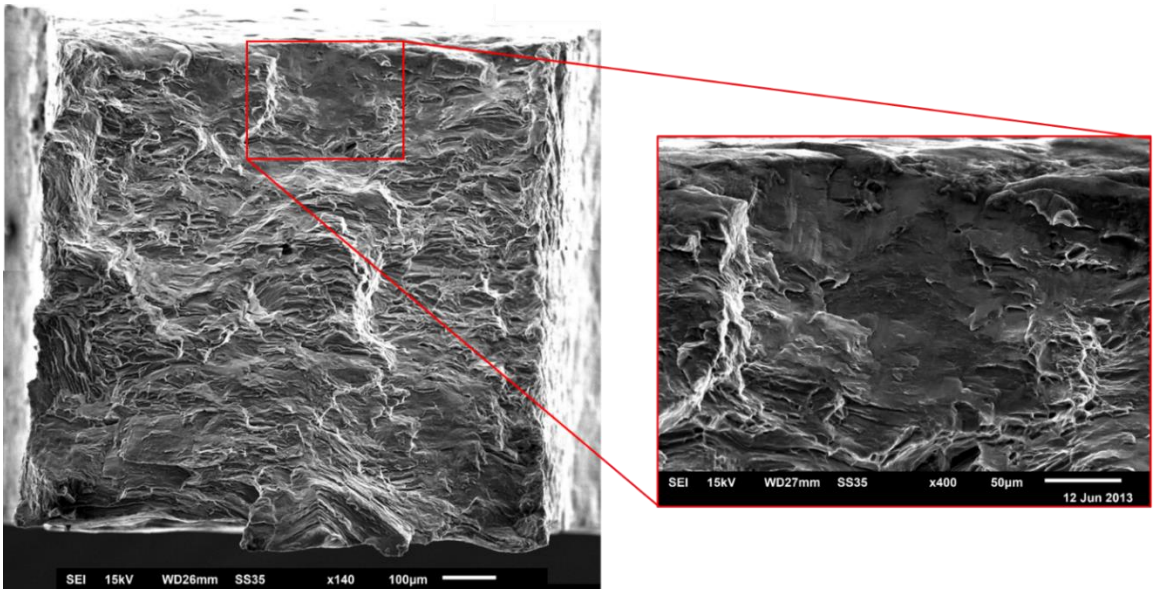

Figure 6.20: Fracture surface of tomography sample and magnified view showing the irregular characteristics.

Figure 6.21 shows the deformation history of one of the samples analyzed using the crystal plasticity finite element approach. At a strain of 0.02 there is a large twin visible. The twin was adjacent to a grain boundary which showed a strong localization of tensile strain. Once the failure of the grain boundary initiated the crack propagated along the twin boundary and the fracture surface characteristics associated with the twin boundary are shown in the figure. The same faceted characteristics described above are observed where the twin boundary failed. Furthermore, the optical microscope image of the sample at fracture shows shear characteristics associated with the failure. As a result, a tomography scan of the fractured sample was carried out to examine this observation in greater detail. An advantage to using tomography in fracture surface analysis is that the model can be rotated freely and the internal structure can be evaluated through virtual sectioning. Figure 6.22 shows the 3D model of the bottom half of the sample and a tomogram which reveals the shear nature of the fracture. The plane in which the tomogram was obtained is defined by the red line in the figure. The failure of the twin boundary is associated with shear fracture which occurs through thickness at an angle of approximately 48° with respect to the normal of the tensile axis.

The fracture characteristics described above have also been observed in the materials containing holes tested in the previous chapters. The addition of tomography to the fracture surface analysis reveals information that is not obvious from the surface characterization techniques.

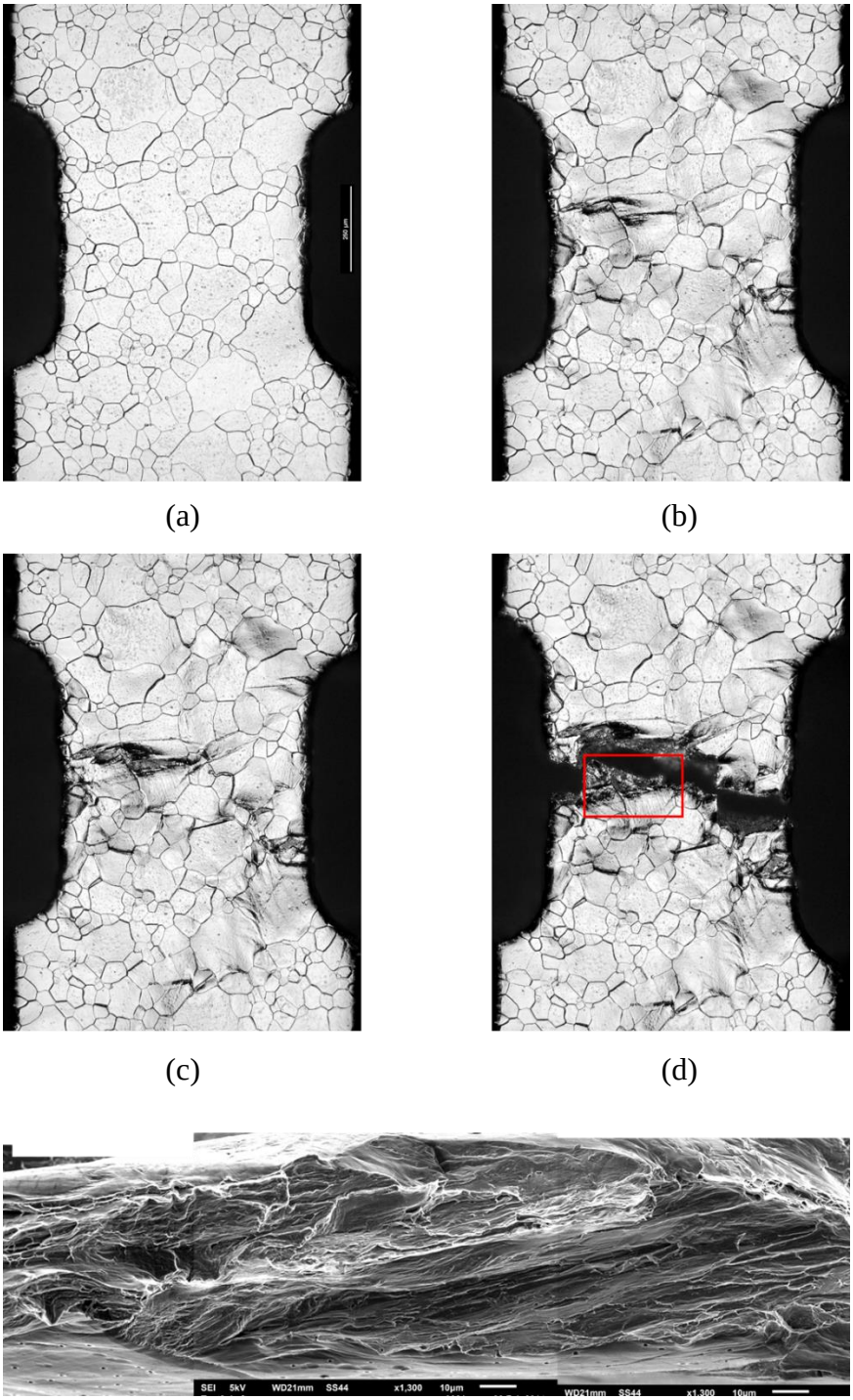

Figure 6.21: Deformation and fracture of hole free thin foil material at far field strain values of (a) 0.000, (b) 0.020, (c) 0.022, (d) fracture and (e) corresponding fracture surface of the area highlighted by the red box.

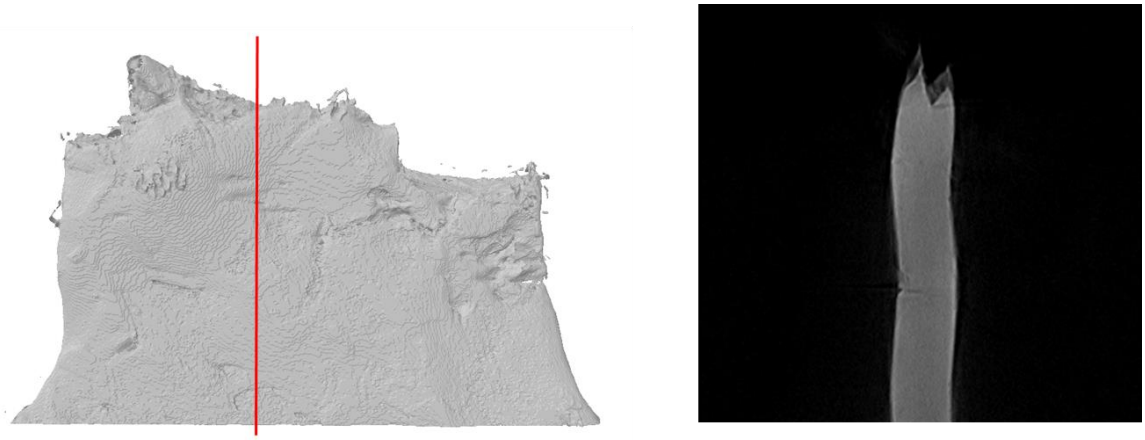

(a) (b)

Figure 6.22: (a) 3D model of the bottom half of the fractured sample and (b) corresponding tomogram slice obtained along red plane.

Figure 6.23 shows a fractured sample tested with holes perpendicular to the tensile axis and the corresponding region on the fracture surface. The shark fin type characteristic is not fully revealed using the surface characterization techniques shown in Figure 6.23(a). A slice was defined by the yellow plane and the tomogram was observed shown in Figure 6.23(b). The tomogram reveals the shear nature associated with the fracture. Shear characteristics are indicated by the fracture surface and the irregular shape of the hole, which initially ran straight through the sample thickness. EBSD analysis reveals that the crack deviated along a twin plane on the sample surface. The two holes contained within this shark fin feature were observed to link on the opposite surface, i.e the one which was not observed during the ESEM experiments. The result shows the complex nature of the fracture observed in the magnesium materials. Furthermore, the SEM fracture surface contains the faceted characteristics and several irregular features described above

suggesting that the fracture mechanisms are consistent through all of the samples investigated in this work.

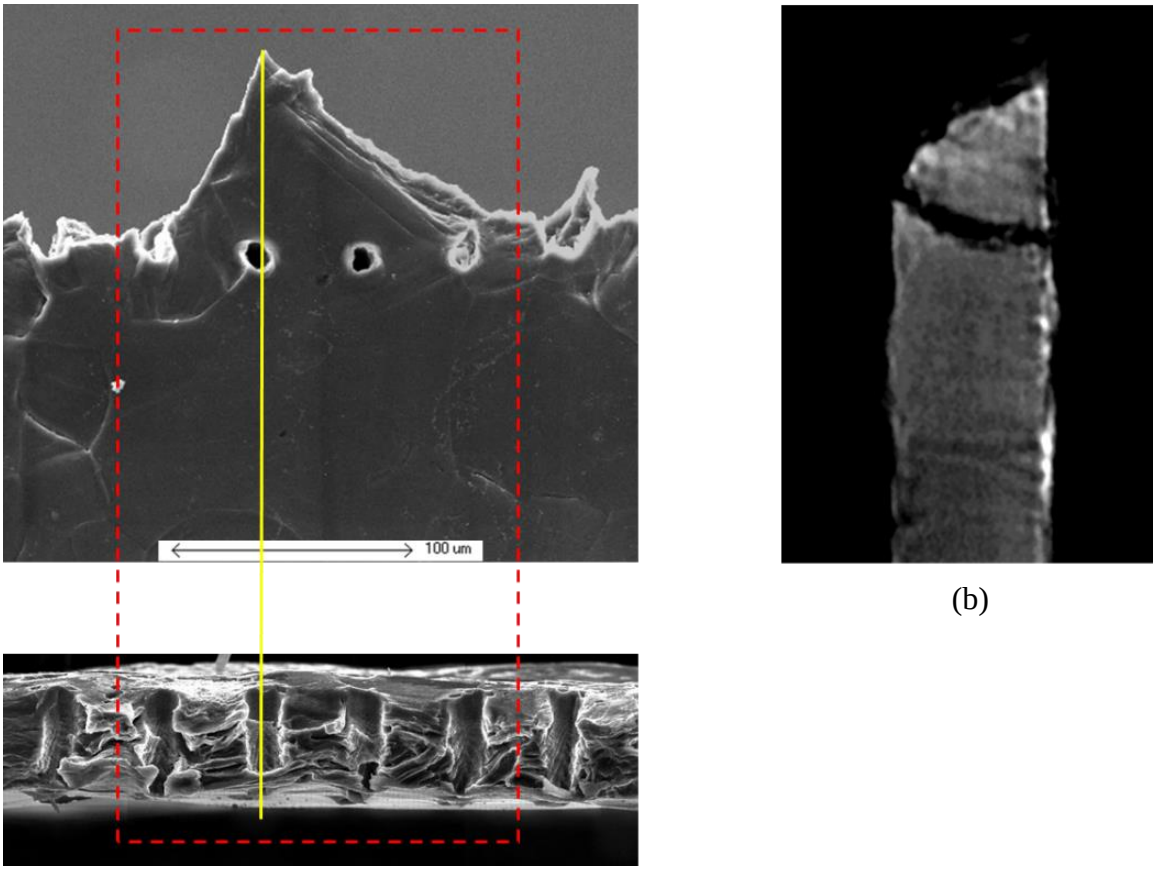

(a) (b)

Figure 6.23: (a) Fractured material with holes perpendicular to the tensile axis showing the corresponding region on the fracture surface and (b) sectioned tomogram slice defined by the yellow plane.

The shear characteristics observed through the thickness of the sample are not as common in the ESEM samples examined containing larger void orientation angles. Figure 6.24 shows the tomogram slices of a sample with a void orientation angle of 30°. The front, top and side slices are defined by the green, red and blue planes respectively. It was

established that the magnesium materials have a tendency to shear through the thickness. This type of sample geometry forces the holes to shear on an angle in relation to the width of the sample. The sharp features between the ligaments of the holes suggest that the mode of failure was dominated by shear of the holes. Observation of the tomogram showing the side view does not reveal a significant amount of shear through the thickness.

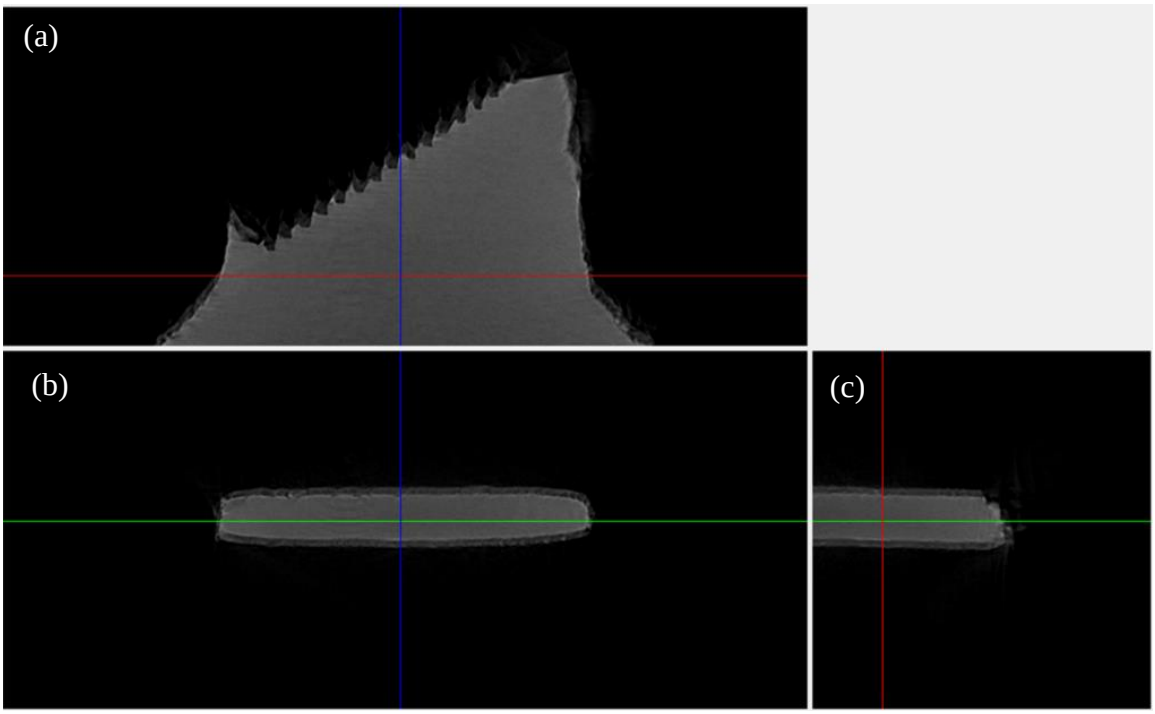

Figure 6.24: Tomogram slices of the (a) front, (b) top and (c) side views of a sample with a void orientation angle of 30°.

Figure 6.25 shows the fracture surfaces of a sample with holes perpendicular to the tensile axis as well as one with holes with a void orientation angle of 30°. For the sample with the holes running perpendicular to the tensile axis the facets run perpendicular to the

through thickness direction. This observation is consistent with what has been presented earlier in this section.

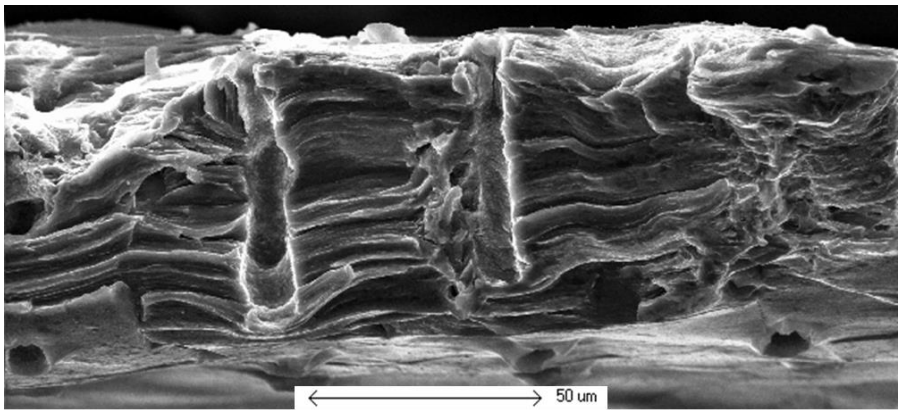

(a)

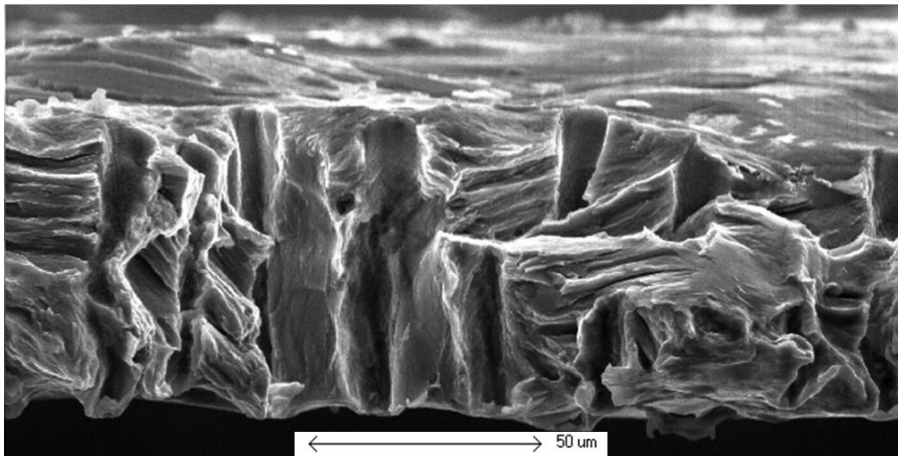

(b)

Figure 6.25: Fracture surface comparison of (a) holes perpendicular to the tensile axis and (b) holes with void orientation angle of 30°.

The fracture surface of the sample with the void orientation angle of 30° is not so straightforward. In the samples with larger void orientation angles the shear component induces the voids to shear in the width direction. The results presented in this section show that the fracture tends to favor shear in the through thickness direction. As a result there is

a mixed mode of fracture which is observed on this fracture surface. One ligament shows shear fracture throughout the entire thickness of the sample. The ligament adjacent to this shows shear through approximately half of the sample and then the faceted structure on the other half of the thickness. Two holes were sheared severely through the thickness. The results confirm that there is a competition of fracture mechanisms based on the sample geometry and crystallographic texture.

Void nucleation, growth and linkage have been observed in 3D using an x-ray microtomography system. The nucleation of large irregular shaped voids was observed to occur in the early stages of plastic deformation. Once nucleated the voids grew preferentially with their major axes aligned on an angle with respect to the thickness direction. The cross section of the tomography samples were approximately 1:1. This suggests that the preferential direction of growth has a relationship with the crystallographic texture of the material as it is just as likely to shear with respect to the width direction from a geometrical standpoint. Furthermore, the growth of the holes was observed to occur rapidly. The linkage of the holes was qualitatively different from what has been observed in FCC materials. The characteristics of void linkage in the magnesium materials tested did not reveal any shear or internal necking features suggesting the damage was driven by the failure of twin and grain boundaries. Tomography samples were examined under the optical microscope to reveal the surface characteristics which caused damage. Twin and grain boundary fracture dominated on the sample surface and observation of the fracture characteristics suggests that these mechanisms were also

responsible for damage in the sample interior. The fracture surfaces revealed two main features; a faceted structure which tended to have a preferential orientation with respect to the sample surface and irregular features associated with defined boundaries. The results suggest that there is a competition of strain localizations created by the sample geometry and localizations created by the local crystallographic texture. These characteristics were also observed in the samples examined in the previous chapters which enforces the fact that the fracture mechanisms have been consistent throughout all of the samples tested in this work.

6.7 Summary

The key observations and conclusions drawn from the work presented in this chapter are summarized below:

- Void nucleation occurs relatively early in the plastic region of deformation due to the failure of grain and twin boundaries.

- Several samples were tested to determine the nucleation strain of detectable voids with a size of at least 575 μm^3. These voids were detected in samples at strains as low as 0.042, however, on average the nucleation of these holes occurred at a strain of approximately 0.105.

- The voids exhibited flat irregular characteristics from the onset of deformation. The sphericity of the larger voids were evaluated as a function of true strain to determine

if a Rice and Tracey type approach was adequate to predict the void growth behavior.

- As deformation proceeded the voids became more irregular in shape. The holes had low values of sphericity which decreased with strain and as a result, the Rice and Tracey approach was not used.

- A simple model proposed by Pilling and Ridley was used to predict the average growth of the holes in the magnesium samples examined.

- The void growth parameter was relatively large compared to values in the literature suggesting that voids in magnesium grow rapidly once they nucleate.

- Void growth was observed to occur in a preferential direction. The major axis of the holes tend to align on angles with respect to the through thickness of the material. This suggests a relationship between the growth of the holes and the crystallographic texture.

- Void linkage occurred by the failure of twin and grain boundaries and displayed a similar relationship with the sample geometry. The macroscopic failure of all of the materials tested occurred by a shear process through the sample thickness.

- The width to thickness ratio of the samples were approximately 1:1, therefore, from a geometrical standpoint it is just as probable to shear with relation to the width direction as it is to shear through the thickness. The result suggests a competition

of fracture mechanisms; one imposed by strain associated with the sample geometry and one due to the local crystallographic orientation.

- Tests were carried out under the optical microscope to observe the tomography tensile sample surface during deformation. Twin and grain boundaries were observed to cause damage.

- The characteristics of the fracture surface were consistent throughout the entire sample geometry suggesting that the fracture mechanisms observed on the surface were also responsible for damage within the bulk of the material.

- The fracture surface revealed two main characteristics; facets with a geometrical relationship to the sample and irregular features. The facets were found to occur roughly perpendicular to the through thickness direction and the irregular features occurred along defined boundaries with no relationship to the sample geometry or crystallographic orientation. The result shows the competition between failure of boundaries with unfavorable geometrical orientations related to the sample geometry and those with unfavorable crystallographic relationships along the boundary.

- The fracture characteristics were compared with the samples tested in the previous chapters and similar features were observed suggesting that the fracture mechanisms were consistent for all of the materials examined in this work.

Chapter 7

Conclusions and Future Work

The primary focus of this research project was to use a variety of experimental, characterization and modelling techniques in order to understand the deformation and fracture of CP magnesium. These results are particularly important for the development of magnesium materials with enhanced properties. The main contributions are described below.

In Chapter 4, void growth and linkage was visualized in magnesium model materials using tensile testing coupled with electron microscopy. The growth of the holes was observed to occur non-uniformly, which revealed the heterogeneous nature of deformation in magnesium. An isotropic finite element analysis was carried out using part files and material properties obtained from the samples tested. Not unexpectedly, the finite element analysis failed to predict the growth of the holes. This is because texture evolution and interactions between the holes and the surrounding microstructure play a major role in the local evolution of the holes and their linkage. The interactions of the holes with twin and grain boundaries were observed to have the most significant impact. These features introduce a length scale in which continuum mechanics cannot be used to predict the behavior.

Several mechanisms of void linkage were observed which include internal necking, shear fracture and failure associated with twin and grain boundaries. The dominating fracture mechanisms observed in all of the hole configurations investigated were failure associated with twin and grain boundaries. EBSD analysis revealed that both extension twins and contraction twins contributed to the final fracture. Grain and twin associated failure caused premature linkage of the holes. As a result, the void fraction and void orientation did not show a correlation with the hole dimensions at failure. The results indicate that a Brown and Embury or Thomason approach is not sufficient to predict failure in magnesium.

In Chapter 5, tensile testing coupled with microscopy and the DIC method was used to obtain quantitative information related to the deformation associated with twin and grain boundaries. Strain concentrations were observed at preferentially oriented grain and twin boundaries. Model materials were tested and boundary related failure was observed in all of the configurations. As a result, the effects of void fraction and void orientation on the strain at failure were not apparent. However, the high resolution strain grids allowed for the strain to be quantified at boundaries adjacent to the holes. The maximum point strain in each sample just before fracture was obtained and showed a normal distribution when compared amongst all of the samples tested. The result suggests that the boundary related failure occurs at a critical strain value.

Another advantage of the technique presented in Chapter 5 is that the experimental results can be directly compared with a crystal plasticity finite element approach. This type

of modelling technique accounts for texture evolution and local microstructural features. Part files were created from digitized EBSD data in order to reproduce the microstructure of the samples tested. The material property was defined by a UMAT and each grain was partitioned and assigned the corresponding Euler angels. This modelling technique was able to predict the hot spots in the material with excellent precision. The results give valuable information on the role of the various hardening parameters during the room temperature deformation of magnesium. It was established that basal dislocation slip and extension twinning play a significant role in the early stages of deformation. Strain localizations were observed early in deformation where basal slip was the only active deformation mechanism. Prismatic slip becomes more significant at intermediate stages of deformation and there is a small contribution from pyramidal slip in the later stages of deformation. The results also helped to understand the role of twinning. In the early stages of deformation, twinning (contraction and extension) is essential in accommodating strain concentrations along the c-axis. However, once nucleated, the twin introduces a boundary which creates additional obstacles for dislocation movement as well as another boundary for compatibility stresses to accumulate along. In the later stages of deformation, preferentially oriented boundaries exhibit strain concentrations too large to maintain compatibility and failure occurs.

In Chapter 6, in-situ tensile testing and x-ray microtomography were used to observe the fracture processes in bulk magnesium samples. The goal of these experiments was to learn how the results obtained in the previous chapters could be applied to

commercial materials. The nucleation of flat, irregular shaped voids occurred during plastic deformation. Furthermore, the voids were tracked as a function of deformation to understand the growth rate. The larger voids were observed to grow rapidly in preferential directions related to the sample geometry and crystallographic orientation. As a result, the final failure exhibited the same relationship. Fracture occurred by a macroscopic shearing process through the thickness. The fracture surface revealed two main features; facets aligned perpendicular to the through thickness and irregular features associated with defined boundaries.

The fracture surfaces were compared with the observations presented in the previous chapters to relate the fracture characteristics with the microstructure. The failure of twin boundaries was observed to occur by a shear process and related to the faceted characteristics on the fracture surface. Furthermore, the irregular features were associated with the failure of grain boundaries. It was established that twin and grain boundary failure are the dominant fracture mechanisms in all of the magnesium samples tested. However, in terms of material engineering, twinning should not be supressed. This deformation mechanism accommodates strain in the earlier stages of deformation. In addition, the samples tested in Chapter 4 exhibited a randomized texture in the region adjacent to the holes. These holes experienced more deformation prior to fracture compared to the samples with a strong basal texture. Therefore, alloy or process design strategies with the objective to randomize the texture are headed in the right direction to obtain good ductility.

The work presented resolves the controversy in the literature regarding the role of twinning on the deformation and fracture of magnesium. Several studies report that certain twin types are beneficial for the microstructure during deformation while others are detrimental. The results show that the initial purpose of twinning is to accommodate strain incompatibilities along the c-axis. However, once nucleated the twin inevitably acts as a boundary. Both extension and contraction twins were observed to contribute to the final fracture. Furthermore, the failure associated with twin and grain boundaries introduces a new length scale, which changes the way we need to look at modelling such behavior. Classical continuum theories cannot predict the deformation and fracture of the magnesium materials investigated in this work. As a consequence, a crystal plasticity finite element approach has been used in order to gain a better understanding of this behavior. In general, the hardening values that are input into crystal plasticity simulations are obtained from macroscopic measurements. This project illustrates a new method for obtaining hardening parameters based on microscopic measurements. Finally, the results presented in this work reveal the significance of grain and twin boundaries on damage accumulation. Perhaps material engineering efforts should be aimed at strengthening grain boundaries or increasing the activity of <c+a> slip in order to enhance the ductility of magnesium alloys.

The work presented here should be viewed as a foundation in which further work can aid in the development of magnesium technology. Here is a proposal of future experiments that could push the frontiers of magnesium research.

- The experiments presented in Chapter 4 could be carried out using x-ray tomography. The surface characteristics observed are just as probable to occur on the surface that was not in view. EBSD maps can be obtained on both surfaces and the samples could be tested in a system capable of in situ tomography in order to observe the 3D fracture process.
- The crystal plasticity finite element approach has proven to be a very effective tool in pinning down the hardening parameters in CP magnesium at the microscopic level. Up to this point the majority of hardening parameters reported in the literature for various magnesium alloy systems are compared to macroscopic properties. The experiments presented in Chapter 5 can be extended to alloy systems to understand the hardening behavior at the microscopic level.
- Synchrotron radiation sources can now be used to map texture in 3D. It was established that the microstructure played a significant role in the deformation and fracture of magnesium. Precise 3D microstructures could be inputted into the crystal plasticity finite element method in order to understand the deformation and fracture of bulk materials.
- Finally, x-ray tomography is a powerful technique which enables the fracture process to be observed in 3D. The results presented in this thesis show that twin and grain boundaries are void nucleation sites in CP magnesium. Therefore, the work presented in Chapter 6 can be extended to alloy systems in order to understand the nucleation process and the role of particles in these materials.

Bibliography

Abràmoff, Michael D, Magalhães, Paulo J, & Ram, Sunanda J. (2004). Image processing with ImageJ. Biophotonics international, 11(7), 36-43.

Agnew, S. R., Yoo, M. H., & Tome, C. N. (2001). Application of texture simulation to understanding mechanical behavior of Mg and solid solution alloys containing Li or Y. Acta Materialia, 49(20), 4277-4289.

Agnew, Sean R., & Duygulu, Ozgur. (2003). A mechanistic understanding of the formability of magnesium: Examining the role of temperature on the deformation mechanisms. Paper presented at the Proceedings of the Second Osaka International Conference on Platform Science and Technology for Advanced Magnesium Alloys 2003, January 26, 2003 - January 30, 2003, Osaka, Japan.

Akhtar, A., & Teghtsoonian, E. (1969). Solid solution strengthening of magnesium single crystals. II. The effect of solute on the ease of prismatic slip. Acta Metallurgica, 17(11), 1351-1356.

Argon, A. S., & Im, J. (1975). SEPARATION OF SECOND PHASE PARTICLES IN SPHEROIDIZED 1045 STEEL, Cu-0. 6PCT Cr ALLOY, AND MARAGING STEEL IN PLASTIC STRAINING. Metallurgical Transactions A (Physical Metallurgy and Materials Science), 6 A(4), 839-851.

Argon, A. S., Im, J., & Safoglu, R. (1975). CAVITY FORMATION FROM INCLUSIONS IN DUCTILE FRACTURE. Metallurgical Transactions A (Physical Metallurgy and Materials Science), 6 A(4), 825-837.

Babout, L., Brechet, Y., Maire, E., & Fougeres, R. (2004). On the competition between particle fracture and particle decohesion in metal matrix composites. Acta Materialia, 52(15), 4517-4525.

Barnby, J. T. (1967). The initiation of ductile failure by fractured carbides in an austenitic stainless steel. Acta Metallurgica, 15(5), 903-909.

Barnett, M. R. (2007a). Twinning and the ductility of magnesium alloys. Part I: "Tension" twins. Materials Science and Engineering A, 464(1-2), 1-7.

Barnett, M. R. (2007b). Twinning and the ductility of magnesium alloys. Part II. "Contraction" twins. Materials Science and Engineering A, 464(1-2), 8-16.

Barnett, M., Arhatari, B., Stanford, N., Beer, A., Keshavarz, Z., & Ma, X. (2008). Some issues relating to the ductility of wrought magnesium alloys. Paper presented at the TMS 2008: Linking Science and Technology for Global Solutions: TMS 2008 Annual Meeting and Exhibition.

Baruchel, José, Buffiere, Jean-Yves, & Maire, Eric. (2000). X-ray tomography in material science.

Benzerga, A. A. (2002). Micromechanics of coalescence in ductile fracture. Journal of the Mechanics and Physics of Solids, 50(6), 1331-1362.

Benzerga, AAmine, & Leblond, Jean-Baptiste. (2010). Ductile fracture by void growth to coalescence. Advances in Applied Mechanics, 44, 169-305.

Brown, L. M., & Embury, J. D. (1973). INITIATION AND GROWTH OF VOIDS AT SECOND PHASE PARTICLES. Institute of Metals (London), Monograph and Report Series, 1(3), 164-169.

Brown, L. M., & Stobbs, W. M. (1976). The work-hardening of copper-silica. V. Equilibrium plastic relaxation by secondary dislocations. Philosophical Magazine, 34(3), 351-372.

Calhoun, C., & Stoloff, N. (1970). The effects of particles on fracture processes in magnesium alloys. Metallurgical Transactions, 1(4), 997-1006.

Cox, T. B., & Low, J. R., Jr. (1974). An investigation of the plastic fracture of AISI 4340 and 18 nickel-200 grade maraging steels. Metallurgical Transactions A (Physical Metallurgy and Materials Science), 5(6), 1457-1470.

Day, A, & Trimby, P. (2004). Channel 5 manual. HKL Technology Inc., Hobro, Denmark.

Drucker, DC. (1960). Structural Mechanics. Paper presented at the Proceedings of the First Symp. Naval Structural Mechanics, Pergamon Press, Oxford.

Dunne, Fionn, & Petrinic, Nik. (2005). Introduction to computational plasticity: Oxford University Press New York.

Goldstein, Joseph, Newbury, Dale E, Echlin, Patrick, Joy, David C, Romig Jr, Alton D, Lyman, Charles E, Lifshin, Eric. (2012). Scanning electron microscopy and X-ray microanalysis: a text for biologists, materials scientists, and geologists: Springer Science & Business Media.

Goods, S. H., & Brown, L. M. (1979). Overview No. 1: The nucleation of cavities by plastic deformation. Acta Metallurgica, 27(1), 1-15.

Granta. (2013). CES Selector.

Greenwood, J. Neill, Miller, D. R., & Suiter, J. W. (1954). Intergranular cavitation in stressed metals. Acta Metallurgica, 2(2), 250-258.

Griffith, Alan A. (1921). The phenomena of rupture and flow in solids. Philosophical transactions of the royal society of london. Series A, containing papers of a mathematical or physical character, 163-198.

Hartt, WH, & Reed-Hill, RE. (1967). The irrational habit of second-order/1011/-/1012/twins in magnesium.

Hazeli, K., Askari, H., Cuadra, J., Streller, F., Carpick, R. W., Zbib, H. M., & Kontsos, A. (2015). Microstructure-sensitive investigation of magnesium alloy fatigue. International Journal of Plasticity, 68, 55-76

Hazeli, K., Cuadra, J., Vanniamparambil, P. A., & Kontsos, A. (2013). In situ identification of twin-related bands near yielding in a magnesium alloy. Scripta Materialia, 68(1), 83-86.

Hill, Rodney. (1950). The mathematical theory of plasticity.

Hosokawa, Akihide. (2011). Void growth and coalescence studied by X-ray computed tomography. (NR73993 Ph.D.), McMaster University (Canada).

Hosokawa, Akihide, Wilkinson, David S., Kang, Jidong, & Maire, Eric. (2012). Effect of triaxiality on void growth and coalescence in model materials investigated by X-ray tomography. Acta Materialia, 60(6–7), 2829-2839.

Hosokawa, Akihide, Wilkinson, David S., Kang, Jidong, & Maire, Eric. (2013). Onset of void coalescence in uniaxial tension studied by continuous X-ray tomography. Acta Materialia, 61(4), 1021-1036.

Hsu, Eugene. (2007). Study of ultrashort pulse laser induced surface ripples and investigation of other applications of ultrashort pulse laser micromachining and ablation.

Huang, Y. (1991). Accurate Dilatation Rates for Spherical Voids in Triaxial Stress Fields. Journal of Applied Mechanics, 58(4), 1084-1086.

Instruments, Oxford. (2015). Retrieved from http://www.ebsd.com/

Kanetake, N., Nomura, M., & Choh, T. (1995). Continuous observation of microstructural degradation during tensile loading of particle reinforced aluminium matrix composites. Materials Science and Technology, 11(12), 1246-1246.

Kang, Jidong, Ososkov, Yuriy, Embury, J. David, & Wilkinson, David S. (2007). Digital image correlation studies for microscopic strain distribution and damage in dual phase steels. Scripta Materialia, 56(11), 999-1002.

Kang, J., Wilkinson, D. S., Mishra, R. K., Embury, J. D., Essadiqi, E., & Javaid, A. (2013). Microstructural Aspects of damage and fracture in AZ31 sheet materials. Journal of materials engineering and performance, 22(5), 1386-1395.

Kelley, EW, & HOSFORD, WFJR. (1968). Plane-strain compression of magnesium and magnesium alloy crystals. Trans Met Soc AIME, 242(1), 5-13.

Keralavarma, S. M., Hoelscher, S., & Benzerga, A. A. (2011). Void growth and coalescence in anisotropic plastic solids. International Journal of Solids and Structures, 48(11–12), 1696-1710.

Kobayashi, T., Koike, J., Yoshida, Y., kamado, S., Suzuki, M., Maruyama, K., & Kojima, Y. (2003). Grain size dependence of active slip systems in an AZ31 Magnesium alloy. Journal of the Japan Institute of Metals, 67(4), 149-152.

Koike, J., & Ohyama, R. (2005). Geometrical criterion for the activation of prismatic slip in AZ61 Mg alloy sheets deformed at room temperature. Acta Materialia, 53(7), 1963-1972.

Koike, J., Ohyama, R., Kobayashi, T., Suzuki, M., & Maruyama, K. (2003). Grain-boundary sliding in AZ31 magnesium alloys at room temperature to 523 K. Materials Transactions, 44(4), 445-451.

Le Roy, G., Embury, J. D., Edwards, G., & Ashby, M. F. (1981). A model of ductile fracture based on the nucleation and growth of voids. Acta Metallurgica, 29(8), 1509-1522.

Lecarme, L., Maire, E., Kumar K.c, A., De Vleeschouwer, C., Jacques, L., Simar, A., & Pardoen, T. (2014). Heterogenous void growth revealed by in situ 3-D X-ray microtomography using automatic cavity tracking. Acta Materialia, 63, 130-139.

Lhuissier, P., Scheel, M, Salvo, L., Di Michiel, M., & Blandin, J. (2012). IN SITU 3D CHARACTERISATION OF DAMAGE INDUCED BY HIGH TEMPERATURE DEFORMATION OF MAGNESIUM ALLOYS. Paper presented at the Mg2012: 9th International Conference on Magnesium Alloys and their Applications.

Li, Jing. (2013). Two-Dimensional Investigation of Void Growth and Coalescence during Deformation. Open Access Dissertations and Theses.

Li, Shaofan, & Wang, Gang. (2008). Introduction to micromechanics and nanomechanics (Vol. 278): World Scientific.

Martin, G., Sinclair, C. W., & Lebensohn, R. A. (2014). Microscale plastic strain heterogeneity in slip dominated deformation of magnesium alloy containing rare earth. Materials Science and Engineering: A (Structural Materials: Properties, Microstructure and Processing), 603, 37-51.

McClintock, Frank A. (1968a). A criterion for ductile fracture by the growth of holes. Journal of applied mechanics, 35(2), 363-371.

McClintock, Frank A. (1968b). Local criteria for ductile fracture. International Journal of Fracture Mechanics, 4(2), 101-130.

McMeeking, R. M., & Hom, C. L. (1990). Finite element analysis of void growth in elastic-plastic materials. International Journal of Fracture, 42(1), 1-19.

Mises, R von. (1928). Mechanik der plastischen Formänderung von Kristallen. ZAMM-Journal of Applied Mathematics and Mechanics/Zeitschrift für Angewandte Mathematik und Mechanik, 8(3), 161-185.

Miura, H., Sakai, T., Nogawa, H., Yang, X., Watanabe, Y., & Miura, S. (2005). Orientation dependence of ductility of Mg single crystals at elevated temperature. Paper presented at the International Conference on Magnesium - Science, Technology and Applications, September 20, 2004 - September 24, 2004, Beijing, China.

Nemcko, Michael J, Wilkinson, David S, & Kang, Jidong. (2012). THE 2 DIMENSIONAL ANALYSIS OF VOID GROWTH AND COALESCENCE DURING DEFORMATION IN MAGNESIUM.

Nemcko, Michael J., Mas, Pauline, Bruhis, Moisei, & Wilkinson, David S. (2014). Characterization of damage in magnesium using digital image correlation and electron backscattered diffraction patterning. Paper presented at the Magnesium

Technology 2014 - TMS 2014 143rd Annual Meeting and Exhibition, February 16, 2014 - February 20, 2014, San Diego, CA, United states.

Nemcko, Michael J., & Wilkinson, David S. (2013a). In situ damage examination during room temperature deformation of commercially pure magnesium using X-ray micro-computed tomography. Paper presented at the Materials Science and Technology Conference and Exhibition 2013, MS and T 2013, October 27, 2013 - October 31, 2013, Montreal, QC, Canada.

Nemcko, Michael J., & Wilkinson, David S. (2013b). Investigation of void linkage in magnesium using SEM and micro computed X-ray tomography. Paper presented at the 13th International Conference on Fracture 2013, ICF 2013, June 16, 2013 - June 21, 2013, Beijing, China.

Obara, T., Yoshinga, H., & Morozumi, S. (1973). {112 2}<1123> Slip system in magnesium. Acta Metallurgica, 21(7), 845-853.

Ohyama, Ray, Koike, Junichi, Suzuki, Mayumi, & Maruyama, Kouichi. (2004). Texture dependence of elongation anisotropy in an AZ61 magnesium alloy sheet. Nippon Kinzoku Gakkaishi/Journal of the Japan Institute of Metals, 68(1), 27-33.

Pardoen, T., & Hutchinson, J. W. (2000). An extended model for void growth and coalescence. Journal of the Mechanics and Physics of Solids, 48(12), 2467-2512.

Partridge, P. G. (1967). Deformation and fatigue of hexagonal close packed metals. Univ. of Surrey, UK, Guildford, UK.

Pilling, J, & Ridley, N. (1986). Effect of hydrostatic pressure on cavitation in superplastic aluminium alloys. Acta Metallurgica, 34(4), 669-679.

Puttick, KE. (1959). Ductile fracture in metals. Philosophical magazine, 4(44), 964-969.

Qiao (2015). [Crystal Plasticity Finite Element Approach].

Reed-Hill, R. E., & Robertson, W. D. (1957). The crystallographic characteristics of fracture in magnesium single crystals. Acta Metallurgica, 5(12), 728-737.

Reuss, A. (1930). Berücksichtigung der elastischen Formänderung in der Plastizitätstheorie. ZAMM-Journal of Applied Mathematics and Mechanics/Zeitschrift für Angewandte Mathematik und Mechanik, 10(3), 266-274.

Rice, J. R., & Tracey, D. M. (1969). On the ductile enlargement of voids in triaxial stress fields∗. Journal of the Mechanics and Physics of Solids, 17(3), 201-217.

Schmid, Erich, & Boas, Walter. (1968). Plasticity of crystals, with special reference to metals. London: Chapman & Hall.

Simulia, Dassault Systemes. (2012). Abaqus 6.12 documentation. Providence, Rhode Island, US.

Skyscan. (2005). Skyscan 1172 Desktop X-ray Microtomography Instruction Manual.

Skyscan. (2010). Skyscan Material Testing Stage User Manual.

Skyscan. (2011). Skyscan NRecon User Manual.

Somekawa, H., Singh, A., & Mukai, T. (2009). Fracture mechanism of a coarse-grained magnesium alloy during fracture toughness testing. Philosophical Magazine Letters, 89(1), 2-10.

Standard, ASTM. (1996). E112: Standard Test Methods for Determining Average Grain Size. West Conshocken.

Steglich, D., & Morgeneyer, T. F. (2013). Failure of magnesium sheets under monotonic loading: 3d examination of fracture mode and mechanisms. International Journal of Fracture, 183(1), 105-112.

Tanaka, K., Mori, T., & Nakamura, T. (1970). CAVITY FORMATION AT THE INTERFACE OF A SPHERICAL INCLUSION IN A PLASTICALLY DEFORMED MATRIX. 21(170), 267-279.

Taylor, Geoffrey Ingram, & Quinney, H. (1932). The plastic distortion of metals. Philosophical Transactions of the Royal Society of London. Series A, Containing Papers of a Mathematical or Physical Character, 323-362.

Team, R Core. (2000). R Language Definition: Available from CRAN sites.

Techniques, GOM Optical Measuring. (2005). Aramis v5. 4 user manual. GOM mbH.

Tekoğlu, C., Leblond, J. B., & Pardoen, T. (2012). A criterion for the onset of void coalescence under combined tension and shear. Journal of the Mechanics and Physics of Solids, 60(7), 1363-1381.

Thomason, P. F. (1981). Ductile fracture and the stability of incompressible plasticity in the presence of microvoids. Acta Metallurgica, 29(5), 763-777.

Thomason, P. F. (1985). Three-dimensional models for the plastic limit-loads at incipient failure of the intervoid matrix in ductile porous solids. Acta Metallurgica, 33(6), 1079-1085.

Thomason, PF. (1990). Ductile fracture of metals. Pergamon Press plc, Ductile Fracture of Metals(UK), 1990, 219.

Wadell, Hakon. (1933). Sphericity and roundness of rock particles. The Journal of Geology, 310-331.

Weck, A., Crawford, T. H. R., Borowiec, A., Wilkinson, D. S., & Preston, J. S. (2007a). Femtosecond laser-based fabrication of a new model material to study fracture. Applied Physics A (Materials Science Processing), A86(1), 55-61.

Weck, A., Crawford, T. H. R., Wilkinson, D. S., Haugen, H. K., & Preston, J. S. (2008). Laser drilling of high aspect ratio holes in copper with femtosecond, picosecond and nanosecond pulses. Applied Physics A: Materials Science Processing, 90(3), 537-543.

Weck, A., & Wilkinson, D. S. (2008). Experimental investigation of void coalescence in metallic sheets containing laser drilled holes. Acta Materialia, 56(8), 1774-1784.

Weck, Arnaud G. (2007). The role of coalescence on ductile fracture. (NR36050 Ph.D.), McMaster University (Canada), Ann Arbor.

Weck, Arnaud, Segurado, Javier, Llorca, Javier, Wilkinson, David, & Bohm, Helmut. (2007b). Numerical simulations of void linkage in model materials using a nonlocal ductile damage approximation. International Journal of Fracture, 148(3), 205-219.

Wonsiewicz, B. C., & Backofen, W. A. (1967). Plasticity of magnesium crystals. Transactions of the metallurgical society of AIME(239), 1422-1431.

Worswick, M. J., & Pick, R. J. (1990). Void growth and constitutive softening in a periodically voided solid. Journal of the Mechanics and Physics of Solids, 38(5), 601-625.

Wu, P. D., Guo, X. Q., Qiao, H., & Lloyd, D. J. (2015). A constitutive model of twin nucleation, propagation and growth in magnesium crystals. Materials Science and Engineering A, 625, 140-145.

Yang, Y., Wang, L., Bieler, T. R., Eisenlohr, P., & Crimp, M. A. (2011). Quantitative Atomic Force Microscopy Characterization and Crystal Plasticity Finite Element Modeling of Heterogeneous Deformation in Commercial Purity Titanium. Metallurgical and Materials Transactions A (Physical Metallurgy and Materials Science), 42(3), 636-644.